Alma Mater Studiorum - Università di Bologna

DOTTORATO DI RICERCA IN

Ingegneria Civile, Ambientale e dei Materiali

Ciclo: **XXIX**

Settore Concorsuale di afferenza: **08A1**

Settore Scientifico disciplinare: **ICAR/01**

Development, analysis and comparison of two concepts for wave energy conversion in the Mediterranean Sea

---

Presentata da: Adrià Moreno Miquel

Coordinatore Dottorato:

Prof. Luca Vittuari

Relatore:

Prof. Renata Archetti

Co-Relatore:

Prof. Alberto Lamberti

Esame finale anno 2017

Abstract

The investigations carried out during this Ph.D. programme relate to the marine engineering field, more specifically to wave energy conversion. Two different wave energy converters have been modelled numerically with the aim to assess the feasibility of wave energy conversion in the Mediterranean Sea. Moreover, the ability of the open source CFD software REEF3D to generate and absorb waves has been studied through wave reflection analysis.

The first studied wave energy converter, named HPA-LG, is a heaving point absorber with a linear generator placed at the seabed. Two variants of the WEC have been examined. Firslty, the classical configuration with floater and generator has been analysed. Afterwards, a third body has been added in order to modify the natural period of the system. The third body is a submerged sphere of neutral buoyancy placed 25 metres below the water surface. Both devices have been tuned to the Mediterranean wave climate, paying particular attention to the floater dimensions and to the geometrical design of the PTO. Initially, only the heave mode has been modelled and the performance of both devices has been analysed. Subsequently, the surge mode has been added to the model. Finally, the effect of the surge in prevalent heaving point absorbers has been studied.

For the two-body device, although the dynamic behaviour changes when the surge is included, no relevant differences are observed regarding the power production. When studying the three-body device, results show two clear trends. On the one hand, for steep waves the surge leads to a decrease in the production, since the PTO geometrical limits are reach. On the other hand, for flatter waves it affects positively the power absorption. However, the overall the negative contribution is more relevant.

The MoonWEC is the second studied wave energy converter, it merges several working principles with the aim to benefit from the assets of each single principle. It consists in a hollow floating structure, where water fills a central whole creating a moonpool. The idea is to create a relative motion between the floater and the moonpool water and then, absorb the energy via a Wells turbine placed in the moonpool. The model takes into account the structure motion in heave, surge and pitch; the relative displacement of the moonpool and the Wells turbine rotation. Device optimization has also been carried out according to the Mediterranean wave climate, six different CALM mooring

configurations and three Wells turbines have been tested.

Both device show similarities in their performance, their production is maximised for a specific range of wave conditions. The HPA-LG has a broader optimal range. However, the MoonWEC is more efficient for mild wave conditions and as a result, its annual energy production is $[50-100]$ % higher, depending on the location and HPA-LG variant. Also, its design properties makes it less vulnerable to breakdowns.

The 3D numerical wave tank feature of REEF3D includes different methods to generate and absorb waves; two different relaxation methods, which use two different relaxation functions and the active wave absorption. All methods can be implemented either in the wave generation area and/or at the other edge of the tank. A sensitivity analysis has been conducted in order to quantify and compare the differences, in terms of absorption quality and computational performance between these methods. The reflection analysis developed by Zelt & Skjelbreia (1992), based on an arbitrary number of wave gauges, has been adopted to conduct the study. Tests include: reflection analysis in an empty tank with linear, 2^{nd} and 5^{th} order Stoke waves, solitary waves, Cnoidal waves and irregular waves. Furthermore, wave-structure interaction with a fixed vertical cylinder and a constant slope bed have been studied relating forces and wave breaking to reflection. In addition, a comparison with another CFD open source (OpenFOAM) code has been carried out.

Results are promising; showing good agreement with theoretical values. Although some differences have been observed depending on the wave generation and absorption method, high overall absorption rates have been achieved for all methods.

Contents

List of Figures

LIST OF FIGURES

List of Tables

Acronyms

AAR	Active Area Ratio.
AEP	Average Energy Production.
ALC	Articulated Loading Column.
AWA	Active Wave Absorption.
BC	Boundary Condition.
BEM	Boundary Element Method.
CAD	Computer Assisted Design.
CALM	Catenary Anchor Leg Mooring.
CFD	Computational Fluid Dynamics.
CFL	Courant–Friedrichs–Lewy.
CoG	Centre of Gravity.
CS	Control Surface.
DC	Direct Current.
DoF	Degree of Freedom.
FPSO	Floating Production Storage Unit.
FTM	Fixed Tower Mooring.
GHG	GreenHouse Gas.
HPA-LG	Heaving Point Absorber Linear Generator.
IFFT	Inverse Fourier Transform.
IPCC	Intergovernmental Panel on Climate Change.

IRF	Impulse Response Function.
JONSWAP	JOint North Sea WAve Project.
KC	Keulegan-Karpenter.
LG	Linear electric Generator.
LHEEA	Laboratoire d'Hydrodynamique,Énergétique et Environnement.
MBL	Minimum Breaking Load.
MIT	Massachusetts Institute of Technology.
MoonWEC	Moonpool WEC.
MPI	Message Passing Interface.
MWD	Mean Wave Direction.
MWL	Mean Water Level.
NACA	National Advisory Committee of Aeronautics.
NRBC	Non-Reflective Boundary Condition.
NWT	Numerical Wave Tank.
O&M	Operation and Maintenance.
ODE	Ordinary Differential Equation.
OWC	Oscillating Water Column.
PDF	Probability Distribution Function.
PM	Permanent Magnet.
PML	Perfectly Match Layer.
PMSG	Permanent Magnet Synchronous Generator.
POT	Peak Over Threshold.
PTO	Power Take-Off.
RANS	Reynolds-Averaged Navier-Stokes equations.
RAO	Response Amplitude Operator.
RM	Relaxation Method.
RON	National Italian Wave Measurement Network.

SALM	Single Anchor Leg Mooring.
SG	Synchronous Generator.
SI	International System.
TLP	Tension Leg Platform.
TVD	Total Variation Diminishing.
W-T	Wells turbine.
WEC	Wave Energy Converter.
WENO	Weighted Essentially Non Oscillatory.

1

Introduction

1.1 Renewable Energies

For the past century and a half continuous wealth creation and economic growth have reached unprecedented levels throughout human history. A society can only be developed properly if large amounts of energy are available. With the industrial revolution and the discovery of fossil fuels as a primary energy resource, the world we live in nowadays was made possible. Therefore, it can be stated that the world's current economic model is based on fossil fuels consumption, see figure 1.1.a). These however, bring along some undesired side effects, such as geopolitical instabilities and large GreenHouse Gas (GHG) emissions. The latter are the major cause of the climate change we are immersed in, which could cause an increase of the global averaged temperature up to $5°C$ by the year 2100 according to the 5^{th} assessment report of the Intergovernmental Panel on Climate Change (IPCC) (30), see figure 1.1.b).

Needless to say that this scenario would be catastrophic for humankind and for life on planet earth in general. In order to prevent such predictions from becoming a reality, a new energetic model has to be developed. One of the strategies pointed by the IPCC, along with efficiency increase and demand decrease, is to reduce fossil fuels consumption and increase, as much as possible and as fast as possible, renewable energy sources as a primary energy resource, see figure 1.3. A renewable energy resource is understood as an energy source that can be replenished at the same rate as it is consumed. A renewable energy can emit GHG, however these ought not to be accounted since they are absorbed by the planet at the same pace they are emitted and therefore, the global net balance is zero.

Many are the renewable energy resources. They can be classified in four major

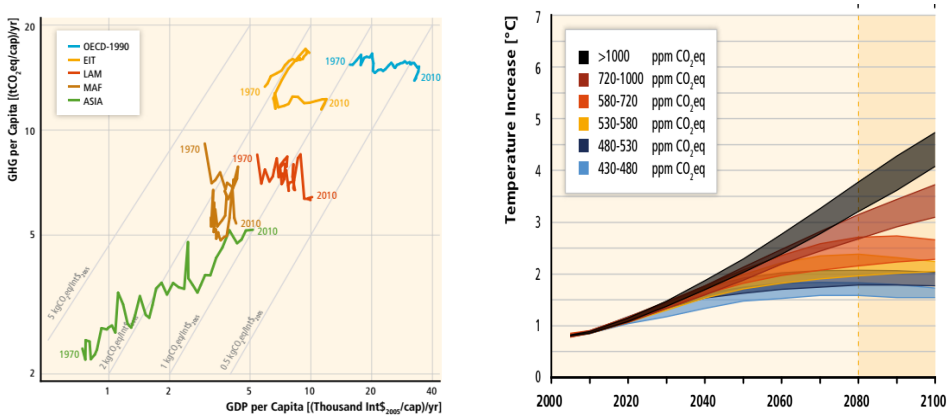

Figure 1.1: *a) GHG emissions per capita vs GDP per capita. b) Temperature increase forecast based on CO_{2eq} concentration on the atmosphere. (30)*

categories according to its nature: geothermal, hydroelectric, biomass and solar. The first exploits internal earth's heat stored underneath the planet's surface. Among its advantages there is its constancy and among its drawbacks there is its availability. It is a very stable energy resource, however usually hard to reach, since mostly is found far deep down the earth crust. The second merely takes advantages of the potential energy stored in high quoted water reservoirs typically found in mountainous systems. Biomass, is the oldest and predominant renewable energy resource until the date, see figure 1.2. Despite not being exempt of GHG emissions, those are not accountable in global GHG emission balance since they are rapidly absorbed by the same vegetation that is then used as biomass. Biomass is partially considered as a solar type of energy resource, since plants in order to thrive need to capture energy from the sun by means of photosynthesis.

Energy coming from the sun can be harvested directly and indirectly. Direct solar energy is divided into two main categories, photovoltaic, taking advantage of the semiconductor properties of silicon, and thermal, in which sun beams are focused onto a reduced area. This energy, concentrated in the form of heat, is then stored in a fluid, typically water.

Wind energy is an indirect form solar energy. Energy coming from the sun is distributed irregularly throughout the planets surface, reaching its maximum at latitudes near the equator and decreasing gradually as moving away from it. This causes remarkable pressure differences in the atmosphere, which in turn creates winds, trying to displace huge amounts of air from high pressure regions towards low pressure re-

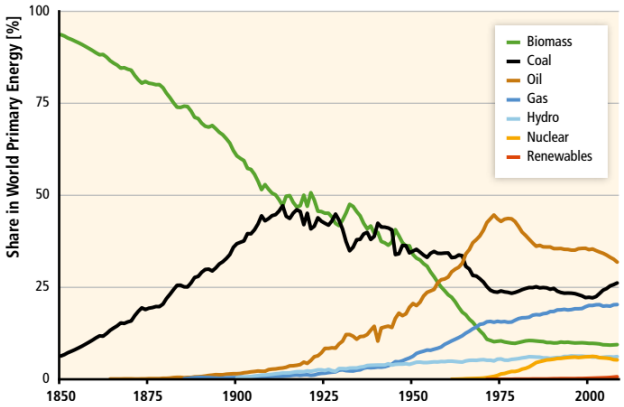

Figure 1.2: *Historical energy source utilization. (10)*

gions. This process causes an energy density increase as wind energy ($0.5kW/m^2$), as in average is 5 times more concentrated than solar energy ($0.1 - 0.3kW/m^2$), (95).

When winds blow over the water surface, part of its energy is transferred to the water by friction thus, generating waves. Again, energy in waves ($2 - 3kW/m^2$) is denser than both, wind and solar. Even though most of solar irradiation energy is lost in this transmission chain, the gain in energy density is a factor that should attract expectation for future energy harvesting.

1.2 Wave Energy

Waves are generated far from the coasts, where wind and storms constantly blow over the fetch and then travel vast distances with practically no loss of energy. As a result, it becomes also a very constant source of energy, there is no need of site-specific climatic events in order to ensure the presence of waves, as waves reaching the shore may have been generated thousands of miles away a few days in the past. Furthermore, wave energy is a highly predictable resource, nowadays wave propagation computer models provide accurate forecast of incoming waves up to a week in advance.

Above 2/3's of the planet surface is covered by oceans and approximately 1/2 of the world's population lives within a $100km$ from the coast. Furthermore, electricity demand and wave seasonal variability match quite well, specially in northern countries where peaks occur during late autumn and winter. The great availability of the resource is another factor to take into account when estimating its potential.

In addition, very low environmental impact has been proved to occur when installing

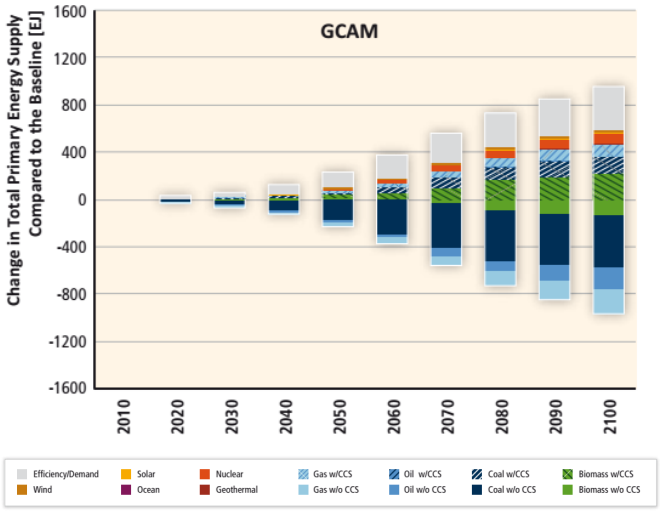

Figure 1.3: *Global forecasted energetic mix for policy scenario GCAM (34)*

Wave Energy Converters (WECs). Due to its reduced size and its typical deployment location (offshore) visual impact is null as well as other impacts for the majority of other human activities, the only exception could be ship routing. Studies on marine life surrounding WECs show concern since the issue has still be studied thoroughly; great uncertainties still prevail on how wave energy may affect the marine ecological system even showing plausible positive impact since the submerged structures are used as artificial reefs by the marine fauna, (24).

For all the stated above, the World Energy Council has appraised the wave energy production potential to be around $2TW$, which is roughly the double of the world's actual electricity production.

1.2.1 History Review

Despite Wave energy conversion has not fully reached the commercial stage yet, is not a young discipline. The first patent ever presented in the field is dated from 1799 in France by the Girards (father and son). Yet it was not until the 1940s when the first prototypes where developed. Yoshio Masuda (1925-2009), who is considered to be one of the fathers of wave energy exploitation, conceived the Oscillating Water Column (OWC) converter concept. By the 1960s, he developed a navigation buoy in which an OWC system was embedded in order to generate the guiding light. In the late 1970s, Masuda deployed at open sea the first large scale WEC, the Kaimei, shown in figure 1.4.

Figure 1.4: *Kaimei WEC*

Meanwhile in the USA, the US Naval Academy was also working on the OWC concept, (72).

In the meantime in Europe, Stephen Salter, from the University of Edinburgh, UK, invented and developed a very different wave energy converter named the Duck, See (85). Salter's publication in the influential scientific journal of Nature first brought the attention of the international scientific community towards wave energy conversion. Subsequently, the British Government developed and ambitious Research&Development program on wave energy. The global economy was immersed in an important crisis due to the rocketing prices of oil. Later in the 1980s due to oil price stabilization and a change of Government policy, the British Wave Energy Program came to a halt without any full-sized prototype having been built and tested.

Simultaneously, control strategies were being developed in Norway by Johannes Falnes and Kjell Budall (1933-89), who introduced the concept of phase-control by latching. See (41). In 1985, the less ambitious Norwegian program went on to the construction of two shoreline prototypes, deployed in the coast near Bergen. It is called the TAPCHAN and consists of an over-topping device with a converging channel, a reservoir and a low-head hydraulic turbine and a OWC with a vertical axis air turbine. See figure 1.5

Until the early 1990s the R&D on wave energy in Europe remained mostly academic. The situation changed drastically with the decision made in 1991 by the European Commission, of including Wave Energy in their R&D programme on Renewable Energies. Since then, many projects have been funded by the European Commission, involving a large number of European teams. Several OWC prototypes have been built from the early 1990s, the LIMPET prototype, built in 1991 in the island of Islay, Scotland, was replaced by a more powerful ($500kW$) version in the year 2000, (99). Pico, in the Azores Islands, Portugal, is hosting another prototype ($400kW$) since 1999. In 2011, the first breakwater-integrated WEC array was installed in the port of Mutriku in the Basque Country, Spain.

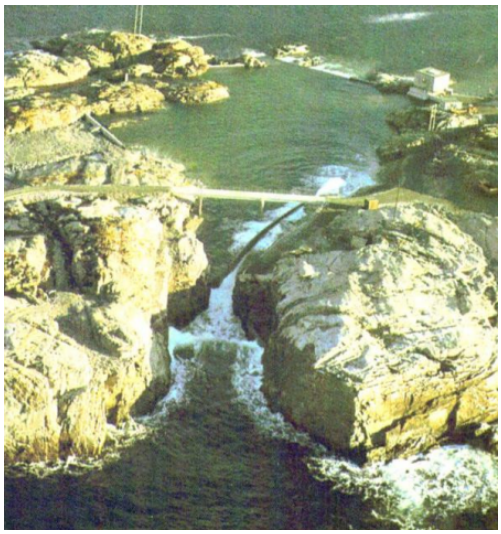

Figure 1.5: *Tapchan WEC*

To sum up, there is a wide variety of WECs, at different development stages, accounting with different shapes, sizes and working principles competing against each other. Unlike the case of large wind turbines, one could say that for wave energy conversion the race is still open.

1.2.2 Protoype Classification

As no uniformity has been reached yet in the wave energy sector, different ways to catalogue the ever increasing number of devices have been established. One of the most basic ones it classifies the devices according to their deployment location; until now, three are the classes that this classification offers: in the shoreline, near shore and offshore. Another common way to distinguish between WECs is to arrange them according to their size and orientation with respect to the wave front. A device with reduced typical dimensions with respect to the incident wave length it is commonly referred to as a point absorber; if this device has more than a body interacting, then one may classify it as a Multibody system. If the typical dimension of the device is of the same order of magnitude as the incident wavelength, but no direction predominates upon another, then the name of Large absorber is adopted. Moreover, if there is a predominant orientation of the device with respect to the wave front the class changes. On the one hand, if the orientation of the prototype is perpendicular to the to the wave front the device is denominated as an Attenuator; on the other hand, if the device orientation is parallel to the wave front it becomes a Terminator device. See figure 1.6

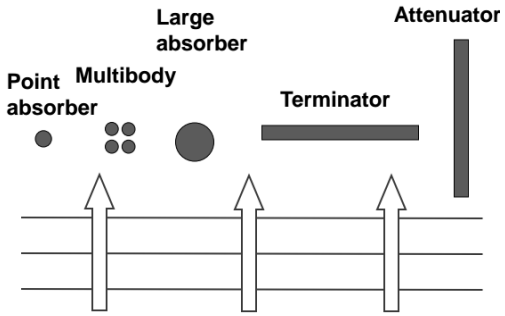

Figure 1.6: *Wave Energy Converter classification according to size and orientation.*

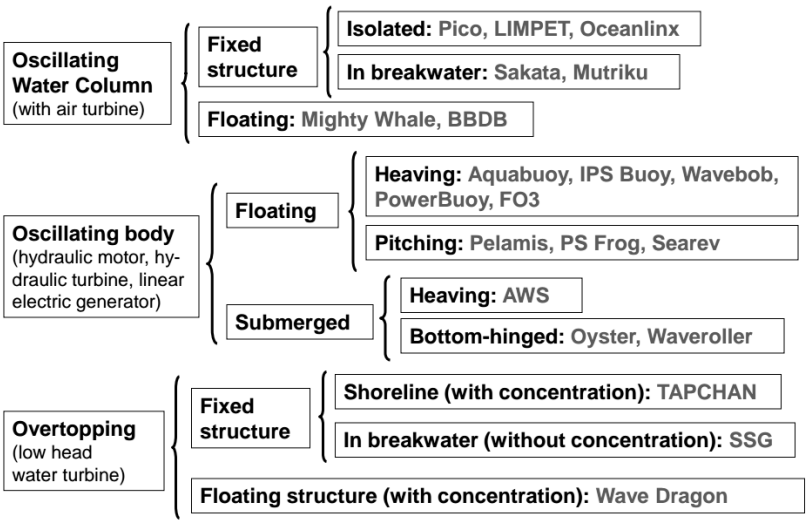

Figure 1.7: *Wave Energy converter Classification based on(40).*

Alternatively, the most widely used classification is done according to the working principle of the device. This methodology (40), divides the converters in three main classes, the Oscillating Water Columns, the Oscillating bodies and the Overtopping devices. Then, a sub-classification, which divides the prototypes according to the type of structure, floating or fixed, is applied. Finally, one last subdivision is done with respect to the motion used to convert to electricity. Figure 1.7 maps this classification system and gives some real examples. The following paragraphs are dedicated to explain in detail the working principles shown in figure 1.7.

1.2.2.1 Oscillating Water Column

Oscillating water column devices are usually composed by a caisson, which is partially submerged and where air is trapped in the upper part. The chamber is open to the sea at the bottom and to the atmosphere at the top. When waves approach pressure differential excites the water column of the chamber, which in turn forces the air contained in it to flow through the top opening. A self-rectifying turbine attached to an electrical generator is usually placed in that opening in order to use the air flow to produce electricity. OWCs can be located at the shore line, either in ad-hoc facility or integrated in breakwaters, or offshore where the caisson is part of a floating structure subjected to the action of waves. Figure 1.8 shows the two phases of the working cicle of OWCs.

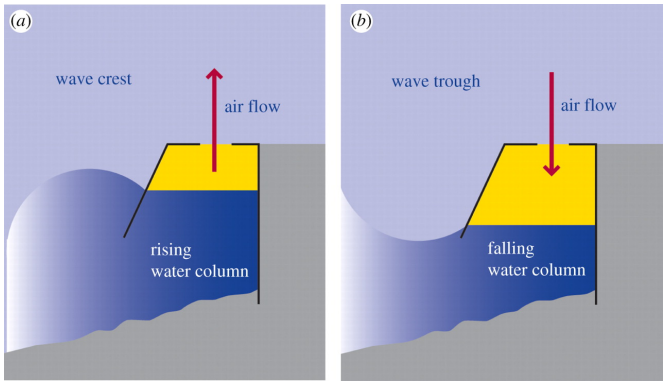

Figure 1.8: *OWC working principle schematic.a) Air outtake phase. b) Air intake phase.*

1.2.2.2 Oscillating Bodies

Unlike OWCs, this type of devices absorb mechanical power from the wave by interacting directly with it. A structure is placed in the water and then excited by waves as these pass through. Energy conversion can be carried out by motion absolute difference with respect to a fixed point or by relative difference with respect to another moving structure, as in the case of a multibody system. This motion however, is usually restricted to a degree of freedom, whether it be in the vertical direction (Heave), in the horizontal direction (surge), rotation (pitch) or even a combination between them. In addition, the structure can be placed near-shore or offshore and floating or attach to a fixed frame, giving a large number of combinations in which to achieve energy conversion, each one with its advantages and drawbacks. Figure 1.9 exemplifies some of the concepts previously described.

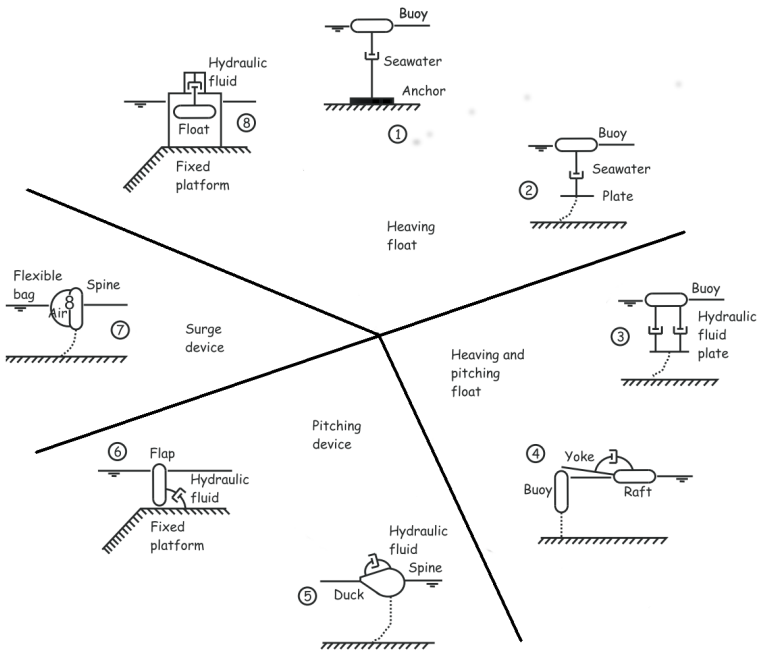

Figure 1.9: *Different types of existing oscillating bodies WEC. Adaptation from (52)*

1.2.2.3 Overtopping

Overtopping devices take advantage of wave potential energy by storing water in an reservoir placed at a higher quota that the mean sea level. Waves provide the energy needed to transfer the water into the basin. Once there, water is slowly released back to the sea through a low-head turbine connected to an electrical generator. Like in the oscillating water column devices, overtopping devices can be designed as floating structures placed offshore or deployed in the shore line held by fixed structures. A way to reduce construction and maintenance costs is to build such prototypes integratedly in port facilities such as breakwaters. Figure 1.10 displays an example of floating overtopping device, the Wave Dragon, and an example of a port-integrated prototype.

1.3 Scope of the thesis

Even though quite a remarkable amount of research has been devoted to wave energy conversion over the past quarter of century, it has not been uniformly distributed throughout the planet. Some areas, such as the Atlantic front in Europe or the USA and Japan, have lead this field since its birth. Reasons for that may be whether the

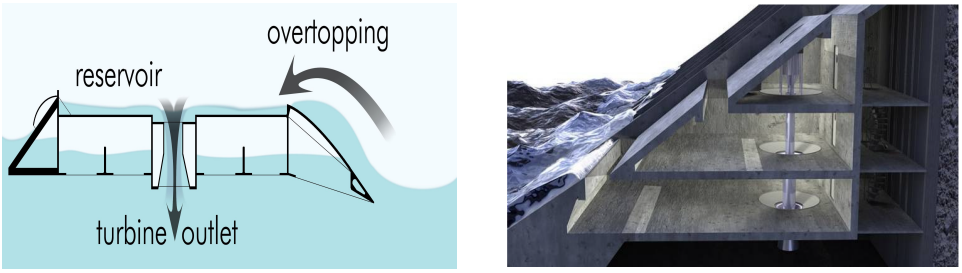

Figure 1.10: *a) Floating overtopping device. b) Breakwater-integrated overtopping device*

economic predominance of such regions, whether to be on hold of the predominant resource. Higher wave energy fluxes contribute to the thought that a specific territory may be more appropriate for wave energy exploitation. However, experience has shown it is not always the case, numerous failures in deployment operations and sea trials have strengthen the thought that areas with lower average wave energy fluxes may be also opportune at such purpose. In other words, less powerful wave climates imply less undesired effects related to stormy conditions and survivability of the devices, which makes it in turn more economically convenient and that, makes these areas attractiveness grow considerably. As a consequence, regions with minor wave energy potential, such as the Mediterranean, Black and Baltic Sea areas, have recently started to focus their attention in this topic.

Following the logic exposed above, this document aims to assess wave energy conversion in the Mediterranean Sea. In order to do so, two different wave energy converter prototypes specifically tuned for the Mediterranean wave climate are presented. Numerical models have been developed and tested for several Mediterranean locations, relying in wave data gathered over 25 years by the buoys of the National Italian Wave Measurement Network (RON). Both devices have been designed from scratch and dimensioned according to the conditions given at the deployment sites. Finally, a comparison between them has been carried out in order to identify the specific traits that makes a device more suitable than other and proof that the original hypotheses were correct.

While one of the devices is an adaptation based on the review of an existing concept, the other one has been built upon a new concept which intends to merge several working principles. This new approach allows to select and stack the advantages of each single working principle while cancelling out the negative effects the single working principle can produce when applied at mild wave climates.

1.4 Concepts

In the following section, the developed devices in this thesis will be exposed. Detailed explanation of their working principle will be given paying special attention to the different components of the devices, how they work and why they have been chosen.

The terminology used to refer to such devices is somewhat descriptive on the device characteristics. The first device has been named HPA-LG, acronym which derives from Heaving Point Absorber Linear Generator. The first three letters describe the WEC typology whereas the last two describe the PTO typology. The second device name is MoonWEC instead, and it gives reference to a key structural part of the WEC, which is a moonpool.

1.4.1 HPA-LG

The HPA-LG has been the the first of the two devices to be modelled. It is a three body device composed by a floating structure, a submerged body of neutral buoyancy and the power take-off body, used to generate the electricity. The floating structure has a cylindrical shape and will usually be referred to as a buoy. The submerged body has a spherical shape and is located at half of the distance between the water free surface and the sea bottom. The third body is the translator of the electric linear generator used for the energy conversion and it is placed at the seabed. Figure 1.11, which shows a schematic layout of the device, aims to reinforce the understanding of the reader and therefore, dimensions shown are not in scale to the modelled device.

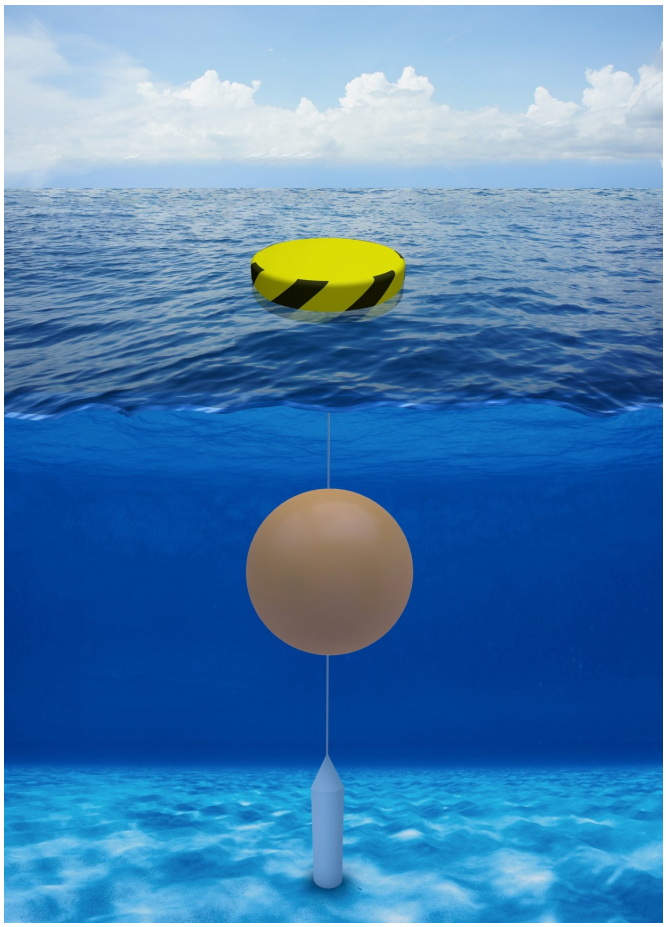

Figure 1.11: *Device Layout*

The HPA-LG can be classified as a Point Absorber since the buoy dimensions are relatively small compared to the typical wavelength of the incident waves given at the deployment site. It could also be classified as a multi-body WEC; however, the author believes the point absorber class fits better the characteristics of the device since only one body, the cylindrical buoy, is directly interacting with waves. When assuming the deployment location classification, the HPA-LG has been conceived to be installed at depths between $50 - 100\ m$, hence it is set into the offshore device category. When making reference to the classification shown in figure 1.7, it clearly falls into the oscillating bodies family and when referring to figure 1.9 it is a heaving float (the main degree of freedom is the vertical one), more precisely number one.

The purpose of the submerged sphere is to tune the natural frequency of the system in order to match it with the most common wave climate frequencies given at the deployment site. By adding an additional body the mass of the system is augmented

and by placing it at a sufficient depth, the majority of radiation the induced by the body is avoided, minimizing the total loss of energy.

The wave motion nature has always been the main challenge when it comes to perform its energy conversion. The characteristic periodicity of waves makes it very difficult to achieve the efficient electric conversion directly through a traditional rotative machine. One of the solution that requires less transformation of the mechanical power absorber is the electric linear generator. The particularity of this PTO systems is that the movement used to generate the electricity is no longer rotational but translational. The translator is conformed by permanent magnets oriented in a alternate pole configuration. The stator, surrounding the translator, is filled with winding coils. In this way, when the translator moves an electromagnetic field is induced in the stator coils. The main drawback of this system is that when the translator reaches the extreme position (rest or trough of the wave), there is a change in the sign of motion, implying reduced velocities at that point, which in turn is translated into low electric power generation, since electromagnetic induction is strictly related to the translator velocity.

The HPA-LG is interconnected by lines, the float and the submerged body are attach through a steel wire and the submerged body is also attached to the translator of the linear generator by another wire. Finally, the translator is linked to the stator of the linear generator by a very stiff spring. The linear generator is fixed at the bottom by a dead-weight (concrete base) acting, together with the interconnecting lines as the mooring system of the device.

Table 1.1 reports the general characteristics of the HPA-LG device synthesizing what described in this subsection.

1.4.2 MoonWEC

The has been conceived from a fresh start. Inspired in the Oxyflux device (14, 15), this concept cannot fit in any of the previous classification systems and at the same it could suit more than one simultaneously. The novelty of MoonWEC is that encompasses distinct working principles as formulated in the previous section.

It is composed by to bodies, a floating structure and a Wells turbine. The floater has a hollow cylinder with its axis coincident to the structure's vertical axis. When placed in water this cylinder is filled by water creating what is commonly known as a moonpool. When set under the action of waves, not only the structure is excited but so is the moonpool creating a third virtual body. The moonpool then behaves as a deformable body, thus being able to reach the resonant state if well tuned. The energy conversion

Parameter	Value	Unit
depth	50	m
Buoy ø	5.0	m
Buoy height	1.25	m
Buoy draft	0.25	m
Buoy Mass	4000	kg
Submerged body ø	3.0	m
Submerged body mass	21736	kg
Distance between bodies	25	m
Wire stiffness	$5 \cdot 10^6$	N/m
End stop stiffness	$5 \cdot 10^6$	N/m
PTO stiffness	$5 \cdot 10^4$	N/m
PTO Nominal Power	10	kW
Translator length	1.867	m
Stator length	1.264	m
Translator mass	100	kg

Table 1.1: *HPA-LG characteristics.*

is supposed to be carried out by taking advantage of the relative motion between the floating structure and the moonpool. In order to maximize its relative motion, both bodies need to be resonating synchronously with completely opposite phases.

Energy conversion is then performed by the Wells turbine. This type of turbine is usually in air as performing fluid. The author however, believes, and has found no evidence against using it in other fluid flows such as water flows. The reason for applying it under highly pressurized air flows is to maximize the turbine rotational speed in order to achieve a good kinematic coupling with the electric generator. The choice of the Wells turbine relies on the fact that is a self rectifying turbine. A self rectifying turbine can handle bidirectional flows without varying the sense of rotation. By taking advantage of this property, electricity can be generated with a conventional rotative electric generator, which is cheaper and more efficient than the alternatives commonly used in wave energy conversion.

The MoonWEC is moored to the seabed through a particular catenary system commonly known as CALM system. Catenary systems are specially suitable for heaving WECs since they mainly block other degrees of freedom while releasing the heave mode free and thus, not interfering with energy conversion motion.

To sum up, the MoonWEC can be considered a point absorber, with oscillating body in heave and an OWC device. The overtopping principle can also be taken into account

if considered that water can overflow the floating structure causing an extra discharge in the moonpool. However, this effect has not been taken into consideration in this thesis as it could be the topic of another Ph.D. thesis itself due to its complexity.

Figure 1.12 displays a representation from the MoonWEC including the moonpool and table 1.2 outlines its general characteristics.

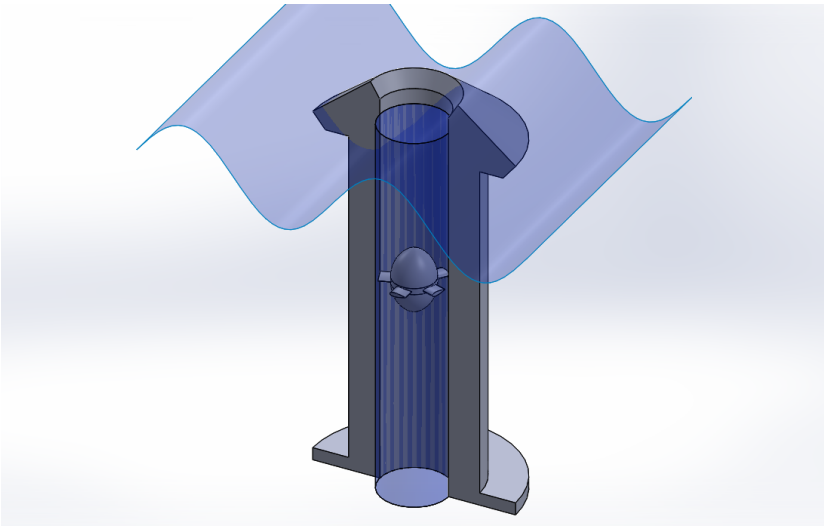

Figure 1.12: *Device Layout*

1.5 Structure of the Thesis

This document is divided into 7 chapters, including the introduction. The second chapter is devoted to gather all the theoretical knowledge used to produce this dissertation. Therefore, theories from diverse scientific fields are exposed in it. Beginning with wave theory, which is the core of development of the thesis, the Airy theory is developed thoroughly. Afterwards, theory enticing body dynamics and specially wave-structure interaction will be carefully described. Following on, theory behind electric linear generators, which includes the laws of electromagnetic induction, will be stated. Subsequently, an overview of the moonpool hydrodynamic behaviour will be exposed. In the next section of the chapter, different types of mooring systems are exposed and its behaviour is explained. Finally, aerodynamics of Wells turbines are formulated.

In the third chapter, a characterisation of the wave resource in the Mediterranean Sea is carried out identifying the two most promising locations off the Italians coasts. A thorough analysis of the wave climate at both locations has been performed and the

Parameter	Value	Unit
depth	50	m
MoonWEC ø	5.0	m
Structure height	10.0	m
Structure draft	9.0	m
Structure Mass	150	ton
CoG	4.3	m
Moonpool ø	2.2	m
Wells turbine profile	NACA0021	-
Wells turbine solidity	0.47	-
Wells turbine hub-to-tip ratio	2/3	-
Wells turbine chord length	0.5	m
PM Generator Nominal power	50	kW
Mooring wire type	Six Strand	-
Mooring wire ø	75	mm
Mooring wire length	150	m
Anchor point	120	m

Table 1.2: *MoonWEC general characteristics.*

most common conditions have been identified. Furthermore, the extreme wave events statistics have been studied in order to ensure the devices' survivability.

In the fourth chapter, the mathematical modelling used to describe the behaviour of the simulated wave energy converters is described in full detail. Two family models have been applied numerically in order to simulate the WECs. The first model is based on the wave potential theory, which follows a Lagrangian approach. On the other hand, an open source software called REEf3D has also been used. Results have been compared in order to validate the potential model. REEf3D is a Computational Fluid Dynamics (CFD) code which follows an Eulerian approach to solve the Reynolds Averaged Navier-Stokes equation at each cell of the fluid domain.

The fifth chapter goes through the dimmensionig of both wave energy converters. Using first a very simple empirical approach, in order to set the basic parameters defining the devices. Afterwards frequency domain models are used to reach a higher level of detail allowing to tune most of the parameters defining the prototypes. Subsequently, the time domain models are developed. Lying in the time domain allows to include all the effects that have a non-linear behaviour. Level of accuracy reached with time domain can already be considered satisfying.

In the sixth chapter, the results obtained in this study, for both devices and for all

the models described in the previous paragraph, are presented and compared. Finally, in the last chapter the pertinent conclusions are drawn and some possible future work development are stated.

2

Theoretical background

2.1 Wave Mechanics

2.1.1 Linear wave theory

The linear wave theory (11) is based on the velocity potential concept, which is the spatial integral form of the velocity. Laplace and Bernoulli formulated, in equations 2.1 and 2.2 respectively, the equations of motion of the fluid within the domain.

$$\nabla^2\phi = \frac{\partial^2\phi}{\partial x^2} + \frac{\partial^2\phi}{\partial y^2} + \frac{\partial^2\phi}{\partial z^2} \tag{2.1}$$

$$\frac{\partial\phi}{\partial t} + \frac{1}{2}|\nabla\phi|^2 + \frac{p}{\rho} + gz = 0 \tag{2.2}$$

These equations with the right Boundary Conditions (BCs) become the basis of the ideal wave motion theory under the following hypothesis:

- Inviscid fluid
- Irrotational motion
- conservative forces

Furthermore, experimental studies have demonstrated that another constrain must be added to maintain the theory validity. The period of the sea waves must be within the following range $1.1s < T < 30s$. However, this is not a major problem since practically the totality of wind-generated sea waves rely within that range.

In the following paragraphs the linear wave theory, also known as first order theory, will be developed. the theory is applied within the boundaries of a domain. The adopted domain has four boundaries, two lateral ones, the bottom boundary and the free surface boundary.As previously stated, in order to make such theory valid, all the boundaries need to be linear. Firstly, the free surface BC is linearised. This constrain is composed by two equations, the kinematic equation 2.3 and the dynamic equation 2.4, which have the following expressions:

$$\frac{\partial \eta}{\partial t} + \frac{\partial \phi}{\partial x}\frac{\partial \eta}{\partial x} + \frac{\partial \phi}{\partial y}\frac{\partial \eta}{\partial y} - \frac{\partial \phi}{\partial z} = 0 \text{ for } z = \eta(x, y, t) \tag{2.3}$$

$$g\eta + \frac{\partial \phi}{\partial t} + \frac{1}{2}[(\frac{\partial \phi}{\partial x}^2 + \frac{\partial \phi}{\partial y}^2 + \frac{\partial \phi}{\partial z}^2] = 0 \text{for} z = \eta(x, y, t) \tag{2.4}$$

The non linearity of the equations is obvious for the unknown parameters η ϕ but there is another implicit non linear condition in $z = \eta(x, y, t)$ which is part of the solution and therefore, another unknown parameter. The linearisation of these equations requires the introduction of new constrains. Figure 2.1 fully describes a progressive periodic wave and all its parameters; this wave propagates in a flat-bottomed channel, following the x axis, and is mainly defined by the period T, its wavelength L and its wave height $H = 2a$. Analysing the figure, the proportion among the different parameters is clear and the orders of magnitude can securely be determined:

$$\eta = O(H)\frac{\partial \eta}{\partial t} = O(\frac{H}{T}\frac{\partial \eta}{\partial x} = O(\frac{H}{L} \tag{2.5}$$

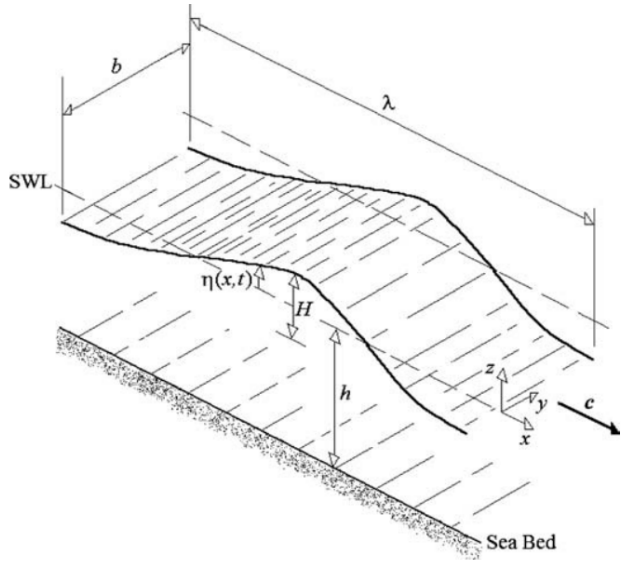

Figure 2.1: *Notation and Sketch of the domain for the linear wave theory (73)*

The maximum velocity of the water particles can be approximated to $\pi H/T$, which leads to the next expression

$$u_{max} = v_{max} = w_{max} = \frac{\partial \phi}{\partial x}_{max} = \frac{\partial \phi}{\partial y}_{max} = \frac{\partial \phi}{\partial z}_{max} = \frac{\pi H}{T} = O(\frac{H}{T} \tag{2.6}$$

Knowing that, in addition to the wave celerity $c = L/T$, the non linear terms of the equations 2.3 and 2.4 have the following orders of magnitude:

$$\frac{\partial \phi}{\partial z} = O(\frac{H}{T}) = O(c\frac{L}{T}) \tag{2.7}$$

$$\frac{\partial \eta}{\partial t} = O(\frac{H}{T}) = O(\frac{\partial \phi}{\partial z}) \tag{2.8}$$

$$\frac{\partial \phi}{\partial x}\frac{\partial \eta}{\partial x} = \frac{\partial \phi}{\partial y}\frac{\partial \eta}{\partial y} = O(c\frac{H^2}{L^2}) = \frac{H}{L}O(\frac{\partial \phi}{\partial z}) \tag{2.9}$$

These relations proof that the non linear terms have an order of magnitude H/L times that of the linear terms, and assuming that the wave slope is $\varepsilon = H/L <<< 1$, the non linear terms of the free surface BC can be neglected due to its small influence. Once the quadratic terms have been suppressed there is still the implicit non linearity which needs to be dealt with. If the free water surface is given the value of zero, the

critical condition can be expanded using the Taylor series, showing the following result:

$$\eta\frac{\partial^2\phi}{\partial z^2}(x,0,t) = O(\frac{H}{T}\frac{H}{h}) = O(c\frac{H}{L}\frac{H}{h}) \tag{2.10}$$

In which the term ε can be identified again, also note that $H/h <<< 1$. Thus, making the order of magnitude close to zero and therefore identifying this term as negligible. After performing the dimensional analysis and the pertinent transformations, the free surface BC expressions are linearised under the form of:

$$\frac{\partial\eta}{\partial t} - \frac{\partial\phi}{\partial z} = 0 \text{for} z = 0 \tag{2.11}$$

$$g\eta + \frac{\partial\phi}{\partial t} = 0 \text{for} z = 0 \tag{2.12}$$

To simplify even more these BCs, both expressions can be merged into a single equation to form the BC at the free water surface. See equation 2.15. The following BC is the bottom BC, assuming an impermeable seabed and constant depth, one can show that vertical velocity at the bottom must be zero, being this BC already linear, as equation 2.16 shows. Finally, the well known linearised form of the Bernoulli's equation can be also used as shown in 2.14, where p^+ is the pressure excess induced by the wave in the fluid. Up to this point, all the equations describing the dynamics of the fluid have been linearised and the mathematical problem is governed by the following expressions.

$$\nabla^2\phi = \frac{\partial^2\phi}{\partial x^2} + \frac{\partial^2\phi}{\partial y^2} + \frac{\partial^2\phi}{\partial z^2} \tag{2.13}$$

$$p^+ = p + \rho g z = -\rho\frac{\partial\phi}{\partial t} \tag{2.14}$$

$$\frac{\partial^2\phi}{\partial t^2} + g\frac{\partial\phi}{\partial z} = 0 \text{for} z = 0 \tag{2.15}$$

$$\frac{\partial\phi}{\partial z} = 0 \text{for} z = -h \tag{2.16}$$

A solution for the velocity potential and velocity field can now be found. However, a new hypothesis and a simplification need to be formulated in order to solve the problem. The former is the periodicity hypothesis, stating that waves need to be periodic either in the temporal domain and in the spatial domain, which implies a constant period of waves and a constant shape of waves throughout the domain. Equations 2.17 and

2.18 define mathematically the temporal and spatial periodicity hypothesis respectively. The latter is a simplification by means of a reduction of the domain by considering bi-dimensional in the xz plane, hence neglecting the y component of the velocity potential in equation 2.13.

$$\frac{\partial \phi}{\partial x}(x,z,t) = \frac{\partial \phi}{\partial x}(x,z,t+T) \tag{2.17}$$

$$\frac{\partial \phi}{\partial x}(x,z,t) = \frac{\partial \phi}{\partial x}(x+L,z,t) \tag{2.18}$$

The periodicity hypothesis shows that the previously described phase celerity relation $c = L/T$ is constant, finding a valid link between the the spatial and the temporal domain. This link can be used by formulating a new variable *theta*, which fulfils the conditions described above:

$$\theta = 2\pi(\frac{x}{L} - \frac{t}{T}) \tag{2.19}$$

Dependencies now change from $\eta(x,t)$ and $\phi(x,z,t)$ to $\eta(\theta)$ and $\phi(\theta,z)$. Two new parameters need to be introduced in order to achieve full determination of the equations of motion (2.13 -2.16). These are called the wave number $k = 2\pi/L$ and the angular frequency $\omega = 2\pi/T$. Applying the changes, the simplified Laplace system of equations of acquires the following shape:

$$\theta = kx - \omega t \tag{2.20}$$

$$\frac{\partial^2 \phi}{\partial z^2} + k^2 \frac{\partial^2 \phi}{\partial \theta^2} = 0 \tag{2.21}$$

$$p^+ = p + \rho g z = -\rho \frac{\partial \phi}{\partial t} \tag{2.22}$$

$$\frac{\partial \phi}{\partial z} + \frac{\omega^2}{g}\frac{\partial^2 \phi}{\partial \theta^2} = 0 \text{for} z = 0 \tag{2.23}$$

$$\frac{\partial \phi}{\partial z} = 0 \text{for} z = -h \tag{2.24}$$

$$\frac{\partial \phi}{\partial \theta}[\theta = -2\pi\frac{t}{T}, z] = \frac{\partial \phi}{\partial \theta}[\theta = -2\pi(1 - \frac{t}{T}), z] \text{periodicity} \tag{2.25}$$

Equation 2.21 can be identified as an Ordinary Differential Equation (ODE), the solution by means of the proper application of the BCs yields the velocity potential solution and the free water surface:

$$\phi(\theta, z) = \frac{ag}{\omega} \frac{\cosh[k(h+z)]}{\cosh(kh)} \sin\theta \tag{2.26}$$

$$\eta = a\cos\theta \tag{2.27}$$

However, the problem is not yet fully defined since the wave number k is still an arbitrary number however, given that no relation between ω and k has been provided yet, and thus a wavelength cannot be computed for a fixed period. Combining the free surface BC in equation 2.27 and the derivative of equation 2.26 the following expressions are obtained:

$$[\frac{\partial\phi}{\partial z}]_{z=0} = \frac{ag}{\omega} \tanh(kh) \sin\theta \tag{2.28}$$

$$[\frac{\partial^2\phi}{\partial t^2}]_{z=0} = -ag\omega \sin\theta \tag{2.29}$$

Substituting both equations 2.28 and 2.29 into equation 2.15 the relation of dispersion (equation 2.30 is obtained and it reports the relation of wave energy loss in wave propagation depending on the frequency.

$$\omega^2 = gk \tanh(kh) \tag{2.30}$$

Once the relation of dispersion is found the velocity field can easily be calculated by applying the spatial derivatives of the velocity potential. Since the domain is bi-dimensional only two components are yielded, the horizontal velocity u and the vertical velocity w.

$$u(\theta, z) = \frac{\partial\phi}{\partial x} = \frac{agk}{w} \frac{\cosh[k(h+z)]}{\cosh(kh)} \cos\theta \tag{2.31}$$

$$w(\theta, z) = \frac{\partial\phi}{\partial x} = \frac{agk}{w} \frac{\sinh[k(h+z)]}{\cosh(kh)} \sin\theta \tag{2.32}$$

Three different groups can be distinguished in equation 2.31 and 2.32, the first group expresses the wave characteristics i.e. wave amplitude, wave number and wave angular frequency; the second group reflects the velocity variation with respect to the vertical

position and the third group states the harmonic behaviour of the wave. See 2.2

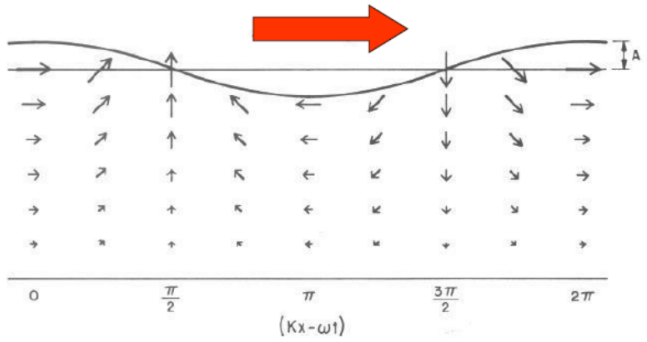

Figure 2.2: *Water particle velocities in a wave*

Water particle trajectories and acceleration are then found by time integration and time derivatives respectively. To reach a better understanding of the linear wave theory water particle trajectories are derived as example:

$$x_p(t) = x_0 + \int u[x(t), z(t)]dt z_p(t) = z_0 + \int w[x(t), z(t)]dt \tag{2.33}$$

Performing the integral and after some mathematical simplification passages the particle trajectory expressions are obtained:

$$x_p(t) = x_0 - a\frac{\cosh[k(h+z_0)]}{\sinh(kh)}\sin\theta_0 \tag{2.34}$$

$$z_p(t) = z_0 + a\frac{\sinh[k(h+z_0)]}{\sinh(kh)}\cos\theta_0 \tag{2.35}$$

Where $\theta_0 = \omega t - kx_0$. Using the terms:

$$\alpha = a\frac{\cosh[k(h+z_0)]}{\sinh(kh)}\beta = a\frac{\sinh[k(h+z_0)]}{\sinh(kh)} \tag{2.36}$$

Dividing equations 2.34 and 2.35 by α and β respectively, squaring them and then adding them, the obtained result is the well known ellipse equation:

$$\frac{[x_p(t) - x_0]^2}{\alpha^2} + \frac{[z_p(t) - z_0]^2}{\beta^2} = 1 \tag{2.37}$$

The parameters α and β, which define the shape of the ellipse vary according with the water depth. For deep waters conditions the particle trajectories are perfect circles, which radii decrease with depth, see figure 2.3.a. If the sea bed is close enough to the

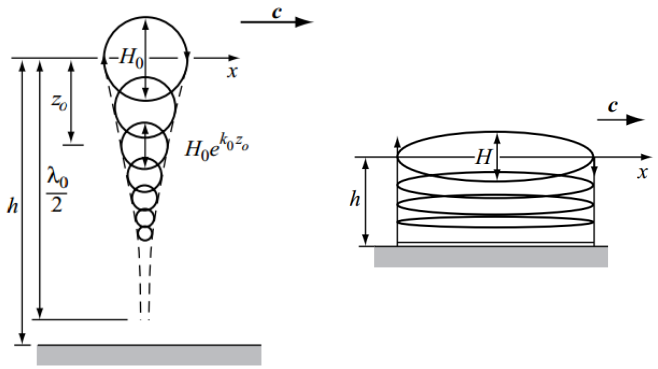

Figure 2.3: *a) Deep water particle paths b) Shallow water particle paths. (73)*

water surface to exert an influence on the wave behaviour, i.e. shallow water conditions, then the ellipse has different major and manor radii, and the latter decreases with water depth, due the bottom BC, where only horizontal trajectories are found. See figure 2.3.b

The pressure distribution throughout the fluid domain is obtained through the linearised Bernoulli's equation 2.14:

$$p^+ = -\rho\frac{\partial\phi}{\partial t} = \rho ag\frac{\cosh[k(h+z)]}{\cosh(kh)}\cos\theta = \rho g\eta(\theta)\frac{\cosh[k(h+z)]}{\cosh(kh)} = \rho gK_p\eta(\theta) \quad (2.38)$$

Where K_p is the pressure response factor and fulfils the following relation $K_P <= 1$ depending on the value of z. If the equation 2.38 is substituted into the equation 2.14 the entire pressure profile is yielded:

$$p = p^+ - \rho gz = \rho g(K_p\eta - z) \quad (2.39)$$

When $z = 0$ then $K_p = 1$ thus resulting in a pressure $p = \rho g\eta$. Therefore in the crest of the wave the pressure is $p = \rho ga$ and in the trough of the wave the pressure is $p = -\rho ga$. As the depth of the study point grows also the pressure does having the component p^+ less important, since the hydrostatic component after a certain value is dominant. See figure 2.4

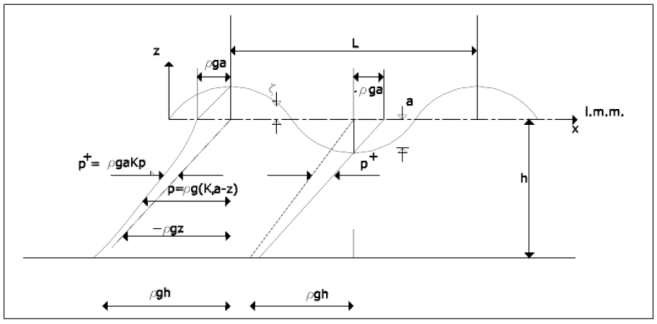

Figure 2.4: *Wave pressure distributions along the vertical axis in the crest and trough of the wave*

In the linear wave theory all dissipative phenomena are neglected and therefore, the energy related to the wave motion is composed only by two components, the potential energy and the kinetic energy. As an oscillating motion, the energy at a certain point (x, z) is time dependant. However, the energy at a certain point at a certain time is not really a matter of major interest from the engineering point of view. A much more used term is the specific energy, defined as the mean energy (in time) per unit of surface or, in other words, the density of energy. In the following paragraphs the expressions of potential and kinetic energy will be derived separately and finally merged together.

Figure 2.5.a shows the schematic geometric basis to compute the potential energy. An elementary fluid column is the studied area of interest. That column has a unitary width (perpendicular to the xz plane), a differential length dx and a height of $h + \eta$. The elementary potential energy is:

$$d\bar{E}_{p1} = gh_G dm \tag{2.40}$$

The mass of the fluid column is equal to:

$$dm = \rho(h + \eta)dx \tag{2.41}$$

This can be substituted into equation (2.40):

$$d\bar{E}_{p1} = \frac{1}{2}\rho g(h + \eta)^2 dx \tag{2.42}$$

Which in turn, is implicitly time dependant, owing to the free surface $\eta(x, t)$. The final step to obtain the potential energy density is to integrate equation 2.42 over x and

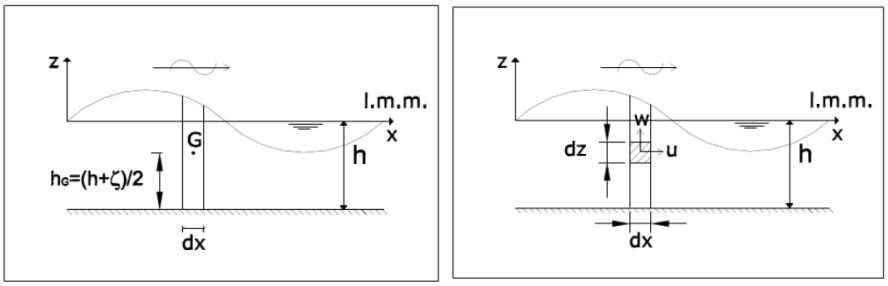

Figure 2.5: *a) Geometric configuration to compute potential energy b)Geometric configuration to compute kinetic energy*

t:

$$\bar{E}_{p1} = \frac{1}{LT}\int_t^{t+T}\int_x^{x+L} d\bar{E}_{p1} = \frac{\rho g}{2LT}\int_t^{t+T}\int_x^{x+L}(h+\eta)^2 dxdt \tag{2.43}$$

After some trigonometrical manipulation equation (2.43) reaches the simplest form of:

$$\bar{E}_p = \rho g\frac{a^2}{4} \tag{2.44}$$

To developed the kinetic energy expression the schematic shown in figure 2.5.b is followed. The study area is also an elementary region of fluid mass, which length, height and width are respectively dx, dz and 1. The resulting expression is:

$$d\bar{E}_C(t) = \frac{1}{2}(u^2+w^2)dm = \frac{\rho}{2}(u^2+w^2)dxdz \tag{2.45}$$

Integrating along the vertical and averaging with respect to time and length the following expression is obtained

$$\bar{E}_C = \frac{1}{LT}\int_t^{t+T}\int_{-h}^{0}\int_x^{x+L} d\bar{E}_C dxdzdt = \frac{\rho}{2LT}\int_t^{t+T}\int_{-h}^{0}\int_x^{x+L}(u^2+w^2)dxdzdt \tag{2.46}$$

After some mathematical manipulation and trigonometric operations the final simplified expression of the kinetic energy is obtained:

$$\bar{E}_C = \rho g\frac{a^2}{4} \tag{2.47}$$

Finally the only remaining passage to obtain the total energy is to sum the kinetic

and potential terms:

$$\bar{E} \equiv \bar{E}_C + \bar{E}_P = \frac{1}{8}\rho g H^2 \tag{2.48}$$

It is important to remember that this expression is valid for a unitary horizontal section, that is why is called energy density. Another interesting conclusion is that the energy density is not function of the wave period, it only depends on its wave height. Reason why the wave height is the main design parameter for coastal structures.

At thins point the bases of the linear wave theory have been exposed. Despite the initial hypothesis, the linear wave theory accepts slight variations of the hypothesis by suffering small modifications, such as water depth or propagation direction variation. Monochromatic waves are scarcely ever found in real seas, even a reduced portion of sea surface is composed by a large number of different waves, which have different heights,directions, periods and phases. Groups of waves and reflected waves will be treated in the following paragraphs.

The principle of superposition of waves and its effects is also valid within the linear wave theory premises, such principle is stated in equation 2.49:

$$\eta(x,t) = \sum_n \eta_n = \sum_n a_n \sin(k_n x - \omega_n t + \delta_n) \tag{2.49}$$

Some particular cases can be identified:

a) Waves that propagate in the same direction and have same periods

a.1) If their phases are equal

- $$\eta(x,t) = (a_1 + a_2)\sin(kx - \omega t + \delta) \tag{2.50}$$

a.2) If their phases are π rad opposed

- $$\eta(x,t) = (a_1 - a_2)\sin(kx - \omega t + \pi) \tag{2.51}$$

b) Waves that propagate in the same direction and have different periods

- $$\eta(x,t) = 2a[\cos(\delta k - \delta\omega t - \delta)\sin(kx - \omega t)] \tag{2.52}$$

c) Waves that propagate in opposed direction (reflected)

c.1) Total reflection: if $a_i = a_r$

•

$$\eta(x,t) = 2a_r \cos(kx)\cos(\omega t) \tag{2.53}$$

c.2) If waves amplitudes are different

d) The minimum and maximum values of the free surface elevation are:

d.minimum)

$$|\eta_{min}| = a_i - a_r \tag{2.54}$$

d.maximum)

$$|\eta_{max}| = a_i + a_r \tag{2.55}$$

Reflection is measured with the reflection coefficient $C_R = \frac{a_r}{a_i}$. When more than one wave is present a group of waves is formed. Wave groups have a particular behaviour depending on the characteristic of each component wave. A wave group has a specific shape, defined by its envelope, and celerity, which is different from the individual wave celerity. The group celerity is the velocity in which the energy contained in the group propagates, and also determines the envelope variation. The find the group celerity the dispersion relation is needed and its final expression can be simplified depending on the depth i.e. shallow or deep waters.

$$c_g = \frac{c}{2}(1+G) \tag{2.56}$$

Where G derives from the relation of dispersion and assumes the following shape $G = \frac{2kh}{\sinh(2kh)}$, after some mathematical manipulation one can show that:

$$c_{g0} = \frac{1}{2}c_0 \text{for deep water} c_g = c = \sqrt{gh} \text{for shallow water} \tag{2.57}$$

After finding the group celerity the next logical step is to describe the energy propagation in a group of waves. The energy flux in a wave group is the energy of the wave multiplied by the group celerity:

$$\bar{E}_f = c_g \bar{E} = \frac{1}{16}\rho g H^2 c[1 + \frac{2kh}{\sinh(2kh)}] \tag{2.58}$$

When approaching the shoreline, in the area called surf or near-shore, the seabed starts having a significant influence in the wave behaviour. The first wave response at the presence of seabed is called shoaling. When the wave reaches that area has gradually less space to propagate while the energy remains constant, keep in mind that in the linear wave theory there is no energy loss until wave breaking where the theory

is no longer valid. As a result, an initial smooth decrease in wave height is given to give place to a sudden substantial increase of the wave height as the bottom keeps getting closer, see figure 2.6. The shoaling development is represented by the shoaling coefficient K_S:

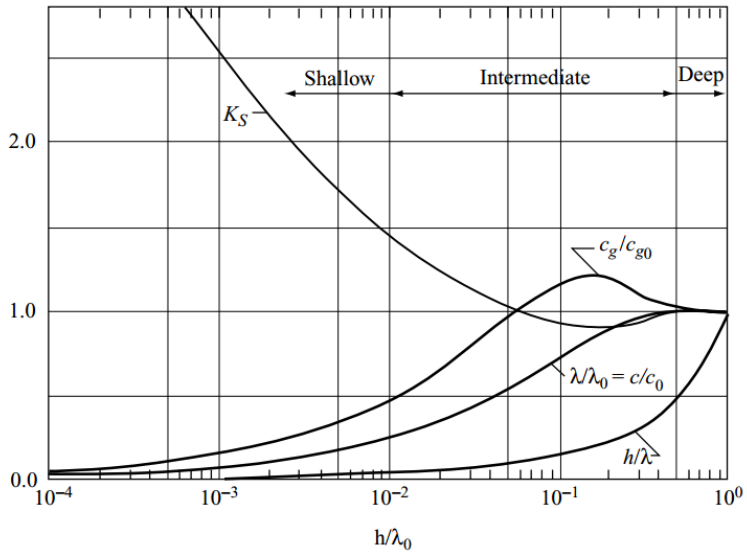

Figure 2.6: *Evolution of wave height and length over a changing depth for a horizontal seabed (73)*

$$K_S = \frac{H}{H_0} = \sqrt{\frac{c_0}{2c_g}} = \frac{1}{\sqrt{\tanh(kh)(1+G)}} \tag{2.59}$$

The offshore direction of propagation of waves is not always perpendicular to coastal line; however when breaking, waves have turn and oriented perpendicularly to the coast. This phenomenon is called refraction and follows the law of Snell, developed for light waves but also valid for sea waves, which delivers the refraction coefficient K_r. Figure (2.7) shows a geometric representation of the Snell's law applied in the near-shore area, determining the wave front width used to compute the refraction coefficient in the following way: $K_r = \sqrt{\frac{L_1}{L_2}}$.

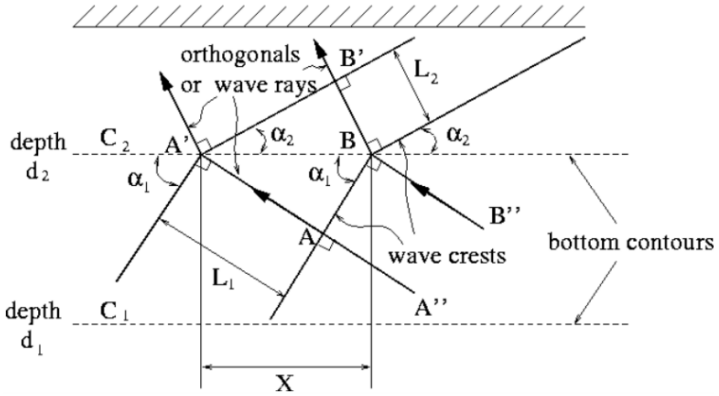

Figure 2.7: *Geometric representation of the Snell's law applied for ocean waves at the nearshore area*

Depending on the coastline shape, the wave height can increase or decrease when refracted, i.e. if the coast is a bay (concave form) waves will tend to spread into a wider area and therefore, their height will decrease. On the contrary, if the coast is a cape (convex form) the waves will tend to concentrate towards the tip of the cape and their height will grow, see figure 2.7. The height in this case is computed by combining both coefficients, the shoaling and the refraction coefficient: $K_r K_s = \frac{H}{H_0} = \sqrt{\frac{c_0}{2c_g}}\sqrt{\frac{L_1}{L_2}}$.

Finally, the last part of the linear wave theory is based on another particular phenomenon, also found in light waves, called diffraction. When a wave finds an obstacle when propagating, right after overtaking it there can be a sudden change in the wave propagation direction. Diffraction will occur depending on the obstacle size; if this is bigger than one order of magnitude less than the wavelength will take place, if the obstacle is smaller, the wave has enough energy to overcome it without particularly feeling its presence. The German mathematician Helmholtz proposed an adaptation of the Laplace equation in order to capture the diffraction phenomenon:

$$\phi(x, y, z, t) = \Im f(z)\Phi(x, y)e^{-tiw} \tag{2.60}$$

$$\eta(x, y, z, t) = \Re H(x, y)e^{-tiw} \tag{2.61}$$

Where $f(z) = \frac{\cosh[k(h+z)]}{\cosh(kH)}$. After some mathematical operations and simplification the Helmholtz version of the Laplace equation yields:

$$\frac{\partial^2\Phi}{\partial x^2} + \frac{\partial^2\Phi}{\partial y^2} + k^2\Phi = 0 \tag{2.62}$$

This equation which results in an elliptic form, has been proved valid for the following cases:

- Straight hurdle of semi-infinite length.
- Finite gap in an infinite length straight hurdle.
- Isolated obstacle made of a straight hurdle of finite length.
- Isolated obstacle which horizontal section is circular.

The last of these cases could be a sufficiently big floating structure. Diffraction is an element that needs to be considered when designing wave energy converters depending on the size of the device. This subject will be further exposed in depth in the following sections. Figure 2.8 illustrates the typical behaviour of diffracted waves for different types of obstacles.

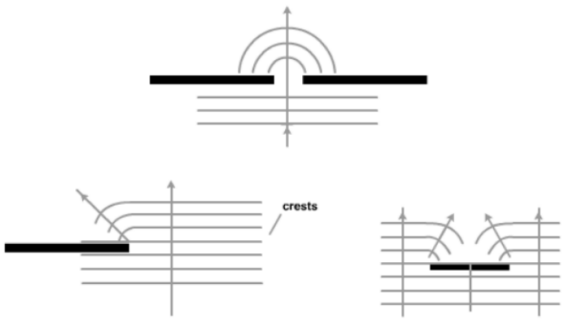

Figure 2.8: *Wave diffraction according to different obstacles*

2.1.2 Wave Generation

The most common waves in the spectrum of sea waves are those generated by the wind. Wind-generated waves are much more complex than the typical mono-chromatic wave widely used in literature. To achieve a complete outlook of the behaviour of waves it is crucial to understand how they are generated. It is essential to have a means to quantify and predict the action of wind-generated waves, especially under extreme conditions, usually set as primary design parameter in engineering. A record of water surface at a given location under stormy conditions shows a very irregular pattern. A wave record at a nearby location can show a very different shape but has similar statistical properties. The records of a particular area can contain locally wind-generated waves as well as

swells which have propagated thousands of kilometres away ranging very differently in height and period.

The average wave height and period of wind-generated waves strongly depends on t he wind velocity, duration, and fetch. For a given wind velocity and, unlimited fetch and duration there is an upper limit over which waves cannot grow due to energy dissipation given by wave breaking and water surface turbulent phenomena. When the energetic balance is reached is known as fully developed sea state condition. Fortunately, this condition is rarely attained, even in the event of large storms.

Waves within the generation process have shorter and random crests. These, not only propagate in one direction but within a range which spans from the predominant wind direction. As they propagate throughout the area over which the wind is blowing they gradually grow in average height and period. After leaving the area of active wind generation, the surface profile becomes smoother forming what is commonly known as swell. Swells propagate large distances with minimum losses of energy, such as air resistance, internal friction or angular speeding of the wave field. Once the surf zone, also known as near-shore, is reached some particular phenomena, such as shoaling, reflection, refraction and diffraction start taking place, mainly due to the interaction of the wave with the seabed. Finally, the wave breaking occurs releasing most of the energy transported by the wave.

Wind blowing over the surface of a water body will transfer energy energy into the water in the form of surface current and by generating waves on the water surface. There are turbulent pressings in the wind field that apply a fluctuating pressure on the water surface. These fluctuations are not strictly periodic and can quickly vary in magnitude and frequency, they move forward within a range of velocities. They cause the water surface to undulate, develop and grow. This growth is mainly achieved as a results of resonant interaction that takes place between the forward moving fluctuations and the free waves propagating at the same velocity as the pressure fluctuations. Once the wave is born and somewhat consolidated another mechanism takes action, as the wind blows over a forward moving wave, a complex air flow is formed over the wave. This flow causes a secondary air circulation around the parallel wave crest axis. Consequently, below that axis, where the wind velocity is equal to the wave celerity, the air flow is reversed from the relative forward moving point of view of the wave. As opposed, above the axis, the air relative velocity has the same sign as the wave celerity and therefore, a flow circulation in the vertical plane above the wave surface is created. That flow causes a pressure distribution on the surface that is out of phase with the surface displacement and thus, resulting in a momentum transfer to the wave that selectively amplifies the

wave steepness, i.e. the steeper the wave the faster it grows. There exist also shear effects on the growth of waves but they have been proved to have minor relevance. Wave to wave interaction also causes substantial on wave growth, being the smaller wave that transfers the energy to the bigger one under certain conditions, depending on the phase and direction.

For wave prediction, wave climate analysis, design of coastal and offshore structures is convenient to choose a single wave height and period as representative parameters of a full wind-waves spectrum. Sorting the heights of a wave records and then averaging the highest $n\%$ the H_n is obtained. The most used representative wave height is the H_{33} and is commonly known as the significant wave height H_S. The value of the 33% it is chosen since it is the value an experienced observer would report when visually estimating the height of a sea state. The significant wave period T_S is the wave period that corresponds to H_S.

Whether the significant wave height and period or the resulting spectrum, are strictly related to the Fetch F, wind velocity W and duration t_d. Other factors, such as the fetch width, the water depth, the atmospheric stability, the temporal and spatial variability in the wind field or the bottom characteristics (under shallow water conditions) can, to a certain extent, affect the waves characteristics. As previously stated, waves have not a single direction but they spread around the predominant direction. When propagating throughout the fetch waves increase their period whereas its directional spreading decreases. For this reason, the narrower the fetch is the fewer the possibilities are that short waves remain within the fetch limits. Water depth affects the water surface shape and kinematics. Bottom friction also dissipates energy decreasing the growth rate and thus the ultimate wave size and the atmospheric stability directly affects the wind field. However, all these factors are usually neglected due to their small contribution to wave formation and growth, leaving the fetch length F, the wind velocity W and the duration of the wind t_d as the only accountable parameters.

When the duration exceeds the time required for the waves to travel the whole fetch, $t_d > \frac{F}{C_g}$, waves will grow continuously and their characteristics at the end of the fetch will only depend on F and W, this is known as the fetch limited conditions and is represented by the line OAB in figure 2.9. On the contrary, when the duration of the the wind does not allow waves to travel the whole length of the fetch under its influence, waves reach a certain size and the stabilize, which is known by the term duration limited condition, shown in line OAC in figure 2.9. When the fetch is extremely long and the fetch limited conditions are fulfilled, note that line OAB in figure 2.9 will reach a horizontal asymptotic behaviour, having reach the fully developed sea condition

as previously mentioned.

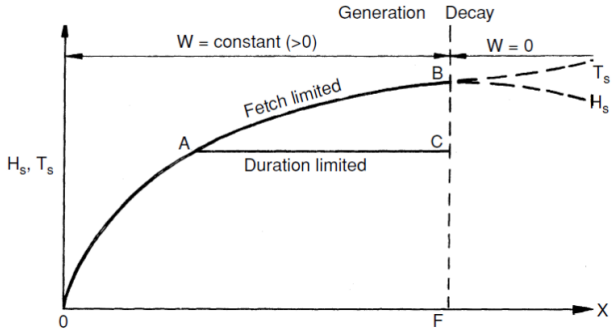

Figure 2.9: *Graphical representation of the wave generation process.*

A wave spectrum is a plot of the wave energy density at each frequency component. Figure 2.10 shows the evolution of wave spectrum as the waves propagate along the fetch and confirms what stated above. A decrease of the peak frequency can be identified, confirming the growth in period. Furthermore, the area below spectrum increases during the process endorsing the growth in height. Finally, the shape of the spectrum evolves as well getting more peaked and narrow, explaining that diverse and disperse waves tend to merge forming a predominant type of wave.

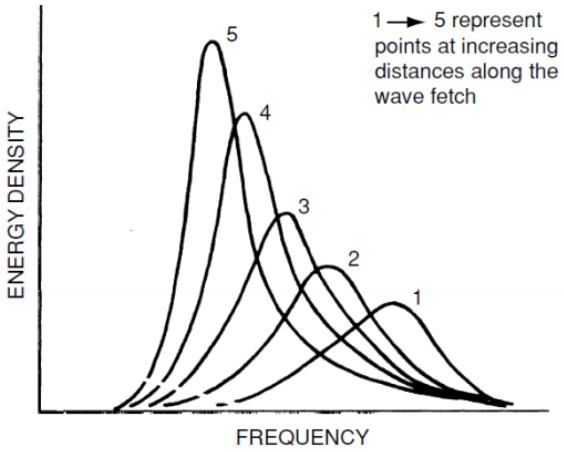

Figure 2.10: *Variation of the wave spectrum along the length of the fetch.*

2.1.3 Wave analysis and statistics

The general understanding of wind-generated waves comes mostly from the analysis of wave records. Most of these records are point measurements of the water surface

variation at a fixed location. There are two recurrent methods to analyse wave data, relying in two different domains, the time domain and the frequency domain. The former consists in identifying individual waves in the record and analyse statistically its properties. The latter consists in conducting a Fourier analysis of the wave record to develop a full wave spectrum. Both methods are described in this section following the previous order.

Figure 2.11 is a graphical representation of a short fragment of a typical wave record. In time domain, the most commonly used analysis procedure is the zero-crossing method, which has two variants, the zero-down-crossing and the zero-up-crossing. Both methods have exactly the same validity and the results are totally equivalent, the only difference lies in referencing framework. However, the most commonly used method is the zero-up-crossing (46). A mean water surface elevation is set and each point that crosses the mean surface elevation is registered. The elapsed time between two consecutive points is the wave period and the maximum absolute vertical distance with respect to the mean level, that is to say, the difference between the wave crest and trough, is the wave height. In the zero-up-crossing procedure, waves are counted when water surface level crosses the zero level switching from negative to positive values as opposite to the zero-down-crossing where the values switch from positive to negative. Small fluctuations are left apart from the counting, filtering out the high frequency components.

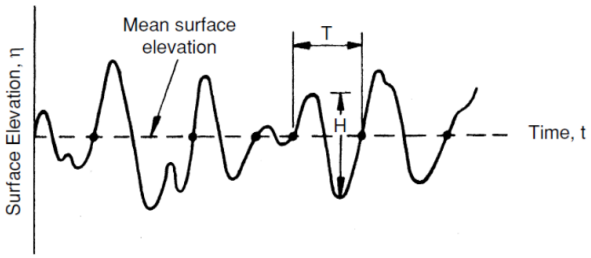

Figure 2.11: *Illustration of the water surfer elevation variation in time*

A major concern in the analysis is the distribution of height in the record. Wave heights can be plotted as a height-frequency distribution, note that in this case the term frequency refers to frequency of occurrence and not the inverse of the wave period; that is probability. Figure 2.12 represents an example of such distribution, where $p(H)$ is the frequency of occurrence and H is the wave height. The shaded area is the upper one-third of the wave height and its averages gives the significant wave height.

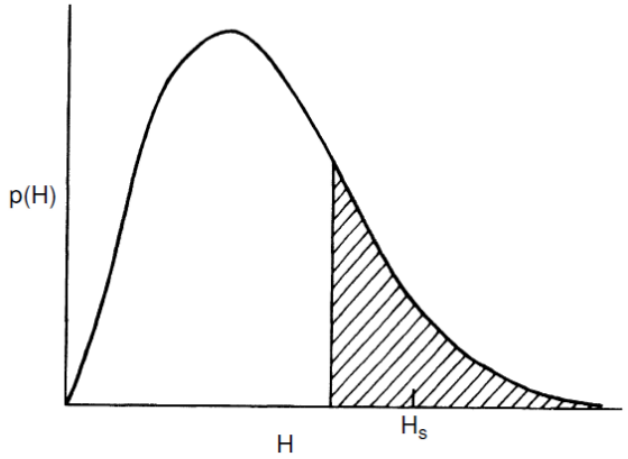

Figure 2.12: *Probability distribution of wave heights registered in a wave record*

For engineering purposes the most important distribution of wave heights is the one generated by storms. Longuet-Higgins (67) proved that this kind of distributions is well defined by the Rayleigh probability distribution, which can be written with the following expression:

$$p(H) = \frac{2H}{H_{rms}^2} e^{-\frac{H}{H_{rms}}^2} \tag{2.63}$$

Where the root mean squared height H_{rms} is given by

$$H_{rms} = \sqrt{\sum_{i=1}^{N} \frac{H_i^2}{N}} \tag{2.64}$$

Where H_i is the individual wave height among the N waves contained in the wave record. From the Rayleigh distribution the following useful relationships can be extracted, $H_S = 1.416 H_{rms}$ and $H_1 00 = 0.886 H_{rms}$. The cumulative probability distribution results in:

$$P(H) = \int_0^H p(H) dH = 1 - e^{-\frac{H}{H_{rms}}^2} \tag{2.65}$$

For engineering purposes is much more interesting to know the percentage of waves having a greater height that the give threshold.

$$1 - P(H) = e^{-\frac{H}{H_{rms}}^2} \tag{2.66}$$

Nesting the relationship which links H_S and H_rms in equation 2.66 the following relation is obtained: $1 - P(H_S) = e^{-}(1.416)^2 = 0.135$, revealing that 13.5% of waves during a storm might have higher waves than the significant wave height. Figure 2.13 is a very useful adapted form of the Rayleigh's distribution, line a displays the probability P of a certain wave with height H to occur with respect to the ratio $\frac{H}{H_rms}$ whereas line b shows the average height of the n highest fraction of waves.

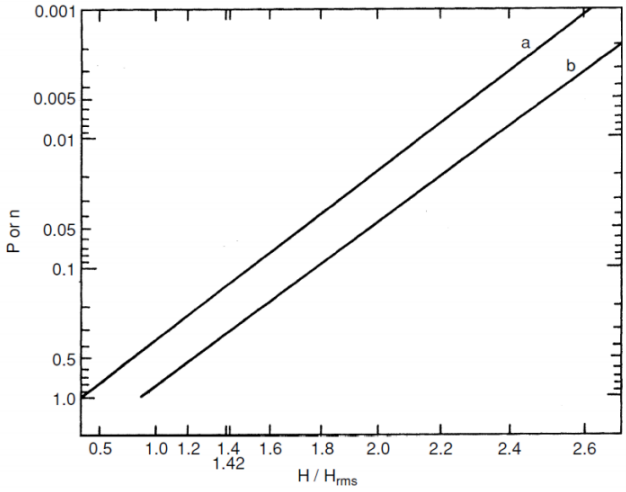

Figure 2.13: *Logaritmical Rayleigh distribution*

When a sea state, defined by a spectrum of waves reaches the shore, wave breaking limits the wave height distribution at a higher end. Some authors have modified the Rayleigh distribution to match that behaviour. There is no upper limit to the wave heights specified by the Rayleigh distribution. Longuet-Higgins (67) demonstrated that for a storm with relatively large number of waves N, the expected value of the highest wave is:

$$H_max = 0.707 H_S \sqrt{lnN} \tag{2.67}$$

This relation is valid in the offshore areas where the waves are not affected by the seabed and there are no breaking conditions, which due to its highly non-linear behaviour void the validity of this expression.

The joint wave height-period probability distribution is also of interest. Figure 2.14 shows the distribution of the wave height versus the wave period, note that the values are non-dimmensionalized according to the average value of the record. The contour lines denote equal probability of occurrence. The significant wave period T_S is considered

to be more stable statistically than the average period and therefore, is preferred to represent the records.

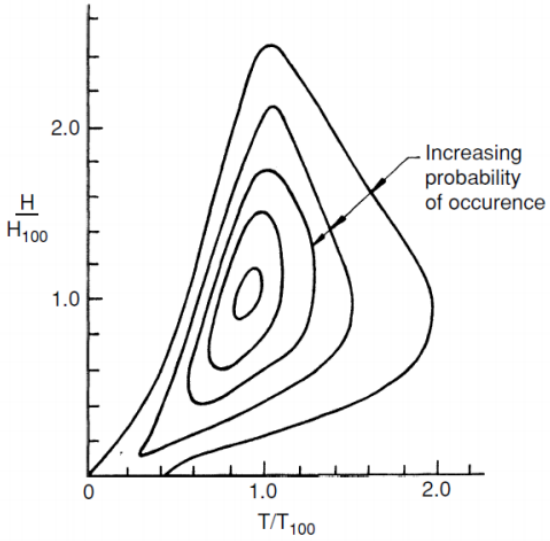

Figure 2.14: *Curves of equal-probablity of non-dimmensionalized wave height over non-dimmensionalized wave periods.*

The frequency domain analysis consists in analysing the resulting spectrum of a wave record. A water surface profile can be reproduced by a series of sine waves with different amplitudes,periods,phases and propagation directions. A full representation of it can be achieved by s directional wave spectrum, which is produced when the sum of the energy density of the components $S(f,\theta)$ is discretized versus the wave frequency f and direction θ. However, in most of the cases, a θ corresponding to the mean wave direction is picked and the spectrum is represented only as a function of the frequency $S(f)$. From the linear wave theory, the energy density of a monochromatic wave is $\frac{\rho g H^2}{8}$. The fluid density ρ and the acceleration of gravity g are constant values can be left apart from the following expression:

$$S(f,\theta)df\,d\theta = \sum_{f}^{f+df}\sum_{\theta}^{\theta+d\theta}\frac{H^2}{8} \tag{2.68}$$

Where H is the wave height in the record, this expression is further simplified for

the one-dimensional spectrum as:

$$S(f,\theta)df\,d\theta = \sum_{f}^{f+df} \frac{H^2}{8} \tag{2.69}$$

The exact scale and shape of the a wave spectrum depends on the generating factors, stated on section (2.1.2), takes the following general form

$$S(f) = \frac{A}{f^5} e^{\frac{-B}{f^4}} \tag{2.70}$$

Where A and B are adjusting scale factors that can be written as function of the wind-wave generating parameters or as function of the representative wave parameters such as the significant wave height and period (H_S,T_S). An important way to define a wave spectrum can be by means of the spectral moments, the n^{th} moment is the defined as:

$$m_n = \int_0^\infty S(f) f^n df \tag{2.71}$$

For instance the 0^{th} moment the area below the spectral curve and states the total energy of the sea state. From the linear wave theory, the total energy density is twice the potential energy and is written as:

$$\overline{E} = 2\overline{E}_p = \frac{2}{T_*} \int_0^{T_*} \rho g \eta(\frac{\eta}{2}) dt \tag{2.72}$$

Where T_* is the length of the analysed wave record and the bar over the E denotes the energy density. Equation 2.72 can be rewritten as:

$$\overline{E} = \rho g \overline{\eta}^2 = \frac{\rho g \sum \eta^2}{N_*} \tag{2.73}$$

In that occasion the bar over E denotes the average of the sum of N_* water surface values from a wave record of length T_*. From the definition of H_rms and H_S the energy density can also be expressed as:

$$\overline{E} = \frac{\rho g H_r ms^2}{8} = \frac{\rho g H_S^2}{16} = \rho g m_0 \tag{2.74}$$

Rearranging equation 2.74 the significant wave height of a spectrum is yielded: $H_S = 4\sqrt{m_0}$. and hence, H_S takes the name of H_{m_0} in the frequency analysis.

The Rayleigh distribution is a useful model for the expected distribution of wave

heights for stormy conditions, but clearly not enough and thus needs to be complemented by spectral information. Several one-dimensional wave spectra have been proposed and they all derive from the expression 2.70. The two most commonly used spectra are presented and described in the following lines. The first type is the Pierson-Moskowitz Spectrum (78). The authors analysed wave and wind records from the British fleet operating in the north Atlantic and selected records representing, in the majority of the case, fully developed seas for wind velocities between 20 and 40 knots to generate the spectrum reported below:

$$S(f) = \frac{\alpha g^2}{(2\pi)^4 f^5} e^{-0.74(\frac{4g}{2\pi W f})^4} \tag{2.75}$$

Where W is the wind speed measured at 19.5 meters above the mean sea level. Other wind-generated wave formation parameters such as the fetch length or the duration are not taken into account due to the fully developed sea conditions. The α coefficient is a scale factor and usually set to 8.1×10^{-3}. The following relationships can be derived from the Pierson-Moskowitz spectrum formula: $H_{m_0} = \frac{0.21W^2}{g}$ and $f_p = \frac{0.87g}{2\pi W}$.

(54) is the other spectrum model described in this thesis and, by far the most widely used. stands for JOint North Sea WAve Project and it was elaborated by laboratories from four different countries. Wave and wind measurements were taken with sufficient wind durations to produce a deep water fetch limited model. The model development begins with a simple association, if the wind velocity W is isolated from the peak frequency relation of the Pierson-Moskowitz spectrum and the substituted into equation 2.75 the following equation is obtained:

$$S(f) = \frac{\alpha g^2}{(2\pi)^4 f^5} e^{-1.25(\frac{f_p}{f})^4} \tag{2.76}$$

Hence, the JONSWAP spectral equation is a slight modification of equation 2.76 achieved by developing relationships for α and f_p with the wind speed and the fetch. Finally, enhancing the spectrum peak by a factor of γ, which aims to adapt the spectrum to different types of sea conditions, the final JONSWAP spectrum is obtained:

$$S(f) = \frac{\alpha g^2}{(2\pi)^4 f^5} e^{-1.25(\frac{f_p}{f})^4} \gamma^a \tag{2.77}$$

Where

$$a = e^{-[\frac{(f-f_p)^2}{2\sigma^2 f_p^2}]} \sigma = 0.07 \text{when} f < f_p \sigma = 0.09 \text{when} f >= f_p \tag{2.78}$$

The coefficient α, γ and f_p are given by the following relationships:

$$\alpha = 0.076(\frac{gF}{W^2})^{-}0.22 \tag{2.79}$$

$$f_p = \frac{3.5g}{w}(\frac{gF}{w^2})^{-}0.33 \tag{2.80}$$

$$\alpha = 7(\frac{gF}{W^2})^{-}0.143 \tag{2.81}$$

However, In the JONSWAP spectrum the parameter γ has a range of values from 1.6 to 6 and for wind seas the $\gamma = 3.3$ is generally used. Nowadays, the JONSWAP spectrum has become the most widely used spectrum for engineering design and for laboratory irregular wave experiments. Figure 2.15 plots the generic shape of both spectra; depending on the chosen γ parameter, the JONSWAP spectrum accentuates its energy density at the peak value, differences outside the peak range are rather low.

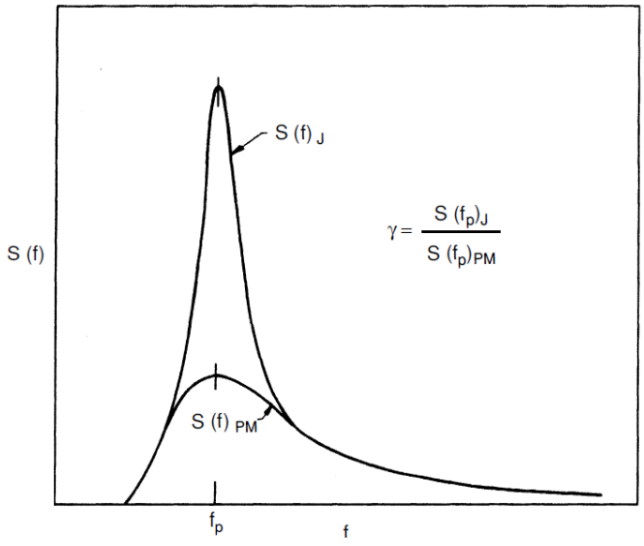

Figure 2.15: *JONSWAP and Pierson-Moskowitz spectra*

2.2 Floating structures

Wave-structure interaction is a key subject in this thesis. In order the maximize the WECs performance, the dynamical behaviour of the device needs to be tuned to meet specific requirements, such as resonance for certain wave conditions. Therefore, this

Mode #	Component	Mode Name
1	$u_1 = U_x$	surge
2	$u_2 = U_y$	sway
3	$u_3 = U_z$	heave
4	$u_4 = \Omega_x$	roll
5	$u_5 = \Omega_y$	pitch
6	$u_6 = \Omega_z$	yaw

Table 2.1: *Rigid body modes of motion.*

section is aimed to describe thoroughly all the phenomena affecting floating bodies under the action of waves.

The first step when studying floating structure dynamics is to create a reference coordinate framework upon which all variables will be based. The most widely used reference system is the Cartesian coordinate system in which (7), three axis: x, y and z are defined. For simplicity, the centre of the coordinate system is usually set at the centre of gravity of the studied structure or at the Mean Water Level (MWL). Each axis is orthogonal to the other, defining the normal vector of three planes that describe the three-dimensional space. A free-moving body has six DoFs, three of them describing the translations and the other three, the rotations. Therefore, in mathematical formulae the subscripts $1-3$ are linked to the translations and $4-6$ to the rotations. Modes $1, 2$ and $4, 5$ are ambiguous, specially if the structure is axisymetric with respect to the z axis and therefore they may be interchanged. However, common praxis is to remove this ambiguity when there is an incident wave; orienting the structure so as to make the wave propagation direction coincide with the x-axis of the structure, see figure 2.16. In marine structures, each DoF is associated to a particular name, as reported in table 2.1.

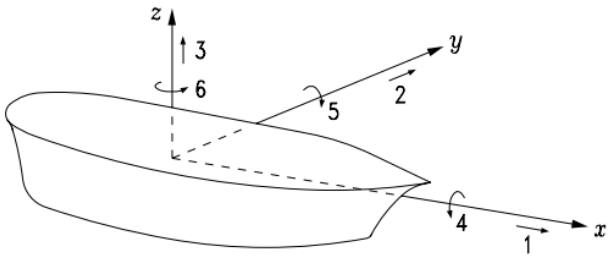

Figure 2.16: *Rigid body six modes of motion*

Rigid body dynamics are governed by the Newton's second law.

$$\sum \vec{F} = m\vec{a} \tag{2.82}$$

Where $\vec{F} = F_1, F_2, F_3, F_4, F_5, F_6 \equiv F_x, F_y, F_z, M_x, M_y, M_z$ is the force vector for each mode, m is the mass matrix of the body, in which the first three components of the diagonal are the mass of the body and the last three are the moments of inertia and $\vec{a} = a_1, a_2, a_3, a_4, a_5, a_6$ is the acceleration vector of the body for each mode. For floating bodies the $\sum \vec{F}$ is decomposed in two main types of forces exerted by fluids: $\vec{F} = \vec{F}_{hd} + \vec{F}_{hs}$, the hydrodynamic forces and the hydrostatic force respectively.

In this thesis all derivations of hydrodynamic forces have been developed under the linear wave theory hypothesis (section 2.1.1). Consider figure 2.17, where p is the hydrodynamic pressure, thus integrating over the wet surface $p(-n_i)dS = -pn_i dS$ yields the total force for the i^{th} mode:

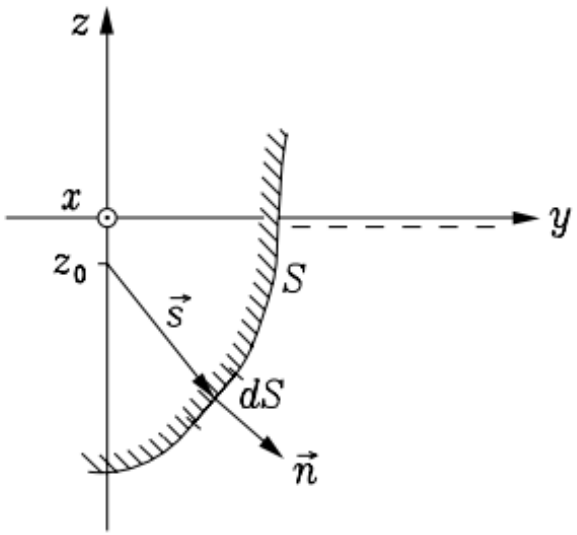

Figure 2.17: *Surface element dS of wet surface S of a rigid body*

$$F_i = -\iint_S pn_i dS \tag{2.83}$$

In terms of complex amplitudes, using the relation $\hat{p} = -i\omega\rho\hat{phi}$ for a given potential

$\hat{phi}$,

$$F_i = i\omega\rho \iint_S \hat{phi} n_i dS \tag{2.84}$$

For $i = [1-3]$ International System (SI) units are (N) and for $i = [4-6]$ SI units are (Nm). These are the general expressions for the hydrodynamic force. However, hydrodynamic forces can be divided into three subcategories: $\vec{F}_{hd} = \vec{F}_e + \vec{F}_r + \vec{F}_{drag}$, the wave excitation force, the radiation damping force and the viscous drag force respectively.

To account only for the effect of an incident wave, the body is held fixed, resulting into a potential $\hat{\phi}$ due only to the disturbance created by the oncoming waves. In such case, being $F_e \equiv F_{e,1}, F_{e,1}, F_{e,1}, F_{e,1}, F_{e,1}, F_{e,1}, = \vec{F}_e, \vec{M}_e$ the generalized excitation force/moment vector. Using equation 2.83

$$F_{e,i} = i\omega\rho \iint_S (\hat{\phi}_0 + \hat{\phi}_d) n_i dS \tag{2.85}$$

Where the wave potential $\hat{\phi}$ is decomposed in two components, $\hat{\phi}_0$ and $\hat{\phi}_d$, which are the undisturbed wave field and the diffracted wave field respectively. The latter is created when the BC for the wet surface is not satisfied and thus the following relation takes over:

$$-\frac{\partial \hat{\phi}_d}{\partial n} = \frac{\partial \hat{\phi}_0}{\partial n} \text{on} S \tag{2.86}$$

The rest of BC, on the seabed $z = -h$ (2.16) and on the free water surface $z = 0$ (2.23 must be fulfilled. If the body dimensions are reduced in comparison of the wavelength, the diffraction problem can neglected. In order to determine this threshold the Keulegan-Karpenter (KC) number is used.

$$KC = \frac{2\pi A}{L} \tag{2.87}$$

Where A is the typical body dimension and L is the wavelength. If $KC > 10$ the body may be considered small and thus, dominated by drag forces. As a result, the diffraction potential may be neglected, resulting in a computational advantage since the the boundary-value problem of equation (2.86) may not be solved. The following linear system for the excitation problem is defined:

$$\hat{F}_e = f(\omega) A \tag{2.88}$$

where A, the input of the system, is the amplitude of the undisturbed incident

wave field at the origin $\hat{\eta}_0(0,0)$ and f the excitation coefficients is the transfer function. As linear waves are adopted the Fourier transforms can be applied to obtain the the frequency-dependant values:

$$F_e(\omega) = f(\omega)A(\omega) \tag{2.89}$$

The inverse Fourier transform of $f(\omega)$ is the impulse response function of the wave excitation force, usually assuming a non-casual behaviour due to the nature of its source, distant storms or oscillating wave-makers. By applying the inverse Fourier transform to equation (2.89),

$$F_{e,t}(t) = f_t(t) * a(t) = \int_{-\infty}^{\infty} f_t(t-\tau)a(\tau)d\tau = \int_{-\infty}^{\infty} f_t(\tau)a(t-\tau)d\tau \tag{2.90}$$

Where $f(t)$ is obtained as follows and $f(\omega)$ is computed by applying with the correct BCs the equation (2.85.

$$f_t(t) = \frac{1}{2\pi}\int_{\infty}^{\infty} f(\omega)e^{i\omega t}d\omega \tag{2.91}$$

If instead of fixing the body and let the incoming wave go through the opposite is done, moving the body and setting the incident wave potential to zero another phenomenon occurs. The structure produce waves as the result of displacing the water around its surface due to its motion. This produced waves are radiated waves and this phenomenon is called radiation, and of course, radiated waves exert a reaction force on the body surface, the so called radiation force. The radiated wave with a velocity potential ϕ_r given by

$$\hat{\phi}_r = \sum_{j=1}^{6} \varphi_j \hat{u}_j \tag{2.92}$$

where φ_j is a coefficient of proportionality and $\hat{u}_j$ is the velocity of the body in the j^{th} mode. The radiation reaction force on the $j^{'th}$ mode deriving from the j^{th} mode is

$$\hat{F}_{r,j,j'} = i\omega\rho \iint_S \varphi_j \hat{u}_j n_{j'} dS \tag{2.93}$$

Regardless the j^{th} mode, $\hat{u}_j$ is a constant throughout the surface as the body is

rigid, thus one can write

$$\hat{F}_{r,j,j'} = -Z_{j,j'}\hat{u}_j \tag{2.94}$$

Where $Z_{j,j'}$ is called the radiation impedance, having SI units (Ns/m) for $Z_{j,j'}(j = 1,2,3,j')$ and (Nsm/rad) for $Z_{j,j'}(j = 4,5,6,j')$ and assuming the following form

$$Z_{j,j'} = -i\omega\rho \iint_S \varphi_j n_{j'} dS \tag{2.95}$$

Using the wet-surface BC one can obtain

$$Z_{j,j'} = -i\omega\rho \iint_S \varphi_j \frac{\partial \varphi_{j'}}{\partial n} dS = -i\omega\rho \iint_S \varphi_j \frac{\partial \varphi^*_{j'}}{\partial n} dS \tag{2.96}$$

Whereas φ_j is complex, $\frac{\partial \varphi_{j'}}{\partial n}$ is real on S in order to fulfil the BC. Hence by applying the conjugate no change. However, the a reciprocity relation can be found as $Z_{j,j'} = Z_{j',j}$ making the 6×6 impedance matrix symmetric. Since ω is real, it is convenient to divide $Z_{j,j'}$ into real and imaginary parts:

$$Z_{j,j'} = R_{j,j'} + iX_{j,j'} = R_{j,j'} + i\omega m_{j,j'} \tag{2.97}$$

where $R_{j,j'}$ is named the radiation resistance matrix, $X_{j,j'}$ the radiation reactance matrix and $m_{j,j'}$ is the added mass matrix, which physical meaning is the fluid mass displaced by the body while moving. Assuming that the body has an harmonic monochromatic monochromatic movement with frequency ω the radiation force can be expressed as

$$F_r(\omega) = -Z(\omega)u(\omega) \tag{2.98}$$

Where $u(\omega)$ is the Fourier transform of $u(t)$ and $Z(\omega)$ is the transfer function of the system, corresponding to the inverse Fourier transform of the radiation impulse response function. Note that, unlike the excitation force case the radiation system is causal

$$z(t) = 0 \text{for} t < 0 \tag{2.99}$$

Meaning that $F_r(t) = 0$ before a $u(t)$ is established, as the body velocity is the only

cause for waves to be radiated. Analogously to equation (2.97) Z can be rewritten as:

$$Z(\omega) = R(\omega) + i\omega m(w) \tag{2.100}$$

The fact that Z is causal allows the derivation of $R(\omega)$ and $m(\omega)$ by the application of the Kramers-Kronig relations. Noting that $m(\omega)$ does not vanish at $\omega \to \infty$ a related transfer function needs to be introduced in order to avoid such singularity

$$H(\omega) = m(\omega) - m(\infty) + \frac{R(\omega)}{i\omega} \tag{2.101}$$

Now, substituting equations (2.100) and (2.101) into equation (2.98) the following expression for the radiation force is obtained

$$F_r(\omega) = F_r^{'}(\omega) - i\omega m(\infty)u(\omega) \tag{2.102}$$

where

$$F_r^{'}(\omega) = -i\omega H(\omega)u(\omega) = -K(\omega)u(\omega) \tag{2.103}$$

Applying the inverse Fourier transform to the extended form of $F_r(\omega)$ the following expression is obtained:

$$F_{r,t}(t) = -k(t) * u_t(t) - m(\infty)\dot{(}u)_t(t) \tag{2.104}$$

where the kernel $k(t)$ of the convolution is found by applying the Kramers-Kronig relations with the causality particularity:

$$k(t) = \frac{1}{2\pi}\int_{-\infty}^{\infty} K(\omega)e^{i\omega t}d\omega = \frac{2}{\pi}\int_{0}^{\infty} R(\omega)\cos(\omega t)d\omega = 2\mathcal{F}^{-1}R(\omega) \tag{2.105}$$

Due to the principle of causality, all the information contained contained in the two matrix functions $R(\omega)$ and $m(\omega)$ is expressed altogether in the real matrix function $k(t)$ and in the constant matrix $m(\infty)$.

As reported in equation (2.87), if the $KC > 10$, then the small body hypothesis can be taken into consideration, stating the drag forces are predominant over the diffraction forces. The drag force has two components, the surface frictional drag and wake pressure drag. The overall effect that the drag force induces to the body is extremely complicated, to such extent that is still not fully understood. Empirical analysis however, have

brought to a formula which is still the widely used to the present date:

$$F_d = \frac{1}{2}\rho C_d A_d u^2 \tag{2.106}$$

Where A_d is the area of the wet part of the body projected onto the normal plane of the velocity, C_d is the drag coefficient, which mainly depends on the shape of the body, the roughness of the surface, the KC number and on the Reynolds number (R_e). Finally, u is the relative velocity between the body and the fluid flow, in equation (2.106 the flow is assumed to be steady. Nonetheless, in the presence of waves the flow cannot be assumed steady as it varies harmonically, the adapted expression for the drag force under the presence of waves is

$$F_d = \frac{1}{2}\rho C_d A_d |u| u \tag{2.107}$$

The absolute value allows predict the oscillatory behaviour of waves by taking into account the sign of the velocity. For simple body shape, C_d can be found tabulated in literature deriving physical experiments. For more complex shapes however; on the one hand, *ad-hoc* experimental tests need to be carried out in order to determine such parameter; on the other hand, the fast growing computation capacity has led to the irruption of a new tool, the CFD which allow to perform simulations in order to determine the C_d parameter in a much more efficient way, either in terms of cost and times.

Finally, the last force force to be determined is the hydrostatic force, caused by the hydrostatic pressure and first postulated by Archimedes. Back in the ancient Greek times, the Philosopher theorized the following principle: *A body placed in a liquid loses and amount of weight equal to the weight of the liquid that it displaces.* Following this observation, the equation of hydrostatics can be derived. Considering a partially submerged body, which displaces a volume V of water. Consider also W the total weight of the body, A its cross-sectional area and d its draft. Then, following the Archimedes principle one can write

$$W = \gamma V = (\rho g) A d \tag{2.108}$$

Where γ is the weight density of the liquid, water in this case. As W is a force, the hydrostatic pressure acting on the bottom of the body can be assumed to $p = -\rho g d$. From its equilibrium position, lets assume the body be given a small downwards vertical displacement $-\delta z$. From the Archimedes theorem the new equilibrium position results

in the following equation:

$$\gamma(\delta V) = -\rho g(\delta z)A = \delta pA \tag{2.109}$$

This variation from the equilibrium, in this example in the vertical axis, causes then a restoring force that tends to bring the body back to its initial equilibrium position. The restoring force, also known as buoyancy force in a more general form is given by the following expression:

$$F_b = -W = (\rho g V)\vec{k} \tag{2.110}$$

Where $\vec{k}$ is the unit vector of the vertical direction in the orientation of the body.

2.3 Electric generators

The power chain in wave energy converters has three main steps. As seen in section (2.1), one of the manifestations of energy transport in the ocean are waves. Part of this energy is then captured by the wave energy converter structure through the mechanical laws, expressed mainly by motion, as reported in section (2.2). Finally, the mechanical energy stored in the device structure needs to be converted in a usable, transportable and continuous form energy. The most efficient kind of energy known to the present day is the electricity. Mechanical energy can be transformed into electrical energy through electrical generators. Countless types of generators have been been invented over the past two centuries, when electricity and its enormous exploitation potential was discovered. Nonetheless, in this thesis only two types of generators are of interest, since are the two most suitable and promising technologies for wave energy conversion.

Firstly, a general outlook on the laws of electromagnetism will be given in order to acquire the generic knowledge that allows full comprehension on the working principle of electromagnetic generators. Secondly, the traditional rotative machine used to convert the electricity in the MoonWEC device will be explained in detail. Finally, the LG, an innovative technology usually adopted in wave energy conversion and used in the HPA-LG will be exposed.

2.3.1 Electromagnetism

Electromagnetic laws are well represented by the Maxwell's equation:

$$\nabla \cdot D = \rho_c \tag{2.111}$$

$$\nabla \cdot B = 0 \tag{2.112}$$

$$\nabla \times E = -\frac{\partial B}{\partial t} \tag{2.113}$$

$$\nabla \times H = J + \frac{\partial D}{\partial t} \tag{2.114}$$

Where B is the magnetic flux density or magnetic induction, D is the displacement field, E is the electric field and H is the magnetizing field or magnetic field intensity. On the other side of the equations there are ρ_c that refers to the charge density and J, which is the free current density. Equation 2.112 states that the flux of the magnetic induction must be zero in the whole domain of the body. In spite of electric fields, magnetic fields must complete a close loop. Equation (2.113) expresses that the curl of the electric must match the reverse variation of the magnetic field in time. The magnetic field intensity can also be expressed by the following equation, having A/m as units:

$$\underline{H} = \frac{1}{4\pi} I \int_C \frac{\vec{dl} \times \vec{r}_l}{r^2} \tag{2.115}$$

Integration is performed over the circuit C that carries the current I. This current gives place to an H-field at the point P. the unit vector $\vec{r}_l$ and the resistance r the direction and distance from the circuit C to the point P. See figure 2.18

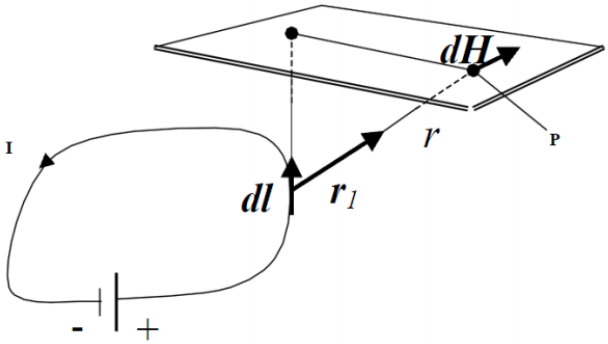

Figure 2.18: *Conceptual scheme of the magnetic induction*

The magnetic field induction is closely related to the force exerted on a conductor carrying an electrical current. The material property known as the permeability constant μ acts as link with the magnetizing field:

$$B = \mu H \tag{2.116}$$

Thus, determining how strong will be its capability to induce a magnetic field in Tesla (T). The magnetic flux through a surface S is measured in Webbers (W) and defined by:

$$\Phi = \int_S \underline{B} d\vec{a} \tag{2.117}$$

Another important concept is he magnetization M. Namely, the magnetic momentum per unit of volume at a point in a given medium, it has the same units as the magnetic field intensity H and contributes to the magnetic induction in the following way:

$$\underline{B} = \mu_0(\underline{H} + \underline{M}) \tag{2.118}$$

Where μ_0 is the permeability of free space, the vacuum. Using the Stokes' theorem, equation 2.114 can be reformulated as follows:

$$\oint_C \underline{H} d\vec{l} = \int_S \underline{J} d\vec{a} \tag{2.119}$$

Equation (2.119) is the Ampere's law and states that the integral of the magnetic field intensity over a closed loop yields the integral of the density of current going

through inner surface S surrounded by the circuit C. This is the theoretical origin of the solenoids or coil turns, the final total current in a coil is the one obtained in equation (2.119) times the number of turns of the coil. The Stokes' theorem can also be applied in the left hand side of equation (2.113) and in the right hand side of equation (2.117), resulting in:

$$e = -\frac{d\Phi}{dt} \tag{2.120}$$

This is known as the Faraday's law for induction. The e is the induced voltage by the total magnetic flux bounded by the circuit. The direction of the induced current is what generates the opposition against the flux change by the magnetic field. As in the case of the Ampere's law, the induced voltage for the circuit is multiplied by the number of turns of the coil. However, none of these behaviours would be as they are without the existence of a kind of materials with unique properties, the ferromagnetic materials. This type of materials are magnetic dipoles that can reach very high levels of magnetization M, this ability is expressed through the relative permeability μ. Equations (2.116) and (2.118) can be combined to show the dependence between M and μ:

$$\mu = \mu_0(1 + \frac{M}{\underline{M}} \tag{2.121}$$

The relative permeability of ferromagnetic materials is quite elevated and therefore, used to build devices to guide the magnetic flux. Each material has a curve of magnetization, in which depending on the applied magnetic field; a magnetic induction is achieved to a greater or lesser extent. When the ferromagnetic material reaches the saturation means that the magnetic induction stabilizes and thus, magnetization no longer increases. See figure (2.19).

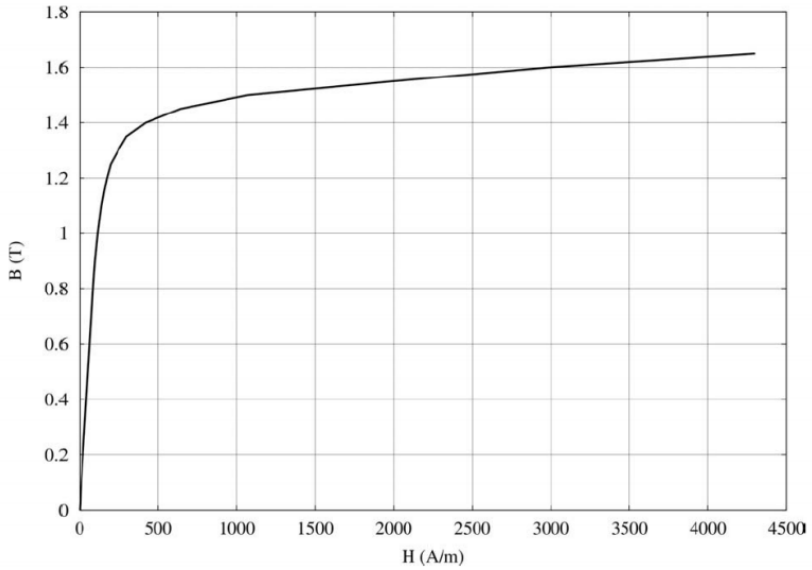

Figure 2.19: *Magnetization curve for a ferromagnetic material*

Each generator has a magnetic equivalent, which has been described in full detail above but also has an electric equivalent, which is usually known as the equivalent circuit, illustrated in figure (2.20). The induced voltage is E_{nl}, it can bee seen as a no load voltage and is the measurable voltage at the coil ends when no electric current is flowing through the generator. X_S is the synchronous reactance and R_C is the resistance of the of the coil windings. R_{load} can be purely resistive, reactive or a combination of both. The meaning of the load is the useful interface in which the output power will be used, could be an appliance, a house or simply the national grid. Finally, U is the voltage used by that interface and is in phase with the current in the armature I_a.

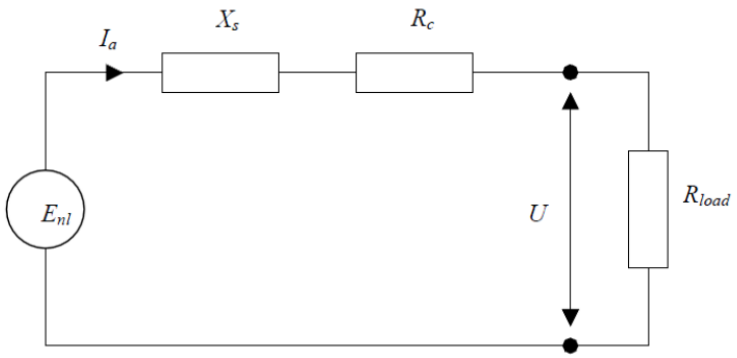

Figure 2.20: *Equivalent electric circuit*

The equivalent circuit equation can be deduced following the Kirschof's law for the tension U:

$$U = E_{nl} - (R_c + jX_s)I_a = R_{load}I_a \tag{2.122}$$

Although the simple appearance of this equation, due to complex numbers and the electric angular velocity deriving it, to solve the problem another schematic way is used, based in trigonometry rather than electromagnetism. Figure 2.21 illustrates a phasor diagram describing the relations between the different parts of the equivalent circuit. This allows to solve the problem rather easily through a trigonometric relation

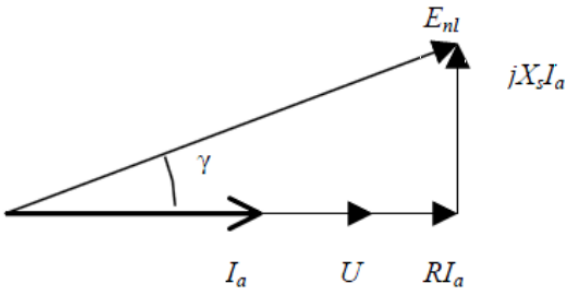

Figure 2.21: *Conceptual representation of the load angle*

The angle δ between the pure resistive load voltage and the real load voltage is called load angle and determines in an easy manner the degree of reactance of the equivalent circuit. Electric theory states that the lower the load angle, the smaller the apparent power and thus, the higher the power factor of the generator.

$$U = E_{nl}\cos\delta - RI_a \tag{2.123}$$

The term RI_a represents the copper losses by the Joule effect, which is power transformed into heat. The copper losses are not the only losses occurring in electric generators. Typical losses found in induction generators are:

- Losses due to the changing magnetic field
  - Hysteresis losses
  - Eddy current losses
- Resistive losses in the coil windings (Joule Effect)
- Mechanical losses due to friction and deformation

The majority of generators have a multi-phase system, which means that the coil windings are composed of several parallel circuits. Each single circuit is called a phase. the most used system worldwide is the three-phase system in which is phase is shifted $2\pi/3$ electrical radians from the other. This system is used because it allows a constant power production in case of rotative machines but not for linear generators. Electric angle for linear generator is not constant, denoting a velocity variation of the translator. Actually, at the end-stop points (crest and trough of the wave) the velocity is zero and so is the instant power output.

The induction generator uses the same principle of the equation 2.120 where a time varying electromagnetic field induces an electromagnetic voltage in the coil windings. The induced voltage in the generator is the sum of all voltages separately at each coil per phase. As the vertical motion of the translator has been assumed sinusoidal monochromatic so the magnetic induction must be:

$$B = \hat{B}\sin(x - \omega t) \tag{2.124}$$

Where $\hat{B}$ is the maximum induction (equivalent amplitude), x is the reference point at the stator and ω is the angular velocity of the translator. The single flux related to a coil at a certain time t is described by the following expression:

$$\Lambda = \frac{\omega}{2\pi} N l \hat{B} \int_{-\frac{\pi}{2}}^{\frac{\pi}{2}} \sin(x - \varpi t) dx = \frac{\omega}{\pi} N l \hat{B} \sin \varpi t \tag{2.125}$$

Where ϖ is the pole width, N the number of turns and l the length of a coil turn. Consequently, the induced voltage yields:

$$e = -\frac{\partial \Lambda}{\partial t} = \varpi N l \hat{B} \cos \varpi t = 2 f \omega N l \hat{B} \cos 2\pi f t \tag{2.126}$$

The effective root mean square voltage E is defined:

$$E = \frac{\hat{e}}{\sqrt{2}} = \sqrt{2} f \omega N l \hat{B} \tag{2.127}$$

Were $\hat{e}$ is the maximum voltage.Finally, once the output tension U and the intensity current I are known the electric power can easily be determined, as the result of their multiplication $S = \sqrt{(3)} U I$.

2.3.2 Rotative Generator

According the working principle there are three main categories of electric generators: the synchronous, the induction and the parametric machines (25). Parametric generators have in most configurations doubly salient magnetic circuit structures, that is; the magnetic anisotropy is exploited in both the rotor and the stator. Their simplicity and ruggedness has made them adequate for several applications. However, they suffer from copper losses on the stator and core losses in both the stator and rotor. Induction generators mount a cage rotor and single or dual windings in the stator. The main advantage of such class of generators is that they can either work as motors or generators depending on the driving entity, if supplied to a fixed frequency and voltage becomes a motor, if driven by a prime mover becomes a generator. Synchronous Generator (SG) have a stator magnetic circuit composed by with slots, usually containing three-phase windings and a rotor. The rotor design stablish the SG configuration, which is based on two excitation principles, the heteropolar and the homopolar excitation. Heteropolar SGs subdivide in four categories: the multipolar Direct Current (DC) excited rotor, the claw pole excited rotor, variable reluctance rotor and the PM rotor. The homopolar SGs are usually excited in the stator, whether it be electrically or mounting PMs in the stator.

Lately, PMSGs are being mounted in wind turbines due to its capacity to deliver medium to high power (in the range of tenths of $[5 - 500]kW$) at low rotative speed drive $[20 - 200]rpm$ with high efficiency rates, (63). This allows to get rid of reductors and gearboxes, which usually have a negative effect in efficiency and are often the cause for breakdowns and high maintenance costs. Furthermore, PMSGs are capable to deal with variable rotation speed without a significant loss of efficiency. However, technical difficulties arise in the manufacturing process of PMSGs at the state of the art level leading to high production costs. Working conditions of some types of WECs, such as the MoonWEC are similar to the ones reported. Therefore, it is reasonable to state that direct-driven PMSGs can also be suitable for wave energy conversion.

PM excitation offers high flexibility when it comes to the generator design, shape, size, position orientation of the magnetization direction conform the variables of multiple configurations. The list expands to radial or axial flux machines, longitudinal or transversal flux machines, inner or outer rotor and interior or exterior mounted magnets. The radial flux machine with inner rotor and exterior mounted magnets is the configuration with the most mature manufacturing technology (69), having lower production costs and thus being more competitive than other configurations has been chosen for

the MoonWEC. All radial flux machines are in turn longitudinal flux machines, which means that the plane of the flux path is parallel to the axis of rotation. In a radial flux machine the normal vector to the air gap (distance between the rotor and the stator) is perpendicular to the rotation axis. The choice of the inner rotor position is merely practical. Mainly, PMSGs energy losses are copper losses, which translates into heat, it is convenient to place the stator windings on the outer part of the generator, close to the housing in order to optimize the cooling system. Surface magnets are mounted also for simplicity reasons, magnets are glued to the rotor surface in order to resist centrifugal forces. Moreover, this is the configuration that offers smallest flux leakage resulting in a high power factor. Graphical description of the above described configuration is provided in figure 2.22.

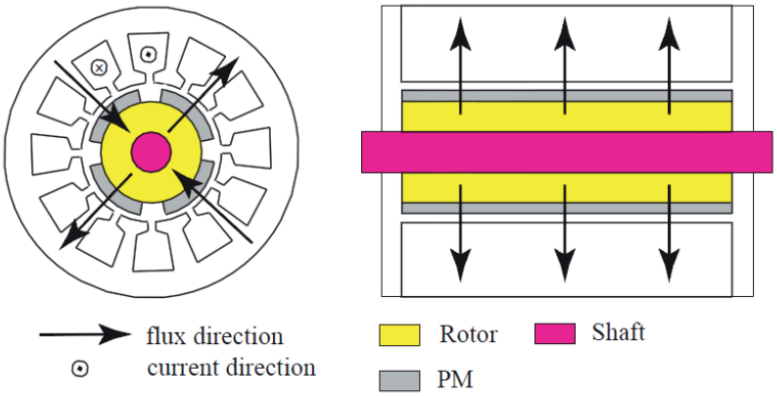

Figure 2.22: *Cross sectional view in radial and axial direction, respectively, of a typical radial flux PMSG (69)*

All synchronous machines are driven by the following relation:

$$n = \frac{f}{p} \tag{2.128}$$

Where n is the rotation speed of the shaft, f is the electric frequency of the generator and p is the number of poles.

2.3.3 Linear Generator

A linear generator is a relatively new concept of electric generator, it hasn't reached the commercial stage in large numbers yet and therefore, a lot of research is currently ongoing in order to optimize its performance. In the wave energy conversion field only

a few prototypes have been built and tested, still most of the research is still computer based by performing simulations. As seen in section 2.3.2, an induction generator is composed of two main components, the rotor and the stator; in linear generators the structure of is the same. However, the rotor no longer rotates but translates, carrying linear trajectories. This alternate motion has some drawbacks, mainly efficiency loss due to the variation of the translator velocity. Nevertheless, it has been conceived to achieve a perfect adaptation to the vertical wave motion; allowing to get rid of extra mechanical components, which decrease the overall efficiency of the system and increase the possibilities of breakdown events.

The only novelty in the stator is that it varies in shape to adapt to the new moving part. Between the translator and the stator there is a small distance called air gap, this is a crucial part of the generator. On the one hand, a really reduced air gap could lead to mechanical failure during the lifetime of the generator. Mainly because of structure deformations caused by the intense loads under which the generator is set. On the other hand, a wide air gap has a tremendous negative effect in the electromagnetic induction efficiency, practically leaving the generator out of use.

The translator is mounted with permanent magnets between pole shoes. These, are steel bars with their poles placed face to face, and its functionality is to guide the magnetic flux towards the air gap and over to the stator. Once the magnetic flux has crossed the air gap is led through the stator-tooth to the stator-yoke where the flux is divided into two parts and sent back to the translator to close the loop in accordance to the Maxwell's equations. The previous process and the LG architecture are reported in figure 2.23. As the translator moves along the stator a time varying magnetic field is created in the stator coils, this variation can be measured by an angle due to the periodicity of the harmonic motion of waves. This angle is called the electric angle and is what causes the variation of w in equation 2.127. Assuming that the translator follows the monochromatic wave, ω can be computed with the following equation:

$$w = \hat{w} sin(\delta t) \tag{2.129}$$

.

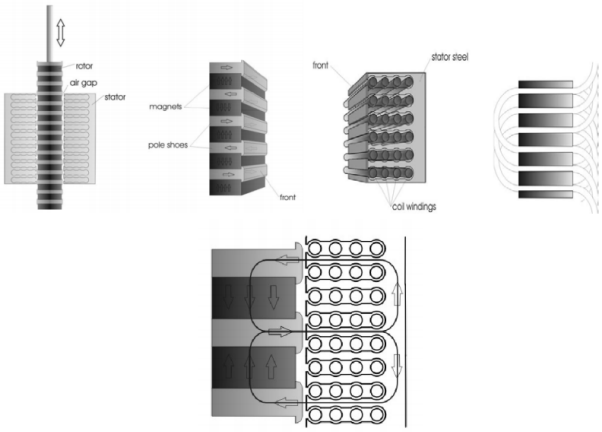

Figure 2.23: *Cross sectional views of a typical LG*

2.4 Moonpool

The moonpool is one of the main characteristics of the MoonWEC (section 1.4.2). A moonpool is water column found in the inner part of a floating structure, usually having a cylindrical shape. This concept was born in the Oil&Gas sector, since many offshore platforms hold one in order to provide space for the risers and give shelter from the open sea for Operation&Maintenance involving subs. Moonpools can also be found in ships for special operations such as in Floating Production Storage Units (FPSOs).

Born as a mere void space for practical reason, the moonpool concept soon grew in relevance as complex phenomena, such as resonant states and swirl currents, were observed to be taking place within the moonpool. Needless to say that this, in general, are undesired effects since endanger either the safety of personnel working in such units either the stability of the whole structure itself. The phenomenon was first described by (9), in which a mathematical model was validated over experimental tests. The relative motion between the moonpool surface and a floating structure in heave was studied under several conditions. It assumed that the water column behaved like a frictionless piston that varies its mass proportionally to the piston position. Hence, the natural frequency of the moonpool was derived

$$\omega_{res} = \sqrt{\frac{\rho g A}{\rho A T + a_h}} \tag{2.130}$$

Where A is the cross-sectional area of the moopool, T is its draft and a_h is the added mass coefficient, derived from the potential theory. Actually, the water motions inside a

moonpool were represented as a spring-mass system by (19). Both of them found that the heave motion of the structure is affected by the characteristics of the moonpool and that can be properly tuned by placing an appropriately designed guide plate, as in (90). (51) derived a 2-DoF coupling dynamic model of a spar in heave highlighting the moonpool hydrodynamic characteristics in predicting the dynamic behaviour of the spar. A 6-DoF nonlinear model of a spar platform was developed by (89) including the risers dynamic behaviour. Finally, the opening rate of the guide plate in spar platform in heave was studied by (66), showing than the response of the platform can totally vary response depending depending on the guide plate configuration.

The water motion inside a moonpool can be derived by using the deformable control volume approach, as the moonpool changes in size over time. Hence, the mass conservation condition must be fulfilled

$$\int_S \rho(\vec{v_{MP}} - \vec{v_S}) \times \vec{n} dA = -\frac{dM_{MP}}{dt} \tag{2.131}$$

where ρ is the water density, $\vec{v_{MP}}$ is the velocity of the water flowing through the control surface, $\vec{v_S}$ is the velocity of the floating structure and M_{MP} is the moonpool mass. Note that $(\vec{v_{MP}} - (\vec{v_S})$ is the relative velocity $\vec{V_r}$ between the moonpool and the floating structure from the moonpool reference frame. The equation of motion of a moonpool is obtained by applying Newton's second law by means of the equation momentum for a deformable control volume as written in (53):

$$\sum \vec{F} = \frac{d}{dt}(\int_{CV} \vec{V} \rho d\Delta) + \int_{CS} \vec{V} \rho (\vec{V_r} \times \vec{n}) dA \tag{2.132}$$

Where $\vec{V}$ is the fluid velocity in the control volume CV, $\vec{V_r}$ is the relative fluid velocity flowing across the control surface CS. The left hand side of equation (2.132) incorporates the forces acting on the control surface and the weight force due to the trapped water particles in the moonpool

$$\vec{F} = -gM_{MP} + p_u S_g \tag{2.133}$$

Where g is the gravity acceleration and p_u is the pressure acting on the upper side of the control surface. The Force acting on the lower side of the control surface can be expressed as follows:

$$F_l = F_h + F_e + F_c + F_r + F_d = p_l S_g \tag{2.134}$$

Where F_h is the force exerted by the hydrostatic pressure, F_e is the wave excitation force, F_r is the radiation force, F_d and F_c is the coupling term of the moonpool and the floating structure, mainly given by inertial constraints. The pressure difference between the two sides of the control surface is the cause of the fluid acceleration. Therefore, the following equation of motion is obtained

$$(p_l - p_u)S_g \times \vec{n} = \vec{F_h} + \vec{F_e} + \vec{F_c} + \vec{F_r} + \vec{F_d} - \vec{g}M_{MP} - \frac{d}{dt}(\int_{CV} \vec{V}\rho d\Delta) + \int_{CS} \vec{V}\rho(\vec{V_r} \times \vec{n})dA = M_{MP}\frac{d\vec{V_r}}{dt} \tag{2.135}$$

By applying the constraints that a specific system imposes into equation (2.135); the dynamics of such system, representing the moonpool, are fully determined.

2.5 Mooring system

A crucial matter in the design of floating structures is how to hold them fixed, for obvious reasons a floating structure may not be left adrift. Depending on the structure purpose the mooring system will have completely different settings. Therefore, the mooring of structure is an extensive field and, in literature, usually treated separately from the pure wave-structure interaction field. On the one hand, a mooring system needs to be sufficiently stiff to allow docking for Operation and Maintenance (O&M) operations, ensure the structure keeping within the tolerances and maintain the specified distances between different mooring lines. On the other hand, it must be compliant enough to reduce the forces on anchors and mooring lines and to accommodate to the tidal range. Ensuring both, operability and survivability regimes is what makes a specific mooring system viable. Mooring systems are composed by two main components; the anchoring system, which guarantees the fixation onto the sea bed, and the mooring lines, which interconnect the structure and the anchors. Mooring systems can be classified according to two principles, reported in figure (2.24).

Geometrical Classification	Functional Classification		
	Passive MS	Active MS	Reactive MS
Turret	✓		✓
Spread	✓	✓	
CALM	✓	✓	
SALM	✓	✓	✓
ALC	✓		✓
FTM	✓		✓
TLP		✓	

Table 2.2: *Mooring Systems according to the two classification systems.*

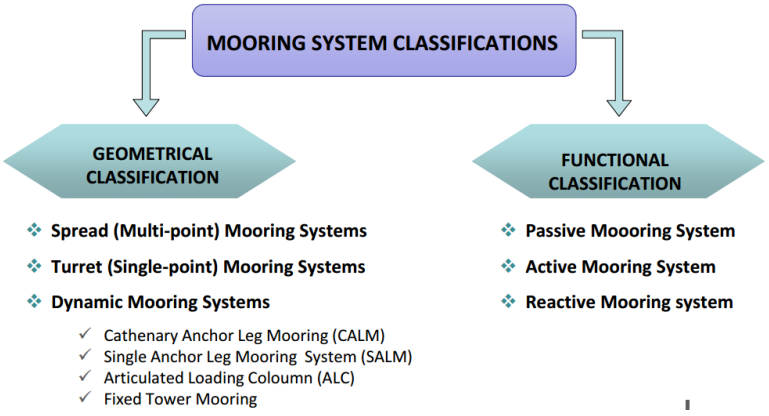

Figure 2.24: *Mooring system types classification scheme*

The geometrical classification, based on the layout configuration, basically states if the structure is connected by a single point (turret), several points (spread) or needs to be linked to a support external auxiliary structure holding the mooring system (dynamic system). Among the most widely used dynamic mooring systems are the Catenary Anchor Leg Mooring , the Single Anchor Leg Mooring (SALM), the Articulated Loading Column (ALC), the Fixed Tower Mooring (FTM) and the Tension Leg Platform (TLP). The functional classification states if, slack (passive) or taut (active) mooring lines are installed, or if a reaction an external reaction force is needed as in assisted mooring by thrusting. Figure (2.25.a), .b), .c), .d) and .e)) show their layout, respectively. Table 2.2 reports the classification of each mooring system.

In this thesis, two types of mooring system are addressed, one for each studies device. The HPA-LG is moored to the sea bed by a variant of the TLP system. The generator, placed at the seabed, acts a gravity foundation and the line interconnecting

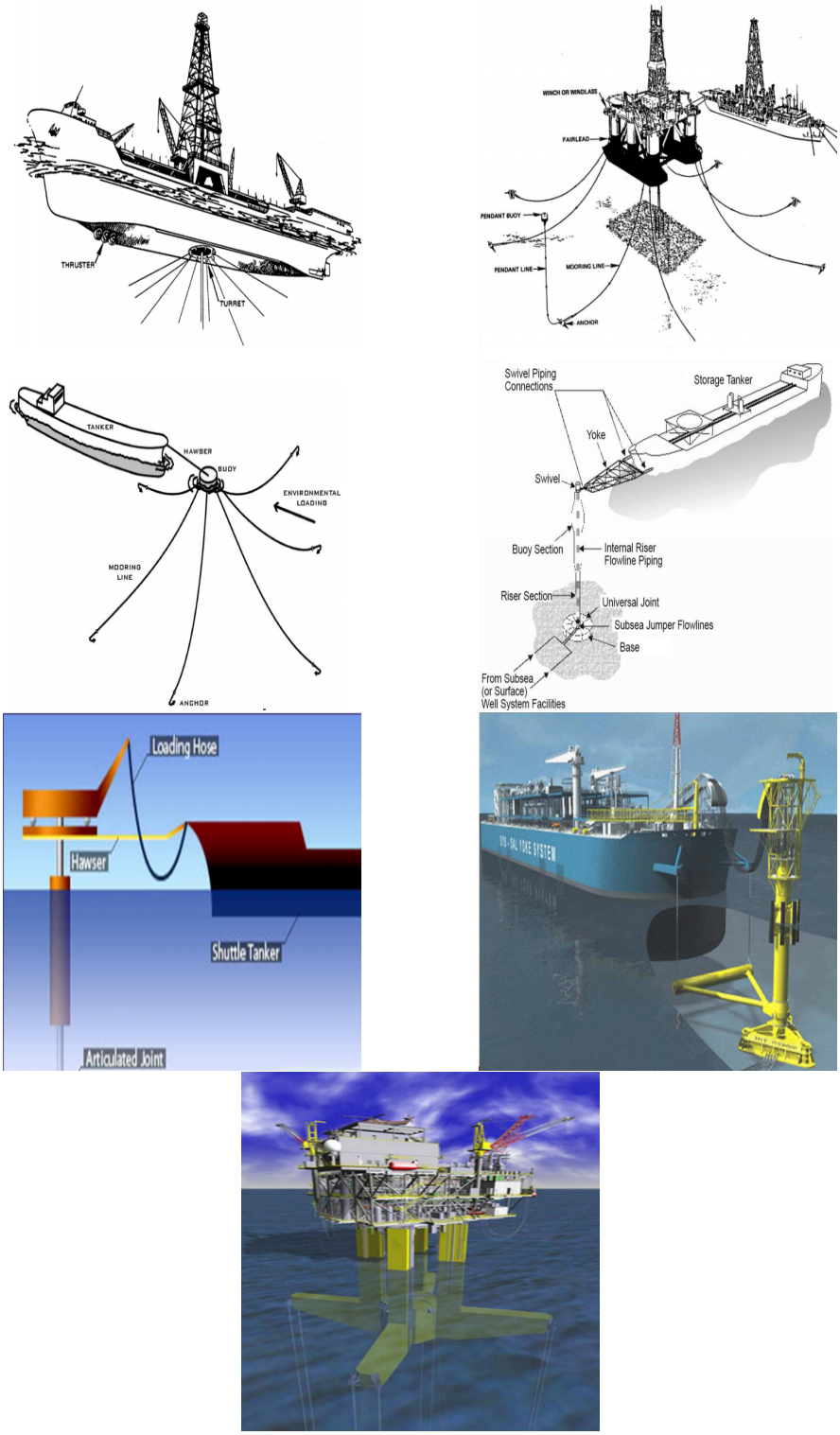

Figure 2.25: *Different mooring system layouts*

the buoy and the translator also operates as the mooring line. Hence, being in tension it assumes the behaviour of a single tension leg. The line, which is a steel wire has a very high axial stiffness restricting to a minimum its elongation. The MoonWEC is moored by means of a CALM system composed by four catenary lines, providing a strong symmetric behaviour with respect to the vertical plane. Thus, in the modelling only two lines have been modelled.

CALM systems are particularly suitable when horizontal displacements need to be reduced by at the same time leaving free the vertical oscillation. Is for that reason that has been chosen to moor the MoonWEC device. The dynamic behaviour of the CALM system is quite complex, accounting with a highly nonlinear response, mainly due to the high inertia and drag of the lines. The size of the lines makes so that such effects may not be neglected. Therefore, its dynamics cannot be decoupled and are integrated into the overall floating structure dynamics. Figure (2.26) shows the layout of a floating platform moored by a CALM system. The deriving simplified equation of motion for the surge mode results in

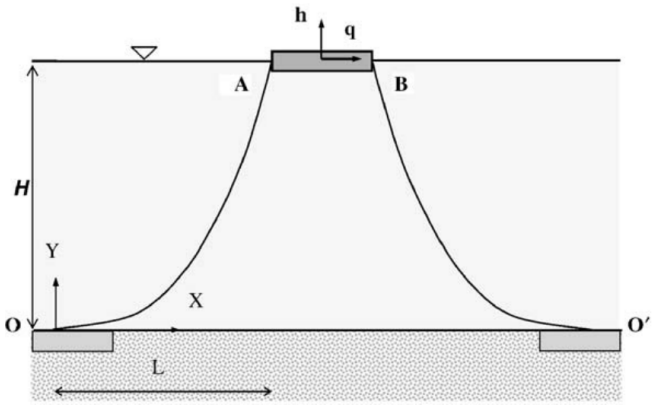

Figure 2.26: *Layout of the Platform-CALM system, warning figure needs to be updated*

$$m\ddot{q} + C_d\dot{q} + (S_x^l - S_x^r) = F_e \tag{2.136}$$

Where m is the platform mass, C_d is the linearised drag coefficient, S_x^l and S_x^r are the horizontal components of the chain tension at the points A and B respectively and F_e is the wave excitation force in the surge mode. Since the chain inertia cannot be neglected the Newton's second law must stated at the chain level, nesting it to the

general equation of motion as follows

$$S_x^l = T_0^l + m_c \ddot{x}_c^l S_x^r = T_0^r - m_c \ddot{x}_c^r \tag{2.137}$$

Where T_0^l and T_0^r are the horizontal chain tension at the equilibrium position for the A and B points respectively, m_c is the mass of the line and $\ddot{x}_c^{l,r}$ are the acceleration of the left and right chain at its centroid respectively. $T_0^{l,r}$ are found by performing a static analysis of the line configuration at its equilibrium position.

Figure (2.27) illustrates the shape of a deep water catenary line. The origin of its reference frame is located at the zero slope point, where the line lies on the seabed $(x_0, y_0, z_0) = (0, 0, 0)$. The anchoring point is defined by the coordinates (x_m, y_m, z_m) and the point of attachment to the floating structure is denoted by the coordinates (x_T, y_T, z_T). l_{eff} is the suspended length of the line, where l is its horizontal projection and l' is the total horizontal distance from the structure to the anchoring point. h is the water depth and $\theta(s)$ is the slope angle of the line with respect to the plane (x, y) at the point s.

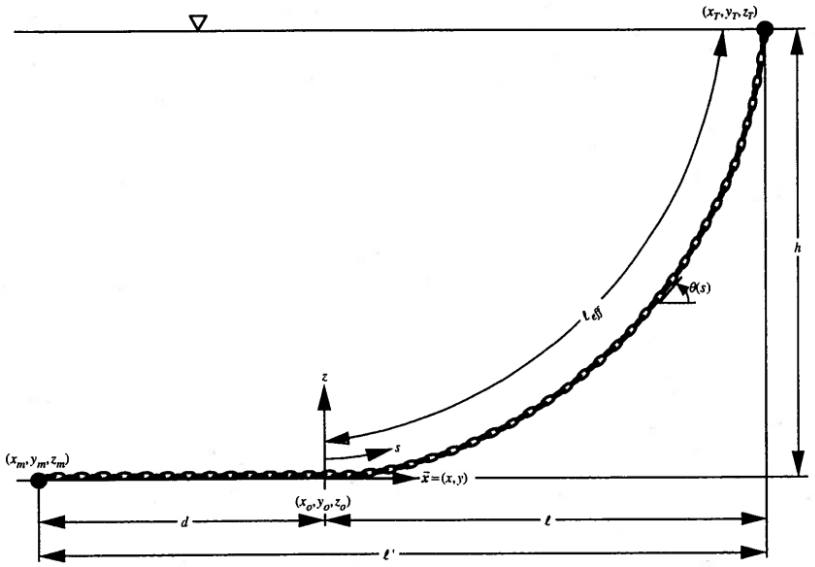

Figure 2.27: *Geometry of a deep water catenary line*

The geometric configuration is given by $(x(s), y(s), z(s)$ and $\theta(s)$ for $0 \leq s \geq l_{eff}$. Introducing the following dimensionless parameters

$$X_1 = \frac{Pl}{T_0} L = \frac{Pl_{eff}}{T_0} H = \frac{Ph}{T_0} \tag{2.138}$$

Where P is the linear specific weight, in wet conditions, of the line and T_0 is the horizontal tension in the (x, y) plane, the catenary equations result in

$$X_1 = \sinh^{-1}(L) \tag{2.139}$$

$$H = \cosh(X_1) - 1 \tag{2.140}$$

By squaring equations (2.139) and (2.140) and then subtracting them the following relation is obtained

$$L^2 - H^2 = \sinh^2(X_1) - \cosh^2(X_1) + 2\cosh(X_1) - 1 = 2(\cosh(X_1) - 1) = 2H \tag{2.141}$$

$$L = \sqrt{H^2 + 2H} \tag{2.142}$$

By reverting the dimensionless form of equation (2.142) by applying the equation (2.138) and subsequently the equation (2.139), two relations between the l_{eff} and T_0 are provided

$$l_{eff} = \sqrt{h(h + 2\frac{T_0}{P}} \tag{2.143}$$

$$l_{eff} = \frac{T_0}{P}\sinh(\frac{Pl}{T_0}) \tag{2.144}$$

Thus, by combining equations (2.143) and (2.144) a expression providing relation between T_0 and the horizontally projected length of the suspend line l is yielded

$$\frac{T_0}{P}\sinh(\frac{Pl}{T_0}) = \sqrt{h(h + 2\frac{T_0}{P})} \tag{2.145}$$

Now, by deriving the following geometric relation from figure (2.27): $l_T - l' - l_{eff} + l = 0$ and combining it with equation (2.143), an expression in terms of the known l_T, l', l and h is derived and solved for T_0

$$\begin{gathered} l_T - l' + l = \sqrt{h(h + 2\frac{T_0}{P}}; \\ T_0 = \frac{P[(l_T - l' + l)^2 - h^2]}{2h} \end{gathered} \tag{2.146}$$

After having found T_0, the chain acceleration needs to be found for the ODE de-

scribing the dynamics of the platform-CALM system be fully determined and may be solved. From figures (2.26) and (2.27) the position of the chain can be derived

$$x_c^l = (l+q) - \beta_t^l(\frac{h+k}{l_{eff,t}}), x_c^r = (l+q) - \beta_t^r(\frac{h+k}{l_{eff,t}}) + w, \tag{2.147}$$

where w is the width of the platform,$l_{eff,t}$ is the effective length of the line at the time t and $\beta^{l,r}$ is a chain shape parameter

$$\beta_t^{l,r} = \frac{P}{T_t^{l,r}} \tag{2.148}$$

where $T_t^{l,r}$ is the instantaneous horizontal chain at each time t. $T_t^{l,r}$ and $l_{eff,t}$ are computed following the same procedure shown for T_0 and l_{eff} using the updated coordinates for the time t. By applying the time derivative twice to $x_c l, r$ the chain acceleration $\ddot{x}_c^{l,r}$ is yielded

$$\ddot{x}_c^{l,r} = \ddot{q} \mp \ddot{\beta}_t^{l,r}(\frac{h+k}{l_{eff,t}}) \mp 2\dot{\beta}_t^{l,r}\frac{\dot{k}}{l_{eff,t}} \mp \beta_t^{l,r}\frac{\ddot{k}}{l_{eff,t}} \tag{2.149}$$

Now, the platform-CALM system is fully determined and can be solved by the ODE integral of the equation of motion.

2.6 Wells Turbine

As introduced in section (1.4.2), the MoonWEC device uses a Wells turbine placed in the moonpool to drive the electric generator. In its simplest form, a W-T consists of several symmetrical aerofoils placed around a hub, with the chord plane perpendicular to the axis of rotation, see figure (2.28). The particularity of this kind of turbines is that, due to the aerofoil symmetry the direction of rotation is always achieved in the same way regardless the flow bi-directionality direction.

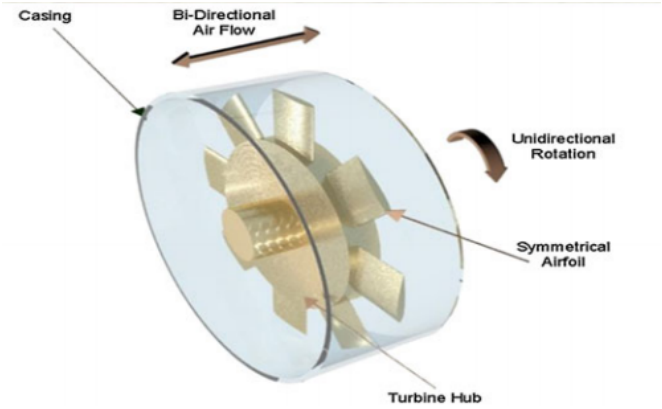

Figure 2.28: *Layout of an air Wells turbine*

The aerofoil profile used in W-T is the NACA four-digit series profile, NACA-ABCD (1). The first digit A, specifies the maximum chamber in percentage of the chord (airfoil length), the second digit B states the position of the maximum chamber in tenths of the chord and the last two digits, C and D indicate the maximum thickness of the airfoil in percentage of the chord. Hence, profiles without chamber, first two digits set to zero NACA00CD, are symmetrical, see figure (2.29).

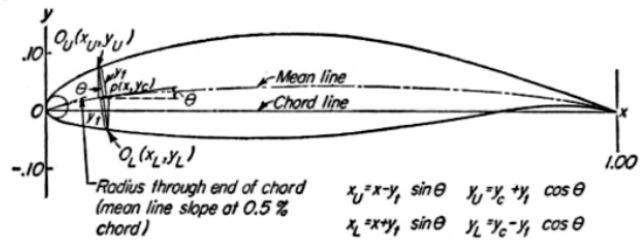

Figure 2.29: *Geometrical layout of a NACA aerofoil*

According to the general airfoil aerodynamics theory, a blade placed into a fluid flow oriented with α degrees from it generates a lift force L normal to the stream direction and a drag force D parallel to it, see figure (2.30). L and D increase with the incidence angle α; however, only up to a limit where beyond flow separation from the aerofoil takes place, this effect is called stall. For angles greater than the stall angle the drag force rockets whereas the lift force, which is the turbine's main driving force, plummets resulting in a dramatic decrease of the turbine's efficiency. Figure (2.30) also shows the velocity triangles, a technique used to then compute the lift and drag forces.

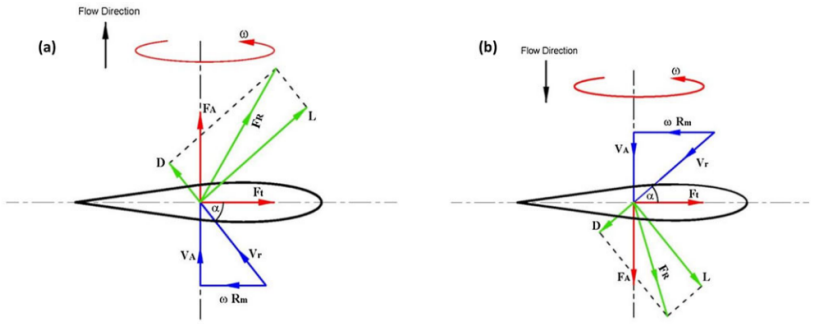

Figure 2.30: *Aerodynamic forces. a) Compression stages. b) Suction stages.*

From figure (2.30), the tangential force F_t, the axial force F_A and the resultant aerodynamic force given by the lift and drag forces are derived

$$F_R = \sqrt{L^2 + D^2} \tag{2.150}$$

$$F_t = L\sin\alpha - D\cos\alpha \tag{2.151}$$

$$F_A = L\cos\alpha + D\sin\alpha \tag{2.152}$$

The performance of a W-T is affected by the mutual aerodynamic interference between the blades. Interferences are given by velocities induced by the blades on each other and by the wakes produced by the blades, mainly called inviscid and viscous effects respectively. These interferences are function of the turbine solidity σ, which is the ratio of gap distance between blades to the blade chord. The main disturbance is an increase in velocities upstream of the blades and a decrease in velocities downstream, that causes an increase of the flow circulation, which in turn leads to a further increase of the lift force in the aerofoil. A simple method of evaluating the interferences is that based on the potential flow theory flat plate aerofoils in cascade at a $\pi/2$ stagger angle (92), which consist in unrevolving the rotor to locate all aerofoils in the same plane, see figure (2.31). According to this study, the value of the lift coefficient C_l for an aerofoil in cascade can be corrected by a factor k such that $C_l = kC_{l0}$, where C_{l0} refers to the lift coefficient of the isolated aerofoil, the analytical formula derived in (86) and further simplified for 90 °angle of stagger in (44) for k shows:

$$k = \frac{2t}{\pi c}\tan(\frac{\pi c}{2t}) \tag{2.153}$$

Where c is the chord length and t is the pitch as illustrated in figure (2.31). As the drag force cannot be predicted by the potential flow theory, it is assumed that the drag coefficient is undisturbed $C_d = C_{d0}$ as the majority of the disturbance occurs normally to the flow. Tangential and axial forces can also be described by means of the C_t and C_A respectively. (79) and (91) suggested that the following relations must be fulfilled

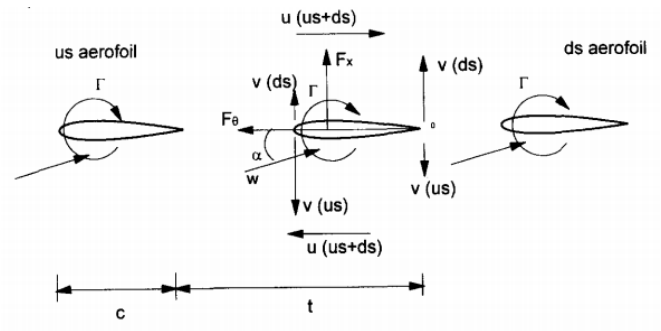

Figure 2.31: *Geometrical layout of the cascade scheme*

$$\frac{C_A}{C_{A0}} = \frac{1}{1-\sigma^2} \tag{2.154}$$

$$\frac{C_t}{C_{t0}} = \frac{C_A}{C_{A0}} \tag{2.155}$$

Where σ is the turbine solidity and, C_{t0} and C_{A0} are obtained from empirical experiments of the isolated blades. C_{t0} and C_{A0} are dependent on C_l and C_d, which in turn depend on several parameters such as the blade chord Reynolds number, the Mach number, the hub-to-tip ratio, tip clearance. To compute the axial and tangential forces from their coefficients the analogous drag equation (2.106), stated in section (2.2), are derived

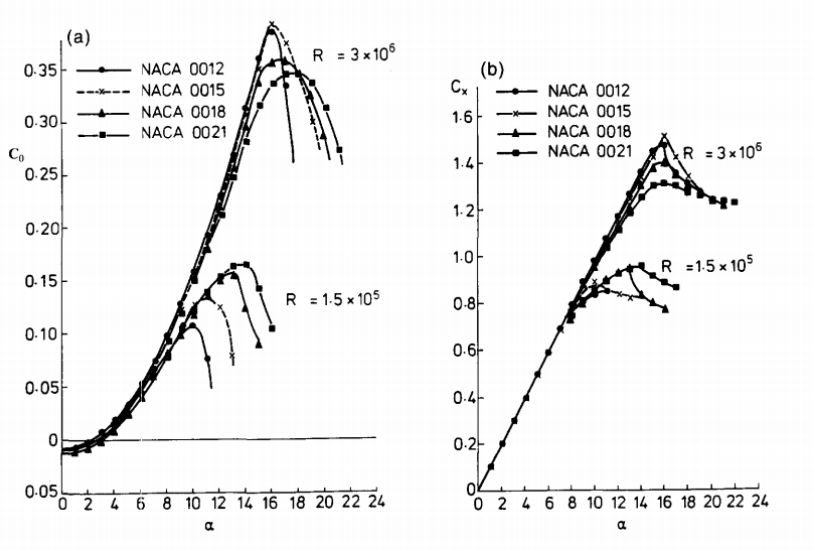

Figure 2.32: *Aerodynamic forces on several symmetrical NACA profiles for several Reynolds numbers a) Variation of the tangential force coefficient with incident angle. b)Variation of the axial force coefficient with incident angle (80)*

$$F_t = \frac{1}{2} N \rho C_t A_b V_r^2 \tag{2.156}$$

$$F_A = \frac{1}{2} N \rho C_A A_b V_r^2 \tag{2.157}$$

Where ρ is the fluid density, N is the number of blades and A_b is the blade planar area and is set equal to c the chord length. Many variants of Wells turbine have been conceived in order to increase its efficiency. Guide vanes may be incorporated on the rotor hub, in order delay the stall conditions. Blades variable pitch angle are also used to increase efficiency and enable self starting, as a particularity of W-T is that assisted start is needed due to the negative C_t values for low incidence angles α, as shown in figure (2.32). Biplanes W-T are also widely used, consisting in adding a second hub to increase efficiency by taking advantage of the swirl created downstream of the first hub, depending on the geometric architecture of the turbine this second hub can rotate in the opposite direction of the first hub. However, for this thesis none of this variants have been considered for simplicity.

3

Wave Resource Assessment

3.1 Global and local wave resource

Waves are a vast resource of energy worldwide, not only for its harvesting potential but also for its elevated energy density. As mentioned in section 1.2, oceans cover approximately $2/3^{rds}$ of the planets surface and half of the world's populations live within a range of $100km$ from the coast. Furthermore, wave energy transport is 5 and 20 times denser than wind energy and solar energy transport, respectively (see (95)). Moreover, wave seasonal variability usually matches with the electricity demand, as higher waves are generated during autumn and winter times, coinciding with the needs of energy to heat buildings.

Waves are not distributed uniformly throughout the oceans. Some areas are usually hit by bigger waves than others. The wave climate of a particular area basically depends on the meteo-climatic conditions and geographical characteristics of such area. Figure 3.1 shows the annual averaged wave power distribution for the WorldWave grid points.

Higher wave energy fluxes are found in open oceans from middle to high latitudes for both hemispheres. Reason for that is the high prevalence of winds at that latitudes and the long fetches, see section 2.1.2. Also, a predominance of higher fluxes in the western coasts of the continents can be identified; born from the global circulation patterns, which mainly generate westerlies over open areas such as oceans. It can also be noticed that shielded areas such as the Baltic and Mediterranean seas, have much lower average fluxes than open oceans, despite being located at the appropriate latitudes. This is due to the small fetches of these areas, or in other words, waves do not have space enough to grow as they do in the big oceans.

This thesis focuses in wave energy conversion on the Mediterranean Sea, more specif-

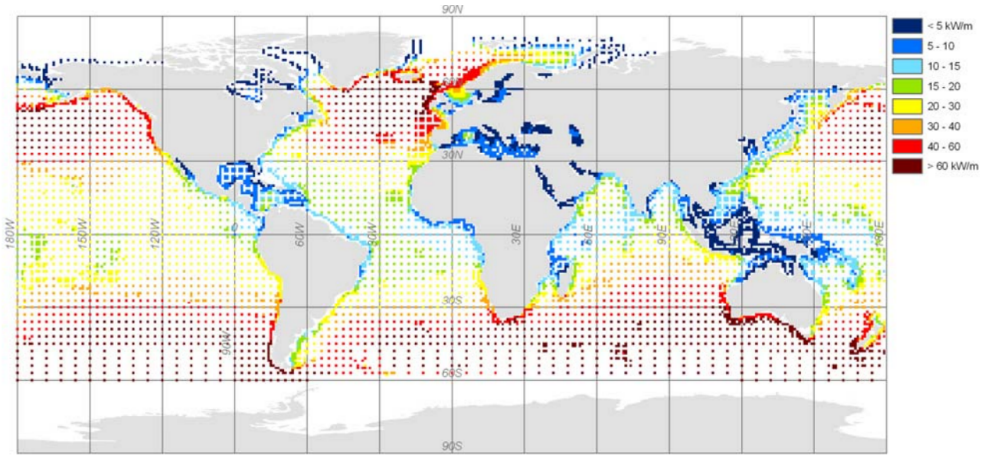

Figure 3.1: *Annual global gross theoretical wave power for all WorldWaves grid points worldwide. (74)*

ically off the Italian coasts. A study by (65) shows that in the most energetic areas of the Mediterranean Sea, the annual average wave energy fluxes range around $(8-15)kW/m$. Figure 3.2 illustrates the distribution of the average wave energy flux on the Mediterranean Sea.

More specifically, in the offshore area entrained between the Balearic island of Minorca and Sardinia, energy fluxes are greater than $15kW/m$ raising a particular interest on such area.

3.2 Deployment sites identification

For this work, eight locations off the Italian coasts have been characterized. The location of the selected sites is shown in figure 3.3. The site selection derives from data availability; as in these sites buoys from the National Italian Wave Measurement Network (2) have been deployed. The gathered wave data spans over a time period of almost 20 years. The buoys are moored in deep water, at depths ranging from 60 m in the Adriatic Sea to about 100 m in the Tyrrhenian Sea. Their distance from shore varies between $1.2km$ (Crotone) and $15.6km$ (La Spezia). Table 3.2 reports the main features and wave energy statistics of the locations, sorted by decreasing wave power potential (original data from (97)). The Mean Wave Direction (MWD) has not been considered for the wave climate analysis. The projected devices present an axysimmetry over the vertical their vertical axis (see figures 1.11 and 1.12). Hence, the device response is not altered by the incoming wave direction.

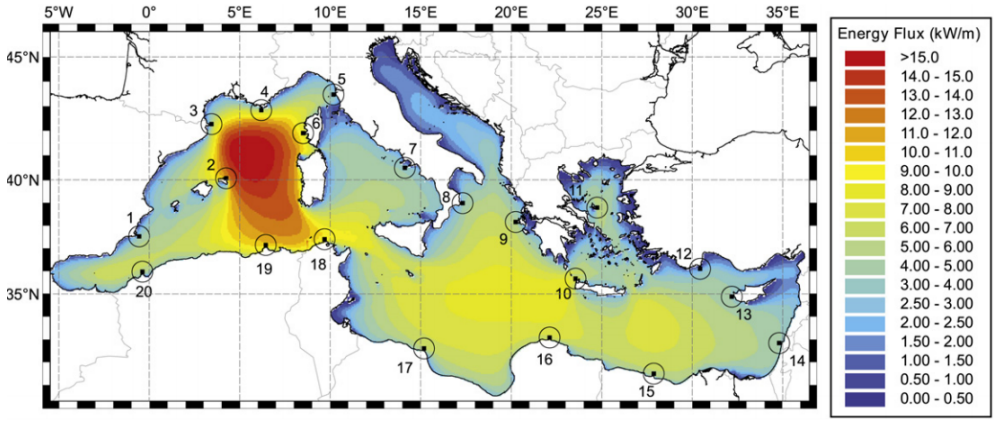

Figure 3.2: *Distribution of average power per unit crest in the Mediterranean between 2001 and 2010. (65)*

Figure 3.3: *Case study locations*

The most energetic sites (1-4 in table 3.1) are located in the Tyrrhenian Sea. The average annual wave power at these sites ranges between $3.5kW/m$ and $9.1kW/m$, values comparable to other sites in the North Sea (32). On the other hand, the least for energetic sites are found in the Ionian and Adriatic Seas; at all these locations, the annual average wave energy flux is lower than $3kW/m$, a value that can be considered as the lower limit for wave energy harvesting. Table 3.2 reflects the seasonal variability of the studied locations.

The monthly average wave power strongly varies over the year; the coefficient of

	Site	Depth (m)	Distance from shore (km)	Wave record duration (y)	Missing data (%)	AEP (kW/m)
1	Alghero	95	5.2	18.8	9	9.1
2	Mazara del Vallo	75	13	18.8	15	4.7
3	Ponza	100	1.44	17.7	10	3.7
4	La Spezia	92	15.6	18.8	13	3.5
5	Crotone	100	1.22	17.5	7	2.9
6	Monopoli	65	6.02	17.7	9	2.1
7	Catania	100	5.1	18.8	9	1.9
8	Ortona	60	10	17.7	12	1.9

Table 3.1: *Main features and statistics of the study sites.*

	Site	CV of average monthly wave power (%)	I	II	III	IV
1	Alghero	48	38	25	11	26
2	Mazara del Vallo	59	42	27	8	23
3	Ponza	50	37	23	11	28
4	La Spezia	36	33	23	14	30
5	Crotone	56	47	23	4	26
6	Monopoli	55	43	24	11	22
7	Catania	63	43	28	6	24
8	Ortona	66	46	22	9	23

Table 3.2: *Main features and statistics of the study sites. Columns I, II, III, IV represent the percentage of the annual wave energy in the months of December-February, March-May, June-August, September-November.*

variation (CV in table 3.2) of the monthly series represents this variation: the most constant sites, in terms of wave power, are located in the Northern Tyrrhenian Sea (La Spezia and Alghero), whereas the highest variability is found in Catania and Ortona. On the one hand, for every location the most energetic months are December-February and provide a large amount of the annual wave energy (varying from the 33% in La Spezia up to the 47% in Crotone). On the other hand, the least energetic months are June-August, accounting for a very small percentage of the annual energy flux (only 4% in Crotone). This high seasonal variability, typical of many renewable energy sources, is strongly correlated to the wind fluctuations, which are smaller in more temperate areas.

The characterization of the wave climate and the wave energy potential in terms of sea states is shown in tables 3.3 and 3.4. The occurrence of $H_S - T_P$ events, at each location, has been obtained from the website of the RON (2). Table 3.3 reports the percentage of occurrence P_o and the percentage of annual energy P_{AE} corresponding different significant wave height H_S intervals and, table 3.4, reports the same amounts according to given peak wave periods T_P intervals. In the design of a WEC, both parameters, P_o and P_{AE} must be taken into account; the wave climate data is needed

	Alghero		Mazara		Ponza		La Spezia		Crotone		Monopoli		Catania		Ortona	
H_S (m)	P_o	P_{AE}	P_o	P_{AE}	P_o	P_{AE}	P_o	P_{AE}	P_o	P_{AE}	P_o	P_{AE}	P_o	P_{AE}	P_o	P_{AE}
< 0.5	31.3	0.4	26.8	0.7	38.7	1.4	42.3	1.7	47.2	2.2	43.5	2.8	55.2	4.8	54.1	3.3
$0.5 - 1$	27.0	3.3	33.4	8.7	30.9	10.6	34.0	13.1	29.0	11.7	35.3	20.1	3.6	18.7	28.2	16.1
$1 - 1.5$	15.0	6.0	19.3	16.0	16.1	17.9	11.9	14.7	12.9	16.7	12.9	22.7	8.4	16.4	10.4	18.2
$1.5 - 2$	9.2	8.2	10.7	19.1	7.6	18.5	5.6	14.8	5.8	16.4	4.5	16.6	3.1	13.5	3.7	13.9
$2 - 2.5$	6.0	9.8	4.9	15.7	3.6	16.0	2.8	13.3	2.3	11.9	2.0	12.9	1.1	8.7	1.5	10.2
$2.5 - 3$	4.0	10.4	2.4	12.7	1.6	11.3	1.6	11.6	0.9	7.9	0.8	8.1	0.5	7.0	0.6	6.4
$3 - 3.5$	2.5	9.5	1.3	9.6	0.8	8.2	0.8	8.4	1.0	12.0	0.6	8.6	0.5	10.1	0.7	11.9
$3.5 - 4$	1.5	8.1	0.6	6.4	0.4	5.7	0.5	7.5	0.5	8.8	0.3	5.3	0.3	8.6	0.4	9.4
$4 - 5$	1.5	11.8	0.5	7.7	0.3	5.9	0.4	8.8	0.4	9.8	0.1	2.4	0.3	9.7	0.3	8.9
$5 - 6$	1.4	18.2	0.1	3.0	0.1	3.2	0.1	4.8	0.1	2.4	0.0	0.2	0.0	2.3	0.0	1.3
$6 - 7$	0.5	9.9	0.0	0.3	0.0	0.6	0.0	1.0	0.0	0.1	0.0	0.0	0.0	0.2	0.0	0.4
> 7	0.2	4.4	0.0	0.1	0.0	0.7	0.0	0.3	0.0	0.0	0.0	0.2	0.0	0.0	0.0	0.0

Table 3.3: *Percentage of Occurrence P_o and Percentage of annual energy P_{AE} corresponding to different wave height intervals.*

	Alghero		Mazara		Ponza		La Spezia		Crotone		Monopoli		Catania		Ortona	
T_P (s)	P_o	P_{AE}	P_o	P_{AE}	P_o	P_{AE}	P_o	P_{AE}	P_o	P_{AE}	P_o	P_{AE}	P_o	P_{AE}	P_o	P_{AE}
< 3	4.3	0.0	3.4	0.1	4.7	0.1	6.7	0.2	6.8	0.2	5.1	0.2	7.1	0.4	9.1	0.3
$3 - 4.5$	15.0	0.5	16.6	1.9	26.6	3.1	22.4	3.1	28.5	3.7	26.9	4.6	23.9	3.8	35.6	5.2
$4.5 - 6$	25.4	2.8	29.3	9.8	35.6	16.6	24.2	7.8	29.0	13.2	32.7	22.2	22.3	10.9	29.8	21.5
$6 - 7.5$	24.7	8.3	27.9	25.1	22.7	30.4	22.1	19.3	19.6	24.1	19.3	33.0	19.2	16.1	15.7	29.4
$7.5 - 9$	15.0	15.7	14.3	28.6	7.3	28.4	14.0	29.8	7.9	24.0	7.7	23.7	10.2	20.8	5.0	30.2
$9 - 10.5$	9.2	27.9	5.7	24.0	1.7	16.6	7.2	31.0	2.9	24.9	1.8	5.9	4.3	27.9	0.9	10.5
$10.5 - 12$	3.5	29.3	1.3	8.6	0.2	2.8	0.9	7.5	0.4	7.4	0.1	0.3	0.9	12.4	0.0	0.1
$12 - 13.5$	0.8	14.7	0.1	1.2	0.0	0.8	0.1	0.1	0.0	0.8	0.0	0.0	0.1	2.9	0.0	0.0
13.5.15	0.0	0.5	0.0	0.0	0.0	0.0	0.0	0.0	0.0	0.0	0.0	0.0	0.0	0.0	0.0	0.0
> 15	1.9	0.2	1.4	0.7	1.2	1.1	2.6	1.2	4.8	1.7	6.4	10.1	12.0	4.8	3.8	2.7

Table 3.4: *Percentage of Occurrence P_o and Percentage of annual energy P_{AE} corresponding to different wave period intervals.*

to maximize the capacity factor (or degree of utilization), i. e.: the amount of time in a year during it is operating at the rated power. On the other hand, the bivariate energy distribution is related to the efficiency of the device, which should be maximal for the range of wave height and peak period providing the bulk of the energy. Unfortunately, this may not always be achieved due to the very complex nature of waves, which does not always make the WEC design process effective.

Wave climate data show that the prevalent sea states are characterized by relatively small waves: in Alghero and Mazara, H_S is below $1m$ during approximately 60% of the year, whereas in other less energetic locations this percentages increases up to 80%. The peak periods with the highest probability of occurrence are around $6s$ for every location, confirming that in the Mediterranean Sea short waves prevail in the climate. The comparison between the percentage of occurrence and the contribution to the annual energy shows that most of the annual wave energy is provided by sea states with a rather low probability of occurrence. From table 3.3 it can be seen that events having wave heights smaller than $1m$, provide only $(4 - 15)\%$ of the annual energy despite having probabilities of occurrence in the range of $(60 - 80)\%$. The same trend is observed for the peak wave period distribution.

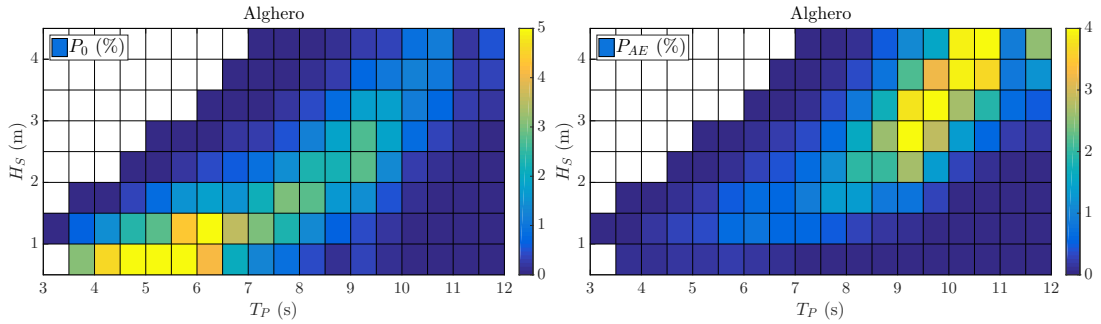

Figure 3.4: *Sea state percentage of occurrence and Percentage of Annual Energy at Alghero.*

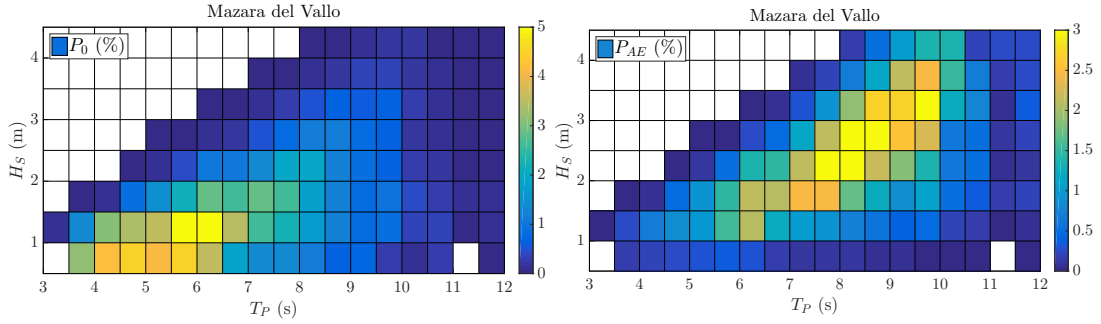

Figure 3.5: *Sea state percentage of occurrence and Percentage of Annual Energy at Mazara del Vallo.*

As this effect is a very limiting factor WECs design, only the two most energetic locations have been selected. Their average annual energy flux is reasonably high enough to foresee feasibility in wave energy exploitation. Also, they are more compact in terms of probability of occurrence and percentage of annual energy. Figures 3.4 and 3.5 show the values in tables 3.3 and 3.4 rearranged in a different manner, plotting now P_o and P_{AE} in two bivariate matrices, depending on H_S and T_P.

Figures 3.4 and 3.5 confirm what already revealed by tables 3.3 and 3.4, the annual wave energy is concentrated in a different climatic area than the wave occurrence. However, it can be appreciated that for the case of Mazara del Vallo the two parameters (P_o and P_{AE}) are closer than at Alghero. This effect sets a disjunctive over the design and tuning strategy. On the one hand, if the device is designed to have its efficiency peak in accordance to the the P_o peak, the device will probably produce less energy but at a more constant pace, having a high capacity factor over a low annual energy production. On the other hand, if the device is tuned to peak in efficiency according to the P_{AE} peak, the total production will probably be higher but produced in a very

reduced amount of time, which makes the capacity factor drop. The optimal procedure would be to widen as much as possible the high efficiency band of the device in order to embrace both peaks. Unfortunately, this is only possible up to a certain level, which may be feasible for Mazara del Vallo but completely unrealistic for Alghero. The author believes a high capacity factor should prevail over the net value of produced energy and therefore, the first strategy adopted is to tune the device according to the P_o peak.

3.3 Extreme wave conditions

The analysis carried out in section 3.2, aimed to identify the working regime conditions of the device. However, in the device design procedure two different regimes must be taken into account. As relevant as the working regime is the survivability regime of the device. On the technical level, the survivability regime often sets more challenges than the operational regime, since the device must resists extreme loads generated by severe storms. Fortunately, having the Mediterranean Sea a milder wave climate its extreme wave events are less severe than in open oceans and thus, increasing the survival probabilities of a well designed device.

Severe storms conditions and recurrence are determined by carrying a statistical analysis of extreme waves. This, aims to identify the sea state height H_{m0}, period T_P and MWD as well as the risk associated to the such conditions, which is generally specified by means of the return period T_r and the occurrence probability during the device lifetime ("encounter probability"). Unlike in the working regimes, where the statistical populations are time-aggregated on the basis of a regular data sampling; the extreme conditions regimes are established on the basis of event sampling of the data, generating time-disaggregated populations. Such events are defined by on partial over-threshold durations. The most used methodology for its identification, defined by (47), is the POT method.

The POT method sets the definition of a "sea storm" allowing to simplify the identification of a sample used for statistical computations. It identifies a sea storm as a time series of sea states characterised by a series of wave heights, periods and direction that vary within a given range. This range is defined by thresholds, thereby its name. For the study area of interest, the central Mediterranean, is given when the following rules take place, (31):

1. Wave height persistence over the threshold of 1.0 m for more than 12 consecutive hours

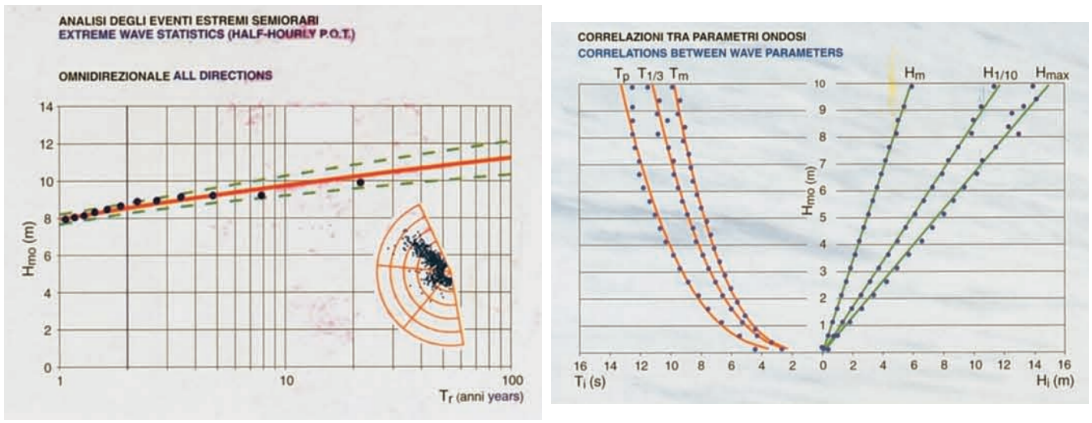

Figure 3.6: *Extreme wave statistics using the half-hourly POT method accounting for all wave directions at Alghero (31).*

2. Wave height decay below the threshold of 1.0 m for less than 6 consecutive hours

3. Original direction belonging to a determined angular sector ($\pm 30°$ with respect to the initial direction)

Occurrence frequencies of various types of storms may be computed by fixing several thresholds, alwats over 1.0 m. Subsequently, a probability model matching the samples must be identified. Usually, three Probability Distribution Functions (PDFs) are used: the Gumbel, Fretchet and Weibull PDFs; whose statistical parameters are chosen to fit the sample data and depend on the wave climate of the location. The Weibull distribution was proposed by (47) and has been used in (31). After tuning the PDF, the return period T_R, which is defined as the mean number of years within the general value H_{m0} is not exceeded, may be calculated or vice versa:

$$H_{T_R} = A[-\ln \frac{1}{\lambda T_R}]^{\frac{1}{k}} + B \tag{3.1}$$

where, A is the scale parameter of the significant wave height PDF, k is the shape parameter of the significant wave height PDF, B is the position parameter of the significant wave height PDF and λ is the mean number of over-thresholds sea storms observed in one year. The Italian wave Atlas (31) provides the data of the extreme wave conditions for the selected locations, shown in figures 3.6 and 3.7 for Alghero and Mazara del Vallo, respectively.

Provided that the design life of must be 25 years, thus $T_R = 25$. From figures 3.6 and 3.7, the 25-year return storm for Alghero and Mazara are: $H_{m0} = 10.5\ m$ and

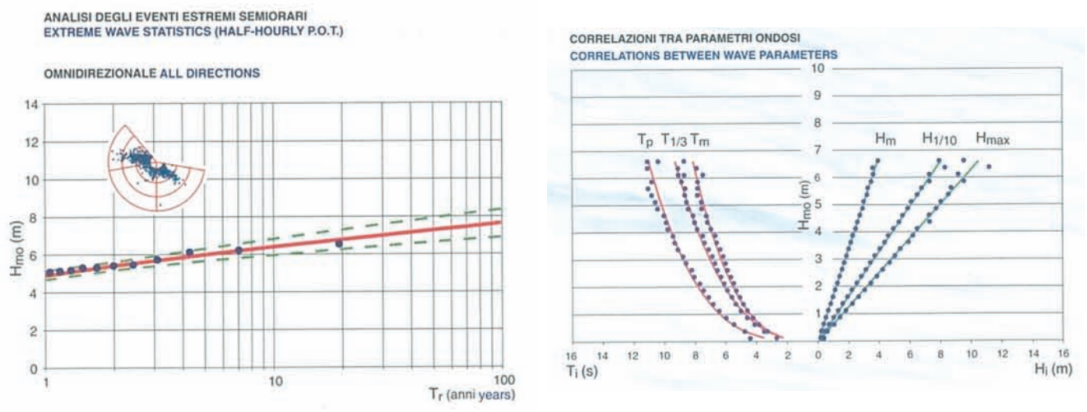

Figure 3.7: *Extreme wave statistics using the half-hourly POT method accounting for all wave directions at Mazara del Vallo (31).*

$T_P = 13.5\ s$, and $H_{m0} = 5.5\ m$ and $T_P = 9.5\ s$, respectively. As the same device is aimed to be deployed at both locations, the conditions for the former must be chosen during the design procedure when taking into account the survivability regime.

4

Mathematical modelling & numerical methods

In this chapter, all the theoretical notions introduced in chapter 2 are put into practice by means of numerical modelling. Two different types of numerical models have been addressed in this thesis. On the one hand, a model based on the potential flow theory that follows a Lagrangian approach has been developed mainly using the coding commercial software Matlab^{TM}with the purpose to model the WECs behaviour. On the other hand, an open-source CFD code has been used to assess the wave reflection on a Numerical Wave Tanks (NWTs). Computational Fluid Dynamics approach is based on the solution of the Navier-Stokes equations from an Eulerian point of view in order to model a fluid domain. The software is named REEF3D and is currently being developed at NTNU in Trondheim, Norway. One of its main advantages is that is focused on the marine environment and therefore, the maritime fluid dynamic characteristics are already embedded in the source code, making it very compact and much easier to use compared to other CFD software, either it be commercial or non-commercial.

4.1 Potential flow model

Figure (4.1) illustrates the working scheme of the potential flow model, which follows the classical modelling architecture, i.e: the model receives a series of inputs; afterwards these inputs are processed in the model core and turned into a series of outputs. The input parameters of the model can be divided into three categories. The first class is related to the environmental conditions, which are defined by data files mainly containing time series of water surface elevation and water particle velocities. The second

input class refers to the device properties, whether it be its geometrical definition, the mechanical attributes, the mooring system characteristics and the PTO system specs. Finally, the last type of input are the so called hydrodynamic parameters, which goal is to link the environmental conditions to the body behaviour.

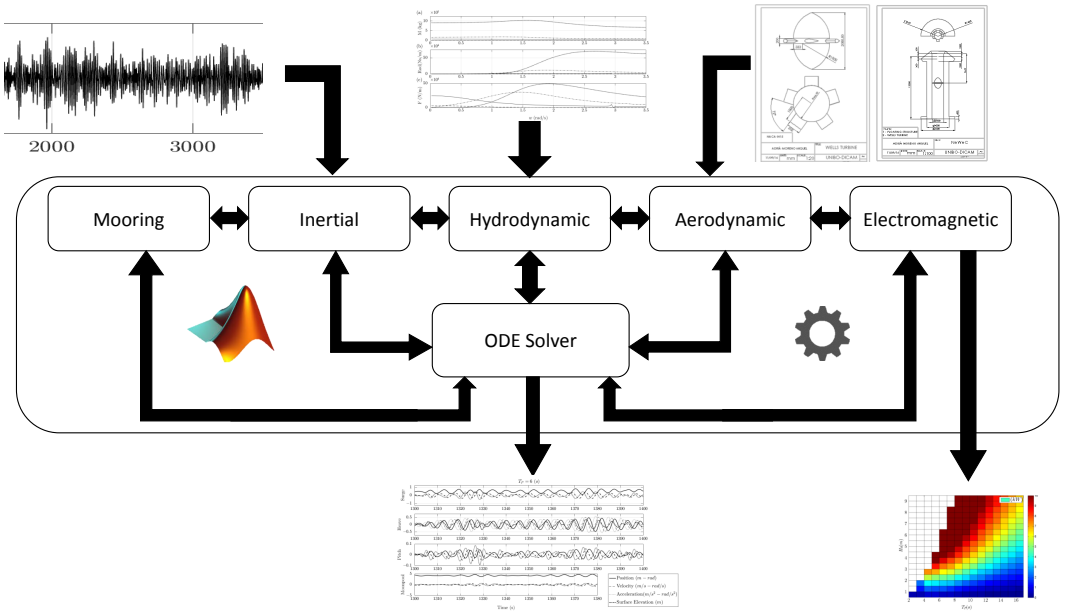

Figure 4.1: *Potential flow model diagram*

The model core deals with the input parameters, by handling each input class in a separate module, according to its nature, and finally coupling all the modules to obtain the overall performance of the device. The modules used in the model are five: the dynamic, the hydrodynamic, the aerodynamic, the mooring and the electric module. Each one resolving a specific component of the device. The model then releases a series of outputs from different nature; on one side, the kinematics of the device are obtained, allowing to study, through its motion, its response to certain conditions, on the other side the averaged electric power for that particular environmental conditions are also gathered, allowing to build the so called power matrix. The power matrix specifies the device production for each possible sea state. Finally, by combining the power matrix with climatic data, long-term site-related performance indicators are obtained such as the device efficiency and annual production.

4.1.1 Wave generation

The first type of input are the environmental conditions, in the wave energy field these may comprehend from waves to water salinity passing through ocean currents and winds. However, for this thesis only waves are considered, since they are the main drivers for wave energy conversion. Waves are generated adopting the linear wave theory (11), introduced in section 2.1.1, and defining the domain with whom the WEC interacts.

Regular and irregular waves are considered in order to study the device performance and behavioural differences between both set-ups. More specifically, water surface elevation and the vertical profile of water particle velocity are retrieved. For the regular wave case, the former and the latter are obtained by applying the modified version of equations (2.27) and (2.31-2.32), respectively:

$$\eta(t) = a\cos(\omega t) \tag{4.1}$$

$$u(t,z) = \frac{agk}{w}\frac{\cosh[k(h+z)]}{\cosh(kh)}\cos(\omega t) \tag{4.2}$$

$$w(t,z) = \frac{agk}{w}\frac{\sinh[k(h+z)]}{\cosh(kh)}\sin(\omega t) \tag{4.3}$$

Note that, the term $\theta = kx - \omega t$ (eq. 2.20) has been reduced to $\theta = \omega t$ since x is set to 0 as the device is placed at the centre of the coordinate system, having x and z as the horizontal and the vertical coordinates of the domain, respectively. a is the wave amplitude, ω is the wave frequency in (rad/s), h is the water depth (m), g is the gravity acceleration (m/s^2), t is the time in (s) and k is the wave number, which has been computed through the dispersion relation (eq. 2.30). In order to obtain irregular wave time series the JONSWAP spectrum has been employed, see section 2.1.3, as it best represents the wave properties given at the selected deployment sites, (16). The expression of the JONSWAP spectrum (eq. 2.76), when rearranged according to H_{m0} and T_P instead of the fetch parameters (F,W) assumes the following shape:

$$S(f) = 0.3125\frac{H_{m0}^2 T_P}{(\frac{f}{f_p})^5}e^{-1.25(\frac{f_p}{f})^4}\gamma^{e^{-\frac{(f-f_p)^2}{2\sigma^2 f_p^2}}} \tag{4.4}$$

Where the peak enhancement parameter is set to $\gamma = 3.3$ as it corresponds for wind-seas. Theoretically, the range of the evaluated frequencies is $f = [0 - \infty)$; however, as numerical models do not work in a continuous domain, a discretization for f needs

to be defined, with an increasing frequency interval Δf and a cut-off frequency f_{co}. The chosen range yields $f = [0 - 3f_p]$ and $\Delta f = \frac{1}{t_e}$, where t_e is the total time of the wave record representing the spectrum. This relation between length of the time series and the frequency discretization interval is chosen in order not to loose spectral energy density when performing the Inverse Fourier Transform (IFFT) $\mathcal{F}^{-1}$, thus, in this way time and frequency domains are univocally related. Nevertheless, there is always a loss of energy related to the cut-off frequencies of the spectrum $(3f_p - \infty)$. An algorithm applying energy compensation has been used. It is based on the ratio of the theoretical m_0 and the value that comes from the numerical integration of the truncated JONSWAP spectrum. The aim is to generate a modified truncated JONSWAP spectrum which has the same total energy as the analytic one. Finally, the surface elevation is obtained by applying the superposition principle to the linear wave theory. Each component of the spectral energy density represents a monochromatic wave of the sea state:

$$\eta = \sum_{i=1}^{N} a_i \cos(\omega_i t + \varphi_i) \tag{4.5}$$

Where a_i is the amplitude of the i^{th} monochromatic wave linked to the spectral density of energy as $a_i = \sqrt{2S_i\Delta f}$. $\varphi_i = [0 - 2\pi]$ is the phase of the wave, which is not represented in the wave spectrum and thus, it has been generated randomly. The same set of φ has been used in all the simulations in order to ensure that the generated wave records are identical. Hence, allowing direct confrontations among different versions of the model.

4.1.2 Internal forces

The dynamics of body motions are controlled by the Newton's second law,which links the external and internal forces, see equation (2.82). In the general equation (4.6), the internal forces are represented by the inertial terms:

$$\begin{bmatrix} \vec{F} \\ \vec{M} \end{bmatrix} = \begin{bmatrix} \overline{\overline{P}} & \overline{\overline{T}} \\ -\overline{\overline{T}} & \overline{\overline{I}} \end{bmatrix} \cdot \begin{bmatrix} \vec{\ddot{\tau}} \\ \vec{\ddot{\theta}} \end{bmatrix} = \overline{\overline{M}} \begin{bmatrix} \vec{\ddot{\tau}} \\ \vec{\ddot{\theta}} \end{bmatrix} \tag{4.6}$$

Where $\vec{F}$, $\vec{M}$, $\vec{\ddot{\tau}}$ and $\vec{\ddot{\theta}}$ are the vector of forces, moments, linear acceleration and angular acceleration respectively. The term $\overline{\overline{M}}$, called the inertia tensor, represents the inertial properties of the system and is a 6×6 matrix for a single body, $\overline{\overline{P}}$ is the mass

matrix, $\overline{\overline{I}}$ is the inertial matrix, $\overline{\overline{T}}$ is the coupling matrix:

$$\overline{\overline{P}} = \begin{bmatrix} M & 0 & 0 \\ 0 & M & 0 \\ 0 & 0 & M \end{bmatrix} \tag{4.7}$$

$$\overline{\overline{I}} = \begin{bmatrix} I_{44} & I_{45} & I_{46} \\ I_{54} & I_{55} & I_{56} \\ I_{64} & I_{65} & I_{66} \end{bmatrix} \tag{4.8}$$

$$\overline{\overline{T}} = \begin{bmatrix} 0 & Mz_{G_0} & -My_{G_0} \\ -Mz_{G_0} & 0 & Mx_{G_0} \\ My_{G_0} & -Mx_{G_0} & 0 \end{bmatrix} \tag{4.9}$$

$$\begin{array}{lll} I_{44} = \int_M (Y^2 + Z^2) dm & I_{55} = \int_M (X^2 + Z^2) dm & I_{66} = \int_M (Y^2 + X^2) dm \\ I_{45} = I_{54} = -\int_M XY dm & I_{46} = I_{64} = -\int_M XZ dm & I_{65} = I_{56} = -\int_M ZY dm \end{array} \tag{4.10}$$

Where I_{ij} are the moments of inertia and X, Y, and Z are the radii of giration of their respective axis.

4.1.3 External forces

External forces are due to the interaction of the body with the surrounding environment. That is, the forces exerted by the fluid, the forces of the mooring system and the forces due to electromagnetic induction caused by the electric generator when converting the mechanical energy into electric energy. The fluid forces can be divided into two major types, the hydrostatic and the hydrodynamic forces. The former being the direct consequence of the balance between the gravity forces. The latter are due to the dynamic pressure and viscous effects.

4.1.3.1 Hydrostatic forces

As introduced in section 2.2, hydrostatic forces are the formalization of the Archimedes principle, which states the relation between the weight of a body and its buoyancy. A floating body at equilibrium must respect the following relations: $Mg = \rho g V_0$, $X_{C_0} = X_{G_0}$ and $Y_{C_0} = Y_{G_0}$, where V_0 is its volume, C_0 its hull centre and G_0 its gravity centre.

Then, the hydrostatic restoring matrix assumes the following shape:

$$\overline{\overline{S}} = \begin{bmatrix} 0 & 0 & 0 & 0 & 0 & 0 \\ 0 & 0 & 0 & 0 & 0 & 0 \\ 0 & 0 & S_{33} & S_{34} & S_{35} & 0 \\ 0 & 0 & S_{43} & S_{44} & S_{45} & 0 \\ 0 & 0 & S_{53} & S_{54} & S_{55} & 0 \\ 0 & 0 & 0 & 0 & 0 & 0 \end{bmatrix} \tag{4.11}$$

Where:

$$\begin{array}{ll} S_{33} = \rho g \iint_{S_W} dV = \rho g S_W & S_{44} = \rho g \iint_{S_W} Y^2 dS + \rho g V_0 (Z_{C_0} - Z_{C_0}) \\ S_{55} = \rho g \iint_{S_W} X^2 dS + \rho g V_0 (Z_{C_0} - Z_{C_0}) & S_{34} = S43 = \rho g \iint_S Y dS \\ S_{35} = S_{53} - \rho g \iint_S X dS & S_{45} = S_{54} - \rho g \iint_S XY dS \end{array} \tag{4.12}$$

To compute the hydrostatic force then, the hydrostatic restoring matrix is multiplied by the body displacement matrix as follows:

$$\begin{bmatrix} \vec{F}_{HD} \\ \vec{M}_{HD} \end{bmatrix} = \overline{\overline{S}} \begin{bmatrix} \vec{\tau} \\ \vec{\theta} \end{bmatrix} \tag{4.13}$$

4.1.3.2 Hydrodynamic forces

As introduced in section 2.2, a rigid floating body under the influence of a wave field is affected by a series of hydrodynamic forces. Due to the dimensions of the studied devices these hydrodynamic forces are basically reduced to the excitation wave force, only due to the incident velocity potential (neglecting diffraction), the radiation force and the viscous drag force. The first two are directly related to the presence of the wave field whereas the latter is due to the viscous effects of the interaction fluid-structure.

The viscous drag force has been modelled according to equation (2.107). The modelled structures, HPA-LG and the MoonWEC, have complex geometries and no general drag coefficients C_d have been found for them. A way to obtain the coefficients could be by means of experimental tests or CFD simulations, however these two methods can be inconvenient due to reduced infrastructure access for the former and high computational costs for the latter. Actually, there is a simpler way to model the general drag force; that is to decompose the structure geometry into several elemental geometries upon each, a different drag force is applied. Being elemental geometries widely studied, it is easy to find their drag coefficients in literature. Table 4.1 has been extracted from

Body	Laminar/Turbulent	Status	C_d
Cube	$Re > 10000$		1.05
Thin Circular Disc	$Re > 10000$		1.1
Cone ($\theta = 30°$)	$Re > 10000$		0.5
Sphere	Laminar $Re \leq 2 \times 10^5$		0.5
	Turbulent $Re \geq 2 \times 10^6$		0.2
Ellipsoid	Laminar $Re \leq 2 \times 10^5$		$0.3 - 0.5$
	Turbulent $Re \geq 2 \times 10^6$		$0.1 - 0.2$
Hemisphere	$Re > 10000$	Concave Face	0.4
		Flat Face	1.2
Rectangular Plate	$Re > 10000$	Normal to the flow	$1.1 - 1.3$
Vertical Cylinder	$Re \leq 2 \times 10^5$	$L/D = 1$	0.6
		$L/D = \infty$	1.2
Horizontal Cylinder	$Re > 10000$	$L/D = 0.5$	1.1
		$L/D = 8$	1
Parachute	Laminar Flow		1.3

Table 4.1: *Drag coefficients for three-dimensional bodies (L:length, D:diameter) (84).*

(84) and used as a reference to pick the correct value of the C_d for each drag sub-force.

The wave excitation force is obtained by convoluting the excitation impulse response function $f_e(t)$ with the water surface elevation, see equation (2.90). The excitation impulse response function is obtained from the frequency dependent excitation coefficient $f_e(\omega)$, derived from equation (2.84). The radiation force has two terms, see equation (2.104). An inertial term related to the mass of fluid displaced by the structure during its motion and a damping term that is also obtained through a convolution between the radiation memory function $k(t)$ and the structure velocity. Analogously to the excitation force, $k(t)$ depends on a frequency dependent coefficient $R(\omega)$ found also with equation (2.84), reported again below for clarity:

$$F_i = i\omega\rho \iint_S p\hat{h}in_i dS \tag{4.14}$$

It all relies in the resolution of the potential velocity $\hat{\phi}$ and its integration with the body surface. Numerically, this operation is achieved by the BEM. Several software offer this capability; among the commercial ones the most widely used are WAMIT ®(6), developed by the Massachusetts Institute of Technology (MIT), and AQWA, included in the workbench package of ANSYS ®(3). For this thesis however, an open-source code has been chosen to obtain the hydrodynamic parameters, it is called NEMOH and it

has been developed for researches from the Laboratoire d'Hydrodynamique,Énergétique et Environnement (LHEEA) laboratory at the Ecole Centrale de Nantes, France, over the past 30 years, (17). Furthermore, NEMOH comes in a package which also includes a meshing tool and a Matlab toolbox to control NEMOH. The mesher allows to control the total number of elements, up to 2000 per body, and the angular discretization in case the structure be axisymmetric. Other than the grid composing the surface of the modelled structure, it also provides the inertia tensor of the body and the hydrostatic restoring matrix, see section 4.1.3.1. The former describes the inertial behaviour of the body whereas the latter accounts for the buoyant response when displaced from its equilibrium position.

BEM The Boundary Element Method solves the fluid velocity potential on the body surface. To do so, the following hypotheses are assumed:

H1 Fluid continuity

H2 Strains are proportional to the deformation velocities (Newtonian Fluid)

H3 Fluid homogeneity and isotropy

H4 Inviscid Fluid

H5 The fluid is initially at rest (only gravity as external force)

H6 Atmospheric pressure assumed above the free surface and surface tension neglected

Hypotheses H1, H2 and H3 allow the derivation of the general form of the Navier-Stokes equation, after applying H4 the perfect fluid equations for irrotational flows are obtained. With H5 the definition of velocity potential is obtained $\vec{V} = \vec{\nabla}\phi$. The problem is then solved as in section 2.1.1 with an additional BC, that of the floating structure surface, assumed to be impermeable and thus forcing the velocity of the fluid to be equal to the normal velocity of the body in the normal direction of the structure surface:

$$\vec{V}\vec{n}|_C = \frac{\partial\phi}{\partial n}|_C = \vec{V}_E\vec{n}_C \tag{4.15}$$

where the subscripts C and E state the body surface and centre of gravity, respectively. Figure 4.2 illustrates a body surface upon which the body BC is computed by

the BEM method. Note that the surface is discretized, being the calculations performed at each element, whose normal defines its properties.

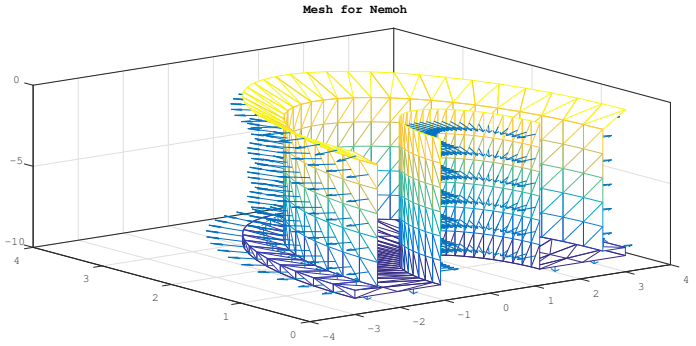

Figure 4.2: *Discretized body wet surface for BEM calculations*

To solve the BC on the body, the free surface and and the bottom the Green's function are used. The solutions of the problem are the velocities and then the potential is obtained from the sources through the influence coefficients. These, need to be discretized and then integrated on the surface panel. In the general form they are written:

$$C = C_1 + C_2 \tag{4.16}$$

$$C_1 = \iint_S f(\frac{1}{MM_1'})dS(M_1'); \text{for} M_1'(x', y', z_1') \tag{4.17}$$

$$C_2 = \iint_S \int_{-\frac{\pi}{2}}^{\frac{\pi}{2}} \ddot{g}(\eta)d\theta dS(M') \tag{4.18}$$

The terms C_1 are computed by an approximation to the analytical Hess formula as in (33). For the terms C_2 first the θ integral is calculated and then the double integral S is obtained numerically. Due to the slow variation of the integration term on the panel, integration in S can be achieved by using the approximation of the one point formula. To compute the integral in θ, the analytical formulae proposed by (75) are used. Through the discretization of the integral equations the following linear systems

are derived:

$$\frac{\partial\tilde{\phi}}{\partial n}\,|_{M_i}=\frac{\tilde{\sigma}_i}{2}+\sum_{j=1}^{N}\tilde{\sigma}_j\tilde{K}_{ij} \tag{4.19}$$

$$\tilde{\phi}|_{M_i}=-\sum_{j=1}^{N}\tilde{\sigma}_j\tilde{S}_{ij} \tag{4.20}$$

$$\tilde{S}_{ij}=\frac{1}{4\pi}\iint_S\tilde{S}(M_i,M')dS(M') \tag{4.21}$$

$$\tilde{K}_{ij}=\frac{1}{4\pi}\frac{\partial}{\partial n}|_{M'}\iint_S\tilde{S}(M_i,M')dS(M') \tag{4.22}$$

Where $\tilde{S}$ is the Green's function of the problem , N the number of bodies and the sign ˜specifies a complex entity. The elemental radiation and diffraction problems $\phi^{\tilde{q}}_{R_i}$ $\tilde{\phi}_D$ are respectively:

$$\frac{\partial\tilde{\phi}_e}{\partial n}|_{\sum_i}=\sigma_i^q \tag{4.23}$$

$$\frac{\partial\tilde{\phi}_e}{\partial n}|_{\sum_i}=-\frac{\partial\tilde{\phi}_I}{\partial n}|_{\sum_i} \tag{4.24}$$

Where $\sigma_i^q=\vec{e}_q.\,\vec{n}$ for $q=1,2,3$ and $\sigma_i^q=(\vec{e}_{q-3}\wedge O\vec{P}_0)$ for $q=4,5,6$ which are the modes corresponding to translational and rotational modes respectively. $\vec{e}_q$ is the unit vector of the axis q. The adoption of complex numbers is not only because of ease of writing but to its savings in computational times. Calculations could be done in real numbers but the unknowns would then be twice as much as with complex numbers, having computation times of the order of $8M^3$ instead of $4M^3$ for a complex system of order M, being M the number of panels.

The radiation problem is stated by a body forced with a sinusoidal motion in completely calm water whereas the diffraction problem is stated by the still body in the presence of monochromatic waves, where the pressure integral of the diffraction an incident potentials gives the excitation force coefficients. As an example, the radiation and excitation force coefficients obtained as a result of applying the BEM on a floating body are reported in figure 4.3. Note that the results are obtained in complex numbers but expressed in real numbers, the real part of the radiation coefficients are expressed as the added mass, the imaginary part of the radiation coefficient is expressed as the

radiation damping and the module of the excitation force coefficients is expressed as the excitation force influence.

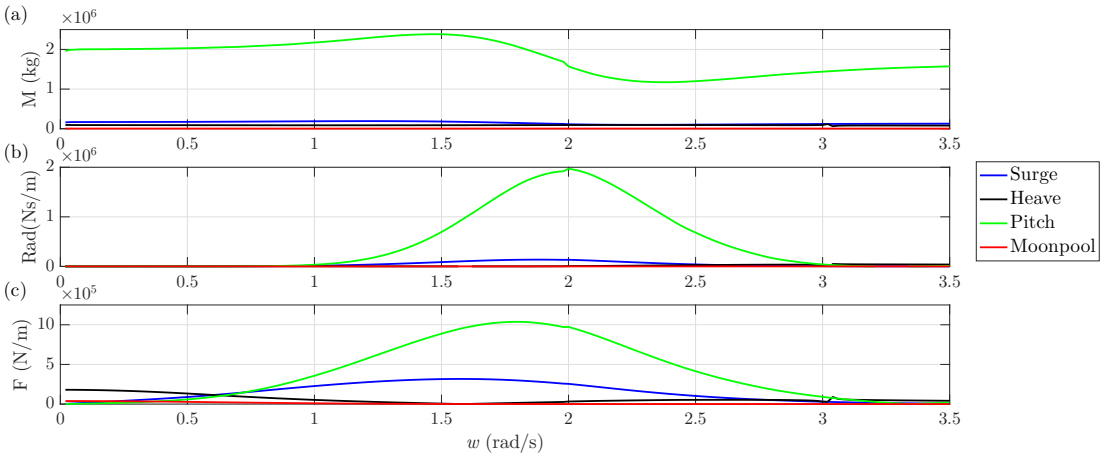

Figure 4.3: *Hydrodynamic coefficients for several DoFs vs. angular frequency. a) Added Mass coeffcient, b) Radiation damping coefficient, c) Excitation Force coefficient*

When using irregular waves a transformation of the radiation coefficients is required as shown in section 2.2. The coefficients at infinite frequency for the added mass and the impulse response function the radiation damping are also delivered by the BEM code NEMOH, see equations (2.105) and (2.104). Other parameters can be obtained by means of the BEM such as far field velocity coefficients used to compute the free surface and drift forces through the Kochin function. However, these are beyond the scope of this study and therefore its derivation is not exposed in this thesis.

Prony's method In order to obtain the radiation damping in irregular waves the convolution of the impulse response function of the radiation damping with the body velocity must be computed, see equation (2.104). This, forces the integration solver to attain to a fixed time step, since the body velocities must be known during the memory time, leading to a considerable increase of the amount of computation time. A method to approximate the retardation function has been developed by Duclos and Clément (43). This method, named the Prony's method is fast and efficient from the computational point of view, (83) and therefore, it has been adopted in this study.

The Prony's approach consists in the approximation of the retardation function by a series of damped exponential parameters. Let's assume that the impulse response

function of the radiation force has the following shape:

$$K(t) \approx \sum_{i=1}^{N} \alpha_i e^{\beta_i t} \tag{4.25}$$

Using the Prony's method one can identify the parameters α_i and β_i to best fit the original curve of $K(t)$. Creating the following variable that aims to substitute the convolution in equation (2.104):

$$I_i(t) = \int_0^{\tau} \alpha_i e^{\beta_i (t-\tau)} \frac{dz}{dt} d\tau \tag{4.26}$$

where τ is the memory time and z the body position. Then, one can say that the radiation force yields:

$$F_{rad} = \sum_{i=1}^{N} I_i(t) \tag{4.27}$$

$$\dot{I}_i(t) = \alpha_i(t) \cdot \frac{dz}{dt} + \beta_i(t) \cdot I_i(t) \tag{4.28}$$

Avoiding the convolution, by means of the introduction of a new variable $I_i(t)$ in the the state-space system composing the ODE equations, decreases the computing time drastically. However, the size of the system increases since for each couple of parameters α_i and β_i a new variable is added to the matrix system. The increase of the size of the system obviously raises the computational costs of the simulation, but at the same time, by avoiding the direct convolution for every time-step, the reduction is by far larger than the increase.

The total length of the $K(t)$, the memory time τ, is chosen as the time when the amplitude of the oscillations have decreased in two orders of magnitude with respect to the initial value. The number N of the pair α_i - β_i is determined through a fitting with the original impulse response function accounting with $R^2 \geq 0.98$. See Fig. 4.4

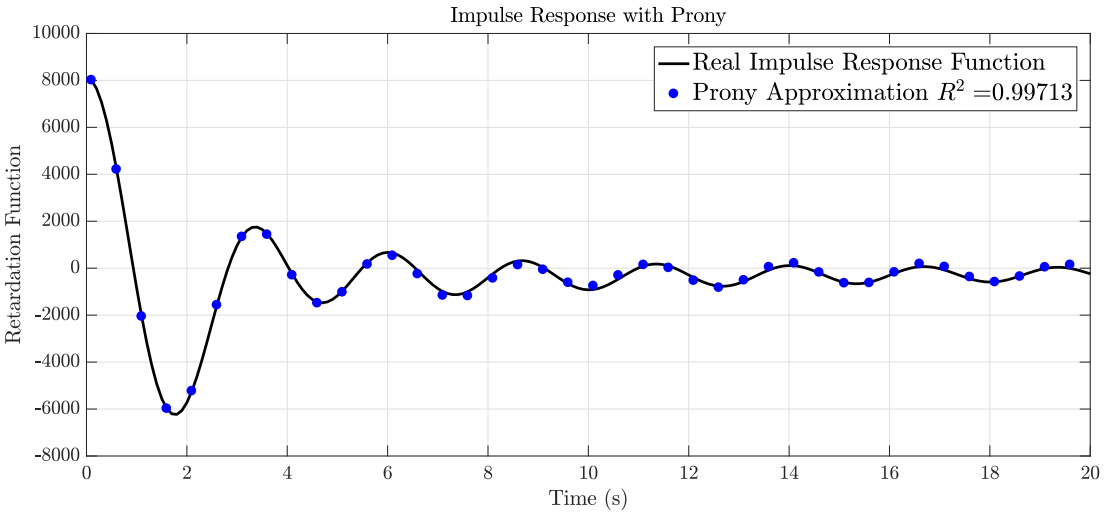

Figure 4.4: *Prony's approximation of the impulse response function*

4.1.3.3 Mooring forces

Each modelled WEC has a different mooring system according to geometrical characteristic and motion constrains, the HPA-LG and MoonWEC are moored with a single TLP system and and CALM system, respectively. Therefore, two models have been developed to account for the mooring forces. In this subsection, the modelling of the forces that keep the structures in place are thoroughly described.

Mono-TLP The HPA-LG is moored to the seabed by gravity, a concrete base, acting as a dead weight is installed onto the sea bottom, the linear electric generator is placed on top of the base and the interconnecting lines, which drive the electric generator, also act as mooring lines, as they keep the floating structures in place, under the form of a single TLP, see section 2.5. Furhtermore, the linear generator accounts with end-stop mechanisms which provide supplementary stiffness to the system, when the translator reaches the the end of its natural path. This is a survivability feature since it is mainly activated under severe stormy conditions to ensure the device integrity. The interconnecting lines have been modelled as very stiff springs acting only in traction, corresponding to wires working in tension. The compression phase has been neglected as, being the elongation negative would correspond to a slack wire, which has no dynamic contribution. Actually, for the sake of the device health and performance this phase ought to be avoided, since the passage from slack to taut wires produces large strains, which derive in slamming effects that produce regime instability and joint fail-

ures. The end-stop mechanism is also modelled as a very stiff spring only activated when a certain threshold is exceeded:

$$F_{line}(t) = \begin{cases} -K_{line}\Delta l(t) & \text{for } \Delta l(t) > 0 \\ 0 & \text{Otherwise} \end{cases} \tag{4.29}$$

$$F_{end}(t) = \begin{cases} -K_{end}(z(t) - Z_{lim}) & \text{for } |z(t)| > |Z_{lim}| \\ 0 & \text{Otherwise} \end{cases} \tag{4.30}$$

where K_{line} is the elastic constant of the wire, $\Delta l(t)$ is the wire elongation computed as the relative displacement between bodies, K_{end} is the elastic constant of the end-stop spring, and Z_{lim} is the activation coordinate of the end-stop mechanism.

CALM system For the MoonWEC device, the CALM system has been implemented to keep the device at place. In section 2.5, the shape equation for a catenary line has been derived and then, this relation is used to compute the global dynamic equation of the line, which depends on the chain acceleration. Equation (2.140) relates the geometrical characteristics with the static tensions given at the catenary line. Equation (2.140), reproduced here for convenience in the dimensional form, has two unknowns, T_0 and l:

$$\frac{Ph}{T_0} = \cosh(\frac{Pl}{T_0}) - 1 \tag{4.31}$$

Where, T_0 is the static tension of the chain in N, P is its linear weight N/m, h is the water depth and l is the horizontal distance from the joint in the structure and the point where the chain lies on the seabed in m, see figure 2.27. By combining equation (4.31) with the geometrical constrain in equation (2.146) and after some mathematical passages and simplifications one can arrive to the following relation:

$$\cosh(\sqrt{(\alpha h)^2 + 2\alpha h} - \alpha(l_T - l')) - \alpha h - 1 = 0 \tag{4.32}$$

Being $\alpha = \frac{P}{T_0}$. Note that equation (4.32) can only be solved iteratively, to carry this operation numerically several methods are available. In this study a Newton-Raphson algorithm of the form (102) has been implemented, using equation (4.32) as the control function:

$$f(\alpha_j) = \cosh(\sqrt{(\alpha_j h)^2 + 2\alpha_j h} - \alpha_j(l_T - l')) - \alpha_j h - 1 \tag{4.33}$$

$$f'(\alpha_j) = [h\frac{\alpha_j h + 1}{\sqrt{(\alpha_j h)^2 + 2\alpha_j h}} - (l_T - l')]\sinh(\sqrt{(\alpha_j h)^2 + 2\alpha_j h} - \alpha_j(l_T - l')) - h \quad (4.34)$$

$$\alpha_{j+1} = \alpha_j - \frac{f(\alpha_j)}{f'(\alpha_j)} \quad (4.35)$$

Where j states the current iteration. The iterative process keeps ongoing while $|\alpha_{j+1} - \alpha_j| > T$ where T is the tolerance, which has previously been established.

Having obtained the horizontal static tension of the chain, the horizontal force exerted by the catenary line can be yielded from equation (2.137). However, the chain acceleration $\ddot{x}_c$ depends also on T_t, which in turn depends on the floating structure position x and thus, on the structure acceleration $\ddot{x}$ as well. This makes so that an integration variable of the ODE system representing the systems dynamics has a direct dependency on another integration variable $\ddot{x}_c(\ddot{x})$, violating the variable independence rule for ODEs resolution. An approximation method of $\ddot{x}_c$ is adopted to tackle this issue. This method, proposed by (38), addresses the problematic by substituting the shape function of the catenary line by the Taylor expansion series to the second order. Considering the shape function of the catenary line for an aleatory position of the floating structure (x, z):

$$h + z = \beta[cosh(\frac{l + x}{\beta}) - 1] \quad (4.36)$$

where $\beta = \beta_0 + \bar{\beta}$, is the time updated value of β_0 from equation (2.148). Applying the Taylor series expansion in terms of the equilibrium position x, see (35):

$$h + z = (\beta_0 + \bar{\beta})[cosh(\frac{l}{\beta_0 + \bar{\beta}}) - 1] + x\sinh(\frac{l}{\beta_0 + \bar{\beta}}) \quad (4.37)$$

Furthermore, the Taylor series expansion may be also written in terms of the parameter $\bar{\beta}$ about its equilibrium position

$$\eta\bar{\beta}^2 + (\xi + \psi x)\bar{\beta} + (z - \varphi x) = 0 \quad (4.38)$$

$$\begin{aligned} &\eta = \tfrac{l}{\beta_0^2}\sqrt{\tfrac{h}{\beta_0}(\tfrac{h}{\beta_0} + 2)}; \quad \xi = \tfrac{l-h}{\beta_0} + \tfrac{lh}{\beta_0^2}; \\ &\psi = \tfrac{l}{\beta_0^2}(\tfrac{h}{\beta_0} + 1); \qquad \varphi = \sqrt{\tfrac{h}{\beta_0}(\tfrac{h}{\beta_0} + 2)} \end{aligned} \quad (4.39)$$

Where the analytical solution of $\bar{\beta}$ yields

$$\bar{\beta} = \frac{-(\xi + \psi x) \pm \sqrt{(\xi + \psi x)^2 - 4\eta(z - \varphi x}}{2\eta}) \tag{4.40}$$

Knowing that $\bar{\beta}(x = 0, z = 0) = 0$ the only possible solution for equation (4.40) is by taking only the + sign. Finally, same procedure has been developed for both dimensions (x, z) where the Taylor series expansion about its stationary points results in:

$$\begin{aligned}\bar{\beta}(x,z) = &(\tfrac{\xi\psi+2\eta\varphi}{2\eta\psi} - \tfrac{\psi}{2\eta})x - (\tfrac{1}{\psi})z + \tfrac{1}{4\eta\psi}[\psi^2 - (\tfrac{\xi\psi+2\eta\varphi}{\xi})^2]x^2 + (\tfrac{\xi\psi+2\eta\varphi}{\xi^3})xz... \\ ... &- (\tfrac{\eta}{\xi^3})z^2 - \tfrac{1}{4\xi^3}[\psi^2 - 3(\tfrac{\xi\psi+2\eta\varphi}{\xi})^2]zx^2 + 3\eta(\tfrac{\xi\psi+2\eta\varphi}{\xi^5})xz^2 - 2(\tfrac{\eta^2}{\xi^5})z^3\end{aligned} \tag{4.41}$$

Now, substituting equation (2.149) into equation (2.137), and the result into equation (2.136) the problem gets fully determined, knowing that $\dot{\beta}$ and $\ddot{\beta}$ can be obtained from the derivatives of equation (4.41), one can show that the equivalent equation of motion of the structure-mooring systems is:

$$F_e(t) = m_{eq}\ddot{x} + C_d\dot{x} + [A + 2Fz + 6Dz^2]x + Ex^3 - C\dot{x}\dot{z} - G\ddot{z} \tag{4.42}$$

Where

$$\begin{aligned} A &= P\tfrac{2\varphi}{\xi}; & F &= P(\tfrac{\xi\psi+2\eta\varphi}{\xi^3}) \\ E &= P\tfrac{\xi\psi+2\eta\varphi}{2\eta\xi^3}[(\tfrac{\xi\psi+2\eta\varphi}{\xi})^2 - \psi^2] & G &= \tfrac{A}{g} \\ D &= P\eta(\tfrac{\xi\psi+2\eta\varphi}{\xi^5}) & m_c &= \tfrac{P}{g}\beta_0\sinh(\tfrac{l}{\beta_0}) \\ m_{eq} &= m + 2m_c - \tfrac{A}{g}h & C &= 2G \end{aligned} \tag{4.43}$$

The convenience of this method relies on its computational efficiency, as the model plummets its computation times for two main reasons. First, the geometrical set-up of the CALM system is pre-calculated at the beginning, when the system is at rest and in equilibrium and therefore, the heavy computations regarding the iterative process to solve equation (2.146) are avoided during the simulation. Second, as the chains acceleration are embedded within the structure dynamics, the system accounts for two

less DoFs, which translated into the numerical model means two less ODEs to solve, with the corresponding savings in computational time.

4.1.3.4 Turbine

The blade of a turbine produces a resistance force to the fluid flow, which by the reaction principle used is then used to drive the turbine. In the case of the Wells turbine, the particular blade geometry (NACA00XX symmetric profile, (1)) makes so that the the tangential component of the resistance force has always the same direction regardless the fluid flow direction. The resistance force (equation (2.150)) can be subdivided in two separated forces, the drag force D and the lift force L. The former is parallel to the flow relative direction but with opposite sign and the latter is perpendicular to the flow relative direction. Through equations (2.151) and (2.152), these two forces can, in turn, be decomposed into a parallel and a perpendicular component to the turbine axis; F_A and F_t, respectively. Figure 4.5 illustrates the force schematic of the Wells turbine blade for both directions of the flow.

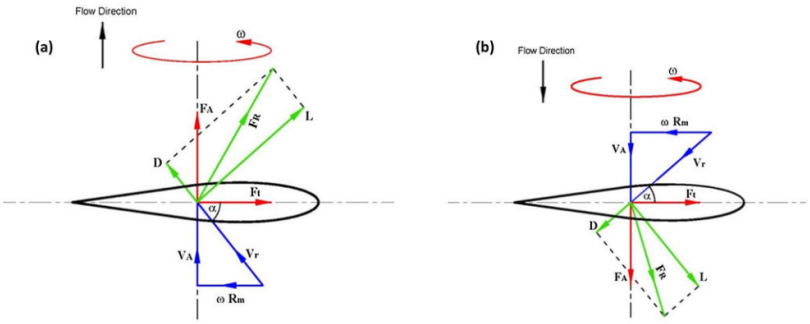

Figure 4.5: *W-T aerodynamic forces and velocity triangles. a) Compression stages. b) Suction stages.*

Since F_t and F_A are a geometrical derivation of L and D, which have the empirical formulation reported in equation (2.106), the same formulation can also be applied to compute the tangential and axial components:

$$F_t = \frac{1}{2}\rho C_{t0} A_b V_r(t)^2 \tag{4.44}$$

$$F_A = \frac{1}{2}\rho C_{A0} A_b V_r(t)^2 \tag{4.45}$$

Where ρ is the fluid density, A_b is the blade planar area, V_r is the relative velocity, obtained from the velocity triangle and, C_{A0} and C_{t0} are the isolated-blade coefficients for the axial and tangential force,respectively. Such coefficients derive from the drag force coefficients and thus, share a common pattern; i.e., they depend on the blade and flow characteristics. On the one hand, the shape characteristic is represented by the angle of attack α, which is the angle of incidence of the relative flow with respect to the blade symmetry axis. On the other hand, the flow characteristics are represented by the MACH and Reynolds numbers:

$$M(t) = \frac{V_r(t)}{c} \tag{4.46}$$

$$R_e(t) = \frac{\rho V_r(t) C}{\mu} \tag{4.47}$$

where V_r is the relative velocity, c is the speed of sound in the sea water, ρ is the sea water density, μ is dynamic sea water viscosity and C is the chord length of the blade. When $M < 0.3$ the flow compressibility can be neglected (49), having in mind that the speed of sound for sea water is $c = 1500\ m/s$, this makes so that $V_r < 450\ m/s$ and as far as this constraint is respected, C_{t0} and C_{A0} won't depend on the MACH number, and equations (4.45) and (4.44) can be applied as is. However, the axial and tangential coefficients do vary according to the attack angle and the Reynolds number. Figure 4.6 shows the dependency on both parameters according to wind tunnel experiments made by (81) on different blade geometries.

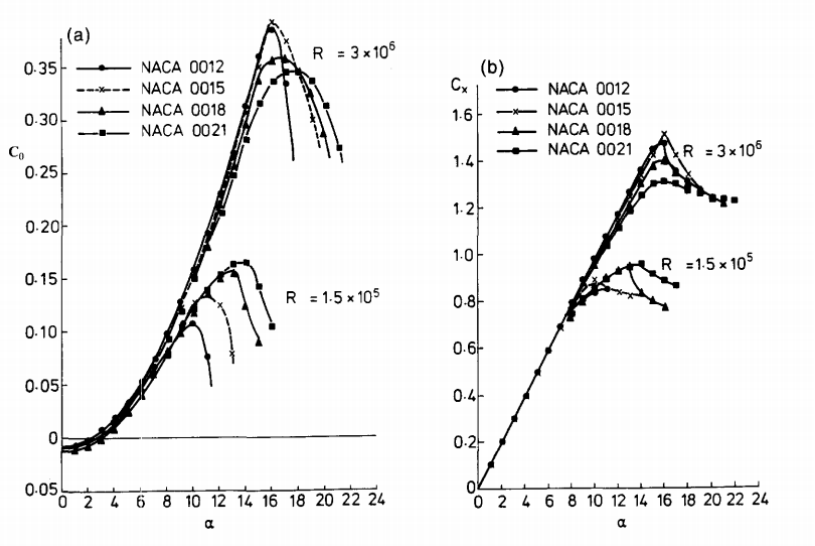

Figure 4.6: *Aerodynamic coefficients on several symmetrical NACA profiles for several Reynolds numbers a) Variation of the tangential force coefficient with incident angle. b)Variation of the axial force coefficient with incident angle (80)*

Figure 4.6 has been digitalized in order to store the coefficients variation as function of α and Re. The free software Plot Digitizer has been used (5) for the digitalization. Since the relative velocity $V_r(t)$ is function of time, so are α and Re. However, the coefficient curves are only available for two different Re number; thus, with the Reynolds number computed at each time-step an interpolation is needed and carried to obtain the correct coefficients for that time-step. From figure 4.6, one can note that the stall angle is also function of the Re number; hence, the interpolation has to be performed also according to the attack angle and not only to the coefficients. The following interpolation procedure has been applied: firstly, the new angle of attack is interpolated according to the Re number; subsequently, a new array of attack angles is created $[0 : \Delta\alpha : \alpha_{stall}]^\circ$, where $\Delta\alpha$ is the incremental step of α that makes this new array the same size as the digitalized ones. Afterwards, the interpolation of the coefficient values is done according to the Re number. Finally, to obtain the single value of the coefficient one last interpolation based on the current angle of attack is computed. If the current angle of attack is greater than the stall angle, then coefficient is assumed to be equal to zero, since after the stall conditions the effective work done by the turbine is null due to flow separation. Figure 4.7 illustrates the digitized curves from figure 4.6 for the NACA0021 blade profile (solid line) and the interpolated curves for other Reynolds numbers (dashed lines).

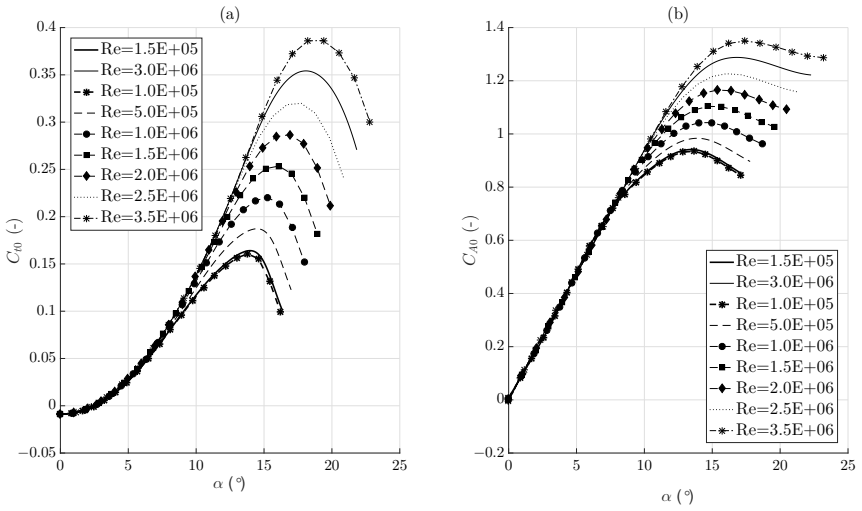

Figure 4.7: *Digitized curves from figure 4.6 for NACA0021 profile (solid lines) and interpolated curves for other Reynolds numbers (discontinuous lines). a) Tangential coefficients, b) Axial coefficients*

Once the coefficients for the isolated foil have been yielded, equations (4.48) and (4.49) are applied to obtain the coefficients accounting for the blade interaction effect:

$$\frac{C_A}{C_{A0}} = \frac{1}{1-\sigma^2} \tag{4.48}$$

$$\frac{C_t}{C_{t0}} = \frac{C_A}{C_{A0}} \tag{4.49}$$

where, σ is the ratio between the blade planar area and the hub-to-tip area. See figure 4.9 illustrates the plan view of the turbines rotor. Finally, these are applied into equations (4.50) and (4.51) to obtain the overall tangential and axial forces generated by the turbine.

$$F_t = \frac{1}{2} N \rho C_t A_b V_r^2 \tag{4.50}$$

$$F_A = \frac{1}{2} N \rho C_A A_b V_r^2 \tag{4.51}$$

Where N is the number of blades of the turbine. F_A is then applied to the floating structure equation of motion, decomposed according to its coordinates. Furthermore, the flow in the moonpool reacts to the presence of the turbine with a pressure drop;

this drop is only due to F_A, as the component of F_t is null due to its normal orientation to the flow direction. Therefore, F_A is also applied in the moonpool equation of motion with reversed sign. Finally, the torque $T = R_{mid}F_t$ generated by the turbine is applied in its rotational DoF equation of motion. R_{mid} is the distance between the middle point of the blade and the centre of rotation of the turbine.

4.1.3.5 Electric Generator

Synchronous generator models are usually based on the hypothesis that the rotation speed is constant, proof of that are some parameters such as synchronous reactance in the equivalent circuit scheme $X_s = \omega L_s$, which is assumed to be a constant constant value; consequently, the electric frequency ω and the inductance L_s must be also constant. However, this is not the case of neither of the studied WEC in this thesis. As described in section 2.3, this constraint is overcome by the introduction of PM generators, whose electric production adapts to the speed of the rotor without being forced to work in the nominal conditions unlike other synchronous machines. However, for the nominal conditions is where the PM generator efficiency peaks, making it the key design parameter.

The pole pair width w_p is defined as the distance from a north pole of the PM to the next one; therefore, the electric angular frequency can be expressed as:

$$\omega(t) = \frac{2\pi}{w_p}\dot{\varphi} \tag{4.52}$$

where $\dot{\varphi}$ is the speed of the rotor. The electric position θ is obtained by integrating the electric angular frequency over time:

$$\theta(t) = \int_0^t \omega(t)dt = \frac{2\pi}{w_p}\varphi(t) \tag{4.53}$$

The magnetic flux, described by equation (2.117), now can be expressed as function of the electric position θ and the load angle δ. The load angle represents a shifting of the position due to the load upon which the generator is subjected. The load concept can be expressed as the destination of the generated electricity. For instance, if the electricity is to be consumed by an appliance, this will be the load, in the case under study, the load is the electric distribution grid. Each load has unique characteristics which are specified by the load angle, resistance and inductance. The induced magnetic

flux results in:

$$\Phi(t) = \Phi_t \cos(\theta - \delta) = \Phi_t \cos[\frac{2\pi}{w_p}\varphi - \delta] \tag{4.54}$$

Where Φ_t is the magnetic flux amplitude, which depends on the magnetic field in a given stator tooth B_t, on the width of the tooth w_t, on the width of the stator stack d, the total number of poles p, the number of slots per pole q and the number windings per slot c. Hence, obtaining the following relation $\Phi_t = B_t w_t dpqc$. To obtain the induced voltage, as dictated by the Faraday's law, equation 2.120 is applied in terms of equation (4.53), yielding:

$$e(t) = \frac{2\pi B_t w_t dpqc}{w_p}\dot{\varphi}\sin[\frac{2\pi}{w_p}\varphi - \delta] \tag{4.55}$$

The computed voltage corresponds to a phase voltage, as stated in section 2.3, PM generators being studied for WECs are three-phase generators. Three-phase systems stabilize electromagnetic induction by minimizing the amplitude of oscillation of the induced voltage, since when the induced voltage of a certain phase is null the other two phases compensate the induction by having non-null induced voltages. The optimal configuration of a three-phase system is achieved by shifting the electric position of each phase 120°from the other two phases. Hence, the electric voltage of each phase results in:

$$\begin{aligned} e_a(t) &= \tfrac{2\pi B_t w_t dpqc}{w_p}\dot{\varphi}(t)\sin[\tfrac{2\pi}{w_p}\varphi(t) - \delta] \\ e_b(t) &= \tfrac{2\pi B_t w_t dpqc}{w_p}\dot{\varphi}(t)\sin[\tfrac{2\pi}{w_p}\varphi(t) - \delta + \tfrac{2\pi}{3}] \\ e_c(t) &= \tfrac{2\pi B_t w_t dpqc}{w_p}\dot{\varphi}(t)\sin[\tfrac{2\pi}{w_p}\varphi(t) - \delta - \tfrac{2\pi}{3}] \end{aligned} \tag{4.56}$$

Following the equivalent electric circuit, represented in figure 2.20, the electric current of each phase is computed as follows:

$$\begin{aligned} I_a(t) &= \tfrac{e_a(t)\cos\delta}{R_c + R_{load}} \\ I_b(t) &= \tfrac{e_b(t)\cos\delta}{R_c + R_{load}} \\ I_c(t) &= \tfrac{e_c(t)\cos\delta}{R_c + R_{load}} \end{aligned} \tag{4.57}$$

What is really of interest however, is the voltage at the load bornes as there is where the generated electricity is sent to the grid, see figure 2.20. The tension at the load bornes is obtained:

$$\begin{aligned} u_a(t) &= e_a(t)\cos\delta - R_c I_a(t) \\ u_b(t) &= e_b(t)\cos\delta - R_c I_b(t) \\ u_c(t) &= e_c(t)\cos\delta - R_c I_c(t) \end{aligned} \tag{4.58}$$

Once all the electric conditions have been found, the next logical step is to compute the instantaneous generated power $S_T(t)$. Electric power is measured in VoltAmpere VA in the SI units. The total, or apparent, electric power can divided into two subtypes of power, the active and reactive power. The former is the power that can be used by the load and is measured in watts W. The latter is considered as a loss, and derives from the imaginary part of the inductance of the equivalent circuit, measured in VoltAmpereReactive VAR. For this reason, the reactive part needs to be minimized. The power angle γ, which is derived from the power phasor diagram (analogous to figure 2.21), reports the relation between the active and the reactive power. In the studied case, being the load considered purely resistive, makes so that $\gamma = 0$, condition that makes the reactive power null and thus, the total power equal to the active power as from the phasor diagram one can say that $S = P\cos\gamma$ and in this case, the power factor is $\cos\gamma = 1$. Finally, the total instantaneous power is obtained by adding each phase power.

$$\begin{aligned} S_a(t) &= P_a(t) = u_a(t) I_a(t) \\ S_b(t) &= P_b(t) = u_b(t) I_b(t) \\ S_c(t) &= P_c(t) = u_c(t) I_c(t) \\ S_T(t) &= P_T(t) = P_a(t) + P_b(t) + P_c(t) \end{aligned} \tag{4.59}$$

In order to assess the effective generator performance, by means of the nominal speed and power, the root mean squared parameters have to be derived. These, represent the equivalent to a direct current system and provide a useful reference for performance

reference.

$$\begin{aligned} e_{rms} &= \frac{\mathbf{max}(e_a(t))}{\sqrt{2}} \\ I_{rms} &= \frac{\mathbf{max}(I_a(t))}{\sqrt{2}} \\ u_{rms} &= \frac{\mathbf{max}(u_a(t))}{\sqrt{2}} \\ P_{rms} &= u_{rms} I_{rms} \end{aligned} \tag{4.60}$$

Electromagnetic induction generates also a resistant force F_{rm} that opposes to the movement. The procedure to obtain such forces begins with the computing of of the resistant magnetic power, obtained through the generator electric efficiency. Afterwards, the force is obtained by applying the principle that states that power is force times velocity. This force has to be applied then into the equation of motion of the electric generator coupling effectively the electromagnetic and mechanic models.

$$\begin{aligned} P_{rm}(t) &= \frac{P_T(t)}{\eta_{el}} \\ F_{rm}(t) &= \frac{P_{rm}(t)}{\dot{\varphi}} \end{aligned} \tag{4.61}$$

This procedure can be applied either to the rotative machine coupled to the W-T of the MoonWEC, either to the linear generator of the HPA-LG. However, there is a main difference between both generators, one has a linear motion and the other a rotative motion, which has two basic implications in the modelling. The first difference comes by the representation of the driving velocity of the rotor (or translator) $\dot{\varphi}$. For the LG, $\dot{\varphi}$ is a linear velocity which varies in sign depending whether the translator is going upwards ($\dot{\varphi}>0$) or downwards ($\dot{\varphi}<0$) and its units are the SI units (m/s). For the rotative machine instead, $\dot{\varphi}$ is an angular velocity whose units are revolutions per second and the pole width is computed as the arch length between two consecutive north poles. The second main difference within the magnetic resistant force, in which for the rotative generator is a torque.

4.1.4 Equations of motion

The dynamic behaviour of the studied WECs is governed through the general equation of motion which is expressed in terms of the Newton's second law (see equation(2.82)).

index	Body	Mode	Coordinate
1	Floater	Surge	z_1
2	Floater	Heave	z_2
3	Submerged Sphere	Surge	z_3
4	Submerged Sphere	Heave	z_4
5	LG Translator	Vertical	z_5

Table 4.2: *Organisation of the modelled DoFs for the HPA-LG device.*

It implements the coupling of the components from different nature altogether to obtain global behaviour of the WEC. Each DoF of the system has its own equation of motion, since the dynamics of a certain DoF can have an influence on another DoFs' dynamics, different equations of motions may be correlated by coupling coefficients. Therefore, when the system has more than one DoF the equations of motion are written in the matrix form, having the matrix system a dimension according to the number of modelled DoFs. As the potential flow model follows the Lagrangian approach the system described by the equation of motion can be modelled as a state-space system. This makes so that, all the components composing the equation of motion rely either on the position, velocity or acceleration of it, or any other possible combination between them. A common denominator links the three state-space variable and that is time, as they are directly related by the time derivative. Therefore the equation of motion system becomes and a system of ODEs numerically integrated following a Runge-Kutta scheme of the fifth order.

4.1.4.1 HPA-LG

The HPA-LG prototype has been modelled as a three-body system account with 5 DoFs. The first body is the cylindrical floater which has two DoFs, the surge and heave modes (see figs. 1.11 and 2.16). The second body is a submerged sphere, placed at a depth of 25 m, also accounting for the surge and heave modes. The third body, representing the linear generator translator, has only been modelled in the vertical direction. Table 4.2 summarizes the modelled DoFs and establishes the indexing of the ODE system.

Following the logic declared by table 4.2 the system of equation of motions is reported

below. For clarity each equation of motion has been written independently:

$$
\begin{aligned}
(m_1 + m_1^{\infty})\ddot{z}_1(t) &= F_e^1(t) + F_r^1(t) + F_{moor}^{13}(t) + F_d^1(t) \\
(m_2 + m_2^{\infty})\ddot{z}_2(t) &= F_e^2(t) + F_r^2(t) + F_{moor}^{24}(t) + F_h(t) \\
(m_3 + m_3^{\infty})\ddot{z}_3(t) &= F_{moor}^{31}(t) + F_{moor}^{35}h(t) + F_d^3(t) \\
(m_4 + m_4^{\infty})\ddot{z}_4(t) &= F_{moor}^{42}(t) + F_{moor}^{45}v(t) + F_d^4(t) \\
m_5\ddot{z}_5(t) &= F_{moor}^{5}(t) + F_{pto}(t)
\end{aligned}
\tag{4.62}
$$

Where, m is the mass of the body, m^{∞} is the added mass at ∞ frequency, the different $F_e(t)$ are the wave excitation forces, $F_r(t)$ are the radiation damping forces, $F_d(t)$ are the viscous drag forces, $F_{moor}(t)$ are the forces exerted by the mooring system, $F_h(t)$ is the hydrostatic restoring force and F_{pto} is the force due to the PTO system. For details on the derivation of these forces refer to sections 4.1.2, 4.1.3.1, 4.1.3.2, 4.1.3.2, 4.1.3.2, 4.1.3.3 and 4.1.3.5.

4.1.4.2 MoonWEC

The MoonWEC has been modelled as a three-body system with five DoFs. The first body is the floating structure of the device, which is allowed to move in the surge, heave and pitch modes. The second modelled body is the water entrained in the moonpool orifice, which has been allowed to move freely only along the symmetry axis of the floating structure. The moonpol equation of motion however, has been developed in next section 4.1.4.3, due to its particular dynamic behaviour. The author thinks that by separating the dynamic derivation of both bodies a more thorough local vision is obtained for each body, gaining in clarity and comprehension of the whole system. Finally, the third body is the wells turbine which has one DoF of rotation around the symmetry axis of the MoonWEC's structure.

The surge motion of the MoonWEC is referenced by the x coordinate and the index 1, the heave mode is represented by the coordinate y, the index 2 and the pitch rotation by θ and the index 3 and the rotation of the Wells turbine is stated by the coordinate φ and the index four. As in the previous section, for clarity, the equations of motion are reported individually despite being part of a matrix system.

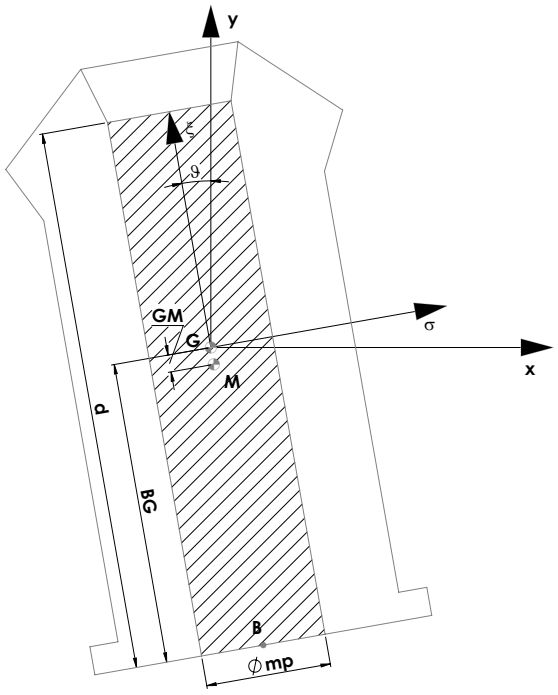

Figure 4.8: *Reference model of the MoonWEC for mathematical characterisation*

$$
\begin{aligned}
&(m_1 + m_1^{\infty})\ddot{x} + (m_{13} + m_{13}^{\infty})\ddot{\theta} = F_e^1(t) + F_r^1(t) + F_r^{13}(t) + F_d^1(t) + F_{moor}^1 + F_{MP}^1 + F_d^{14}(t) \\
&(m_2 + m_2^{\infty})\ddot{y} = F_e^2(t) + F_r^2(t) + F_h^2(t) + F_d^2(t) + F_{moor}^2 + F_{MP}^2 + F_d^{24}(t) \\
&(m_3 + m_3^{\infty})\ddot{\theta} + (m_{31} + m_{31}^{\infty})\ddot{x} = M_e^3(t) + M_r^3(t) + F_r^{31}(t) + M_{moor}^1 + M_{MP}^1 + M_h^3(t) \\
&m_4\ddot{\varphi} = M_l^4(t) + M_{pto}(t)
\end{aligned}
\tag{4.63}
$$

Where, m is the mass of the body, m^{∞} is the added mass at ∞ frequency, the different $F_e(t)$ are the wave excitation forces, $F_r(t)$ are the radiation damping forces, $F_d(t)$ are the viscous drag forces, $F_{moor}(t)$ are the forces exerted by the mooring system, $F_h(t)$ is the hydrostatic restoring force, $M_l(t)$ is the lift torque produced by the Wells turbine and M_{pto} is the resistant torque due to the PTO system. For details on the derivation of these forces refer to sections 4.1.2, 4.1.3.1, 4.1.3.2, 4.1.3.2, 4.1.3.2, 4.1.3.3, 4.1.4.3, 4.1.3.4 and 4.1.3.5.

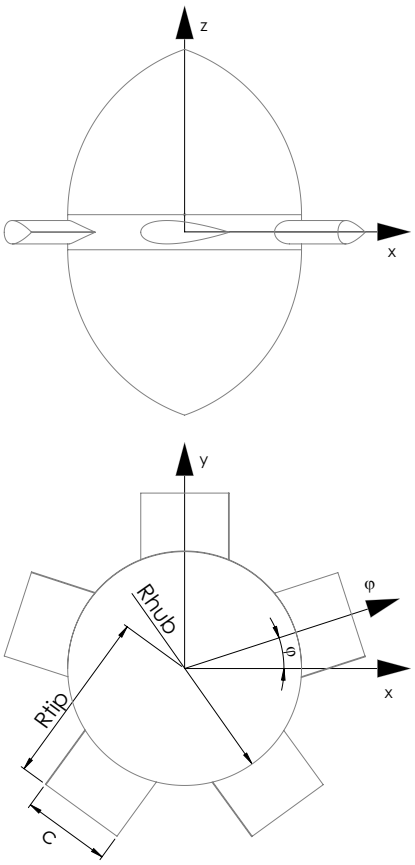

Figure 4.9: *Reference model of the Wells turbine for mathematical characterisation*

4.1.4.3 Moonpool

As introduced in section 2.4, a moonpool is a water column located within an offshore structure whose lower opening is directly connected to the sea. As a result of wave excitation, a mooonpool reacts as any floating structure would, having its own natural period and response to waves. Moonpool dynamics can be approximated as varying draft floating cylinder, as first demonstrated by (9) and later by (51, 66), who presented upgraded versions of the initial model. In this thesis, two main new features have been included in the moonpool model. Firslty, as the dimensions of the MoonWEC are so to make the pitch mode relevant in the device dynamics, the rotational mode the structure forces the moonpool to rotate as well. As the rotation of the moonpool is not around its centre of gravity but the centre of gravity of the MoonWEC, coupling harmonics are induced in both structures, which makes assume a highly non-linear behaviour. Secondly, the drag induced by the wells turbine has also been taken into account by the reaction principle, creating another feedback that increases the overall dynamics complexity. Figure 4.8 shows the system upon which the mathematical model is derived. The moonpool is represented by the dashed area.

Following the deformable volume approach we have that the mass conservation must be respected as stated in equation (2.131), reproduced here for clarity:

$$\int_S \rho(\vec{v_{MP}} - \vec{v_S}) \times \vec{n} dA = -\frac{dM_{MP}}{dt} \tag{4.64}$$

Realising that $(\vec{v_{MP}} - \vec{v_S})$ is the relative moonpool velocity $\vec{v_r}$ and following the notation from figure 4.8, the left and right hand side of equation (4.64) can be rewritten respectively as:

$$\int_S \rho \vec{v_r} \times \vec{n} dA = \rho S_{mp}(v_{MP}\sin(\theta) - \dot{x}, v_{MP}\cos(\theta) - \dot{y}) \begin{pmatrix} -\sin(\theta) \\ -\cos(\theta) \end{pmatrix} \tag{4.65}$$

$$-\frac{dM_{MP}}{dt} = -\frac{d}{dt}\rho S_{mp}(BG + \xi) = -\rho S_{mp}\dot{\xi} \tag{4.66}$$

where S_{mp} is the area of the Control Surface (CS) and BG is the distance from the Centre of Gravity (CoG) of the structure to S. Note that the MoonWEC structure CoG has been selected as the origin of the reference system. Recomposing equation (4.64) from equations (4.65) and (4.66), applying the opportune mathematical simplifications and finally applying the small angle hypothesis, for which $\sin\theta \simeq \theta$ and $\cos\theta \simeq 1$, the

absolute velocity of the moonpool is yielded

$$V_{MP} = \dot{x}\theta + \dot{y} + \dot{\xi} \tag{4.67}$$

where the $\cdot$ on top of a variable expresses its time derivative $\frac{d}{dt}$. The following step is to derive the momentum equation of a deformable volume, written in equation (2.132), and here decomposed for the axes x and y as $\sum \vec{F} = (\sum F_x, \sum F_y)$:

$$\sum F_x = \frac{d}{dt}(\int_{CV} v_x \rho d\Delta) + \int_{CS} v_x \rho(\vec{V_r} \times \vec{n}) dA \tag{4.68}$$

$$\sum F_y = \frac{d}{dt}(\int_{CV} v_y \rho d\Delta) + \int_{CS} v_y \rho(\vec{V_r} \times \vec{n}) dA \tag{4.69}$$

where, CV and CS are the control volume and surface, respectively; v_x and v_y are the horizontal and vertical velocities of the surface point of the moonpool $P = (x_p, y_p)$, which are derived from figure 4.8:

$$\begin{aligned} x_p &= x + \xi \sin\theta; \\ v_x &= \tfrac{d}{dt} x_p = \dot{x} + \dot{\xi} \sin\theta + \dot{\theta}\xi \cos\theta \end{aligned} \tag{4.70}$$

$$\begin{aligned} y_p &= y + \xi \cos\theta; \\ v_y &= \tfrac{d}{dt} y_p = \dot{y} + \dot{\xi} \cos\theta - \dot{\theta}\xi \sin\theta \end{aligned} \tag{4.71}$$

By taking each term of equations (4.68) and (4.69), developing them separately and then reunifying them, the final equations for $\sum F_x$ and $\sum F_y$ are obtained. Note that the small angle hypothesis has also been applied during this procedure:

$$\begin{aligned} &\tfrac{d}{dt}(\textstyle\int_{CV} v_x \rho d\Delta) = \rho S_{mp} \tfrac{d}{dt}((\dot{x} + \dot{\xi}\sin\theta + \dot{\theta}\xi\cos\theta)(BG + \xi)) = ... \\ &... = \rho S_{mp}(\dot{\xi}(\dot{x} + \dot{\xi}\theta + \dot{\theta}\xi) + (BG + \xi)(\ddot{x} + \ddot{\xi}\theta + \ddot{\theta}\xi + 2\dot{\theta}\dot{x}i - \dot{\theta}^2\xi\theta)) \end{aligned} \tag{4.72}$$

$$\begin{aligned} &\textstyle\int_{CS} v_x \rho(\vec{V_r} \times \vec{n}) dA = \rho S_{mp}((\dot{x} + \dot{\xi}\sin\theta + \dot{\theta}\cos\theta)(-v_{MP}(\cos^2\theta + ... \\ &... + \sin^2\theta) + \dot{x}\sin\theta + \dot{y}\cos\theta)) = \rho S_{mp}(-\dot{\xi}(\dot{x} + \dot{\xi}\theta + \dot{\theta}\xi)) \end{aligned} \tag{4.73}$$

$$\sum F_x = \rho S_{mp}((BG+\xi)(\ddot{x}+\ddot{\xi}\theta+\ddot{\theta}\xi+2\dot{\theta}\dot{\xi}-\dot{\theta}^2\xi\theta)) \tag{4.74}$$

$$\frac{d}{dt}(\int_{CV} v_y \rho d\Delta) = \rho S_{mp}\frac{d}{dt}((\dot{y}+\dot{\xi}\cos\theta - th\dot{e}ta\xi\sin\theta)(BG+\xi)) = ...$$

$$= \rho S_{mp}(\dot{xi}(\dot{y}+\dot{\xi}-\dot{\theta}\xi\theta)+(BG+\xi)(\ddot{y}+\ddot{\xi}-th\ddot{e}ta\xi\theta-2th\dot{e}ta\dot{xi}\theta-th\dot{e}ta^2\xi)) \tag{4.75}$$

$$\int_{CS} v_y \rho(\vec{V_r}\times\vec{n})dA = \rho S_{mp}((\dot{y}+\dot{\xi}\cos\theta-\dot{\theta}\sin\theta)(-v_{MP}(\cos^2\theta+\sin^2\theta)+... \tag{4.76}$$

$$... + \dot{x}\sin\theta+\dot{y}\cos\theta)) = \rho S_{mp}(-\dot{\xi}(\dot{y}+\dot{\xi}-\dot{\theta}\xi\theta))$$

$$\sum F_y = \rho S_{mp}((BG+\xi)(\ddot{y}+\ddot{\xi}-\ddot{\theta}\xi\theta-2\dot{\theta}\dot{\xi}\theta-\dot{\theta}^2\xi)) \tag{4.77}$$

Finally, as the moonpool axes are (ξ,σ), the forces $(\sum F_x, \sum F_y)$ are projected accordingly. However, as the surface of the MoonWEC is considered impermeable, the motion is restricted only in the ξ direction, thus only the ξ projected has been carried out, following the logic applied in the previous steps, the small angle hypothesis has been applied in this operation too:

$$\begin{aligned}\sum F_\xi &= \sum F_x \sin\theta + \sum F_y \cos\theta;\\ \sum F_\xi &= \rho S_{mp}(BG+\xi)(\ddot{x}\theta+\ddot{y}+\ddot{\xi}-\theta^2\xi)\end{aligned} \tag{4.78}$$

The term $\sum F_\xi$, together with the hydrostatic pressure constitute the components of the pressure at the control surface S_{mp}. The external side of the CS is exposed to the sea and thus, the pressure exerted on it comprises the hydrostatic term, the inertial and dynamic terms induced by the radiation, the dynamic and inertial terms due to the incident wave and a dynamic term due to viscous effects. The expressions reporting the inner and outer pressures of the CS p_i and p_o yielded

$$\begin{aligned}p_i &= \frac{\sum F_\xi}{S_{mp}} + \rho g(BG+\xi) - p^w = \rho(BG+\xi)(\ddot{x}\theta+\ddot{y}+\ddot{\xi}-\dot{\theta}^2\xi+g) - p^w\\ p_o &= -\rho g(y-BG) + p_{rad} + p_e + p_d\end{aligned} \tag{4.79}$$

where, p^w is the pressure drop generated by the presence of the Wells turbine. The balance between the pressure of the two faces of the CS S_{mp} is what drives the motion of the moonpool, described by the equation of motion. Moreover, despite the fact that the moonpool is treated as body with a deformable volume, the CS remains constant in time as the volume variation occurs only along the normal axis ξ. Hence, enabling to assume the hypothesis of rigid body only in the CS S_{mp}. By multiplying the equation of motion by S_{mp}, the hydrodynamic terms of radiation, wave excitation and viscous drag can be computed as stated in section 4.1.3.2, which leads to the following expression:

$$
\begin{aligned}
&(p_i - p_o)S_{mp} = \sum F_\xi + \rho g S_{mp}(y - BG) + F_d + F_r + F_e + F_d^w; \\
&(\rho S_{mp}(BG + \xi) + m_\infty^\xi)(\ddot{\xi} + \ddot{x}\theta + \ddot{y}) = f_e^\xi * \eta - \tfrac{1}{2} C_d^\xi S_{mp}(\dot{x}\theta + \dot{\xi})^2 - ... \\
&... - k^\xi * (\dot{x}\theta + \dot{\xi}) - \rho S_{mp}((BG + \xi)(-\dot{\theta}^2\xi + g) + g(y - BG)) - m_\infty^\xi \dot{\theta}(\dot{x} - \dot{y}) + F_d^w
\end{aligned}
\tag{4.80}
$$

where m_∞^ξ is the added mass coefficient of the moonpool, C_d^ξ is its drag coefficient, assumed to be equal to an equivalent cylinder drag coefficient, k^ξ and f_e^ξ are the impulse response functions of the the wave radiation and excitation, respectively and F_d^w is the drag force deriving from the presence of the Wells turbine. The pressure drop causing this drag effect is where the energy absorption by the turbine is taking place, used then to generate the electricity.

As seen on the previous paragraphs, the moonpool is free to move along the ξ axis. Nevertheless, the relative motion is blocked along the σ axis by means of the structure walls. This exerts a considerable influence in the MoonWEC dynamics as stated in equation (4.63) through F_{MP}^x and F_{MP}^y, see section 4.1.4.2. Such forces, since their origin is purely inertial, are computed by means of the Newton's second law:

$$
\sum \vec{F} = m_{MP}\vec{a}_M \tag{4.81}
$$

Where, m_{MP} is the moonpool mass, which has been obtained from equation (4.66) and M is the centre of gravity of the moonpool. As a result of the deformable volume condition, the point M (fig. 4.8) is not static with respect to the MoonWEC and its position varies along the ξ axis. Thus, to compute the acceleration its position must be found first. This is done by applying the definition of centre of mass, which is no other than a weighted average along the ξ axis, yielding the following distance $\|GM\|$:

$$
\|GM\| = \frac{-BG^2 + \xi^2}{2(BG + \xi)} \tag{4.82}
$$

Now, taking the centre of gravity of the structure as reference and projecting GM onto the (x, y) axes the coordinates of the point M are obtained. Subsequently, the time derivative of such coordinates is applied twice to find the acceleration and after some mathematical manipulation and the application of the small angle hypothesis the following relations are found:

$$\begin{aligned} x_M &= x + \tfrac{-BG^2+\xi^2}{2(BG+\xi)} \sin\theta \\ y_M &= y + \tfrac{-BG^2+\xi^2}{2(BG+\xi)} \cos\theta \end{aligned} \tag{4.83}$$

$$\begin{aligned} \tfrac{dx_M}{dt} = v_{xM} &= \dot{x} + \tfrac{1}{(BG+\xi)}[\xi\dot{\xi}\sin\theta + \tfrac{-BG^2+\xi^2}{2}(-\tfrac{\dot{\xi}\sin\theta}{(BG+\xi)} + \cos\theta\dot{\theta})] \\ \tfrac{dy_M}{dt} = v_{yM} &= \dot{y} + \tfrac{1}{(BG+\xi)}[\xi\dot{\xi}\sin\theta - (-BG^2+\xi^2)(\tfrac{\dot{\xi}\cos\theta}{(BG+\xi)} + \dot{\theta}\sin\theta)] \end{aligned} \tag{4.84}$$

$$\begin{aligned} \tfrac{dv_{xM}}{dt} = a_{xM} &= \ddot{x} + \tfrac{1}{(BG+\xi)}[\xi^2\theta + \ddot{\xi}\xi\theta + 2\xi\dot{\xi}(\dot{\theta} - \tfrac{\dot{\xi}}{BG+\xi}) + ... \\ &... + \tfrac{-BG^2+\xi^2}{2}(\tfrac{\ddot{\xi}\xi\theta}{BG+\xi} + \dot{\theta}^2\theta + \ddot{\theta} - \tfrac{\dot{\xi}}{BG+\xi}(\dot{\theta} + 1 - \tfrac{2\dot{\xi}\theta}{BG+\xi}))] \\ \tfrac{dv_{yM}}{dt} = a_{yM} &= \ddot{y} + \tfrac{1}{(BG+\xi)}[\dot{\xi}^2 + \ddot{\xi}\xi - 2\xi\dot{\xi}(\dot{\theta}\theta + \tfrac{\dot{\xi}}{BG+\xi}) - ... \\ &... - \tfrac{-BG^2+\xi^2}{2}(\ddot{\theta}\theta - \dot{\theta}^2 + \tfrac{1}{(BG+\xi)}(\ddot{\xi} - 2\xi\dot{\xi}(\dot{\theta}\theta + \tfrac{\dot{\xi}}{BG+\xi})))] \end{aligned} \tag{4.85}$$

Substituting the accelerations into equation (4.81) the forces at the point M are found. However, these need to be projected onto the axis σ to obtain the component that has an effective influence to the MoonWEC structure. Finally, an utter projection of F_σ back to the axes (x, y) yields the forces F^x_{MP} and F^y_{MP} in the correct reference system:

$$\begin{aligned} F_x &= \rho S_{mp}(BG+\xi)a_{xM} \\ F_y &= \rho S_{mp}(BG+\xi)a_{yM} \\ F_\sigma &= F_x\cos\theta - F_y\sin\theta = F_x - F_y\theta \end{aligned} \tag{4.86}$$

$$F_\sigma = \rho S_{mp}[(BG+\xi)(\ddot{x}-\ddot{y}\theta)+2\dot{\xi}\xi\theta+\frac{-BG^2+\xi^2}{2}(\ddot{\theta}+\ddot{\xi}\theta-2\dot{\theta}^2\theta+\frac{1}{BG+\xi}(\ddot{\xi}\xi\theta-\dot{\xi}(\dot{\theta}+1)))] \quad (4.87)$$

$$\begin{aligned} F^x_{MP} &= F_\sigma \cos\theta = F_\sigma \\ F^y_{MP} &= -F_\sigma \sin\theta = -F_\sigma\theta = -\rho S_{mp}[(BG+\xi)\ddot{x}\theta + \tfrac{-BG^2+\xi^2}{2}(\ddot{\theta}\theta - \tfrac{\dot{\xi}\theta(\dot{\theta}+1)}{BG+\xi})] \end{aligned} \quad (4.88)$$

Finally, there is only one term left to fully define the dynamic influence of the moonpool upon the the MoonWEC. It is the moment created by the force F_σ due to the distance between both gravity centres GM, obtained in equation 4.82:

$$M^G_{MP} = GMF_\sigma \quad (4.89)$$

4.2 REEF3D CFD

In thesis, the open source CFD code REEF3D (23) has been used to provide an insight on how different methods of generating and absorbing waves perform in a Numerical Wave Tank. The software provides two options for wave generation; the relaxation method, presented in (71) and further extended by (57), and the Dirichlet approach. Similarly, wave absorption can be achieved using the relaxation method or active absorption, such as in (55). Different simulations combining the above methods have been run in order find the optimal set up.

The rise of computational power in recent years has brought Computational Fluid Dynamics to the forefront as a supplementary tool to physical testing for marine and coastal engineering. A lot of effort has been devoted lately towards wave modelling in CFD. Several models describing wave characteristics and interaction with coastal structures have been developed and validated.

Being able to simulating wave breaking is one of the star features of CFD; since its high level of accuracy makes it the only type of model capable to do so. Different models of spilling and plunging breaking waves models are introduced in (12, 82, 98). Wave transformation over a submerged bar is presented in (60). Also, emerged structure interaction, rip currents on barred beaches and wave run-up are investigated in (56). Different types of porous structures are addressed in (58, 64); regarding their interaction

with solitary and regular waves for the former and irregular waves for the latter.

Simulations are usually carried in enclosed domains, which emulate wave tanks and flumes typically used for physical testing. Wave tanks require a special treatment of the BCs to ensure a good wave generation and an efficient wave absorption. Several methods to prevent reflection have been implemented with success. These methods can be divided into two major categories; namely, passive and active absorption. The former consists in installing a porous medium at the walls of the tank so the energy of the incoming waves is dissipated. The principle of AWA is to generate the same reflected wave that reaches the wave-maker but in the exact opposite direction, so they cancel each other out (42).

In the same way, reflection needs to be dealt within numerical calculations. There are several different theories to absorb waves and all of them rely on the boundaries' properties. The first kind of Non-Reflective Boundary Condition (NRBC) to be used was the Sommerfeld-like NRBC, which defined the *radiation condition*, described by Sommerfeld in (88), to be null at the BC. However, it was soon noticed it could generate relevant spurious waves denoting the presence of large errors in the computed solution. Afterwards, (76) developed a new type of BC which damps the waves, it is colloquially known as a sponge layer and consists in adding an extra volume in the domain which gradually absorbs the waves. At the beginning of the 80's several upgrades to the Sommerfeld NRBC were presented by (21, 36), which consisted in applying some modifications to the the radiation condition, which made them less sensitive to the relative wave direction, nevertheless it still generated serious spurious waves in some cases. These approaches are local, meaning that each element of the boundary has degrees of freedom.

Afterwards, non-local schemes appeared, in which, each element of the boundary is coupled sharing common degrees of freedom with the others. The most famous non-local NRBC is the Dirichlet to Neumann BC, which consists in the coupling of the Dirichlet condition to the Neumann velocities through the DtN map (61). Then, the Perfectly Match Layer (PML) (22, 94) BC was invented, which is essentially an upgrade of the traditional sponge layers (76) with the particularity that their absorption capabilities are independent from wave frequency and direction of attack. Finally, the high-order local NRBC (45) were introduced. They differentiate from (21, 36) in the level of accuracy and in their applicability, the higher the order the more accurate the solution is without increasing the complexity of the computer code implementation. The methods above can be applied to all types of waves. For waves in numerical tanks two types of BC are

mainly used. The sponge layer and the Dirichlet BC.

4.2.1 General equations

REEF3D solves the Reynolds-Averaged Navier-Stokes equations (RANS) using an Eulerian approach and under the assumption of incompressible fluid flow. Continuity within the flow must be fulfilled and thus, the following system is solved:

$$\frac{\partial u_i}{\partial x_i} = 0 \tag{4.90}$$

$$\frac{\partial u_i}{\partial t} + u_j \frac{\partial u_i}{\partial x_j} = -\frac{1}{\rho}\frac{\partial p}{\partial x_i} + \frac{\partial}{\partial x_j}\left[(\nu + \nu_t)\left(\frac{\partial u_i}{\partial x_j} + \frac{\partial u_j}{\partial x_i}\right)\right] + g_i \tag{4.91}$$

where u is the time averaged velocity, ρ is the fluid density, p is the pressure, ν is the kinematic viscosity, ν_t is the eddy viscosity and g is the gravity acceleration. Turbulence in the flow is accounted with the $k-\omega$ model, where k expresses the turbulent kinetic energy and ω the specific turbulent dissipation. This turbulence model provides the eddy viscosity ν_t, for more detailed information on the model refer to (100).

The Chorin's projection method (29) is applied to obtain the pressure gradient term in the RANSs equations for an incompressible flow. Afterwards, the pressure gradient is neglected in the momentum equations. By integrating in time a new velocity is yielded and then, treated as an intermediate velocity u_i^*. Subsequently, the pressure gradient is then updated by applying the Poisson's equation that derives from the divergence of the intermediate velocity field.

$$\frac{\partial}{\partial x_i}\left(\frac{1}{\rho\left(\phi^n\right)}\frac{\partial p}{\partial x_i}\right) = -\frac{1}{\Delta t}\frac{\partial u_i^*}{\partial x_i} \tag{4.92}$$

To solve equation (4.92) the BiCGStab algorithm, presented in (96), has been used. Finally, the intermediate velocity field is corrected with the new pressure obtaining the non-divergent velocities for the next time step in the following way:

$$u_i^{n+1} = u_i^* - \frac{\Delta t}{\rho\left(\phi^n\right)}\frac{\partial p}{\partial x_i} \tag{4.93}$$

This procedure can be applied because a staggered grid is used to discretize the domain. The staggered grid delivers a good coupling between pressure and velocity and therefore, a divergence free solution is obtained. The convective term of equation (4.91) is treated numerically with the fifth-order Weighted Essentially Non Oscilla-

tory (WENO) scheme within the conservative finite-differences discretization framework. Thorough description of the implementation of this method can be found in (59). The weighting of the ENO stencils gives relative importance to each stencil according to its smoothness, thus providing very reliable results even for large gradients. The algorithm reduces to a minimum of third-order in presence of large gradients.

The time-dependent part of the RANS equations is discretized through the Total Variation Diminishing (TVD) Runge-Kutta scheme (87). This method implements a variable time step integration over time using the Courant[Pleaseinsert\PrerenderUnicode{âĂŞ}intopreamble]Fri (CFL) criterion in order to determine the time step. The CFL number links the maximum velocity of the domain and the time step, if it is smaller than 1, numerical stability is achieved with the optimal time step. However, turbulence is not accounted for with the TVD scheme, since its high velocities would require such a reduced time step that would rocket the computational costs. Assuming turbulence is of small entity if compared to the momentum equation, a first order implicit Eulerian scheme can be used to determine the time step of the $k-\omega$ turbulence model without having significative effects on the final results. REEF3D has been parallelized to be run on multiple processors simultaneously by decomposing the spatial domain, its management is carried by the Message Passing Interface (MPI) (Message Passing Interface). Its performance has been tested on NOTUR's computational centre Vilje (4) which has 1440 nodes with two 8-core Intel Sandy Bridge ($2.6GHz$) and 32 GB of dedicated memory per node.

The free surface is determined by the level set method, thoroughly described in (77). This method consists in the definition of a distance function $\phi(\vec{x},t)$. As shown below, this function points out the minimum distance from the interface Γ between the two different fluid phases, water and air in marine applications, being positive for one phase and negative for the other:

$$\phi(\vec{x},t)\begin{cases} > 0 \ if \ \vec{x} \in phase \ 1 \\ = 0 \ if \ \vec{x} \in \Gamma \\ < 0 \ if \ \vec{x} \in phase \ 2 \end{cases} \tag{4.94}$$

The free surface Γ is updated following a velocity field $\vec{u}$ derived from the following classic convective equation, solved using the same methods stated above, WENO for the convective term and TVD for the temporal integration:

$$\frac{\partial \phi}{\partial t} + u_j \frac{\partial \phi}{\partial x_j} = 0 \tag{4.95}$$

In order to keep the signed distance property and the mass conservation principle the level set function needs to be reinitialized at every time step.

4.2.2 Wave generation and absorption

In REEF3D's numerical tank, waves can be produced and absorbed with the RM and the Active Wave Absorption . RM smoothly performs a transition from the analytical values to the numerical ones when generating waves. In the same way, values are taken back to the analytical source when absorbing them. This transition is carried progressively in space and the areas where that occurs are usually denominated relaxation zones. Such transition is defined in the following manner:

$$\begin{aligned} u(\widetilde{x})_{relaxed} &= \Gamma(\widetilde{x})u_{analytical} + (1-\Gamma(\widetilde{x}))u_{computational} \\ w(\widetilde{x})_{relaxed} &= \Gamma(\widetilde{x})w_{analytical} + (1-\Gamma(\widetilde{x}))w_{computational} \\ \phi(\widetilde{x})_{relaxed} &= \Gamma(\widetilde{x})\phi_{analytical} + (1-\Gamma(\widetilde{x}))\phi_{computational} \end{aligned} \tag{4.96}$$

where u, w and ϕ are the horizontal and vertical velocities and free surface elevation respectively at each point $\widetilde{x}$ of the relaxation zone, being $\widetilde{x}$ the normalized length of such relaxation zone. $\Gamma(\widetilde{x})$ is the relaxation function which determines the shape of the relaxation process. REEF3D offers the possibility to use two different relaxation methods, the one proposed by (37) which will be referred to as Relaxation Method 1 (RM 1), and the one developed by (57) which will be called Relaxation Method 2 (RM 2) hereinafter. RM 1 is composed by three different relaxation zones in which two different relaxation functions are applied:

$$\Gamma(\widetilde{x}) = -2\widetilde{x}^3 + 3\widetilde{x}^2 for\ \widetilde{x} \in [0;1] \tag{4.97}$$

$$\Gamma(\widetilde{x}) = 1 - \widetilde{x}^6 for\ \widetilde{x} \in [0;1] \tag{4.98}$$

Equation (4.97) is applied to generate waves and its relaxation area is usually referred as the generation zone and located at the inlet boundary. If $\widetilde{x}$ is substituted by $(1-\widetilde{x})$ in equation (4.97), its symmetrical function is obtained. That, provides extra performance when it comes to absorb waves travelling the opposite direction in the flume, such as reflected waves from structures placed in the numerical tank. Thus, an extra relaxation zone needs to be defined, which has the same length as the generation one and is placed

contiguous to it. At the other extreme of the tank, a sponge layer is defined which is in charge to absorb all the waves reaching that point. Equation (4.98) is in charge to carry this transition.

In RM 2, just one relaxation function is used, either to generate and absorb waves, see equation (4.99). The same symmetry procedure implemented in method 1 is also used here in order to define the wave generating relaxation function and its wave absorbing variant.

$$\Gamma(\widetilde{x}) = 1 - \frac{e^{(\widetilde{x}^{3.5})} - 1}{e - 1} \; for \; \widetilde{x} \in [0; 1] \tag{4.99}$$

Analogously, each relaxation process needs its corresponding relaxation zone, designed following the same premises as in method 1. Namely, one wavelength for the generating and contiguous absorbing zones and two wavelengths for the sponge layer located at the the other side of the tank. For wave generation, velocities and water surface level are transitioned from the corresponding wave theory, whereas for wave absorption velocities are damped down by setting them to zero, water surface elevation to still water level. Graphical description of the relaxation methods is provided in figure 4.10:

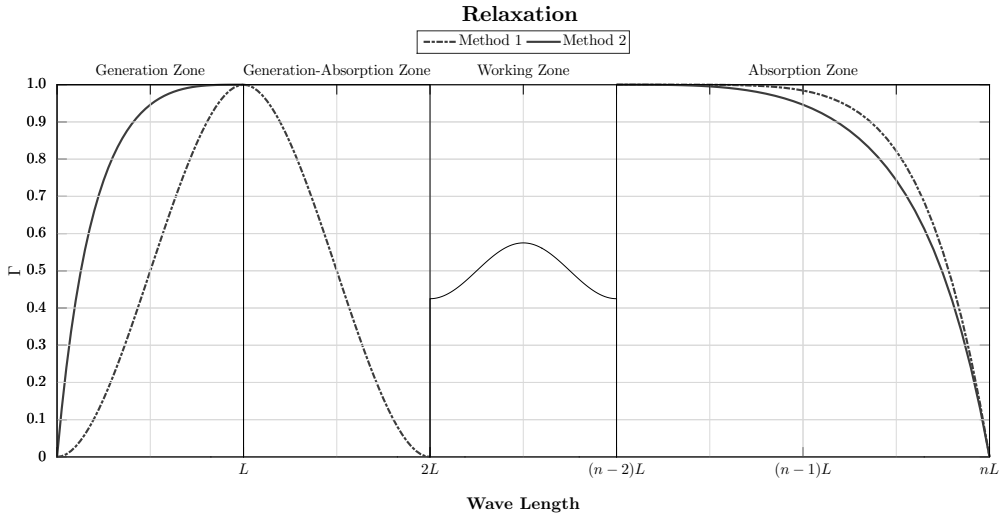

Figure 4.10: *Schematic of a numerical wave tank with wave generation and absorption zones and their respective relaxation functions for the two methods.*

Another possibility REEF3D offers, is to carry wave generation through active wave absorption. In order to do so, the Dirichlet type of BC is assumed, so the velocities

required to generate waves are imposed at the inlet BC. In the same way, to achieve the reflected wave cancellation, the exact same wave needs to be generated in the opposite direction. Assuming shallow waters within the Airy theory makes this approach straight forward for 2D waves, since water particle velocities are considered to be constant along the vertical axis.

This feature can be implemented either in the inlet and outlet boundaries. In the former, the incident wave velocity is compared to the velocity at the face of the inlet, the difference is the correction velocity that needs to be applied in order to obtain the correct waves. In the latter, instead of having incident wave velocities still water is assumed, so the velocity to absorb the incoming waves is exactly the opposite from the ones reaching the outlet.

Independently from the wave generation setting described above, REEF3D is able to generate waves from a wide variety of theories. Such as linear waves, in its three variants (deep, intermediate and shallow waters), 2^{nd} order Stokes waves, 5^{th} order Stokes waves, Cnoidal waves, Solitary waves, irregular and focused waves. This flexibility is given by the fact that the boundaries only need to establish the vertical and horizontal velocity and the water surface level.

4.2.3 Reflection Analysis

In order to assess which is the best performant method to generate and absorb waves, the amount of reflection present in the numerical tank needs to be quantified. There are several existing methods to quantify wave reflection, such as (48), where only two wave gauges were used and noise cancellation was not possible. Mansard & Funke (70) introduced a modified version accounting for three gauges which would filter the noise out. In this work, the method proposed in (101) has been used for the 2D numerical wave tank. With this approach, the least squared method is used to solve the equations and a variable weighting scheme is applied to improve accuracy in the following way:

$$\epsilon_{j,p} = a_{Lj} e^{i\phi j,p} + a_{Rj} e^{-i\phi j,p} - A_{j,p} \tag{4.100}$$

$$E_j = \sum_{p=0}^{P} W_{j,p} \epsilon_{j,p} \epsilon_{j,p}^{*} \tag{4.101}$$

where a_{Lj} and a_{Rj} are the incident and reflected wave amplitude coefficient respectively, for frequency j, $\phi_{j,p}$ is the product of the wave number k_j and the position x_p of

wave gauge p, $A_{j,p}$ is the coefficient obtained after carrying the Fourier analysis of the reading of gauge p for frequency j, $W_{j,p}$ is the assigned weight coefficient and E_j is least squared method parameter to be minimized.The symbol * in $\epsilon^*_{j,p}$, denotes the conjugate form of the complex error $\epsilon_{j,p}$. The number P of chosen gauges is arbitrary, after a sensitivity study on the gauge number it has been concluded that for the simulation conditions 4 gauges is enough. Substituting equation (4.100) to the minimized form of equation (4.101) yields the following equation system, composed by two complex equations and two complex unknowns,a_{Lj} and a_{Rj}:

$$\begin{aligned} a_{Lj}S_j + a_{Rj}\sum_{p=1}^{P} W_{j,p}e^{-2i\phi j,p} &= \sum_{p=1}^{P} W_{j,p}A_{j,p}e^{-i\phi j,p} \\ a_{Rj}S_j + a_{Lj}\sum_{p=1}^{P} W_{j,p}e^{2i\phi j,p} &= \sum_{p=1}^{P} W_{j,p}A_{j,p}e^{i\phi j,p} \end{aligned} \tag{4.102}$$

where $S_j = \sum_{p=1}^{P} W_{j,p}$. Zelt & Skjelbreia (101) propose an *ad hoc* heuristic approach to determine the optimal weight distribution to gauges. This method evaluates the relation between the phase differences related to the wave gauge distances in the following way:

$$G(\Delta\phi_{j,pq}) = \frac{sin^2\Delta\phi_{j,pq}}{1 + (\Delta\phi_{j,pq}/\pi)^2} \tag{4.103}$$

$$W_{j,p} = \sum_{q=1}^{P} G(\Delta\phi_{j,pq}) \tag{4.104}$$

where$\Delta\phi_{j,pq}$ is the phase difference at wave gages p and q for frequency ω_j, $G(\Delta\phi_{j,pq})$ is the goodness function and a large value denotes a correct spacing between gauges p and q for frequency ω_j. For 3D wave tank a variant of (101) has been implemented. This, presented by (50), takes into account the possible crossed-modes generated by lateral reflections and the minimum number of wave gauges required to achieve the necessary accuracy is $P = 5$. The exact same procedure from above has been adopted with the only difference of adding a new variable a_{Cj}, which represents the cross-modes. Consequently, equations (4.100) and (4.102) evolve into equations (4.105) and (4.106), respectively:

$$\epsilon_{j,p} = a_{Lj}e^{i\phi j,p} + a_{Rj}e^{-i\phi j,p} + a_{Cj} - A_{j,p} \tag{4.105}$$

$$
\begin{aligned}
a_{Lj}S_j + a_{Rj}\sum_{p=1}^{P} W_{j,p}e^{-2i\phi j,p} + a_{Cj}\sum_{p=1}^{P} W_{j,p}e^{-i\phi j,p} &= \sum_{p=1}^{P} W_{j,p}A_{j,p}e^{-i\phi j,p} \\
a_{Rj}S_j + a_{Lj}\sum_{p=1}^{P} W_{j,p}e^{2i\phi j,p} + a_{Cj}\sum_{p=1}^{P} W_{j,p}e^{i\phi j,p} &= \sum_{p=1}^{P} W_{j,p}A_{j,p}e^{i\phi j,p} \\
a_{Cj}S_j + a_{Lj}\sum_{p=1}^{P} W_{j,p}e^{-i\phi j,p} + a_{Rj}\sum_{p=1}^{P} W_{j,p}e^{i\phi j,p} &= \sum_{p=1}^{P} W_{j,p}A_{j,p}
\end{aligned}
\tag{4.106}
$$

For regular waves, once a_{Lj} and a_{Rj} are known, it is straight forward to compute the reflection coefficient just by dividing them into the following ratio $K_R = a_{Rj}/a_{Lj}$. For irregular waves, firstly the zero$^{\text{th}}$ moment wave height need to be computed from the obtained incident and reflected spectra and then make the ratio $K_R = H_{m0R}/H_{m0I}$.

5

Dimensioning, Tuning & Optimization

5.1 HPA-LG

In first approach, the HPA-LG has been modelled only in heave and with the PTO translator built-in with the floater. Influence on the floater's shape and draft has been analysed using three different geometries. A cylinder and two composed geometries, a cylinder with a conical base and a cylinder with spherical base. The optimal configuration has been found to be the regular cylinder with $\varnothing = 5m$ and draft of $d = 2.75\ m$, (13). Subsequently, a submerged body has been added to the system in order to shift the device's natural frequency. Table 5.1 shows the optimal dimensions for the device only in heave.

Hereinafter, the effect of the surge mode in the heave-prevailing point absorber HPA-LG is considered. Firstly, the optimal dimension of the submerged body is studied when accounting for the surge. Afterwards, the geometric design of the PTO system is optimized to comply by the new requirements deriving from the introduction of the surge mode. Lastly, a sensitivity analysis on the simulation duration is performed aiming to identify the minimum stable simulation duration, in terms of power production. The different variants of the device studied in this work are shown in table 5.2.

5.1.1 Free oscillation tests

The aim of the submerged body is to maximize the power output by shifting the natural period of the system towards the prevailing wave periods of the study sites sea states.

Parameter	value
Floating body diameter (m)	5
Floating body mass (kg)	4000
Submerged body diameter (m)	5.2
Submerged body mass (kg)	74,840
Distance between bodies (m)	25
PTO Parameters	
Nominal Power (kW)	10
Nominal Speed (m/s)	0.67
Translator length (m)	1.867
Stator length (m)	1.264
Translator mass (kg)	1000
Width of stator sides (m)	0.4
Number of sides $(-)$	4
Pole width (mm)	50

Table 5.1: *HPA-LG geometric properties (26).*

	N. of Bodies	N. of DoFs	Surge
A	2	2	X
B	2	3	✓
C	3	3	X
D	3	5	✓

Table 5.2: *Studied WEC devices.*

The shape of the chosen submerged body is a sphere. After the selection of the shape, the last characteristic to be determined is the radius. For floating bodies, standard procedure to identify the natural modes of the system is the free oscillating test. This, consists in varying the initial position from the equilibrium state and observe the evolution over time under total absence of external disturbances; in this case, represented by a flat sea. The length of the test has been set to 100 s, after this time it has been observed that the oscillations are completely damped and the system has reached back the equilibrium state. Setting the equilibrium condition at the point $(0, 0)$ of the coordinate system $(z_1^1(t), z_3^1(t))$, the initial displacement of the buoy has been established at $(-1.25, -1.25)$, hence for both, surge and heave.

Figure 5.1 shows the results of the free oscillations test for four different variants of the device, the first one without sphere, and the rest accounting with a sphere of different diameter. Figure 5.1.a) shows the evolution of the system over time while figure 5.1.b) shows the result of the frequency analysis. Furthermore, in black, the "climatic spectra "of the deployment sites are shown. These, are obtained by computing the weighted average of each JONSWAP spectrum that characterises the wave climate of the selected locations; the adopted weighting parameter is the frequency of occurrence. The data used to compute the wave climates have been obtained from the measurements given by the RON (2). Climatic spectra give a good insight on which are the most energetic frequencies at both sites, thus they are used to tune the device performance.

As expected, a strong non-linear behaviour is observed in figure 5.1.a) and no clear resonance in the piston is detected in figure 5.1.b). Nonetheless, the influence of the sphere is clear on the dynamic response of the system. Oscillations in the piston increase, in period and amplitude, as the radius of the sphere grows. Judging from the area of interest (the frequency range of the climate spectra) the optimal solution appears to be the device accounting with a 2.00 m radius sphere since it shows the highest amplitudes. However, not only the oscillations grow with the radius but so the non-linearities do, giving place to several undesired effects such as, slamming in the wires, end-stop mechanism activation, translator oscillating outside the productive area. Therefore, the configuration with the sphere of radius 1.50 m delivers the best performance while assuring smooth operation conditions of the device since its response is stable throughout the whole range of interested frequencies.

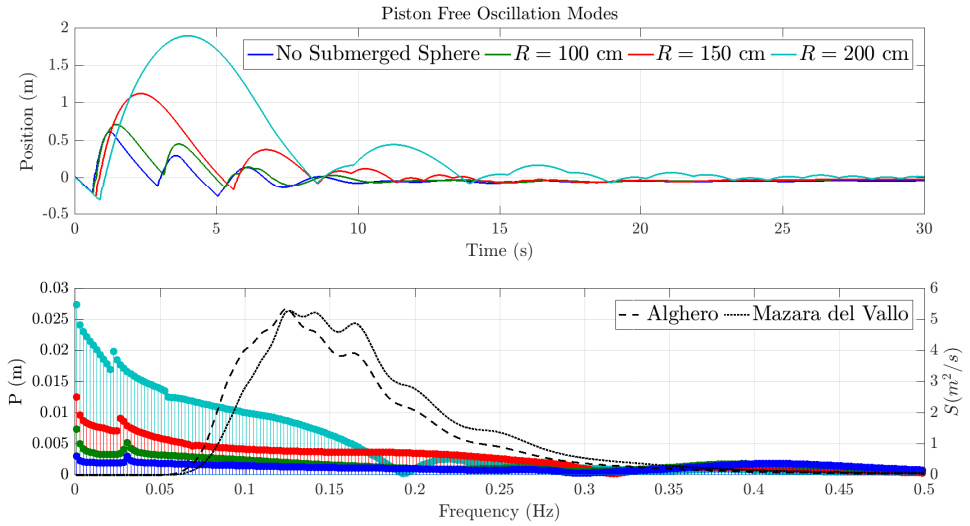

Figure 5.1: *Free Oscillation test of the PTO's translator. a) Influence of the sphere vs. time. b) Spectral analysis of oscillations and climatic spectra from Alghero and Mazara del Vallo*

5.1.2 LG Geometric Design

The surge motion directly causes a variation on the oscillatory regime of the piston. An extra horizontal component is introduced at the buoy and that makes the total displacements larger. The total displacement of the buoy is then transferred to the piston through the steel wire. This produces a shift of the piston mean oscillatory position (see figure 5.1.a) causing a drop of efficiency since the PTO is designed to oscillate around zero. In order to solve this undesired effect the PTO has been redesigned geometrically.

Figure 5.2 shows the mean oscillatory position of the piston for each simulated condition; at the typical working conditions ($T_P = [5.5-7.5](s)$ & $H_S = [1.0-2.5](m)$), the average oscillatory position is about $\bar{x} = 0.25m$. According to such preliminary result, the piston is extended by $2\bar{x}$ and the upper part of the stator is also lengthened by $\bar{x}$, see figure 5.3. This combination allows the lower bound of the maximal production rate to remain unmodified, whereas the upper bound of the minimal production rate is extended by $2\bar{x}$, see figure 5.4. Furthermore, the upper end stop position is also shifted by $\bar{x}$ to ensure that the piston smooth motion conditions are not affected by this change. Figure 5.3 shows the differences between the original design of the PTO and the optimized one.

The active production area is the surface of the stator, entirely or partially, con-

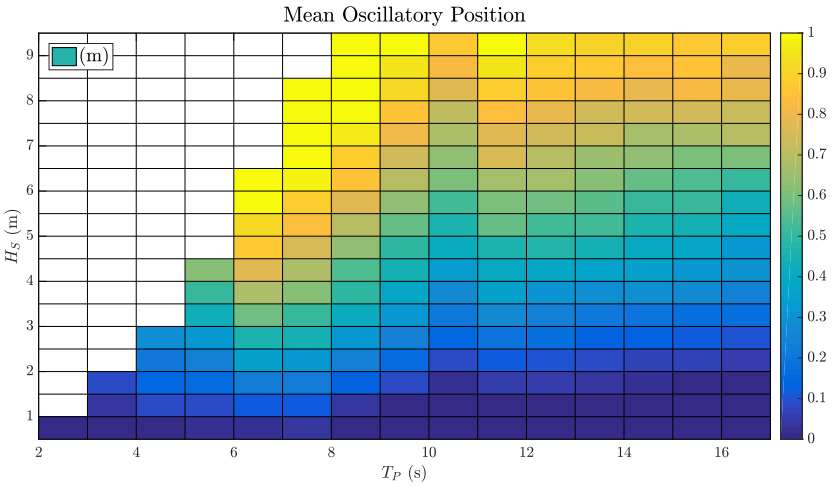

Figure 5.2: *Piston average position at each sea state*

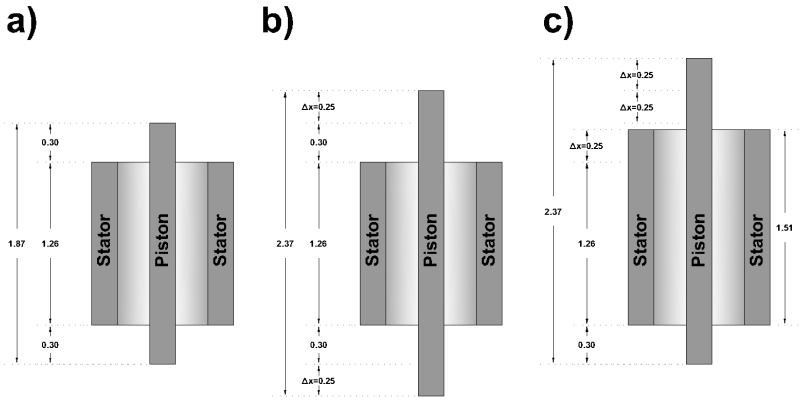

Figure 5.3: *PTO layout. a) Original form. b) Translator modification. c) Translator& Stator modification.*

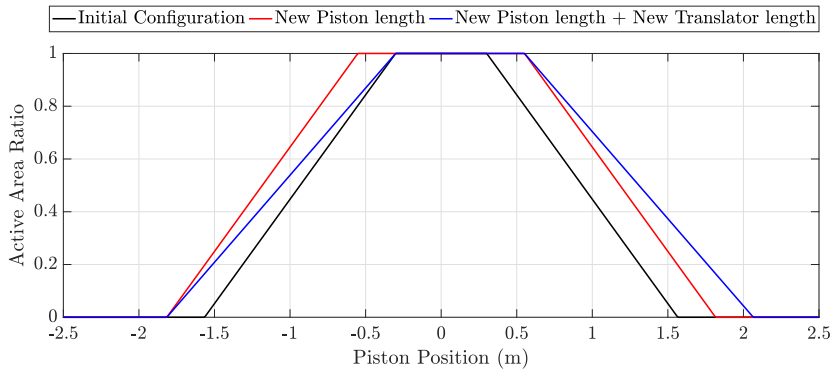

Figure 5.4: *PTO Active Production Area Ratio vs. Piston Displacement.*

taining the translator. If divided by the total area of the stator, the Active Area Ratio (AAR) is obtained. Figure 5.4 maps the differences in the active production area of the PTO for the original and the modified PTO.

5.1.3 Duration of the Simulations

In order to achieve a reliable estimate of the power absorption a standard length of the simulations needs to be defined. Due to the wide range of simulated sea states, a fixed duration of the simulations lacks in consistency, as the system may reach the power production stabilization at different times depending on the input wave characteristics. A suitable indicator of the length of the simulations is the number of waves, it is considered that after 1000 waves the whole wave spectrum is represented by the time series and thus, so it is its energy. Figure 5.5 shows the value of the power output deviation from the 1000-wave value of the system D (tab. 5.2) vs. the number of generated waves. The reason to compute the relative error derives from the fact that the absolute power output strongly varies depending on the sea state characteristics, hence making more difficult to compare the results directly.

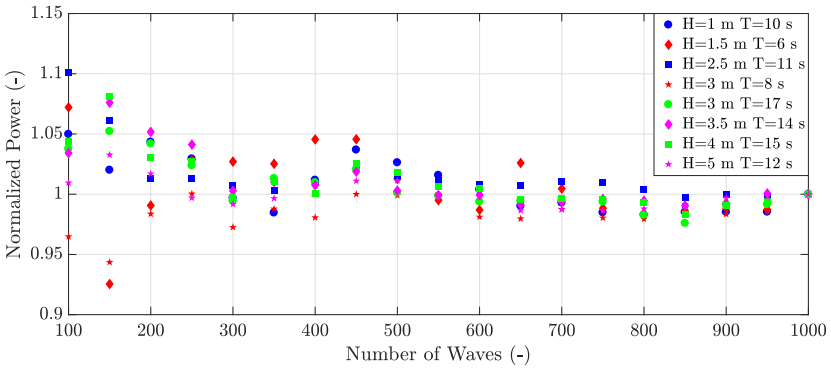

Figure 5.5: *Power output deviation from the 1000-wave value vs. Number of Waves.*

Taking into account the high level of uncertainty at this stage of the research, the authors believe that values below 5% are considered acceptable, if this error is distributed symmetrically around the normalizing value. Therefore, acceptable values lie within the interval $[-2.5 \;\; 2.5]\%$. In Figure 5.5, this condition is satisfied for the first time at 350 waves; thus, the minimum acceptable duration of the time series is 350 waves.

5.2 MoonWEC

The dimensioning, tuning and optimization of the MoonWEC device can be subdivided into three categories, corresponding to a physical part of the device. Firstly, the floating structure and the moonpool are dimensioned. The fulfilment of several requirements has to be assured in order to capture the energy contained in waves in an efficient way. In other words, resonance of the floating structure and the moonpool has to be reached. Furthermore, both resonant motions must have phase lag for in order to maximise its relative movement. Secondly, the mooring system is dimensioned and tuned. The goal is to design a mooring system that prevents the device from drifting away and also assures survivability for extreme wave conditions, while modifying as little as possible the device dynamics for the working conditions. Lastly, the power take-off system, composed by the Wells turbine and the PM generator is tuned in order to convert the energy captured by the moonpool in the most possible efficient manner.

5.2.1 Device

As introduced in sections 2.2 and 2.4, a floating structure can be simplified as mass-spring-damper system. As such, it develops a resonant state if properly excited with a

specific frequency. This frequency, known as the natural frequency of the system, can be found with:

$$\omega_0 = \sqrt{\frac{k}{m}} \tag{5.1}$$

Where k is the elasticity constant of the system and m is its total mass. For complex geometries, k and m might not be constants, as the elasticity may vary with hydrostatics and the mass with the added mass due to wave radiation. However, for the heave mode of the moonpool its derivation is immediate (90); due to its simple cylindrical configuration equation (5.1) can be simplified to :

$$\omega_0 = \sqrt{\frac{g}{d}} \tag{5.2}$$

Where g is the gravity acceleration and d is the moonpool draft. Knowing that the moonpool has to resonate for sea states around $T_P = 6s$, derivation of the moonpool draft, and in turn also the structure draft, is direct yielding $d = 9m$. The diameter of the moonpool will depend on the power take-off system. From figure 4.7, the range of desired Reynolds number, for high efficiency performance of the turbine is retrieved. Supposing a relative velocity between the moonpool and the structre of $V_r = 2\ m/s$, a blade chord of $c = 0.5m$ (see figure 4.9) yields a $Re = 5.5 \times 10^5$, which is in the range of desired Reynolds numbers. A blade chord of half of meter leads to a moonpool radius of $r_m = 1m$. Having determined on a first attempt the dimensions of the moonpool, the structure wrapping the moonpool has to be sized according to the required natural frequency. In first approach, this is done in the frequency domain, by applying the Fourier transforms to the time domain equation of motion an analytical solution is obtained resulting in no need for time integration. Non-linear effects cannot be modelled in the frequency domain; however, at this stage, this is not a major concern as a general outlook of the device response is the goal of this phase of the designing process.

5.2.1.1 Frequency domain

After applying the Fourier transform of the linearised equation of motion (4.63), the following expression is obtained:

$$F_e = X_0(-\omega^2(m + A) + i\omega B + KH) \tag{5.3}$$

Where ω is the frequency of the monochromatic wave exciting the structure, m

is the mass matrix of the system, A is the added mass matrix, B is the radiation damping matrix, KH is the hydrostatic stiffness matrix, F_e is the excitation force coefficient vector and X_0 is the Response Amplitude Operator (RAO), which reflects the unitary response of the system. Except the RAO, which is the unknown variable, all the other coefficients are known; m and KH are solved using the internal forces equations described in section 4.1.2 and the hydrodynamic coefficients A, B and F_e are obtained with the BEM method, section 4.1.3.2.

BEM The first step in finding the hydrodynamic coefficients is to make sure the chosen mesh for the body surface is correct. Checking the X_0 solution convergence with several meshes reveals the minimum number of elements needed in order to obtain an accurate solution. This procedure allows also to reduce to the computation times of the BEM method. Figure 5.6 shows the mesh convergence analysis carried out on a cylindrical floater with similar dimensions as the MoonWEC's.

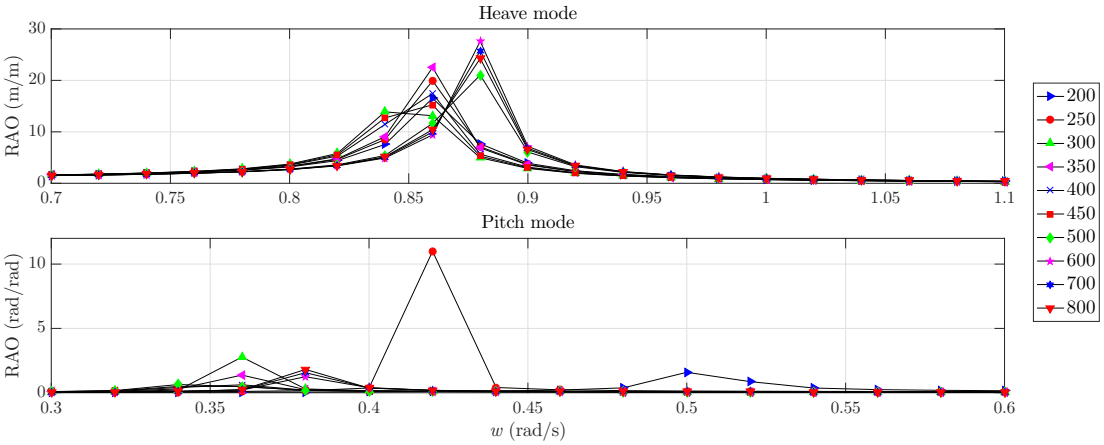

Figure 5.6: *Resonance peak for the heave and pitch modes for simulations carried out with different mesh element number.*

Figure 5.6 shows the RAO in heave and pitch modes within a range of frequencies for meshes with different element sizes. Since the modelled structure is the same, the element size influences only the total number of elements of the mesh. Hence, a mesh with a smaller element size will have a larger number of elements. For the heave mode, peak location convergence is found at 500 elements; peak amplitude convergence is observed after 700 elements. The same trend is identified for the pitch mode where both, peak location and amplitude convergence is reach for 600 elements. The surge mode it is not shown since no resonance is observed, due to the lack of a mooring system,

$D\ (m)$	$\omega_0\ (rad/s)$
3	1.32
4	1.22
5	1.08
6	0.9
7	0.8
8	0.66

Table 5.3: *Resonance Peak location for several structures with different main body diameters.*

which causes the response to tend to infinite for frequencies near zero. For all the stated above, being 700 the number of elements assuring convergence for both modes, it has been selected as the minimum number of elements for the modelling of the structure with the open-source code NEMOH.

Once the minimum number of elements has been found, a recursive analysis on the MoonWEC structure is carried out. The goal is to obtain the resonant state for an excitation period of $T = 6\ s$ which yields an angular frequency of $\omega = 1.05\ rad/s$. As the draft of the structure is fixed by the moonpool constraint, the shape and diameter of the structure are the only variables left to modify. The structure has a cone shape on top in order to guarantee a smooth transition in the free surface region. Also, a damping plate has been installed at the bottom to tune the phase of the device; this effect however, cannot be modelled in the frequency domain as the drag introduced by the plate is non-linear. Therefore, the diameter of the of the body is the parameter upon which the RAO sensitivity analysis has been executed. Table 5.3 reports the resonant response peak frequency in heave of several structures with different diameters.

The expected trend, according to equation (5.1), is observed in table 5.3. As the diameter increases so does the mass of the structure and thus, the natural frequency of the system decreases. The obvious choice according to the target frequency is the structure with a main body diameter of 5 m since, its natural frequency $\omega_0 = 1.08$ practically coincides with most frequent $\omega_p = 1.05$ for the selected locations of Alghero and Mazara del Vallo. Figure 5.7 illustrates both, the final dimension device and the definitive mesh used for the calculation of the hydrodynamic coefficients.

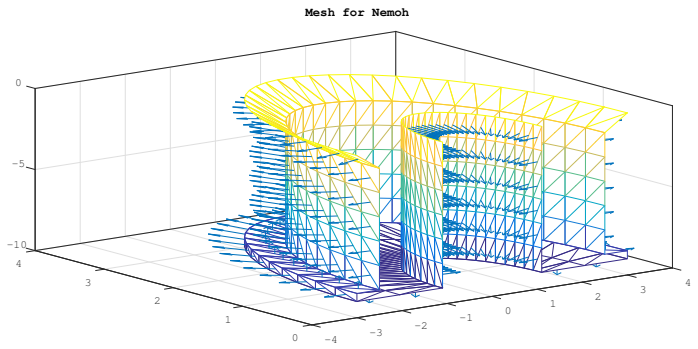

Figure 5.7: *Mesh of the modelled floating structure with the chosen element number and final dimensions.*

Finally, the hydrodynamic parameters of the selected structure are computed, then if substituted to equation (5.3) allow to obtain the response of all 6 DoFs of the device. Since this study is carried in the plane (x, z), the modes of sway, roll, and yaw have been neglected leaving only the surge, heave and pitch modes. Initially, in order to take into account the effect that the moonpool has on the floating structure, its inertia has been added to the floating structure's only in the surge and pitch DoFs. The heave mode has been left unaltered since the moonpool is free to move within the structure in the vertical direction. Figures 5.8 and 5.9 show the hydrodynamic coefficients and the RAOs of the MoonWEC, respectively.

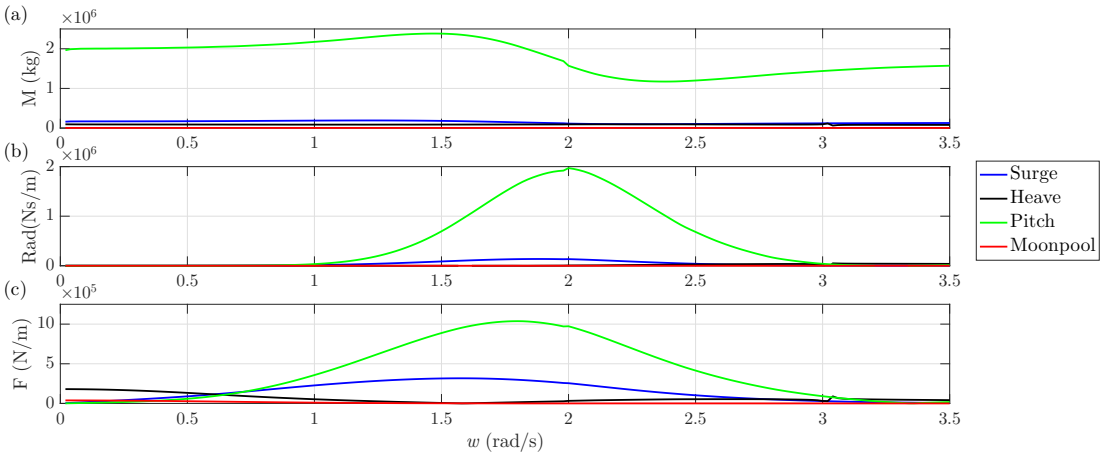

Figure 5.8: *Hydrodynamic coefficients vs. frequency obtained with the BEM approach for the different modelled DoFs. a) added mass coefficients, b) radiation damping coefficients and c) excitation force coefficients*

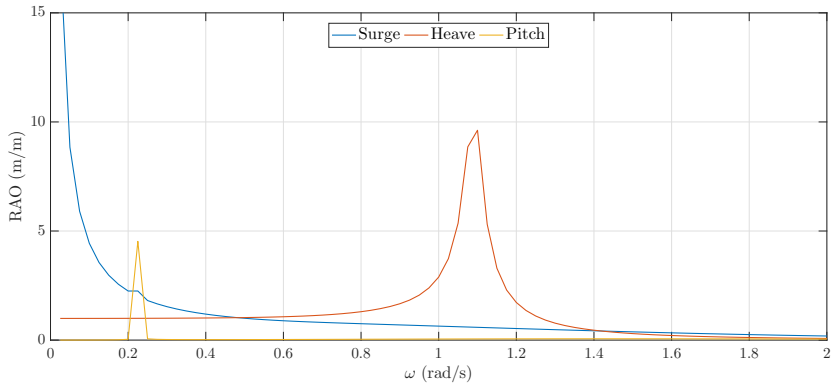

Figure 5.9: *Response amplitude operator of the MoonWEC for the studied DoFs.*

A very differentiated peak can be distinguished for every mode in figure 5.9. The resonance peak in heave mode coincides to the one highlighted in table 5.3, having an amplitude of ten metres for wave height meter. The pitch natural frequency is located at 0.2 rad/s, a relatively low frequency that suits the designing requirements; since at the selected sites, waves matching those frequencies are highly improbable. Unlike in the heave case; the resonance in pitch is an undesired effect which should be avoided. Not only for physical reasons, it is clear that the more the devices swings the less stable the whole WEC dynamics will be, but it should also be avoided for numerical reasons. During the model derivation (see chapter 4), the hypothesis of small angle has been used recursively for two main purposes: computational cost reduction and simplicity of equation derivation. The WEC behaviour in pitch will be a key aspect on the mooring system designing; whose goal will be, among others, to minimize the rotation in pitch. The surge mode shows an asymptotic resonant behaviour towards frequency 0. This is explained because no mooring system has been projected yet and therefore, in the absence of stiffness in the horizontal direction, the device tends to resonate at frequency zero, backing equation's (5.1) prediction.

The next step after concluding the frequency domain analysis is to switch to time domain in order to consider the non-linear effects. The general behaviour of the device should not vary significantly if the pre-design in the frequency domain has been executed properly.

5.2.1.2 Time domain

In the time domain, the determination of the natural frequency of the system for each DoF is achieved through the performance of the decay tests. These tests consist in giving

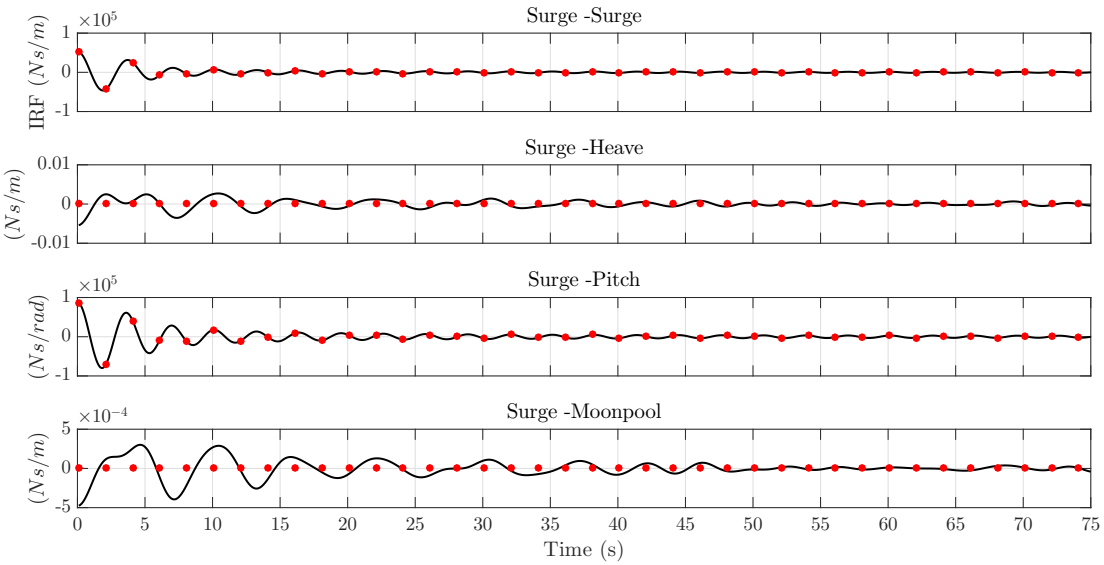

Figure 5.10: *Radiation impulse response functions for the surge mode. Analytical curve (solid line) and approximation with Prony's approach (dots).*

the system an initial state different than that of the equilibrium. Under no external influence, the system will tend to go back to the equilibrium state. This response, measured over the time, gives the information about the natural period of the system.

Before performing the tests a little numerical tuning is needed. As stated in section 2.2, in order to compute the radiation effect, the added mass at infinite frequency and the Impulse Response Function (IRF) need to be calculated from the frequency dependent hydrodynamic coefficients (figure 5.8). Subsequently, the IRF is approximated with the Prony's method. Prony's approximation relies upon two variables, the number of couple coefficients α_i and β_i and the memory time, which is the length of the IRF. The threshold of 2 orders of magnitude is set in order to establish the memory time. Furthermore, the possibility to neglect certain IRFs is also evaluated according to this threshold. Figures (5.10-5.13) show the computed IRFs and their approximation with the Prony's method for the surge, heave, pitch, moonpool and cross-influence DoFs, respectively:

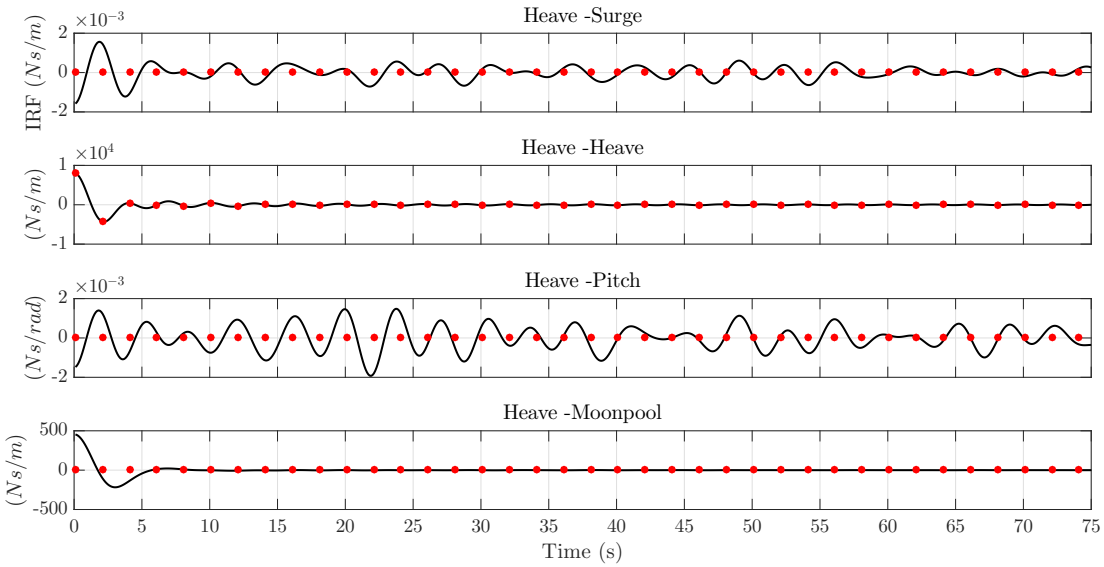

Figure 5.11: *Radiation impulse response functions for the heave mode. Analytical curve (solid line) and approximation with Prony's approach (dots).*

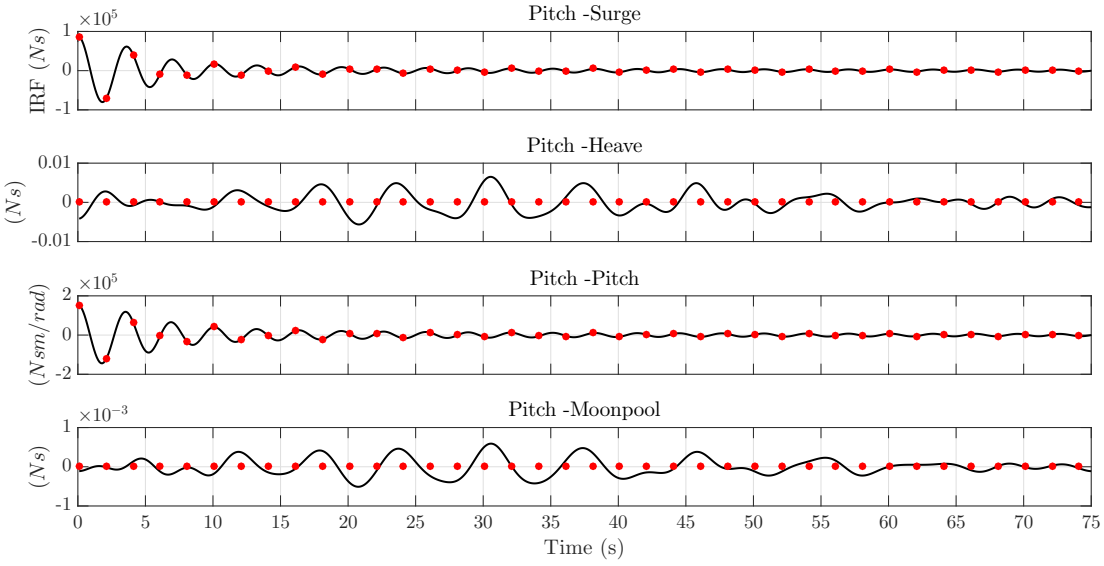

Figure 5.12: *Radiation impulse response functions for the pitch mode. Analytical curve (solid line) and approximation with Prony's approach (dots).*

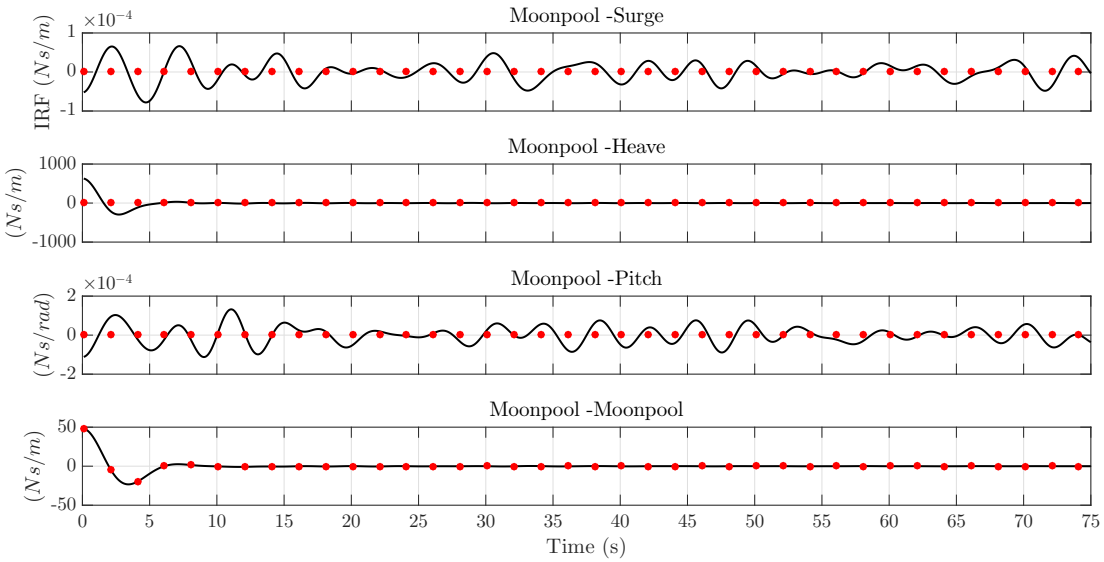

Figure 5.13: *Radiation impulse response functions for the moonpool DoF. Analytical curve (solid line) and approximation with Prony's approach (dots).*

Figures 5.10-5.10 show a very good agreement between the actual curve an its approximation. The Prony's method has been applied using 6 couples of fitting parameters α_i and β_i (see section 4.1.3.2). The resulting memory time, which fulfils the requirement stated in the previous paragraph, is $75(s)$. After this time all the modelled impulse response function have been damped by at least two orders of magnitude. However, not all the radiation IRF have been modelled; some crossed-modes have really reduced impact on the general structure behaviour since they are up to 8 orders of magnitude smaller than their counterparts and therefore, they have been neglected. No relevant interaction is found between: surge-heave modes, heave-pitch modes, moonpool-surge modes and moonpool-pitch, which makes a total of 8 neglected interactions, this number times 6 times 2 results in 96 dimensions saved in the numerical solver.

Having tuned the numerical model, the time domain model is ready and the decay tests can be carried out.

Decay test In this case no external influence means no wave. The chosen initial state of the device is $IS = (x_0, z_0, \theta_0) = (0, -1, -0.15)$ using the SI units. Note that null initial displacement has been set for the horizontal dimension. It is meaningless to test the surge mode when no mooring system has been introduced, since the device won't have a reaction force aiming to bring it back to the equilibrium position. The dynamic response over time of the system is shown in figure 5.14 for the modelled DoFs.

By carrying a Fourier analysis of the response over time the natural frequencies of the system are found, results are reported in figure 5.15.

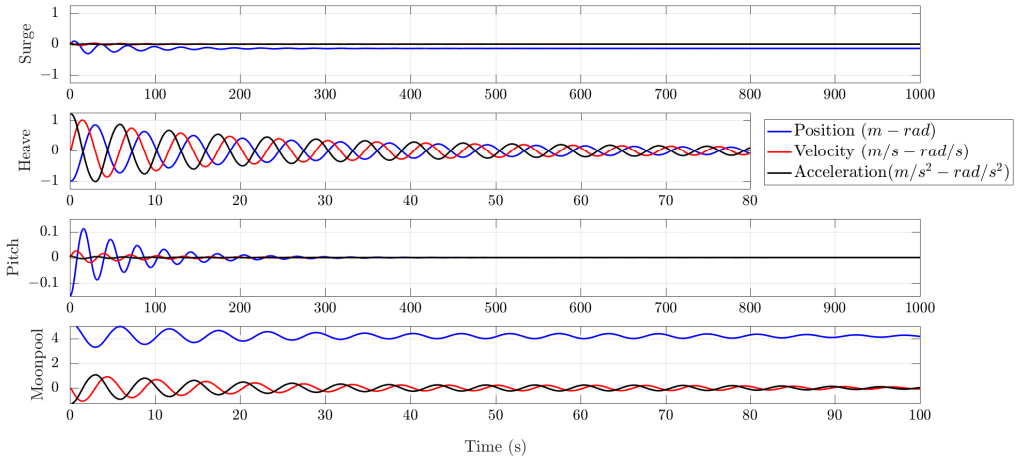

Figure 5.14: *Decay test results time series of the MoonWEC for the studied modes.*

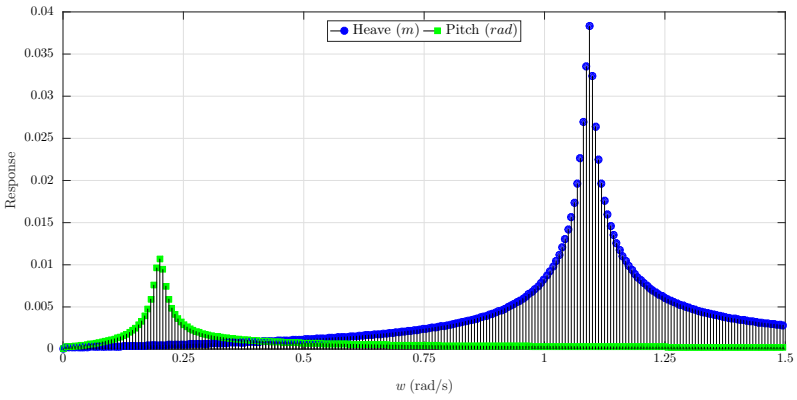

Figure 5.15: *Frequency domain response of the decay test of the MoonWEC for the studied modes.*

No anomalies are observed in figure 5.14, the heave and pitch modes show symmetrical oscillations damped at different rates. The moonpool has an offset of the mean oscillatory position. This shift has been introduced to express that the results for the moonpool are obtained at its free water surface, as opposed to the results of the floating structure which are computed at its centre of gravity. Actually, the observed moonpool dynamics are the same of the heave mode but in reversed direction. This makes sense as the computed coordinate of the model is the relative motion between the structure

and the water in the moonpol (see section 4.1.4.3). Hence, having no external input the water inside the moonpool remains practically still and thus, moving almost oppositely to the floating structure. The surge mode shows small oscillations, which are the result of the cross radiation effect surge-pitch (see figure 5.12). Finally, it assumes a resting position different than zero confirming the lack of a mooring system.

The results of the decay tests in the frequency domain, shown in figure 5.15, reveal the natural frequencies of the system. These, show very good agreement with the frequency domain tests in the case of the heave and moonpool modes, 1.1 (rad/s). This implies that the non-linearities for these modes have little effect under regular conditions. The pitch mode also shows the peak in exact correspondence to the frequency domain tests, 0.2 (rad/s). Such frequency corresponds to a very long wave, practically at the limit of the linear wave theory and despite being far from the wave climate at Alghero and Mazara, it is worth a more thorough study since sea states can contain wave components with these frequencies. Thereby, for survivability the dynamics of the device at that particular frequency must be studied.

Decay tests are very useful for the natural period determination. However, the extent of the system response can not be fully assessed with it due to the lack of forcing input. To such purpose the forced oscillation tests are carried out.

Forced Oscillations The forced oscillation test consists in forcing the device with monochromatic waves to analyse its response. There are three regions of interest, which are determined according to the natural periods obtained in the decay tests. The first region, hereinafter called the sub-resonating region, is defined by a higher forcing frequency than the natural frequency of the system, where the amplification factor, defined as the ratio between the response amplitude and the forcing amplitude, is smaller than one. The second region is the resonating region, found for forcing frequencies similar to the natural frequency. The amplification factor for that region is supposed to be greater than one. Lastly, the third region, given by small forcing frequencies compared to the natural frequency, is referred to as the over-resonating region. The response of the system should adapt to the amplitude of the forcing, resulting in an amplification factor around one. This type of response is also known as static response. However, the damping of the system could change this pattern as for a highly damped systems the response can always tend to zero as the input energy is very rapidly dissipated. In order to make a useful comparison of what explained above, in the frequency domain charts all amplitudes have been non-dimensionalised according to the ruling wave property

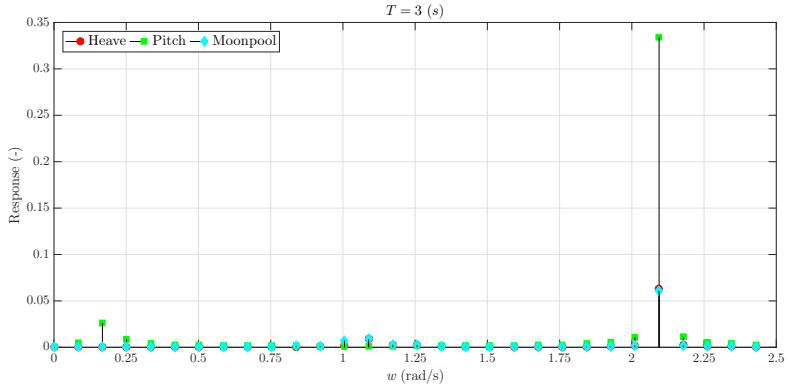

Figure 5.17: *Frequency domain response of the MoonWEC response under the influence of a monochromatic wave of period $T = 3$ s, for the studied modes.*

for each mode. That is, wave amplitude A for heave and moonpool modes and wave steepness $s = H/\lambda$ for pitch mode.

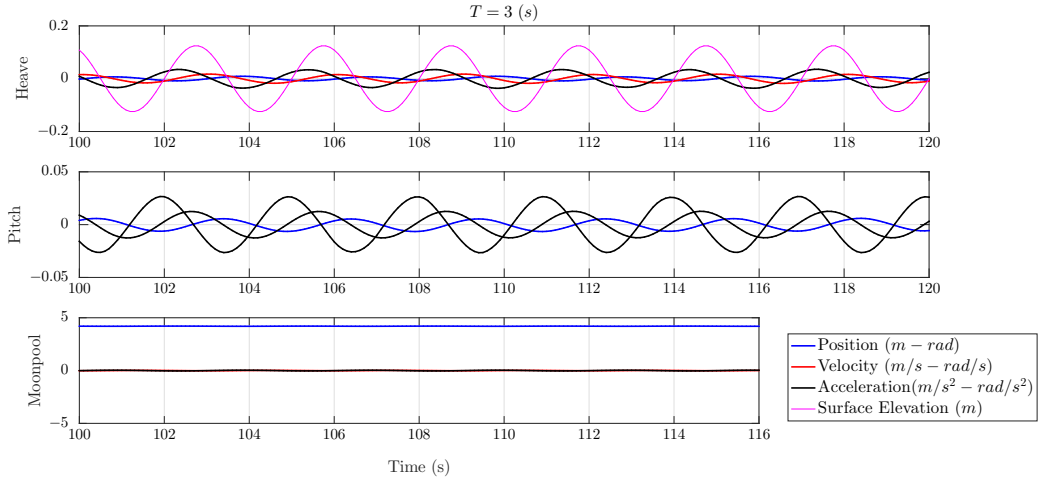

Figure 5.16: *Time series of the MoonWEC response under the influence of a monochromatic wave of period $T = 3$ s, for the studied modes.*

The response of the device for an input wave of $T = 3\ s$ follows the expected behaviour, the system oscillates reacting to the wave perturbation. Figure 5.16 shows a fragment of the entire time series where the device has reached the steady state. In figure 5.17, this response is clearly observed through a predominant peak in every mode for the excitation frequency. The fact that all the response amplitudes lie below the unit reveals the sub-resonating regime of the device, in total agreement to what

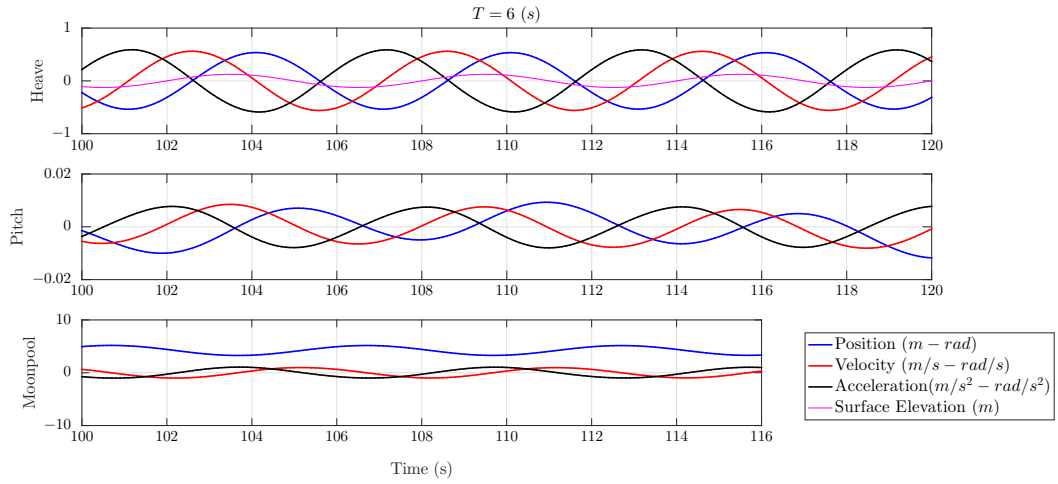

Figure 5.18: *Time series of the MoonWEC response under the influence of a monochromatic wave of period $T = 6$ s, for the studied modes.*

stated in the previous paragraph, as the excitation frequency is higher than the natural frequencies of the system. Besides, some residual harmonics are detected around the natural frequencies of the system. These are introduced by the non-linear behaviour of the system.

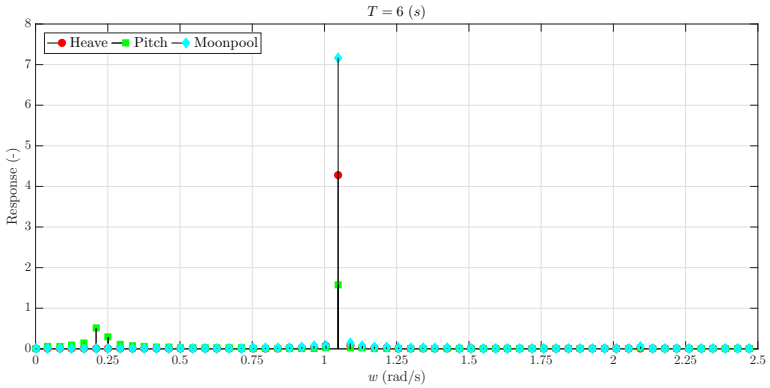

Figure 5.19: *Frequency domain response of the MoonWEC response under the influence of a monochromatic wave of period $T = 6$ s, for the studied modes.*

Figure 5.19 clearly identifies the resonant state of the device for the heave mode and the moonpool. The amplification for the heave mode and moonpool are around 4.5 and 7, respectively. Surprisingly, the pitch mode, which should remain in the sub-resonating region, has an amplification factor of 1.5. This may be due to the presence of the moon-

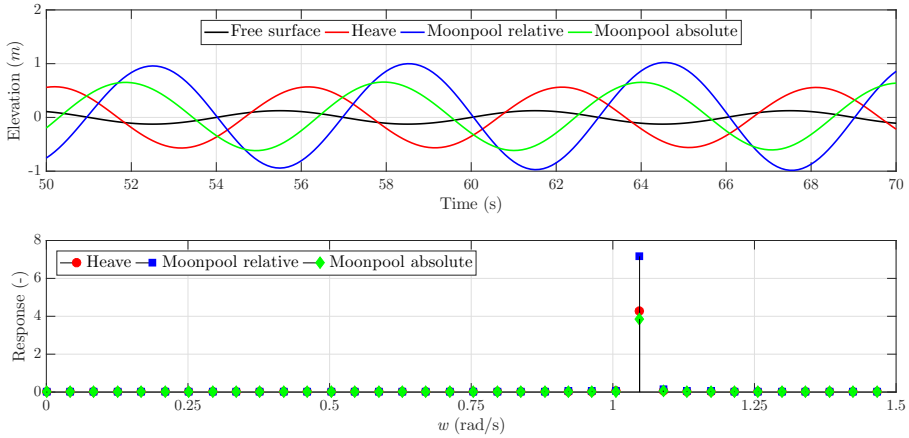

Figure 5.20: *Time and frequency domain MoonWEC response under the influence of a monochromatic wave of period $T = 6$ s, for the heave mode and moonpool absolute and relative displacements.*

pool, which introduces an eccentricity of the system. Whereas the CoG of the floating structure is fixed, the position of the CoG of the moonpool varies in time, consequence of the deformable volume condition. Furthermore, the CoG of the structure has been lifted 30 *cm* in order to reduce the hydrostatic stiffness and bring the pitch natural frequency further apart from the most frequent wave climates. These conditions create a moving metacentre, which in turn, may originate a parametric instability, equivalent to the parametric roll effect butin pitch. Hence, resulting in a force and moment component which depend on this geometric characteristic, changing the dynamic behaviour of the pitch mode.

The fact that the amplification factor for the moonpool is higher than for the heave mode shows a lag between the the heave and the absolute moonpool response. Assuming that the amplitude of motion remains constant regardless its phase angle, if both modes were in perfect phase ($\delta = 0\ rad$), the moonpool relative response would be minimized. On the contrary, if both responses were completely out of phase ($\delta = \pi\ rad$), its relative response would be maximized. The phase of a floating body depends mainly on two parameters: its inertia and its damping dissipation. Very little action can be taken in order to modify the phase of the moonpool as its geometrical constrains do not allow significant modifications. The phase can be more easily tuned for the MoonWEC structure but just to a certain extent. Furthermore, there is always the risk of overdamping the structure, which would result in a loss of energy capturing capacity.

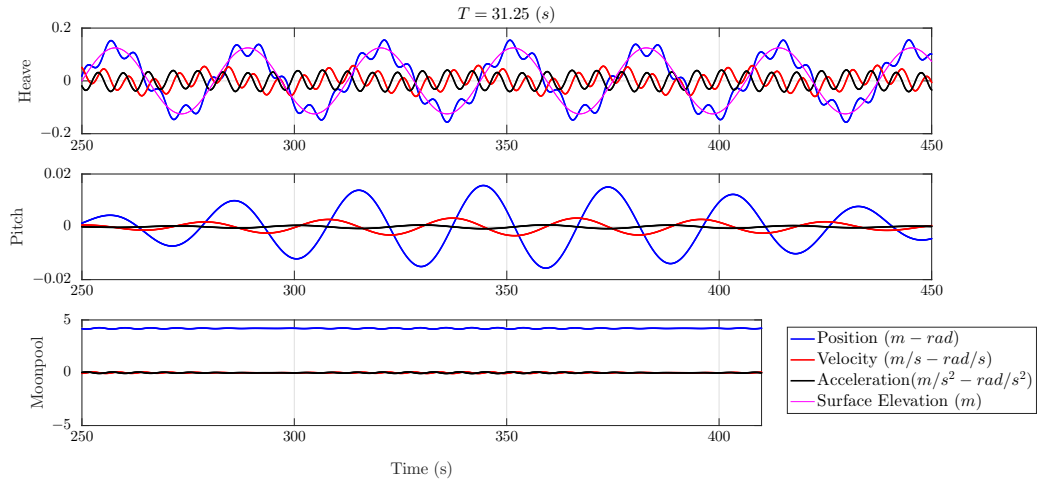

Figure 5.21: *Time series of the MoonWEC response under the influence of a monochromatic wave of period $T = 19$ s, for the studied modes.*

In figure 5.20 the heave displacement and the absolute and relative (to the structure) moonpool displacements are plotted. After performing the phase analysis of the curves with respect to the free surface; the delays found for the structure, the absolute and relative displacements of the moonpool are respectively: $\delta_h = 38.3$ °, $\delta_{Ma} = 151.8$ °and $\delta_{Mr} = 185.9$ °. That makes a relative delay between the structure and the relative motion of the moonpool of $\delta_r = \delta_{Mr} - \delta_h = 147.6°$. The only way to increase this delay this delay would be to reduce the structure delay. However, this is very difficult to accomplish and does not guarantee that the relative amplitude would be higher. The actual values are already satisfying as the moonpool relative amplitudes doubles the absolute one and it is around 60% higher than the structure amplitude.

The test of the device response under the natural period in pitch is shown in figures 5.21 and 5.22. The resonance amplitude factor is 27. Reason for that is the low damping accounting this mode for small frequencies, see figure 5.8. This could be a potential critical factor for the device survivability which needs further investigation. The rest of the modes behave as expected, the heave mode switches to the over-resonating region showing a static response. Also some harmonics can be observed in heave at its natural frequencies.

Irregular wave behaviour The final verification of the device performance is carried out through the analysis of the device response under the influence of an irregular sea state. Since the device is optimized for periods around $T = 6\ s$, a sea state with a

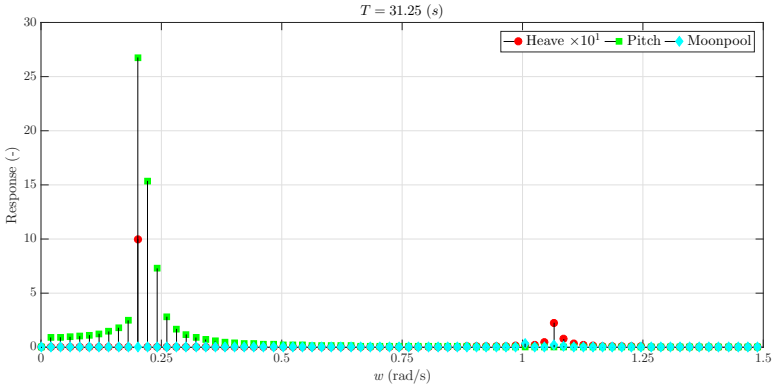

Figure 5.22: *Frequency domain response of the MoonWEC response under the influence of a monochromatic wave of period $T = 19$ s, for the studied modes.*

corresponding peak period of $T_P = 6\ s$ has been selected for this test. In such way, the overall response of the device can be assessed for a frequency range that assumes the most persistent occurrence and therefore, supposedly the most influential on the general device performance, including the energy production. Figure 5.23 plots the different studied modes behaviour under such sea state in the time domain, showing the typical behaviour of a floating structure under irregular wave forcing. Resonance amplification is damped due to wave energy spreading into several frequencies.

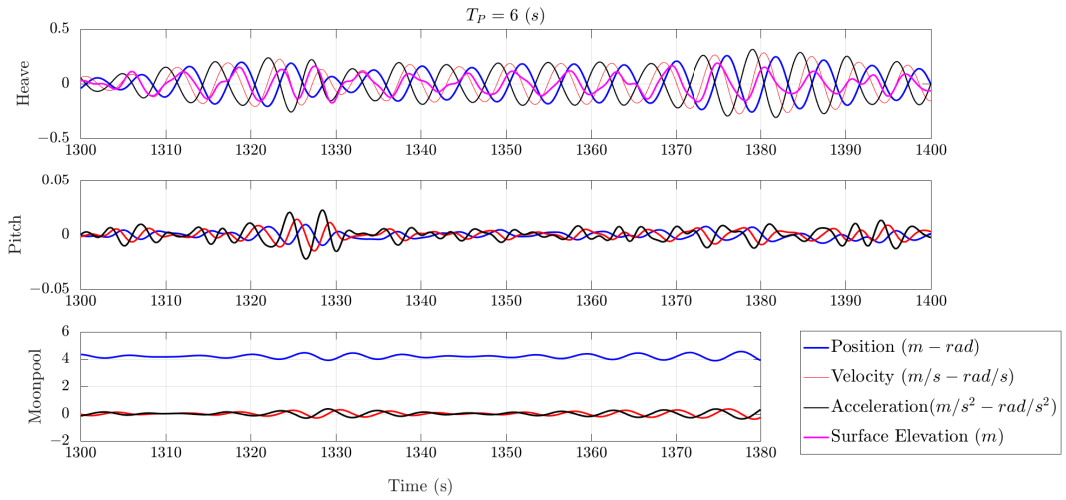

Figure 5.23: *Time series of the MoonWEC response under the influence of an irregular wave sea state with peak period $T_P = 6$ s, for the studied modes.*

In addition, for the frequency domain three more sea states have been simulated,

one with a smaller and two with larger T_P. So that the response of the system can be analysed for the different regions. Figure 5.24 plots the response to the four sea states in the non-dimensional form. This time, the normalizing values are the defining spectrum parameters of the sea state H_S and T_P.

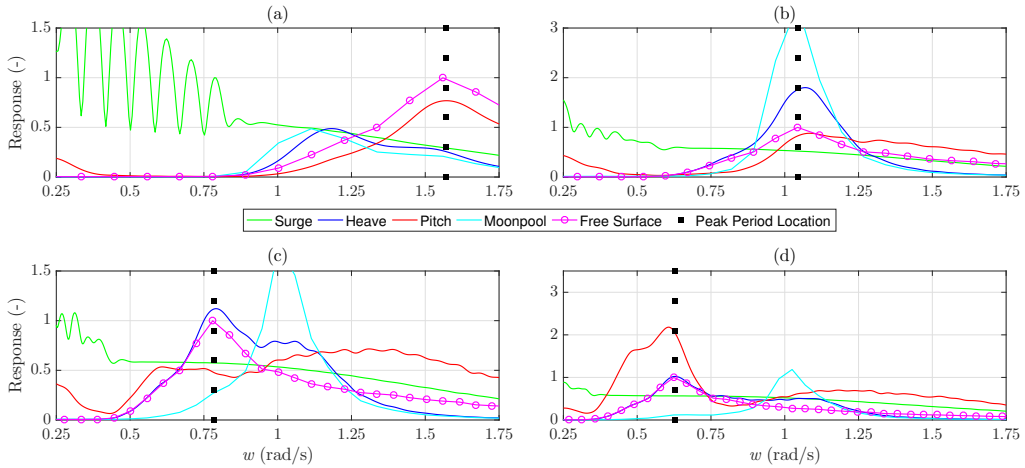

Figure 5.24: *Non-dimmensional Spectra of the MoonWEC studied modes response to irregular wave sea states. a) for peak period $T_P = 4$ s, b) for peak period $T_P = 6$ s, c) for peak period $T_P = 8$ s and d) for peak period $T_P = 10$ s.*

The frequency analysis shows the expected behaviour for the heave mode and the moonpool, resonance is observed independently from the sea state at the corresponding natural frequencies. For the first sea state, shown in figure 5.24.a), an incipient resonance is obtained since the majority of the exciting frequencies lie in the sub-resonating region. In figure 5.24.b), corresponding to the design sea state both resonances are maximized. However, its amplification factor is smaller than in the regular wave case, this is due to the spreading of energy throughout several frequencies, which in turn delivers a less concentrated response, lower at the peak but higher in the surrounding frequencies. The sea states corresponding to the over-resonating region, shown in figures 5.24.c and 5.24.d reveal that, despite losing relevance, resonance still persists for the tuning frequencies, specially for the moonpool relative motion. This attenuation increases with the difference between the current sea state peak period and the design sea state peak period. The pitch mode follows quite linearly the shape of the JONSWAP spectrum for all the simulated cases. Two major traits are observed; firstly, a subtle intensification of the response found for high frequencies, typically from the design period ($T = 6$

s) onwards. As they appear after the resonance of the moonpool, its origin can be attributed to high-order harmonic components deriving from the coupling between the moonpool and the floating structure. Secondly, although lying in the sub-resonating region a relatively high amplitude factor is obtained in figure 5.24.d). Besides the low radiation damping given at such frequencies (see figure 4.3), the parametric resonance effect could be taking in as the oscillation frequencies approach the double of the pitch natural frequency $2\omega_0^p$. Owing to the moonpool motion, the metacentric position of the devices does not have a constant location and therefore a parametric resonance is induced, resulting in an energy transfer from the moonpool to the pitch mode. This effect has already been observed in the regular wave cases and will be further documented in chapter 6.

5.2.2 Mooring System

As introduced in section 1.4.2 and thoroughly described in sections 2.5 and 4.1.3.3, the MoonWEC incorporates a CALM system to avoid drifting. Several characteristics can be modified in a CALM system in order to comply with the mooring specifications. Firstly, the number of lines has to be chosen. At first, being this a two-dimensional study on the plane (x, z), all the configurations bearing wave directionality are disregarded. As a result, a symmetric mooring system is designed where its symmetry axis is oriented vertically and passes through the CoG of the device. Then, the number of lines has to be set. Afterwards, the geometrical set up of the line is to be decided. Finally, the chain or wire constituting the line have to be defined.

For this study, configurations with different number of lines have been studied; one with two lines (one per side of the structure) and another with four lines (two per side of the structure). On the geometric layout of the line (see figure 5.25), only three parameters can be predefined, the total length of the line $l_T = l_{eff} + d$, the horizontal distance between the structure and the anchoring point l', and the vertical distance from the fair-lead to the sea bottom h. The remaining parameters become determined using the procedure described in section 4.1.3.3. The chain length is set in proportion to the water depth and it usually ranges from 3 to 6 times the depth, $3h \leq l_T \leq 6h$. In order to minimize the line weight, a total length of $l_T = 3h$ has been set, taking into account that the water depth is 50 m, then $l_T = 150$ m.

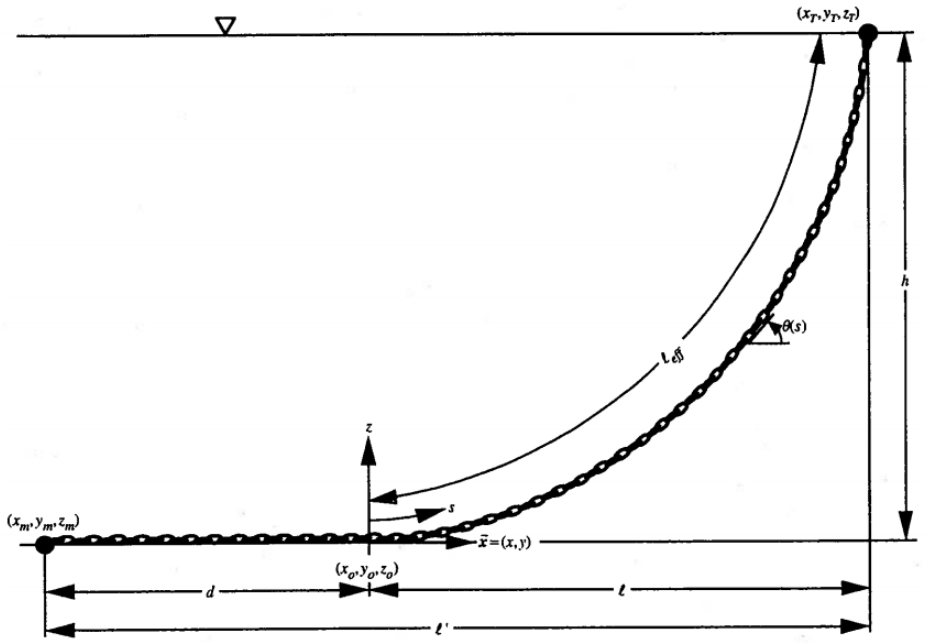

Figure 5.25: *Geometry of a deep water catenary line*

Six geometrical variants have been studied, four accounting with two lines and two composed by four lines. In turn, from the two-line variants, two are linked to the structure at its base and the other two at the CoG quote. The four-line variants are both binded to the structure in the same manner, one fair lead is placed at the base and the other at the edge of the top cone, coinciding with the still water level. Finally, two different anchoring points have been set, one at a horizontal distance $l' = 120\ m$ and the other at $l' = 135\ m$. Table 5.4 summarizes the main characteristics of the chosen mooring configurations, including the maximum displacements before the lines go slack and taut and figure 5.26 illustrates the different variants.

The installed mooring system needs to restrict the motions of structure but not excessively, particularly for the heave mode. Therefore, the choice between a chain or a wire is easily made opting by the wire, as those tend to be roughly ten times lighter than the chains and, as seen on section 4.1.3.3 the linear weight of the line is a key performance parameter since it influences the shape of the line and in turn, the horizontal force. Two main types of wires are used for offshore mooring, spiral strand and six strand. The former are recommended for a design life up to ten years. For longer design life spiral strand wires are usually chosen since they incorporate coatings and sheathings. For all the stated above, the spiral wire has been selected as the

#	# of lines	l' (m)	h (m)	l_t (m)	l_s (m)
1	2	120	41	24.3	11
2	2	135	41	9.3	26
3	2	120	45.8	22.8	15.8
4	2	135	45.8	7.8	30.8
5	4	L_l 120	41	24.3	11
		L_u 151.8	50	24.3	18.8
6	4	L_l 135	41	9.3	26
		L_u 166.7	50	9.3	33.8

Table 5.4: *Geometric properties of CALM system configurations.*

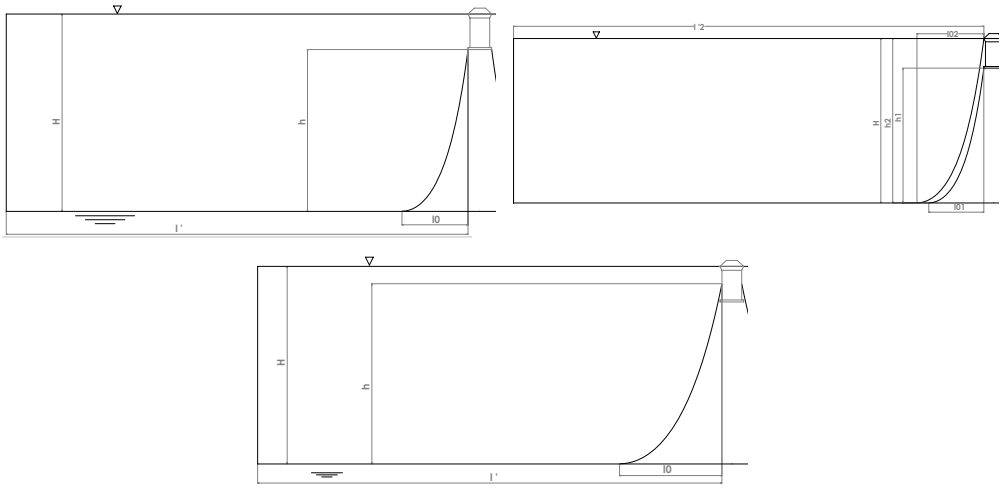

Figure 5.26: *Geometric CALM system layouts.*

#	Nominal diameter (mm)	MBL (kN)	Axial Stiffness (MN)	Nominal Weight (kg/m)		Submerged Nominal Weight (kg/m)	Nominal Steel Area (mm^2)	Sheathing Thickness (mm)
				Unsheathed	Sheathed			
1	76	5647	557	28.4	30.4	23.8	3377	8
2	82	6550	627	33.0	35.1	27.5	3917	8
3	90	7938	760	39.9	42.9	33.4	4747	10
4	95.5	8930	855	44.9	48.1	37.5	5341	10
5	102	10266	982	51.6	55.3	43.1	6139	11
6	108	11427	1093	57.5	61.3	48.0	6834	11
7	114	12775	1222	64.2	68.3	53.6	7640	11
8	121.5	14362	1353	72.2	76.5	59.7	8589	11
9	127	15722	1481	79.1	83.6	66.0	9403	11
10	133	17171	1599	86.8	91.5	72.4	10314	11
11	141	19180	1799	97.5	102.4	81.5	11609	11
12	146.5	20469	1940	105.1	110.2	87.7	12515	11
13	153	22070	2110	114.5	119.7	95.5	13616	11

Table 5.5: *Physical properties of spiral strand wire ropes (8).*

physical constituent of the line. Table 5.5, taken from the anchor manual (8), reports the properties of several spiral strand wire ropes. All the calculations for the moorings have been made relying on this data.

Aiming to minimize the total weight of the system, spiral strand wire nr. 1 in table 5.5 has been selected to model the properties of the lines. As long as the physical constraints of the system are respected this is the least invasive choice, since a reduced mooring system implies a minimization of the device response variation with respect to the unmoored structure. In order to asses the global device response, the same procedure as for the floating structure has been followed. Firstly, decay tests of the structure including the mooring system has been carried out. Subsequently, the natural periods have been tested with regular waves and finally, the global response under irregular waves has been studied. The same method has been used iteratively from mooring system nr. 1 to nr. 6 in table 5.4. Figures 5.27 - 5.36 correspond to the mooring system configuration nr. 1.

Figure 5.27 shows the classic behaviour of a decay test in heave and pitch. Both modes have a clear oscillation period and damping rate. The moonpool, as in the unmoored case, is plotted as the relative motion to the heave mode and thus, in the absence of waves behaves like the heave but in the opposite sense. The response in surge is less typical, the device tends to go back to the equilibrium position with an asymptotic trend. This is actually how the CALM system behaves due to the strong kinematic influence of the wire, which not only depends on its position, but also on its velocity and acceleration. Therefore, the chain damping and inertia slow down its response, even though being driven by the position. A second harmonic is also detected at the initial stage of the simulation, see figure 5.27. The coupling effect between the surge and pitch modes is responsible for these oscillations, partly due to the CALM

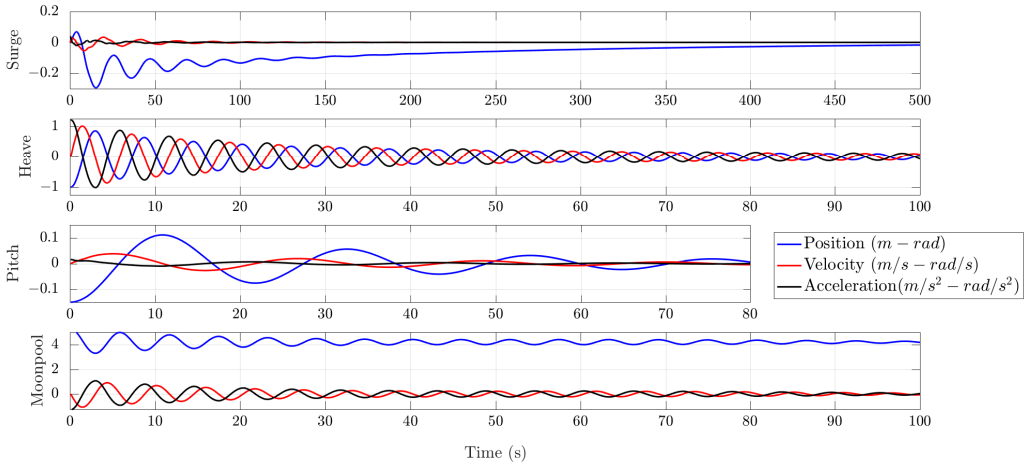

Figure 5.27: *Decay test time series of the MoonWEC for the studied modes. CALM configuration nr. 1 in table 5.4*

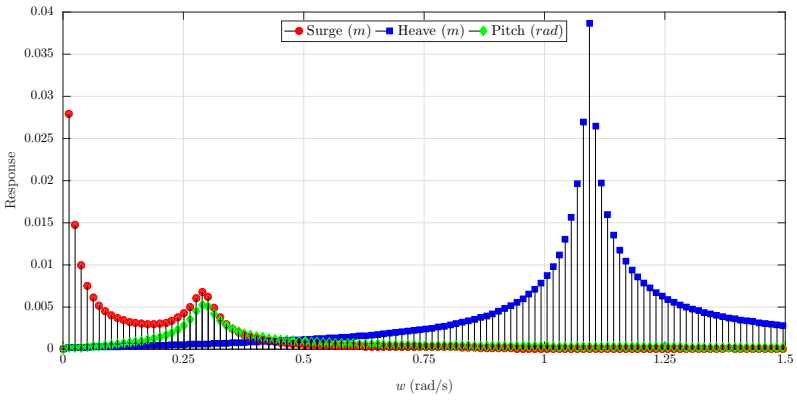

Figure 5.28: *Frequency domain response of the decay test of the MoonWEC for the studied modes.CALM configuration nr. 1 in table 5.4*

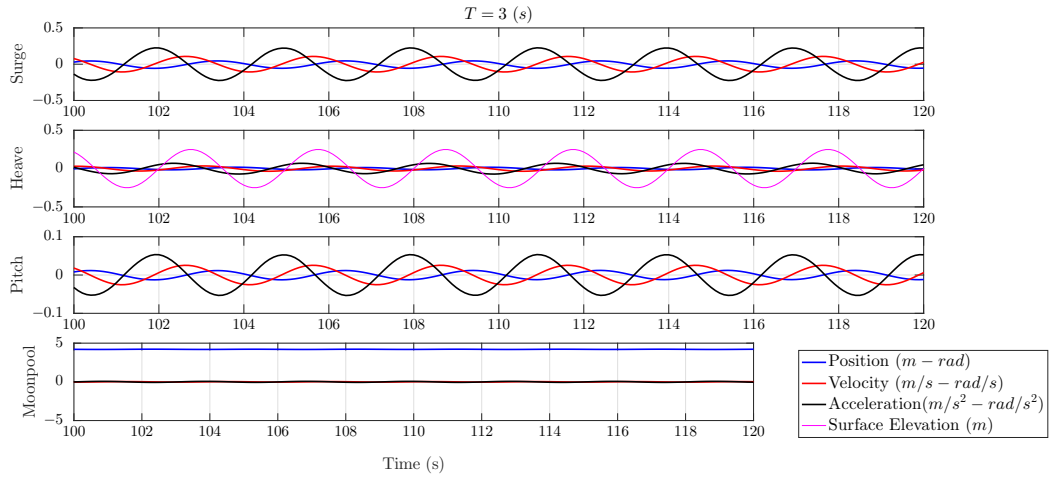

Figure 5.29: *Time series of the MoonWEC response under the influence of a monochromatic wave of period $T = 3$ s, for the studied modes. CALM configuration nr. 1 in table 5.4*

system but mostly owing to the radiation influence between these modes as seen in for the unmoored system in figure 5.14. Figure 5.28, showing the frequency analysis of the decay test, confirms that the heave mode is unaltered by the presence of the mooring system as no differences are appreciated from figure 5.15. The pitch does show a shift in its natural period, which is now set in $T_0^p = 21.75\ s$. As expected, in comparison with the unmoored device, its natural frequency is increased and its amplitude response is damped. The asymptotic behaviour in surge is expressed by the continuous component in the frequency domain and the coupling effect between the surge and pitch modes is also clearly captured by the frequency analysis.

Figure 5.29-5.34 show the response in the time and frequency domains for monochromatic waves inputs with periods $T = 3\ s$,$T = 6\ s$ and $T = 21.75\ s$, respectively. The latter two, correspond to the structures natural periods for the heave and pitch modes. For $T = 3\ s$, the structure shows a sub-resonating behaviour in all of its modes. For $T = 6\ s$, resonance is observed for the moonpool and the heave modes. Also, an amplified response of the pitch mode is detected, which reflects the coupling of the structure with the moonpool. The surge mode still behaves in a sub-resonating way. For $T = 21.75\ s$, a clear resonating behaviour is observed in pitch whereas in heave the over-resonating state has been reached and the moonpool relative motion has almost completely vanished since the moonpool now is totally in phase with the have mode, showing that the moonpool has reached the static response state as well. Furthermore, an harmonic component is shown for the the moonpool around its natural frequency.

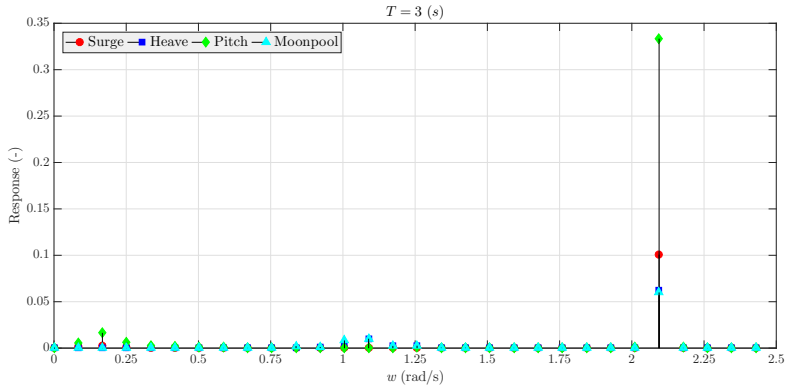

Figure 5.30: *Frequency domain response of the MoonWEC response under the influence of a monochromatic wave of period $T = 3$ s, for the studied modes. CALM configuration nr. 1 in table 5.4*

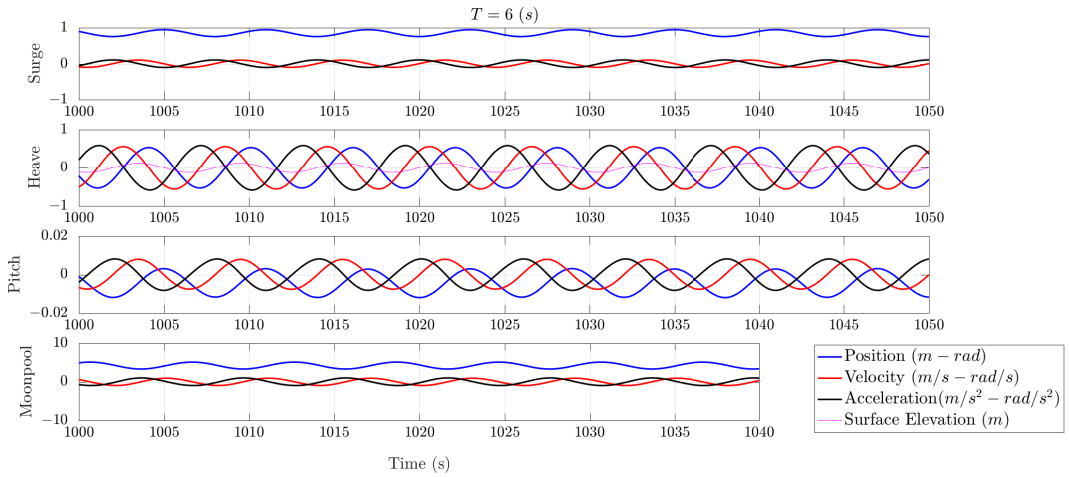

Figure 5.31: *Time series of the MoonWEC response under the influence of a monochromatic wave of period $T = 6$ s, for the studied modes. CALM configuration nr. 1 in table 5.4*

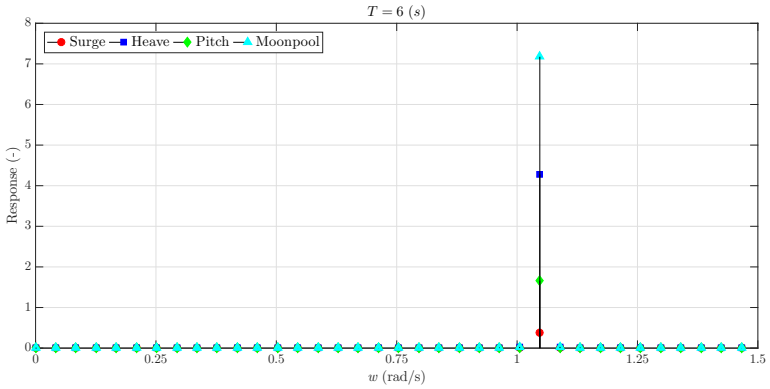

Figure 5.32: *Frequency domain response of the MoonWEC response under the influence of a monochromatic wave of period $T = 6$ s, for the studied modes. CALM configuration nr. 1 in table 5.4*

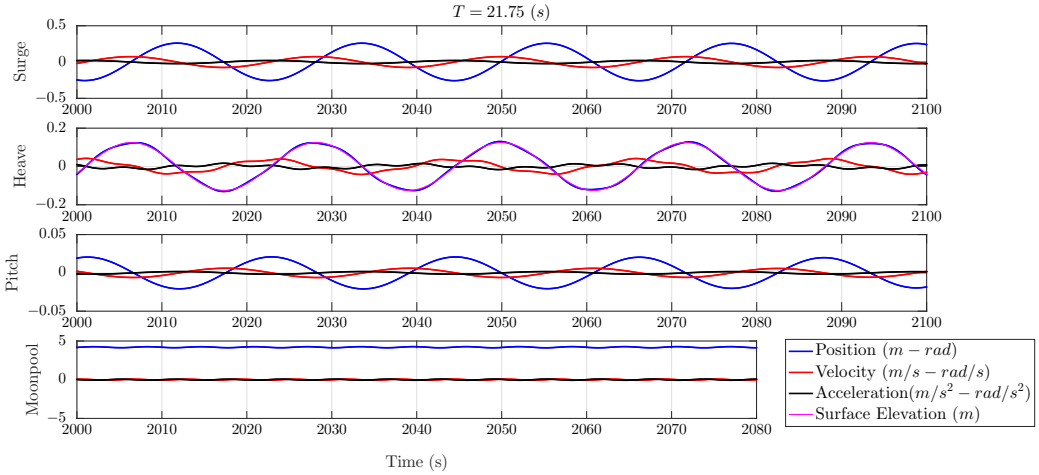

Figure 5.33: *Time series of the MoonWEC response under the influence of a monochromatic wave of period $T = 21.75$ s, for the studied modes. CALM configuration nr. 1 in table 5.4*

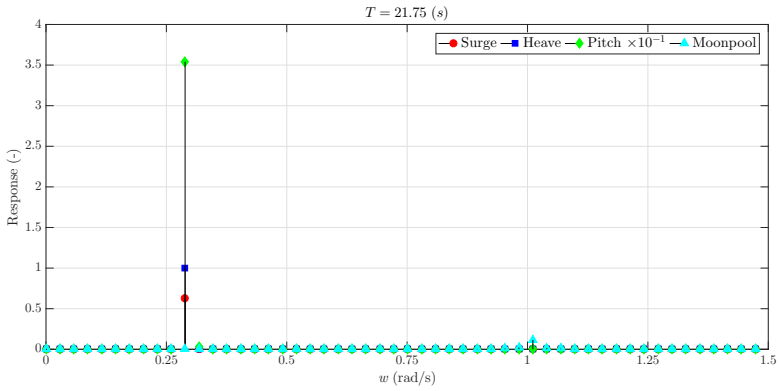

Figure 5.34: *Frequency domain response of the MoonWEC response under the influence of a monochromatic wave of period $T = 21.75$ s, for the studied modes. CALM configuration nr. 1 in table 5.4*

Figure 5.31 shows that when the moonpool is resonating, the mean oscillatory position in surge and pitch shifts. This is originally a consequence of the metacentric oscillations, which originate a cascade effect transferring first its energy to the pitch mode and then to the surge mode by means of the mooring system. This effect is better observed when the moonpool is resonating since the metacentre oscillations are maximized for that regime.

Finally, the device behaviour has been tested under the effect of irregular waves. As for the unmoored device, four sea states have been studied with peak periods $T_P = 4$ s, $T_P = 6$ s, $T_P = 8$ s, $T_P = 10$ s. This analysis allows to understand the transition of the device from the sub-resonating to the over-resonating state. Figure 5.35 shows the time series corresponding to the $T_P = 6$ s and 5.36 show the frequency responses in an non-dimmensional form. Non-dimmensionalisation has been carried out according to the wave spectrum defining parameters H_S and T_P.

Figure 5.36 shows that a slight reduction of the resonant response of the moonpool and the heave mode when compared to the unmoored device. Moreover, the pitch and surge mode show a relevant low frequency response. Denoting an energy transfer mainly from the moonpool to the mooring system. Futhermore, the pitch response in figure 5.36.d), is also larger than its unmoored counterpart, expressing the stiffness increase of the system due to the introduction of the mooring system.

Figures 5.37 - 5.41 correspond to the analysis of the CALM system nr. 2, whose lines have been pre-tensioned with respect the configuration nr. 1.

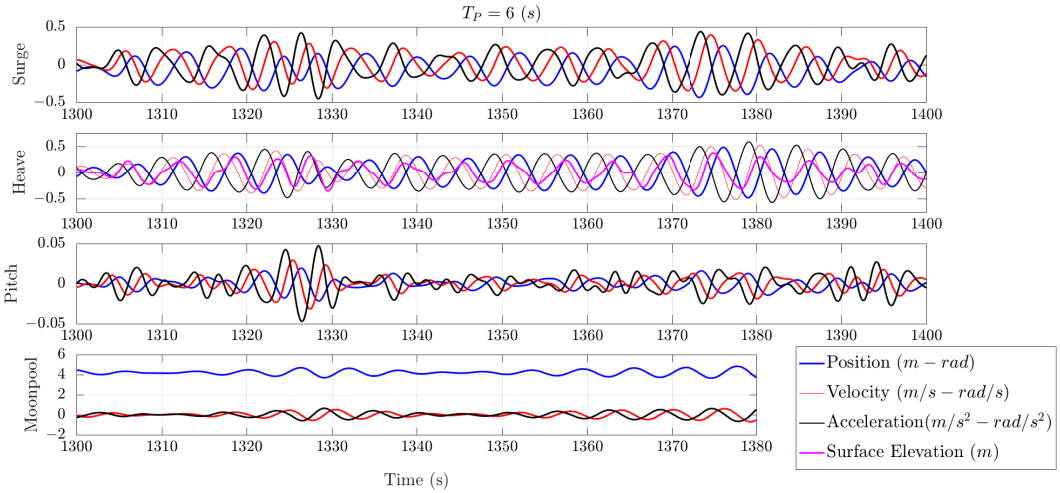

Figure 5.35: *Time series of the MoonWEC response under the influence of an irregular wave sea state with peak period $T_P = 6$ s, for the studied modes. MoonWEC configuration nr. 1*

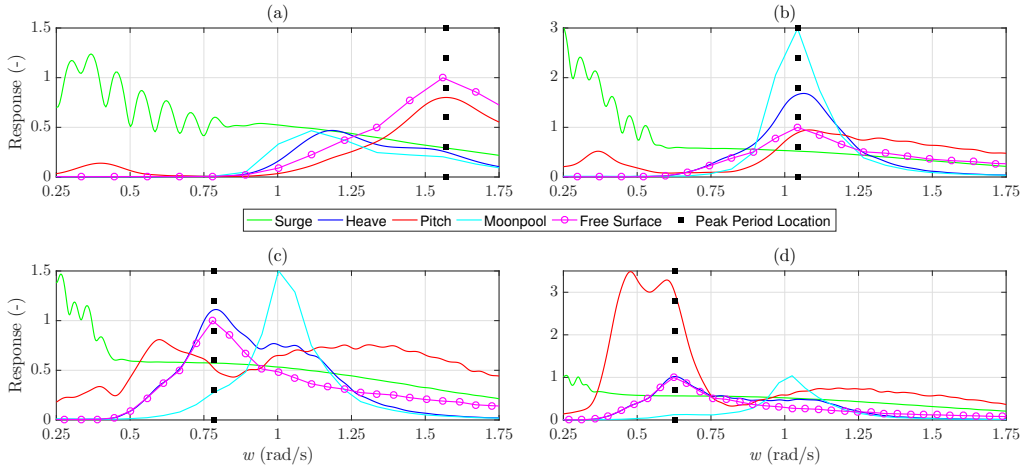

Figure 5.36: *Non-dimmensional Spectra of the MoonWEC studied modes response to irregular wave sea states. a) for peak period $T_P = 4$ s, b) for peak period $T_P = 6$ s, c) for peak period $T_P = 8$ s and d) for peak period $T_P = 10$ s. CALM configuration nr. 1.*

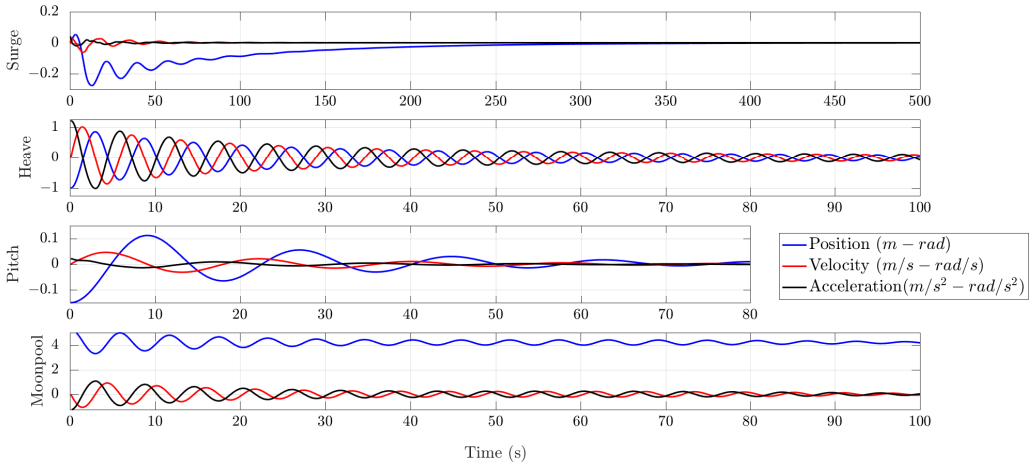

Figure 5.37: *Decay test time series of the MoonWEC for the studied modes. CALM configuration nr. 2*

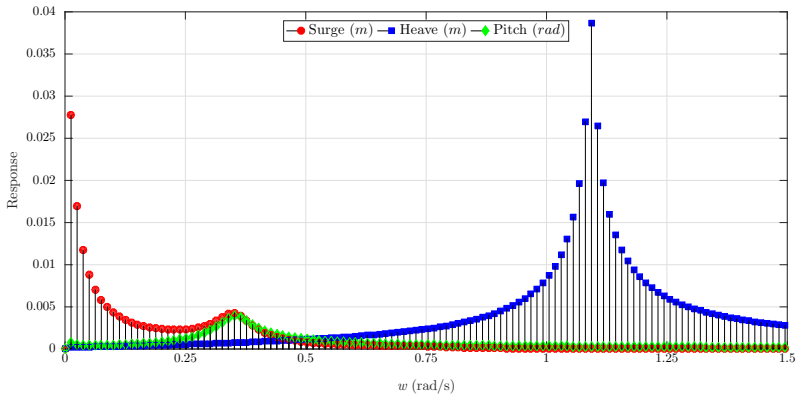

Figure 5.38: *Frequency domain response of the decay test of the MoonWEC for the studied modes. CALM configuration nr. 2.*

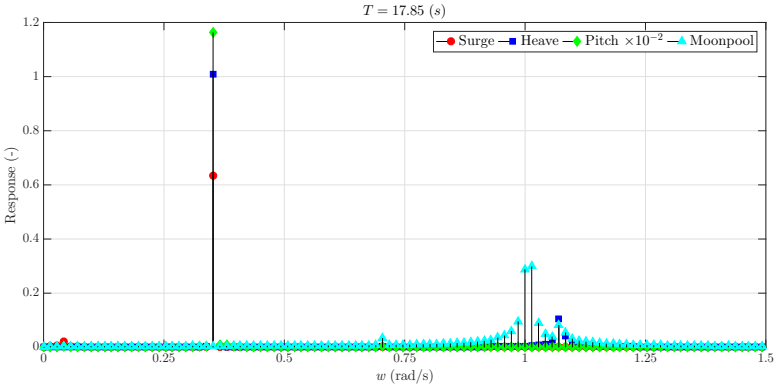

Figure 5.39: *Frequency domain response of the MoonWEC response under the influence of a monochromatic wave of period $T = 17.85$ s, for the studied modes. CALM configuration nr. 2*

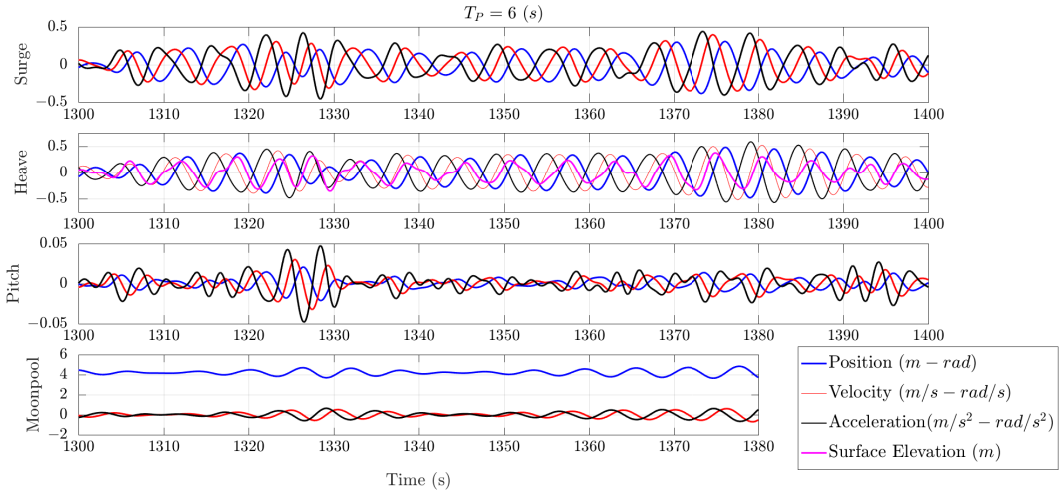

Figure 5.40: *Time series of the MoonWEC response under the influence of an irregular wave sea state with peak period $T_P = 6$ s, for the studied modes. CALM configuration nr. 2*

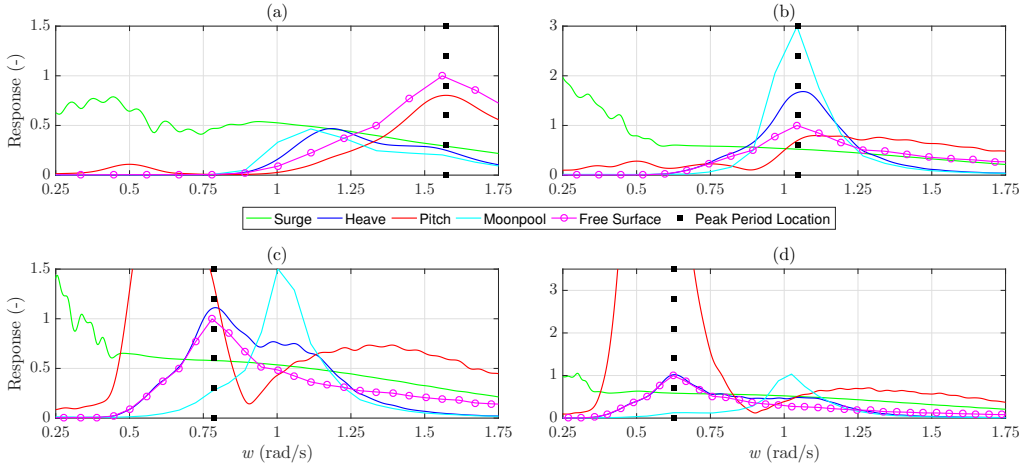

Figure 5.41: *Non-dimmensional Spectra of the MoonWEC studied modes response to irregular wave sea states. a) for peak period $T_P = 4$ s, b) for peak period $T_P = 6$ s, c) for peak period $T_P = 8$ s and d) for peak period $T_P = 10$ s. CALM configuration nr. 2*

This variant of the device presents a slight reduction of the pitch natural period, from $T_0^p = 21.75\ s$ to $T_0^p = 17.85\ s$, as shown in figure 5.38. The pre-tensioning of the lines causes an increase of the rigidity of the system which results in the natural period shift and in an additional decrease of the response for such mode in the decay tests. However, its amplification response is substantially enhanced for its natural frequency and the surrounding frequencies, as depicted by figures 5.39 and 5.41. On the other hand, the surge returns faster to the equilibrium in the decay tests (figure 5.37) and its oscillation shift is reduced (figures 5.40 and 5.41). The moonpool and heave mode do not present any variation with respect variant nr. 1. While the behaviour in surge can be qualified as more appropriate than in configuration nr. 1, the general increase of the response in pitch can pose a threat to the device survivability, as its natural frequency is not so distant from the stormy wave climates at the deployment locations.

In figures figures 5.42 - 5.46 the CALM system nr. 3 analysis is presented. This mooring system variant shifts the position of the fair-leads from the base of the device at its CoG quote while maintaining the pre-tensioning degree of variant nr. 1.

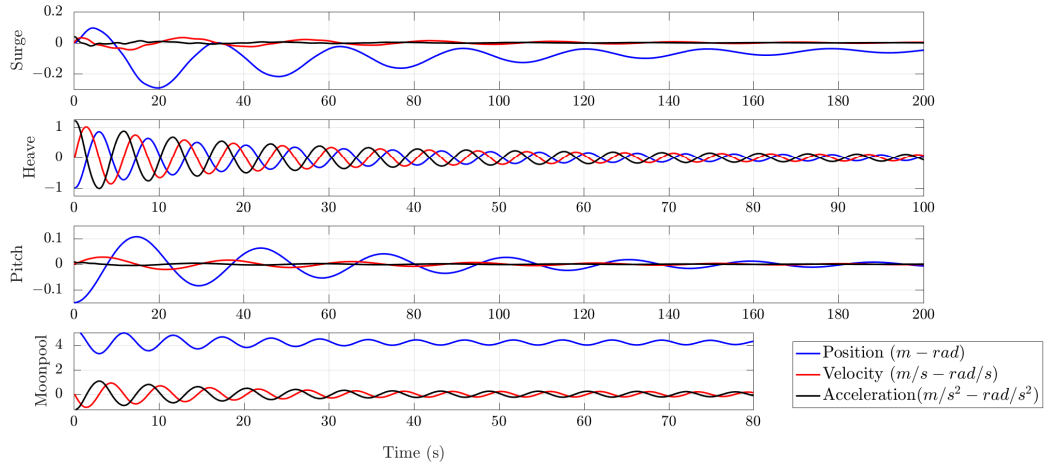

Figure 5.42: *Decay test time series of the MoonWEC for the studied modes. CALM configuration nr. 3.*

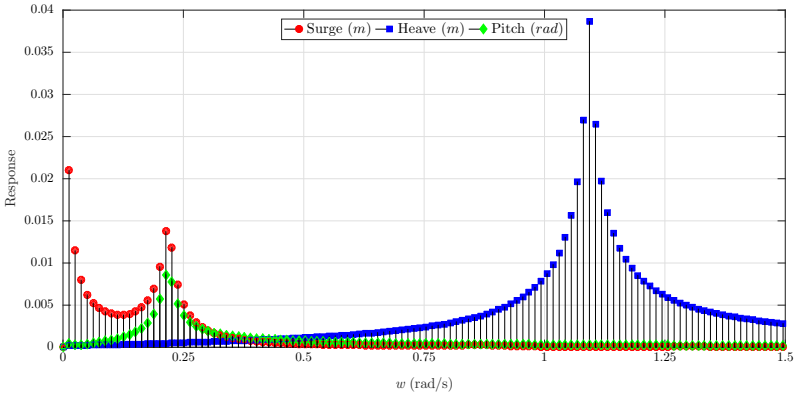

Figure 5.43: *Frequency domain response of the decay test of the MoonWEC for the studied modes. CALM configuration nr. 3.*

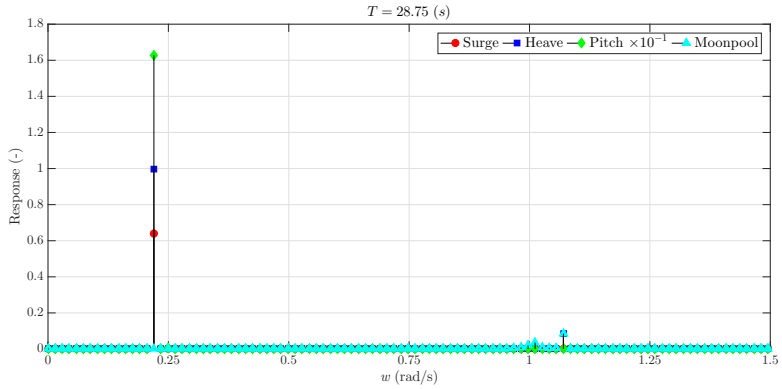

Figure 5.44: *Frequency domain response of the MoonWEC response under the influence of a monochromatic wave of period $T = 28.75$ s, for the studied modes. CALM configuration nr. 3.*

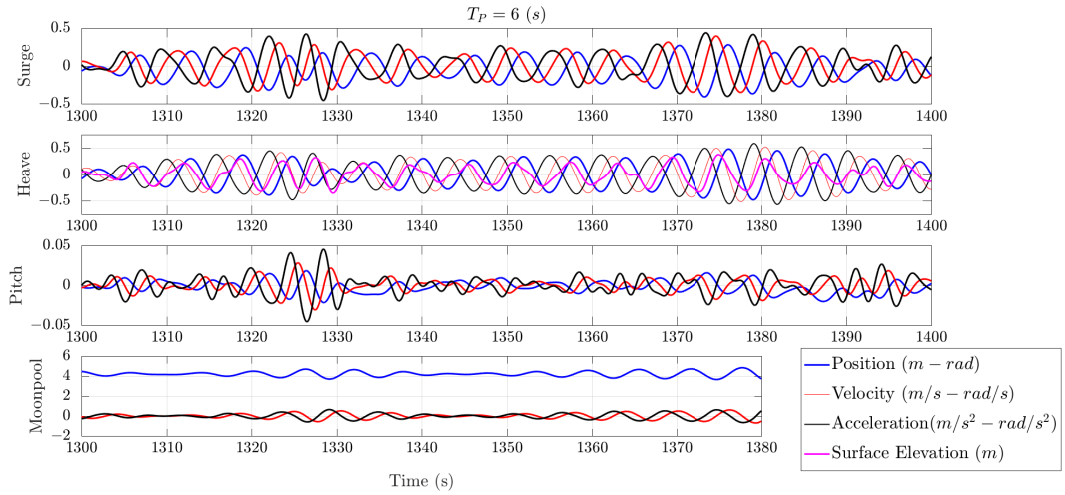

Figure 5.45: *Time series of the MoonWEC response under the influence of an irregular wave sea state with peak period $T_P = 6$ s, for the studied modes. CALM configuration nr. 3.*

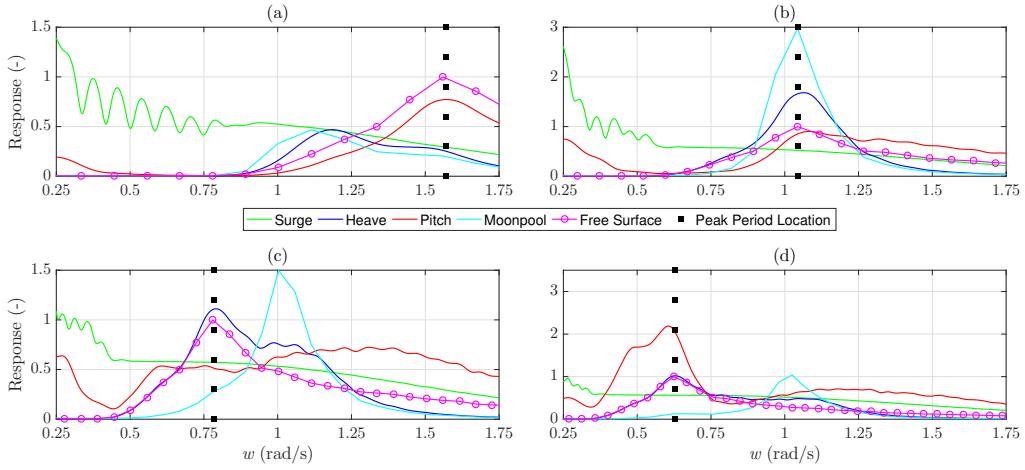

Figure 5.46: *Non-dimmensional Spectra of the MoonWEC studied modes response to irregular wave sea states. a) for peak period $T_P = 4$ s, b) for peak period $T_P = 6$ s, c) for peak period $T_P = 8$ s and d) for peak period $T_P = 10$ s. CALM configuration nr. 3.*

In figures 5.42 and 5.43 is revealed that the heave mode and the moonpool maintain the same response as in the unmoored device and the previous mooring configurations. For pitch mode, a minimal variation of the natural frequency is observed with respect to the device with no mooring, passing from $T_0^p = 31.25$ s to $T_0^p = 28.75$ s. Furhtermore, its amplification factor at the natural frequency for pitch (figure 5.44) is the lowest

amongst the studied variants. As for the other cases, the surge presents an offset in the oscillation centre; however, it is smaller than for the other tested mooring systems as shown in figure 5.45. Figure 5.46 also states that the pitch response for low frequencies is much more moderate than for the previous moorings, specially if compared to nr. 2. To sum up, until now CALM configuration nr. 3 is the mooring variant that shows a better performance. Working regimes for next scheme, variant nr. 4, are shown below in figures 5.47 - 5.52.

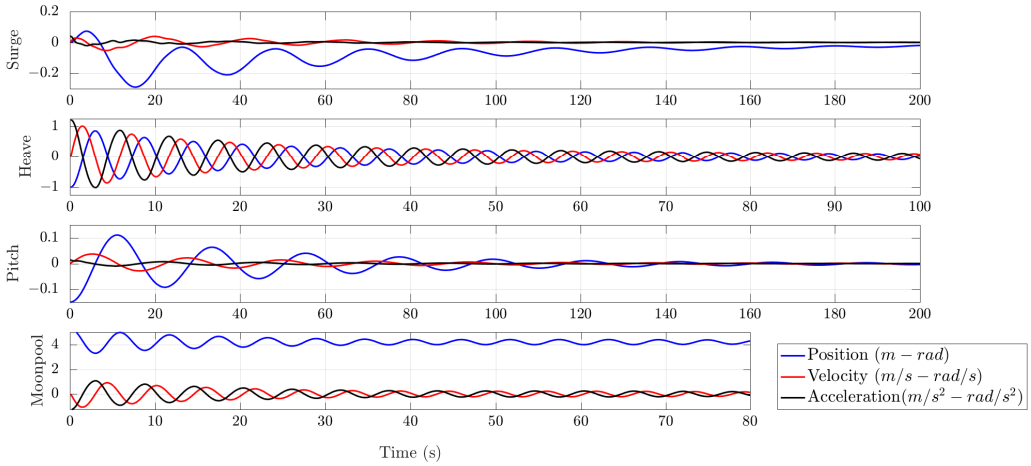

Figure 5.47: *Decay test time series of the MoonWEC for the studied modes. CALM configuration nr. 4.*

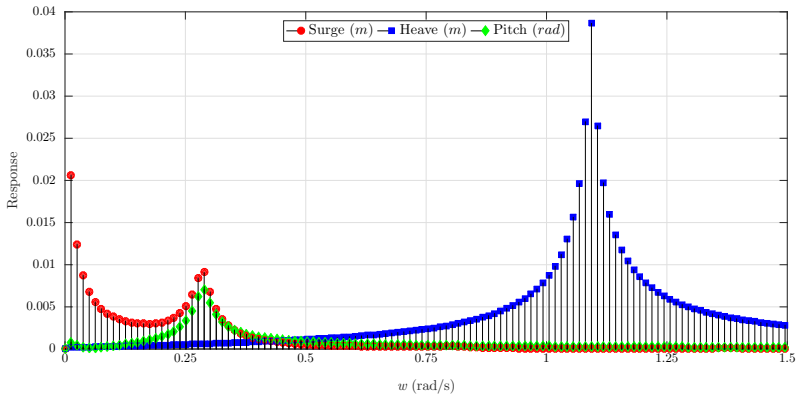

Figure 5.48: *Frequency domain response of the decay test of the MoonWEC for the studied modes. CALM configuration nr. 4.*

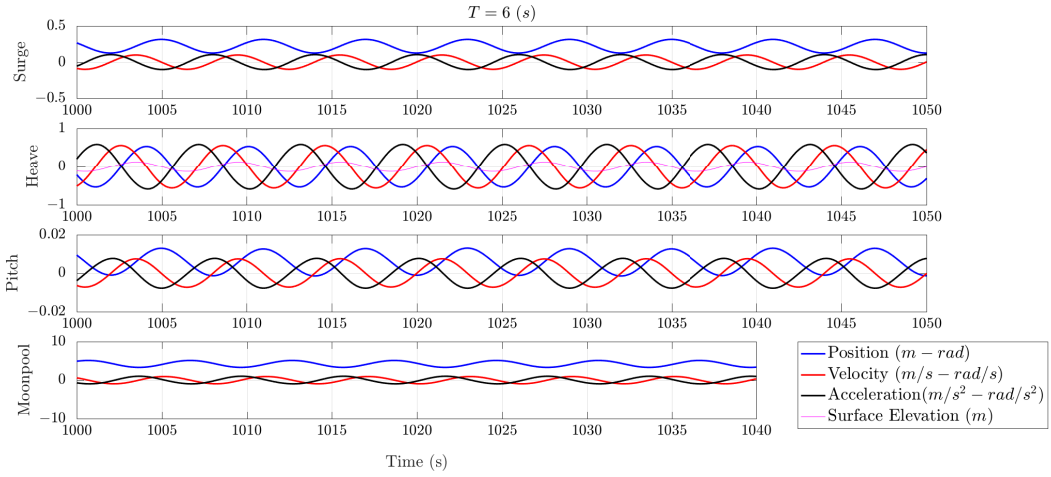

Figure 5.49: *Time series of the MoonWEC response under the influence of a monochromatic wave of period $T = 6$ s, for the studied modes. CALM configuration nr. 4.*

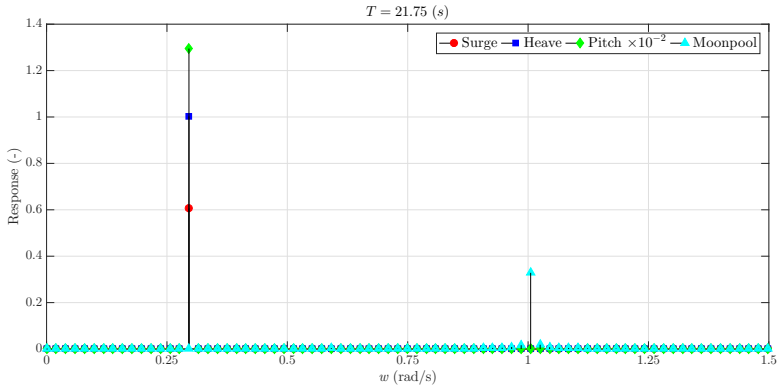

Figure 5.50: *Frequency domain response of the MoonWEC response under the influence of a monochromatic wave of period $T = 21$ s, for the studied modes. CALM configuration nr. 4.*

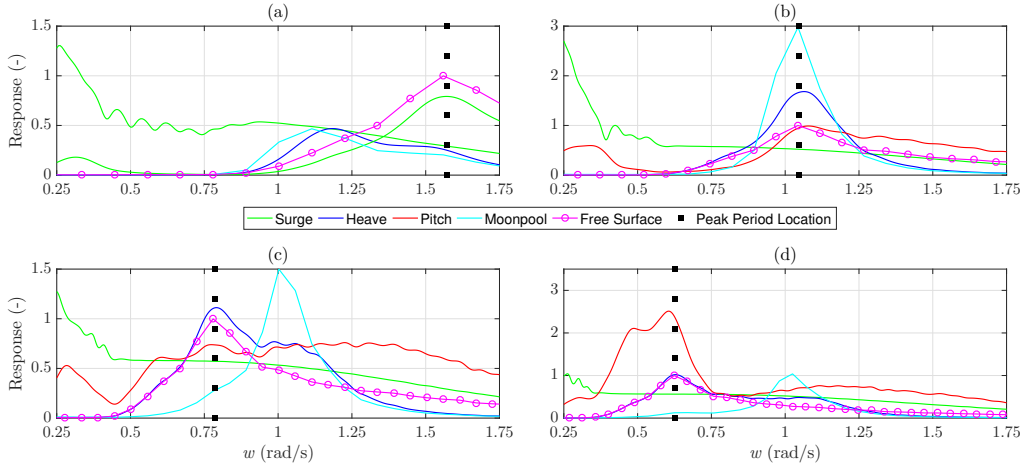

Figure 5.52: *Non-dimmensional Spectra of the MoonWEC studied modes response to irregular wave sea states. a) for peak period $T_P = 4$ s, b) for peak period $T_P = 6$ s, c) for peak period $T_P = 8$ s and d) for peak period $T_P = 10$ s. CALM configuration nr. 4.*

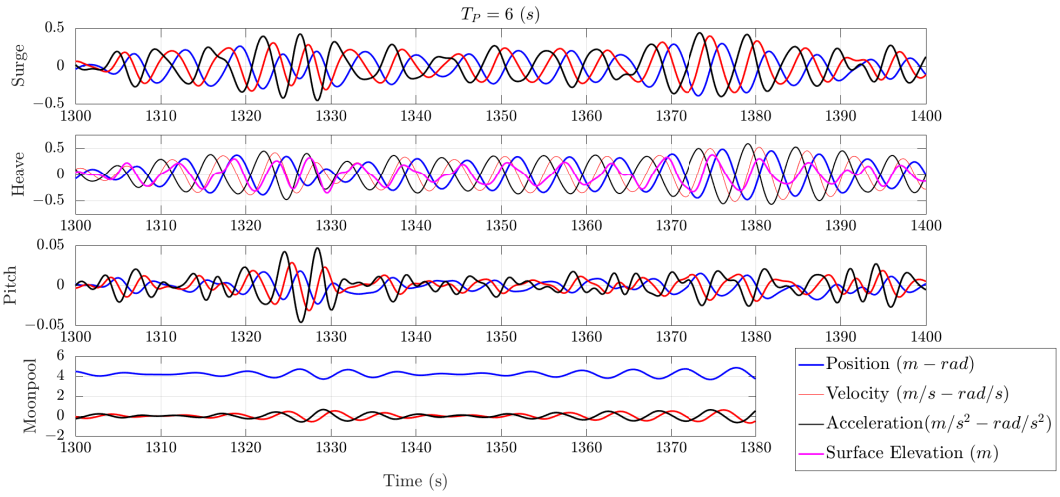

Figure 5.51: *Time series of the MoonWEC response under the influence of an irregular wave sea state with peak period $T_P = 6$ s, for the studied modes. CALM configuration nr. 4.*

As expected, the pitch natural frequency is increased additionally from the one given for variant nr. 3 due to the further pre-tensioning of the mooring lines, see figure 5.48. Moreover, the amplification factor for the natural period in pitch rockets by one order of magnitude with respect to configuration 3 (figure 5.50). On the contrary, its response for low frequencies is slightly reduced. On the surge mode, no relevant differences are

spotted other than a further reduction of the mean oscillation position appreciated in figure 5.51. The responses for the moonpool and for the heave mode remain invariable with respect to the other mooring layouts. Figures 5.53 - 5.56 display the analysis of CALM configuration nr. 5, in which two more lines are added at the top part of the structure, in an attempt to reduce the surge oscillations while keeping bounded the pitch motions.

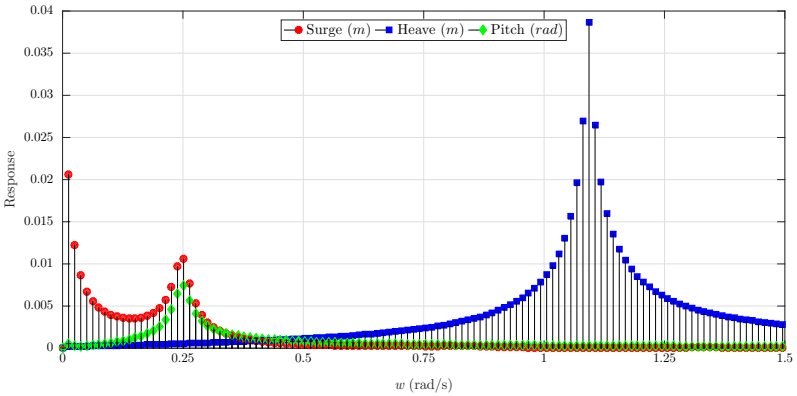

Figure 5.53: *Frequency domain response of the decay test of the MoonWEC for the studied modes. CALM configuration nr. 5.*

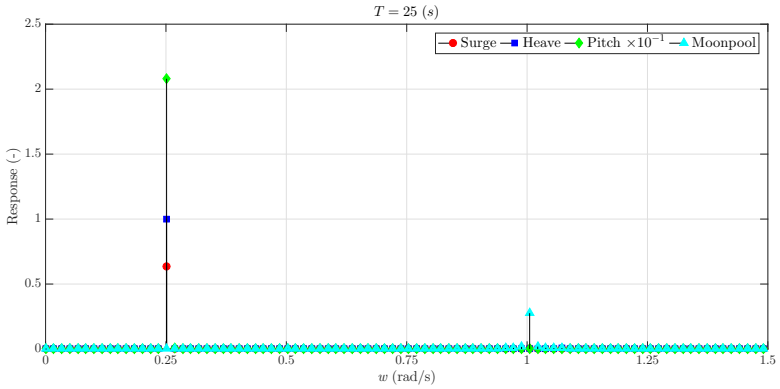

Figure 5.54: *Frequency domain response of the MoonWEC response under the influence of a monochromatic wave of period $T = 25$ s, for the studied modes. CALM configuration nr. 5.*

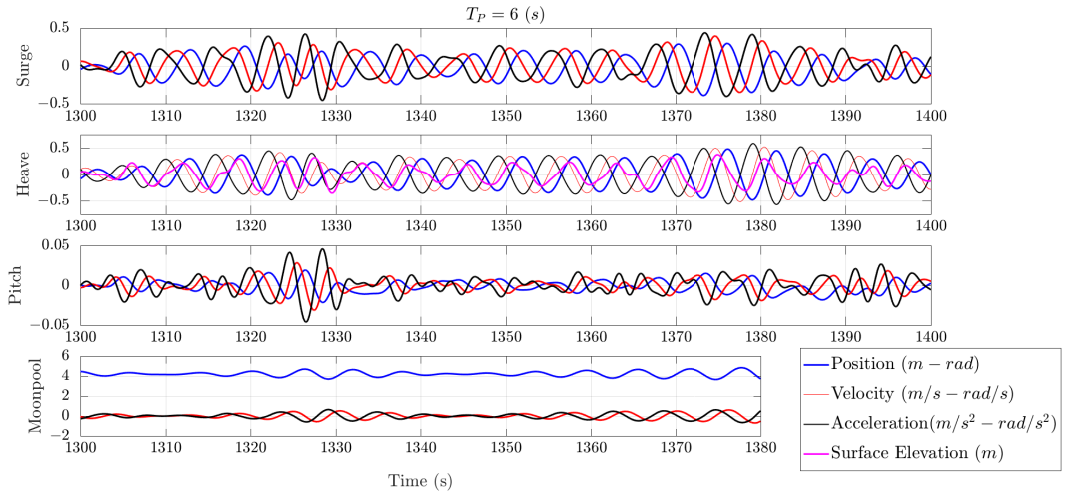

Figure 5.55: *Time series of the MoonWEC response under the influence of an irregular wave sea state with peak period $T_P = 6$ s, for the studied modes. CALM configuration nr. 5.*

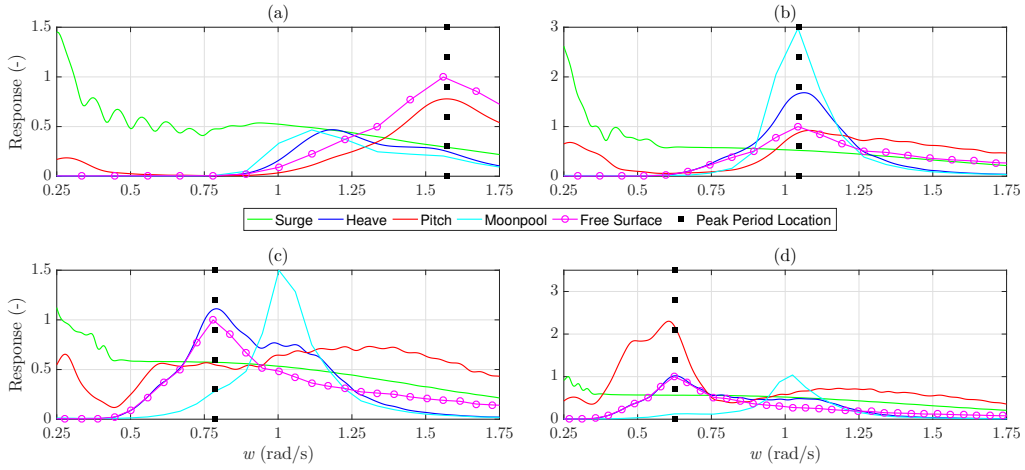

Figure 5.56: *Non-dimmensional Spectra of the MoonWEC studied modes response to irregular wave sea states. a) for peak period $T_P = 4$ s, b) for peak period $T_P = 6$ s, c) for peak period $T_P = 8$ s and d) for peak period $T_P = 10$ s. CALM configuration nr. 5.*

Coinciding with all of the previous schemes, the response of the moonpool and the structure in heave remains invariant. Its pitch natural period is $T_0^p = 25$ s (figure 5.53), being the second largest after variant nr. 3. Also, its amplification factor for that period remains relatively restrained (figue 5.54) and its response in low frequencies, as shown in figure 5.56, is practically identical to the configuration nr. 3. The mean oscillatory

position in surge is further reduced, although its difference from CALM system nr. 3 might not be considered substantial. FINALLY, the analysis of the last mooring system is presented in figures 5.57 - 5.60. In CALM scheme nr.6 the four mooring lines have been further pre-tensioned with respect to configuration nr. 5 seeking to utterly reduce the mean surge shift.

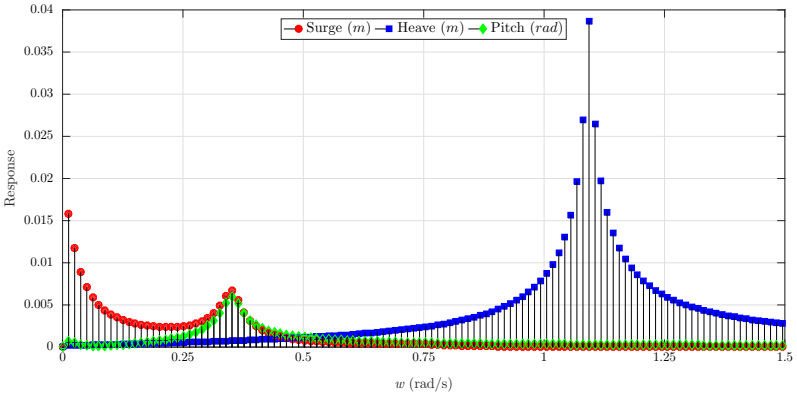

Figure 5.57: *Frequency domain response of the decay test of the MoonWEC for the studied modes. CALM configuration nr. 6.*

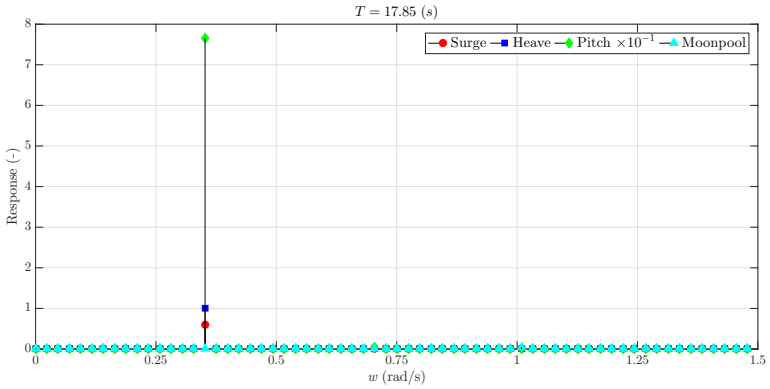

Figure 5.58: *Frequency domain response of the MoonWEC response under the influence of a monochromatic wave of period $T = 21$ s, for the studied modes. CALM configuration nr. 6.*

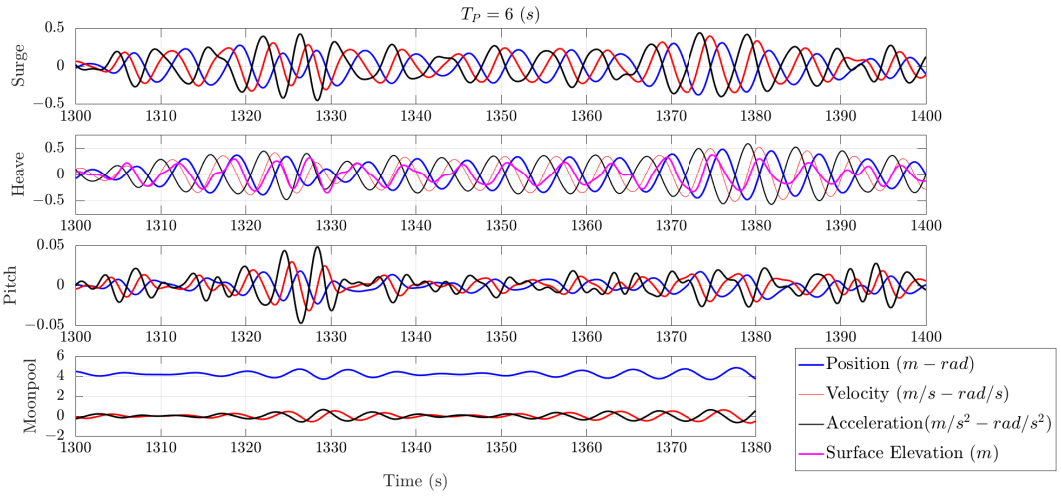

Figure 5.59: *Time series of the MoonWEC response under the influence of an irregular wave sea state with peak period $T_P = 6$ s, for the studied modes. CALM configuration nr. 6.*

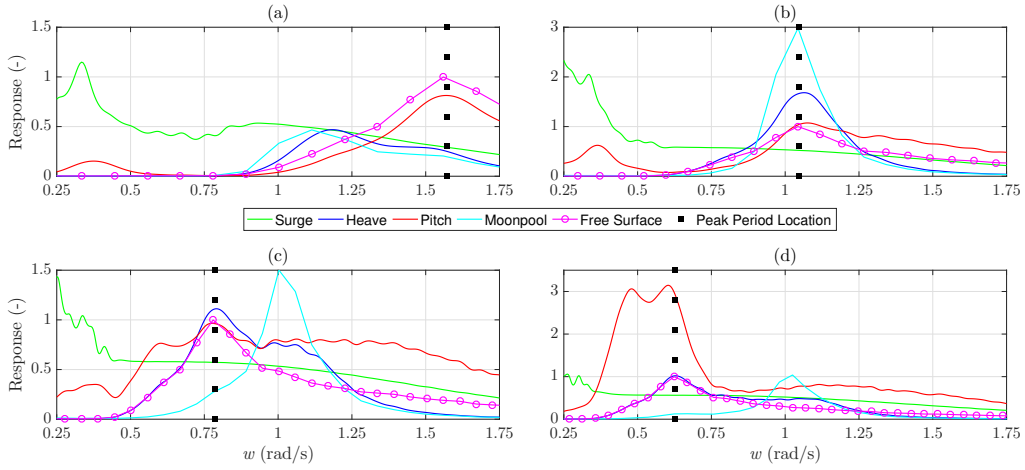

Figure 5.60: *Non-dimmensional Spectra of the MoonWEC studied modes response to irregular wave sea states. a) for peak period $T_P = 4$ s, b) for peak period $T_P = 6$ s, c) for peak period $T_P = 8$ s and d) for peak period $T_P = 10$ s. CALM configuration nr. 6.*

The typical effect of the highly pre-tensioned mooring systems are observed in the analysis. Relatively low natural period for the pitch mode is obtained, its response at that frequency is amplified with respect to the less pre-tensioned systems. Regarding the heave and moonpool modes, again no significant change is fetched detected. For the surge mode, the mean oscillatory position is the lowest amongst all the tested

configurations. Nonetheless, it cannot be completely eliminated since its origin derives from the particularity of the metacentric motion.

In conclusion, over the analysis of the past 6 CALM configurations no relevant change in the dynamics of the structure in heave and the moonpool is detected. The introduction of the mooring system stiffens the response in pitch. This stiffness is accentuated for the most pre-tensioned variants not only in surge but also in pitch. On the one hand, configurations nr. 1 & 2 are quite unstable, especially for low frequencies. On the other hand, configurations nr. 3 & 5 show high overall stability, being the performance of nr. 3 slightly better. Furthermore, the fact of having only two lines instead of four, represents a series of advantages, from economic to design ones.

Until now the working conditions of the system have been analysed. However, for the analysis to be complete, the survivability of the devices has to be ensured. In order to do so, two more issues need to be addressed. Firstly, the stability analysis of the surge motion is carried out to determine its natural periods. Lastly, the system is tested under severe storm conditions and its response is analysed to ensure it complies with all the requirements.

Being the mooring system dynamics highly non-linear, its natural period cannot be determined through the classical procedure of the decay tests. Such non-linearity implies that the resonant state depends on the excitation input; therefore, its natural period in surge will vary at each sea state. As described in (38), in order to stablish the periodicity condition lets rearrange equation (4.42) in the following form, without considering the excitation force:

$$m_{eq}\ddot{x} + Ax = f(x, \dot{x}, t) = [2Fz + 6Dz^2]x + Ex^3 - C_d\dot{x} - C\dot{x}\dot{z} - G\ddot{z} \tag{5.4}$$

Where f, is a continuous periodic real value function. When using the integral equations and Green's function a prediction may be done. Assuming that there exists a positive constant K upon which the following condition is satisfied, $M \leq AK$ where:

$$\begin{aligned} &M = Max|f(x, \dot{x}, t)| : (x, \dot{x}, t) \in Z, \\ &Z = t \in [0, \tau], |x| \leq K, |\dot{x}| \leq \sqrt{A}K \end{aligned} \tag{5.5}$$

Where τ denotes the periodicity condition: $x(0) = x(\tau)$, $\dot{x}(0) = \dot{x}(\tau)$. Through the implementation of the Green's function theorem the homogeneous linear differential

equation $\ddot{x} + Ax = 0$ must be satisfied and therefore:

$$\begin{aligned} &M = Max|[2Fz + 6Dz^2]x + Ex^3 - C_d\dot{x} - C\dot{x}\dot{z} - G\ddot{z}| : (x, \dot{x}, t) \in Z, \\ &M \leq ((C_d + C\dot{z})\sqrt{a} + G\ddot{z} + 2Fz + 6Dz^2 + EK^2)K \end{aligned} \tag{5.6}$$

Finally, if M is substituted in condition $M \leq AK$, the following relation is obtained:

$$K^2 \leq \frac{A - (C_d + C\dot{z})\sqrt{A} - G\ddot{z} - 2Fz - 6Dz^2}{E} \tag{5.7}$$

If one choose a K such that the inequality is respected, then the system will have a periodic solution with a natural frequency $f_0 = \sqrt{A}$. K represents the displacement of the system from the equilibrium at the initial time. Substituting $(z, \dot{z}, \ddot{z})$ by the values corresponding to a wave of the characteristics of each sea state, the natural frequency of the system for that particular sea state is yielded. Results for the CALM configuration nr. 3 are shown in figure 5.61.

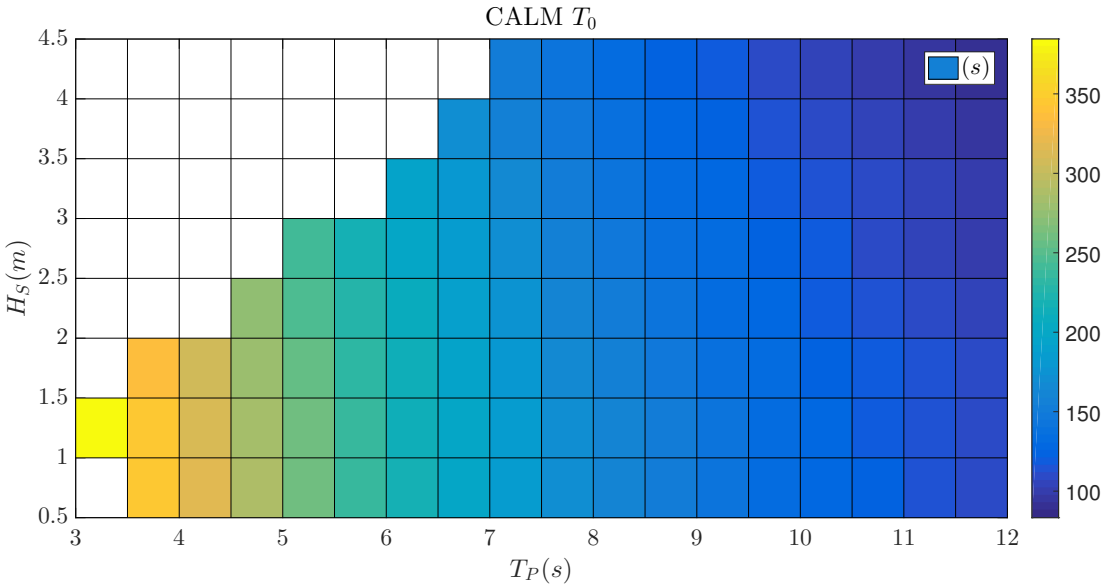

Figure 5.61: *Natural Period of the CALM-structure system in surge depending on the sea state input*

All natural periods are well above the limits of wind-generated waves, ranging from $T_0^s = [100 - 370]$. Therefore it can be stated that the device in surge will have bounded motions and that the resonant state won't be reached, thus ensuring its stability.

Finally, in order to confirm breakdown of the system is not likely to happen during its

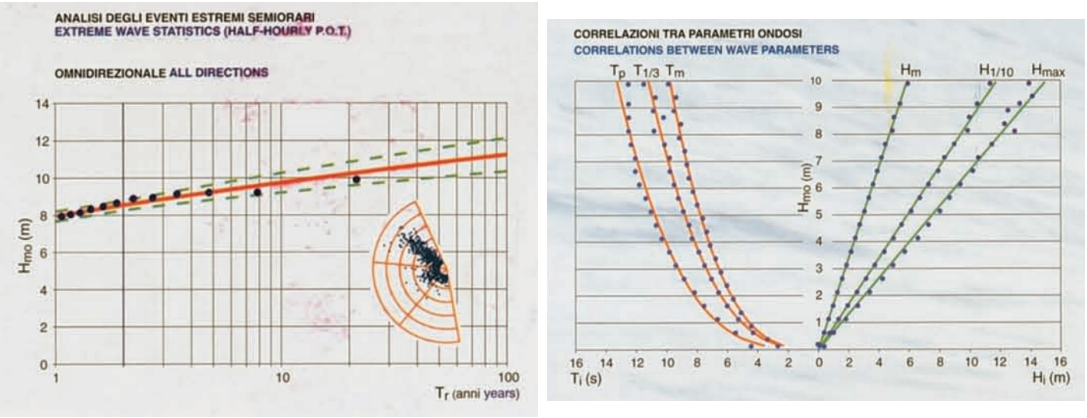

Figure 5.62: *Extreme wave statistics using the half-hourly POT method accounting for all wave directions at Alghero (31).*

design lifetime, which is considered to be 25 years, a test under severe storm conditions is carried out. In chapter 3, the extreme wave statistics of the deployment sites are reported. Figure 5.62 from section 3.3 and reproduced below for convenience, shows that according to the Peak Over Threshold method, the 25 year-return storm for Alghero is defined by a significant wave height of $H_{m0} = 10.5\ m$ and peak wave period $T_P = 13.5\ s$, while for Mazara del Vallo is $H_{m0} = 5.5\ m$ and $T_P = 9.5\ s$, see figure 3.7.

Choosing the most severe conditions, given at Alghero, the limit conditions the mooring system must resist are defined. Such sea state has been simulated for a total length of 1000 waves, which is the number of waves from which the total energy flux reaches stability. Due to the rough environmental conditions in which the device is performing, the oscillations in pitch exceed the maximum angle within the small angle hypothesis is valid. Therefore the model accounting for the pitch mode will be inaccurate and unstable as such inaccuracies may be propagated to the other DoFs via the coupling terms. Consequently, the pitch mode has been blocked for this test, allowing the device to move only in surge and heave. To carry on with the analysis, the device with the CALM system nr. 3. has been simulated for a storm with $H_{m0} = 10.5\ m$ and $T_P = 13.5\ s$. Figure 5.63 plots the time series of the surge and heave displacements as well as the instantaneous axial tension of the line.

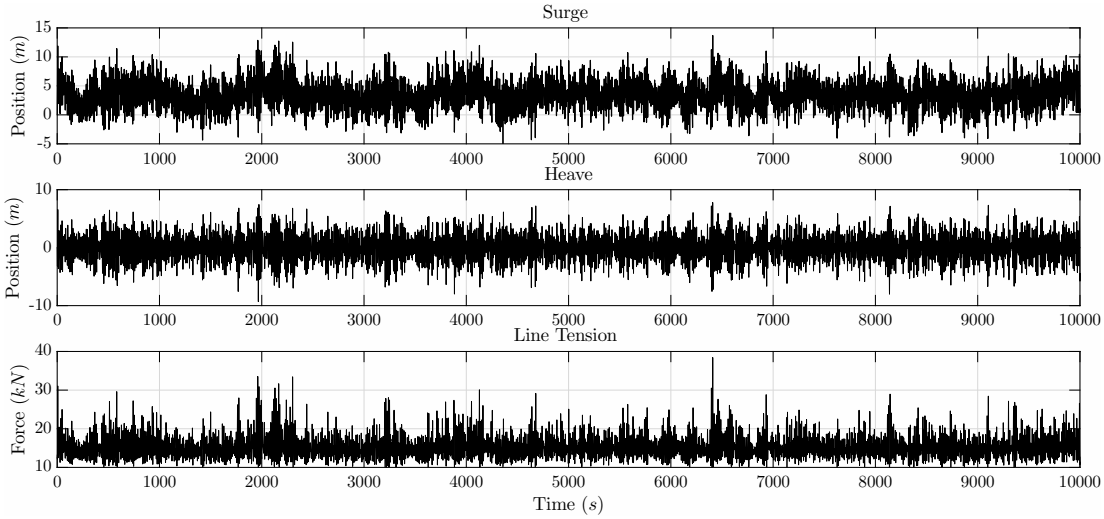

Figure 5.63: *Heave, surge and axial tension vs. time for an input sea state with* $H_{m0} = 10.5$ m *and* $T_P = 13.5$ s

A clear offset in the mean position is observed for the surge mode. However the oscillations remain bounded within the range of $x = [-5 - 15]m$, lying well below the geometric limits established in table 5.4, which are $x_{lim} = [-11 - 23.4]m$. Furthermore, the maximum computed axial load remains two orders of magnitude below the Minimum Breaking Load (MBL), declared in table 5.5. The results shown in figure 5.63 state the low probability the for the mooring system to reach the limit position and therefore, to produce slamming effects. Slamming is a very threatening phenomenon to the device survivability that must be avoided, since tensions can rapidly increase in several orders of magnitude. Actually, it is thought to be the main cause for mooring breakdown. For all the stated above, the chosen mooring configuration for the MoonWEC is the variant nr. 3 (table 5.4) with a six strand wire with a diameter of $\varnothing = 76$ mm (table 5.5)

5.2.3 PTO

The proper design and optimization of the Power Take-Off system (PTO) is as important as the structure and mooring ones. While the last keeps the structure safe and in place and the second last fetches the mechanic energy of waves, the first is in charge to effectively transform the captured energy in a way that can be directly used, stored or transported, usually converting it to electricity. The PTO mounted in the MoonWEC is composed by two elements, a Wells turbine and a PM generator. The former is in charge to direct the energy trapped in the moonpool to a rotative motion and the

latter transforms this rotation in electricity following one of the most classic schemes in engineering. Firstly, the design and optimization process of the W-T is described. Afterwards, this sequence is repeated for the PM generator.

5.2.3.1 Wells Turbine

As seen on section 4.1.3.4, the W-T performance depends on a large number of parameters. Nevertheless, most of them are very closely related and hence, determining a very narrow working regime. Its performance is extremely sensitive to a series of conditions. Namely, the geometric configuration of the blade and the turbine solidity on one side; and the flow characteristics on the other side. The large sensitivity is expressed through the relative conditions between the turbine and the flow, which are mainly characterised by the velocity triangle, see figure 4.5. The relative velocity plays a key role, as is the driving parameter, together with the chord length, of the generated axial and tangential forces (equations (4.51) and (4.50), respectively). The coefficients of these forces, c_A and c_T, are again dependent on the relative velocity by means of the attack angle α and the Reynolds number (equation (4.47)). Furthermore, its working region is quite narrow (see figure 4.7); thus, if α lays outside of the range specified by the figure, stall conditions are verified and turbines efficiency drops suddenly. For this work, the stall conditions have been modelled as a totally unproductive regions resulting in no power production.

Dimensions of the W-T have been set in proportion to the diameter of the moonpool $\varnothing = 2m$. That allows a maximum chord blade of $c = 0.5m$. As stated in (80), a common value in Wells turbines is a hub-to-tip ratio is 2/3, as the tip diameter is set equal to the moonpool diameter, a hub diameter of $\varnothing = 1.34m$ is obtained. Solidity of the turbine σ plays also an important role on the turbine's efficiency. In this work, several solidities have been tested by varying the number of blades, starting from three and increasing by one blade at a time until five. The presence of the turbine implies a reduction in the area the fluid must flow through. Thereby, and as a result of the continuity hypothesis formulated in equation (5.8), the water of the moonpool is accelerated when passing through the turbine. Therefore, in the design process this relation will be applied to the the axial flow velocity. Nevertheless, the results are shown with respect to the moonpool velocity, since it is much more linked to the overall device behaviour.

$$\frac{\dot{m}_1}{\dot{m}_2} = \frac{\rho A_1 v_1}{\rho A_2 v_2} = 1 \tag{5.8}$$

Where ρ is the fluid density, $\dot{m}$ is the mass flow and A is the area perpendicular to the flow velocity v. Without the presence of the turbine, the moonpool can oscillate with a celerity up to $2m/s$ when resonance conditions are met. A goal is set in first approach for the design of the turbine, which goes far beyond the issues addressed in this thesis. The moonpool oscillations have to be reduced to a fourth at least, thus the maximum relative velocity of the moonpool may not exceed $0.5m/s$ with the turbine installed. Part of the energy absorbed by the turbine will be dissipated through the axial component, mainly by viscous drag effects, and part will be converted into rotation due to the generated lift effect. The power of such rotation can be computed as:

$$P = T\dot{\varphi} \tag{5.9}$$

Where T is the torque generated by the turbine, introduced in section 4.1.3.4, and $\dot{\varphi}$ is the rotational velocity. At first stage, a simplification of the electromagnetic resistant torque is simulated by introducing a rotational linear damping to the turbine. The resistant torque can be computed as:

$$T_R = B_w\dot{\varphi} \tag{5.10}$$

Where B_w is the damping coefficient. After identifying the two root parameters, the resistance damping B_w and the moonpool velocity $\dot{\xi}$, and having fixed the dimensional parameters, the parametric space of the turbine is explored. Simulations consist in applying a constant flow velocity and damping and let the turbine reach the stationary state. Then, the rotational velocity, the attack angle, the Reynolds number, the relative velocity and the axial force are yielded. In other words, the turbine working regime of the turbine is determined. The sweeping of the parametric space allows to identify the most productive regions and determine the characteristics of the working regime. Figure 5.64 displays the power produced by the different turbines, accounting with 3,4 and 5 blades, over the parametric space.

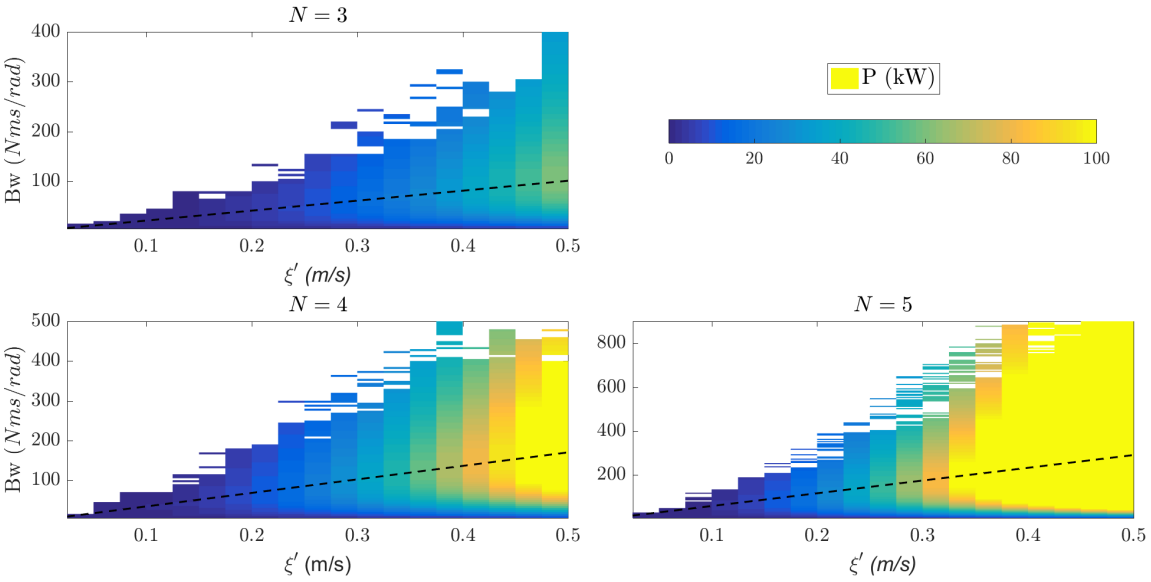

Figure 5.64: *Power produced by the Wells Turbine as function of the damping coefficient and moonpool velocity. Linear regression of the maximum power damping coefficient in the dashed line.*

Two clear areas are observed in figure 5.64, a white region and a coloured region. The white area corresponds to the stall conditions and therefore, no power is produced. A strong variation on the power range can be observed with respect to the number of blades of the turbine. As expected, the greater the number of blades the higher the output power. The damping coefficient corresponding to the maximum power at each moonpool velocity matches a linear regression with an $R^2 > 0.99$ for each case, confirming the linear behaviour of the Wells turbine as stated by (39). The optimal damping coefficient is shown as a dashed line. Figure 5.65 shows the angle of attack for the different turbines.

As expected, the angle of attack increases with the damping until it reaches the stall conditions. For high flow velocities, this increase is more gradual as the working regions expands due to higher Reynolds numbers, see figure 4.7, whereas for low flow velocities this change is extremely abrupt, challenging eventual control strategies. The range of optimal attack angles is around $\alpha \approx 5°$ and does not present substantial alterations with the flow velocity, the damping coefficient and even the number of blades. Finally, the rotational velocity is presented in figure 5.66.

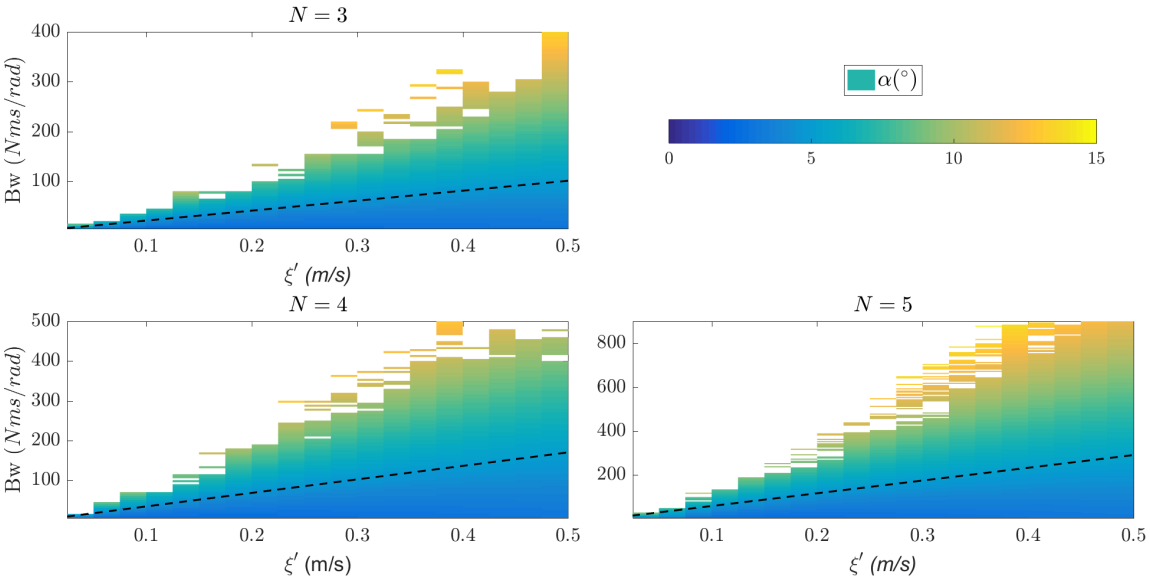

Figure 5.65: *Angle of attack as function of the damping coefficient and moonpool velocity. Linear regression of the maximum power damping coefficient in the dashed line.*

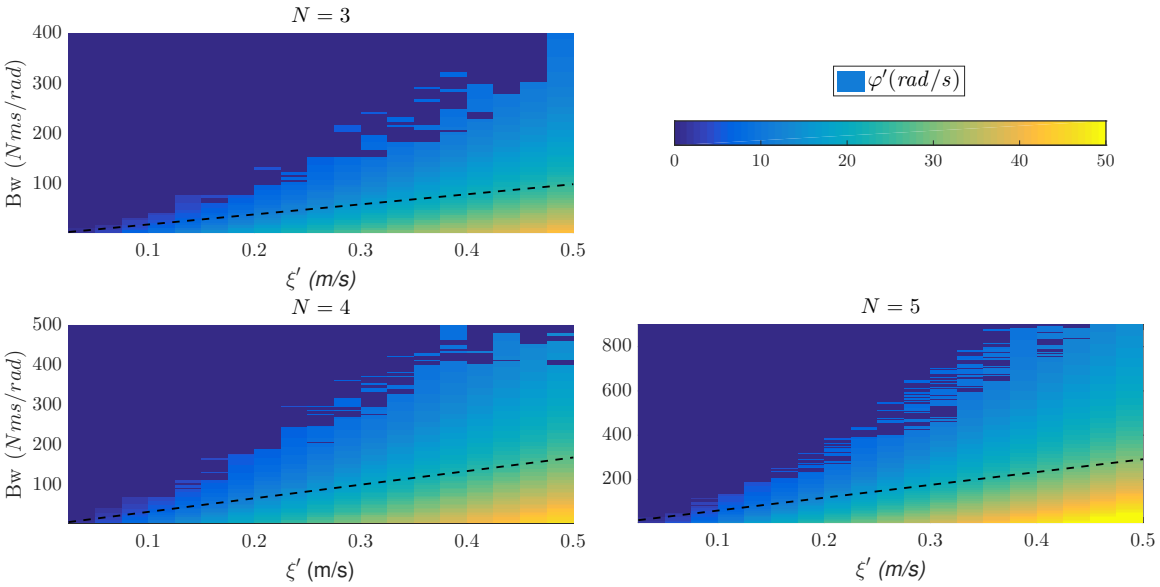

Figure 5.66: *angular velocity as function of the damping coefficient and moonpool velocity. Linear regression of the maximum power damping coefficient in the dashed line.*

Figure 5.66, shows null velocities for high damping coefficients and low flow velocities; and truly high velocities for low damping coefficients and high velocities. Similarly to figure 5.64, the effect of the number of blades is proportional to the increase of the

angular velocity. On the other hand, for the optimal damping conditions no substantial variations are found. Finally, a relation between between the number of blades and the working region is observed. The higher the number of blades the larger the working area is, due to increased capacity to bear with the resistance torque. Figure 5.67 shows the time series of the above described parameters; i.e, the angular velocity and the attack angle, plus the tangential and axial forces F_t and F_A, respectively. Results are shown for the three modelled turbine variants. A fixed moonpool velocity of $\dot{\xi} = 0.25(m/s)$ and the corresponding optimal damping B_W have been chosen to set the simulations up and then have been run until the stationary state is reached.

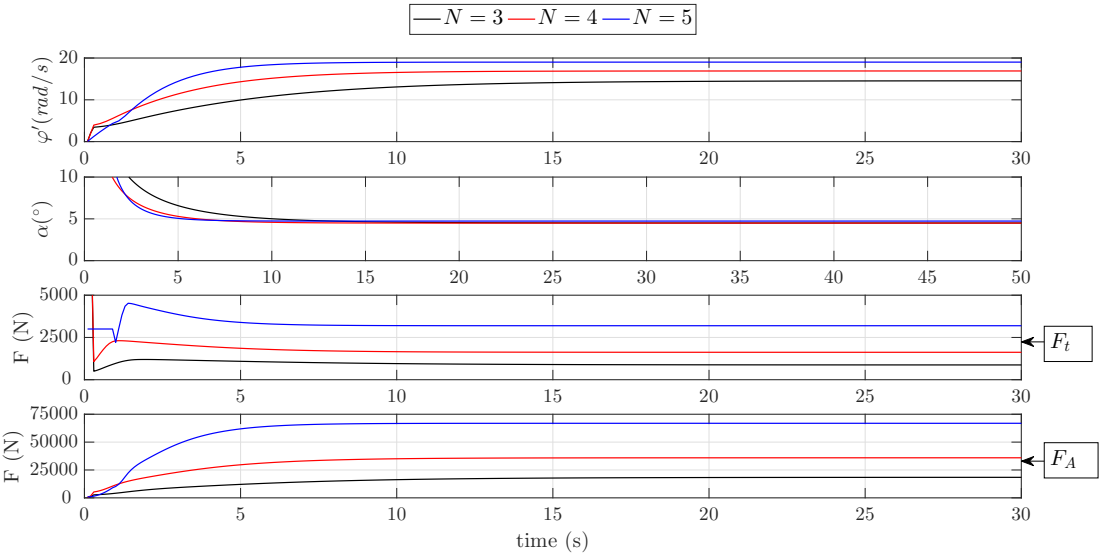

Figure 5.67: *Working conditions of the studied W-Ts for a fixed flow velocity and resistance damping.*

Transient and stationary regimes are clearly differentiated in figure 5.67. Actually, even two different behaviours can be identified in the transient regime, a first strong stroke and a subsequent smooth evolution towards the stationary regime. The cause of that unusual first behaviour is the action of the so-called turbine's launching system. Traditional W-Ts are non self-starting and therefore, need to be put into motion. When the angular velocity of the W-T is zero, its angle of attack will always be $\alpha = 90°$ regardless to the flow velocity. Figure 4.7 shows that an attack angle of 90 ° lies far beyond the working conditions, making it impossible for the turbine to flee from the stall conditions by itself. Consequently, an external torque is imposed to force the transition from the stall to the working regime. Once this is reached, the external

torque is withdrawn leaving the turbine for self-regulation. Technically, this is possible by turning the electric generator into an electric motor through a proper switch in the power electronics system. Figure 5.67 confirms what observed in figures 5.66 and 5.65, the optimal attack angle is independent from the turbines solidity σ, since their stationary values converge despite the different number of blades. On the contrary, the angular velocity, the axial and tangential forces are sensitive to σ, growing with N. Also, it is important to note that the axial force F_A is higher than the tangential force F_t by an order of magnitude; highlighting the W-T major criticality, its low hydrodynamic efficiency. Furthermore, a high risk of over-damping the moonpool is assumed due to the large value of the axial force. To conclude, although the 5 blade W-T seems the most appropriate as its power is maximized, the large damping generated by F_A can cause the moonpool oscillations to vanish almost completely, shifting the working conditions towards very reduced flow velocities, where the absorbed power is minimal.

Having determined the optimal working conditions, the final step is to design an electric generator that fulfils such requirements. Essentially, the resistant torque of the PM Generator must be equal to the torque generated by the turbine.

5.2.3.2 PM Generator

The first step in the design process of the PM Generator is to decide its nominal power. Given the conditions imposed by the W-T, see figure 5.64, the nominal power of the generator has been set to $P_N = 50kW$. Subsequently, according to that value, the rest of the generator parameters are set, see section 4.1.3.5. Table 5.6 provides the values of such parameters and figure 5.68 shows a section view of the of the stator-rotor structure of the generator. Note that, being this field afar from the author's field of expertise, the design process of the generator does not take into account several phenomena, such as hysteresis cycles, temperature analysis, copper-loses and magnetic material properties. Aiming to provide a somewhat realistic approximation of the performance of a PM generator.

Parameter	value	units
B_t	1.55	T
ω_p	$\pi/6$	rad
d	0.05	m
p	16	-
q	3	-
c	6	-
ω_t	$\omega_p/2q$	rad
R_c	0.3735	Ω
L_c	0.0115	H
η	0.791	-
$\dot{\varphi}_N$	21.5	rad/s
P_N	50	kW

Table 5.6: *PM Generator parameters for a Nominal Power of* $50kW$.

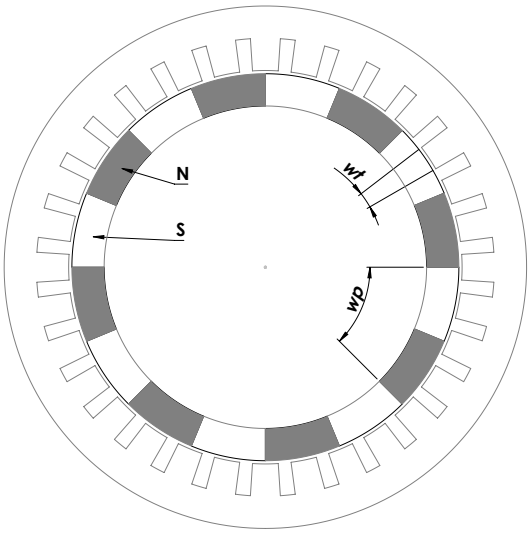

Figure 5.68: *Generated resistant torque and electric Power of the studied PM generator vs. the angular velocity. Nominal conditions marked with squares*

The working conditions of generator are shown in figure 5.69. The resistant torque and electric power are plotted over the angular velocity $\dot{\varphi}$. The nominal conditions are defined by the maximum torque τ. Beyond this point, due to the generator's lack of capacity to further increase the torque, there is a sudden drop of the generator's efficiency; despite fact that the produced power can still grow as a result of the angular velocity increase.

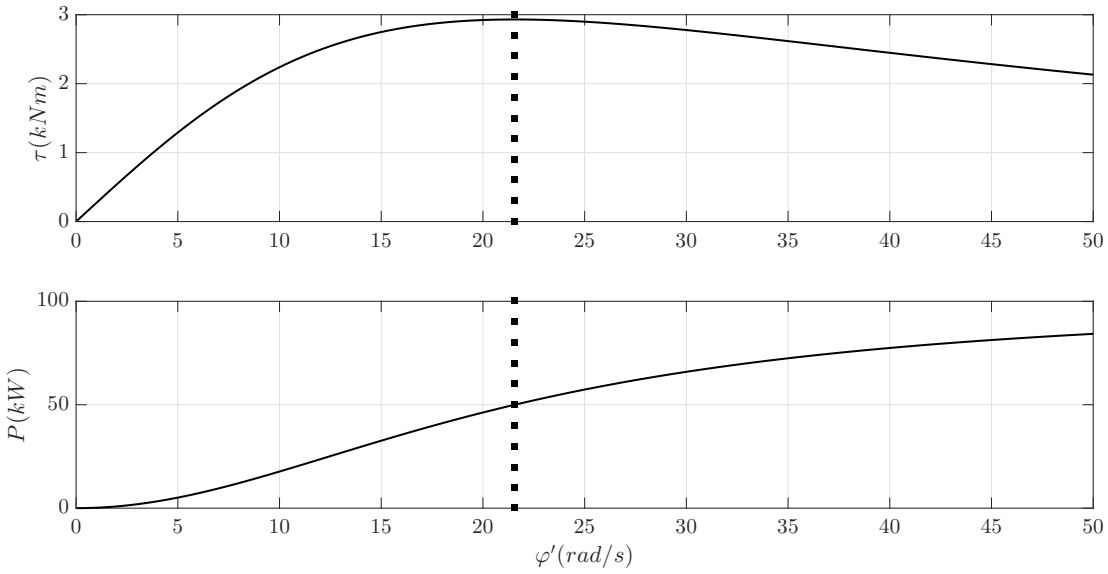

Figure 5.69: *Generated resistant torque and electric Power of the studied PM generator vs. the angular velocity. Nominal conditions marked with squares*

Figure 5.69 shows the nominal power is $50kW$ and the nominal angular velocity is 21.5 rad/s. Furthermore, the loss of efficiency after the nominal conditions can also be observed, as the increase in the power output is substantially moderated. In order to adapt the generator's behaviour to the turbine's specification a control strategy must be designed. From the electric equivalent circuit scheme (figure 2.20), it can be noted that the current intensity and voltage can be modified by varying the value of the load resistance. Hence, the electric power is also altered and therefore, the resistant torque can be modulated. The current state-of-the-art of power electronics allows perfectly to account with a rheostat that not only takes into account the load induced by the grid but also an internal load variation. Furthermore, an active control system, which feedbacks the moonpool velocity to the power electronics central unit, must be implemented. The active control system applies the control law for the moonpool velocity measurements and sends the correct signal to the rheostat in order to obtain the electric resistance that makes the generator operate in the turbine optimal conditions. The active control system decides, depending on the moonpool velocity measurement, which signal has to be sent to the rheostat in order to obtain the electric resistance that makes the generator operate in the turbine optimal conditions.

The control law is obtained by imposing the rotation velocity that ensures the optimal turbine working conditions for a given moonpool velocity, found in figure 5.66.

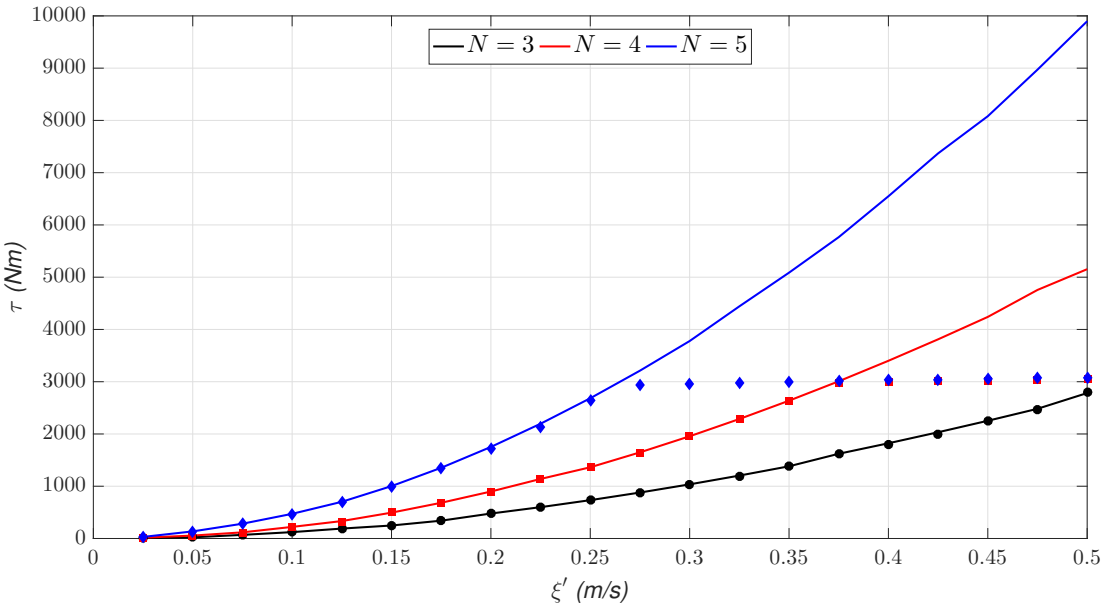

Figure 5.70: *Generated torque by the turbine (lines) and resistant torque of the studied PM generator (markers) vs. the the moonpool velocity*

Then, the resistance load is changed until the resistant torque of the generator matches the driving torque of the turbine. In figure 5.70, the driving torques for the different turbines and the generator torques are plotted as lines and markers, respectively.

The complete matching is achieved for the 3 blade turbine. For the 4-blade the nominal conditions are reached for a $\dot{\xi} = 0.375\ m/s$. The same effect is observed in the 5-blade turbine when $\dot{\xi} \geq 0.275\ m/s$ denoting that the generator is not able to generate required torque by the turbine. Figure 5.71, shows the power absorbed by the turbine and the electric power generated by the generator, in the same conditions reported in figure 5.70.

Unlike in the torque case, no match is obtained in figure 5.71. Electric power values are always below the absorbed power, this is due to generator's efficiency (see table 5.6), which takes into account the Joule effect and mechanical losses. Furthermore, the nominal conditions limitation is still identified for the 5-blade turbine. The results of each marker in figures 5.70 and 5.71 has been obtained with a different load resistance, such values conform a subset that defines the control law. The control laws for the different turbines have been obtained through the fitting of such values with a piece-wise cubic regression. Figure 5.72 shows the obtained control laws for the different turbine variants as well as the electric power produced by the generator in the background.

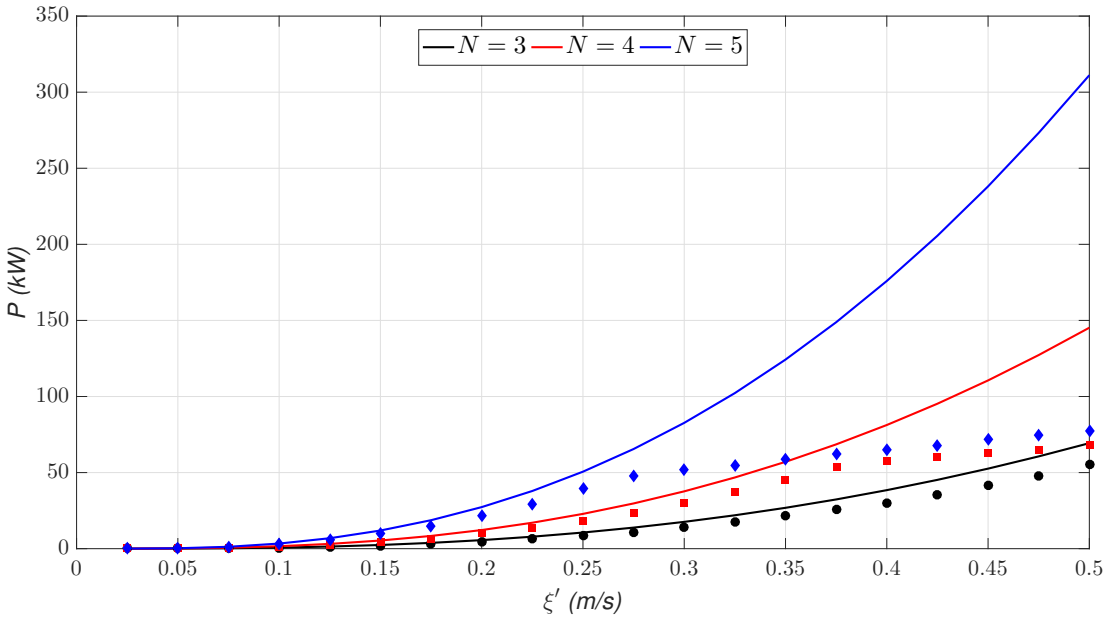

Figure 5.71: *Absorbed power by the turbine (lines) and generated electric power of the studied PM generator (markers) vs. the the moonpool velocity*

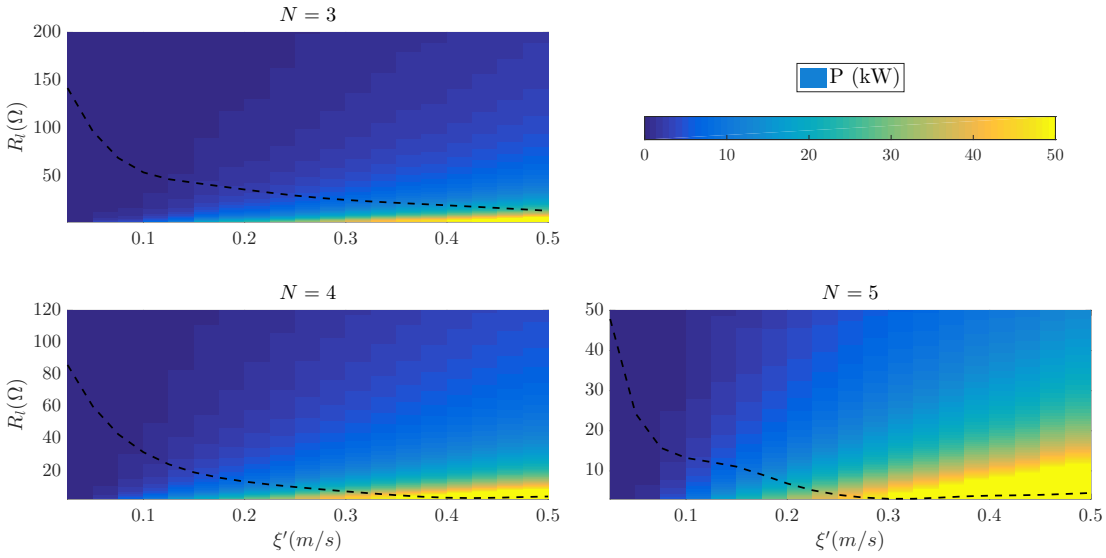

Figure 5.72: *Resistance value dictated by the control laws for the different turbines and the generated electric power of the studied PM generator*

6

Results

6.1 HPA-LG

6.1.1 Generic

102 simulations, corresponding to the full range of sea states that characterize the selected locations wave climate, have been simulated for each of the different device variants, see table 5.2. For each simulation the following data is extracted: displacement and velocity time-series of each device part and instantaneous produced power. The production of the device is obtained by averaging the instantaneous power over the time-series, for each simulated sea state. When combining all the obtained output powers, characterised by the peak period (T_P) and the significant wave height (H_S), a two-dimensional matrix, commonly named power matrix, is obtained. In order to asses the device general performance, the power matrix of each variant is shown in figure 6.1.

Figure 6.1.a) displays the two-body variant free to move only in heave (A in table 5.2), figure 6.1.b) presents the two-body variant accounting for the heave and surge modes (B in table 5.2), figure 6.1.c) summarizes the performance of the three-body device only in heave (C in table 5.2) and figure 6.1.d) reveals the behaviour of the most complete model, accounting for three bodies and five degrees of freedom (D in table 5.2). All the power matrices show the expected behaviour. The general trend shows higher production rates at higher and steeper waves; furthermore, a substantial increase of the produced power is noticed when the third body is added. Yet, no evident differences are observed when the surge is introduced. Therefore, a more thorough analysis is needed to study such effects in depth. In order to quantify the influence that the submerged sphere has in the power production, variants A & C, and D & B are confronted by

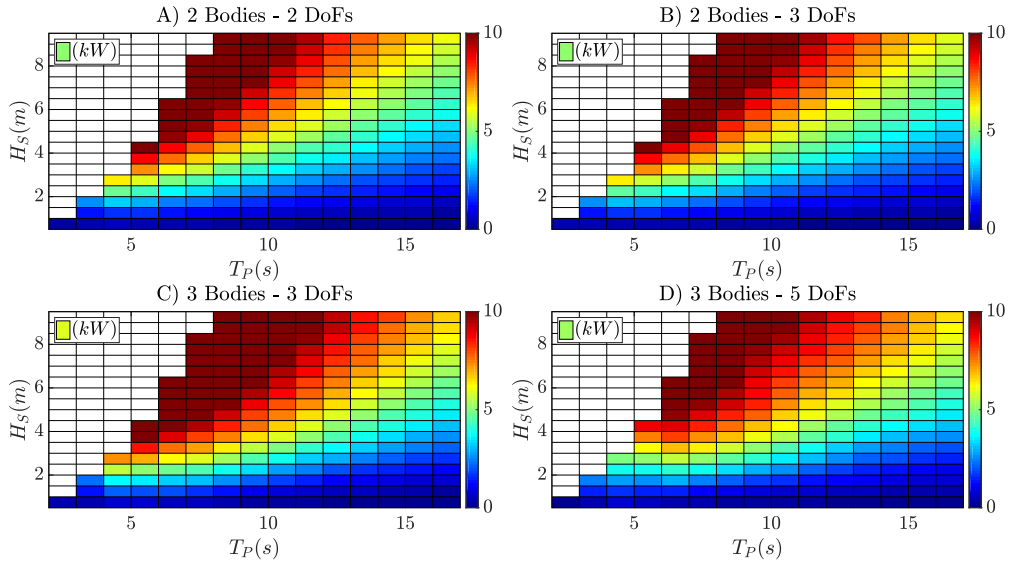

Figure 6.1: *Power matrices for each variant of the device. a) Two bodies only heave, b) two bodies heave & surge, c) three bodies only heave and d) three bodies heave & surge. (as in table 5.2)*

subtracting their power output for every sea state. Results are shown in figure 6.2.

A clear patch is observed in figure 6.2.a), having a production peak between T_P's 7 and 9 seconds, shifting the most productive area towards higher periods, just as pointed in the previous chapter. The same trend is identified in figure 6.2.b) even though the surge effect seems to mitigate it substantially. In addition, for very steep waves, this trend is even reversed and the surge effect is revealed to be counter productive because of the negative values of the production rate. Meaning that the addition of the submerged sphere is not always optimal, specifically if the device is to be deployed in a location

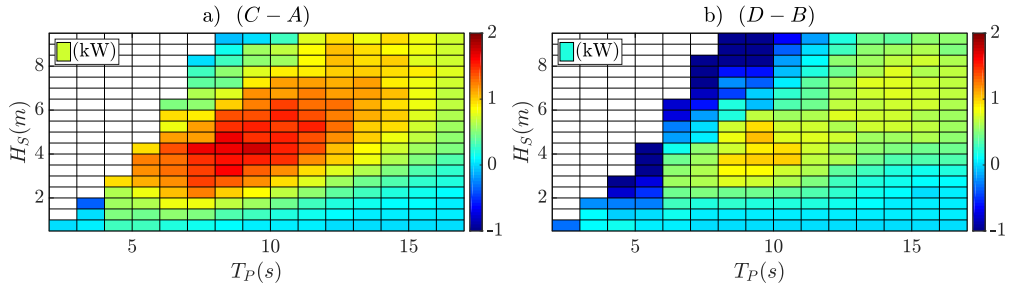

Figure 6.2: *Power matrix differences between the two & three-body devices. a) Heave only. b) Heave & surge.*

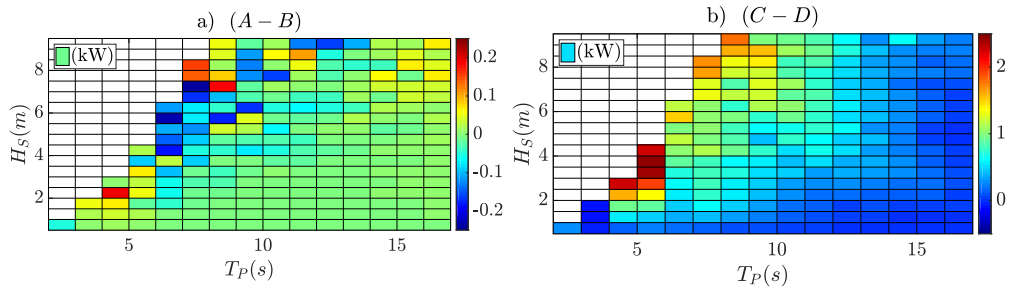

Figure 6.3: *Power matrix differences between the heave-only mode and the heave & surge mode. a) Two-body device. b) Three-body device.*

where wind seas are predominant.

To better explore the device response, the same methodology as in the previous figure has been applied, subtracting $A - B$ and $C - D$. By doing so, the pure surge effect can be analysed for both, the two and three-body device. See figure 6.3.

Figure 6.3 shows contradictory behaviour between devices under the same circumstances. The three-body device confirms a clear negative trend in production rates at the steep-wave area of the matrix whereas a slight positive production rate is identified at the flat-wave region (figure 6.3.b). On the other hand, the two-body device produces slightly more for steep waves when the surge mode is included in the simulation, although no predominant trend can be identified from the results. However, both devices appear to have high sensitivity to wave steepness since in both figures two major areas can be distinguished, corresponding to high and low steepness of the waves. Consequently, the difference in each device's power production has been studied according to wave steepness. Results are presented in figure 6.4.

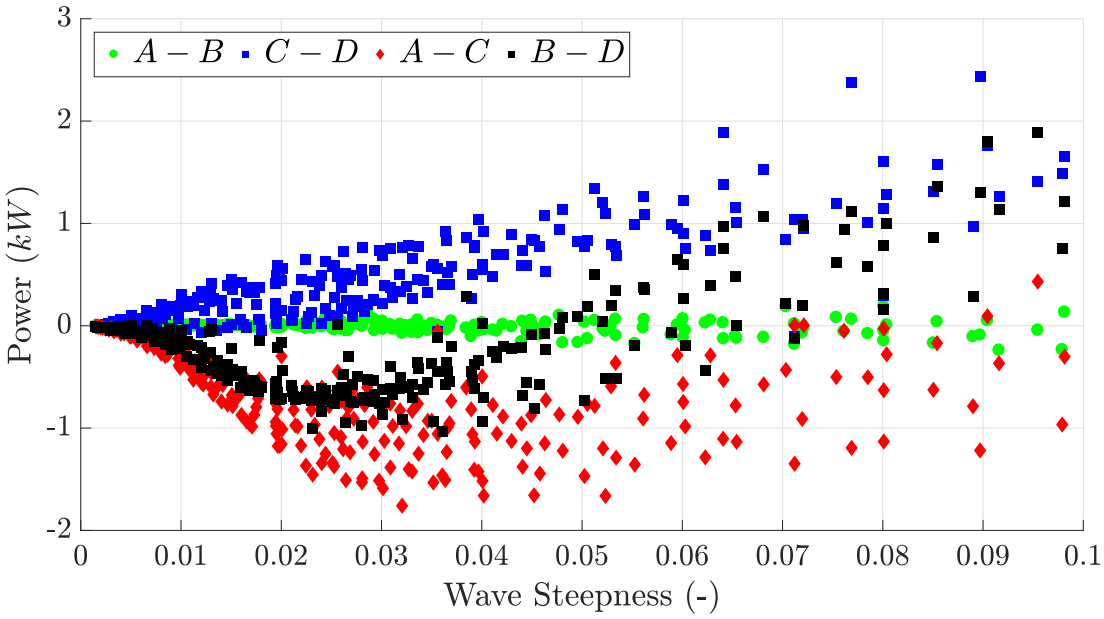

Figure 6.4: *Power output difference vs. wave steepness for each device, scatters related to the model variants specified in table 5.2.*

The two-body device (green cloud) reveals no apparent surge-related sensitivity to wave steepness, since the scatter cloud shows no relevant wave steepness-related ramp and reduced dispersion. On the contrary, the blue-dotted cloud has a clear wave steepness akin trend, which confirms that the inclusion of the sphere has an evident negative contribution when it comes to electric power output, as the power difference increases with the wave steepness. The isolated effect of the sphere (red and black clouds) shows the same general trend regardless the incorporation of the surge in the model. A net increase in power production is obtained for low steepness values; progressively, this increase in power production is mitigated as the the waves get steeper, even reversing the trend when accounting for the surge.

Although the buoy is the body in direct contact with waves, the electric production is carried out by thePTO's piston, which in the case of the three-body device is greatly influenced by the submerged sphere. To study this behaviour, an analysis of three parameters concerning the piston's dynamics has been carried out. The aforementioned parameters are the following: the active area ratio of the PTO (AAR), the average velocity of the piston and average amplitude of the piston's oscillations. The AAR gives very good insight, not only for the amplitude of the oscillations but also for the offset of the centre of such oscillations with respect to the equilibrium position. Furthermore,

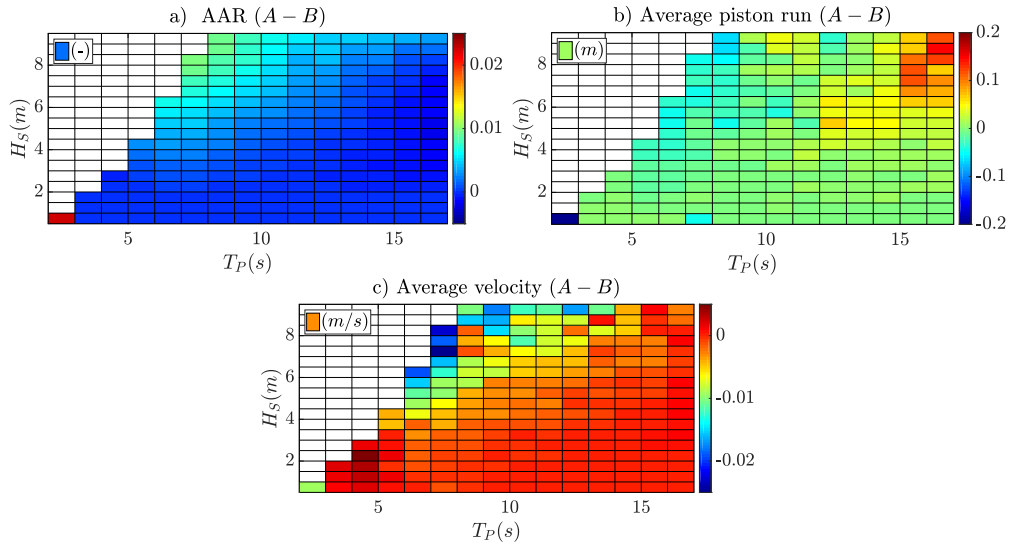

Figure 6.5: *Two-body device difference matrices between heave-only mode and heave & surge mode. a) Active Area Ratio, b) Average amplitude of the piston's motion, c) Average piston's velocity*

the average oscillation amplitude helps to complete the analysis on this regard, since a joint study of both parameters allows to obtain a detailed picture on the piston regime. Finally, it is important to consider as well the average piston's velocity since it is directly linked to the power output through the magnetic induction laws.

Figures 6.5 and 6.6 have been computed following the same procedure adopted in figure 6.3. The values shown are $AAR(A) - AAR(B)$ and $AAR(C) - AAR(D)$, for the a) section of figures 6.5 and 6.6, respectively. The average piston run of $A - B$ at the c) section and the average piston velocity for section b).

The combination of negative average piston run and positive AAR differences given at the top-left corner of the matrix (high and steep waves) shows that the piston presents smaller oscillations when the surge is taken into account and, on top of it, it is doing so outside the range where electricity is effectively produced. However, the velocity differences are also negative at the same area, meaning a higher electricity production. Considering the values, it can be realized that differences are actually very small. This, brings about high uncertainty upon the dominance of a specific parameter over the other. As a matter of fact, this was already observed in figures 6.3.a) and 6.4, where no clear conclusion can be drawn whether the surge effect is either positive or negative for the two-body device.

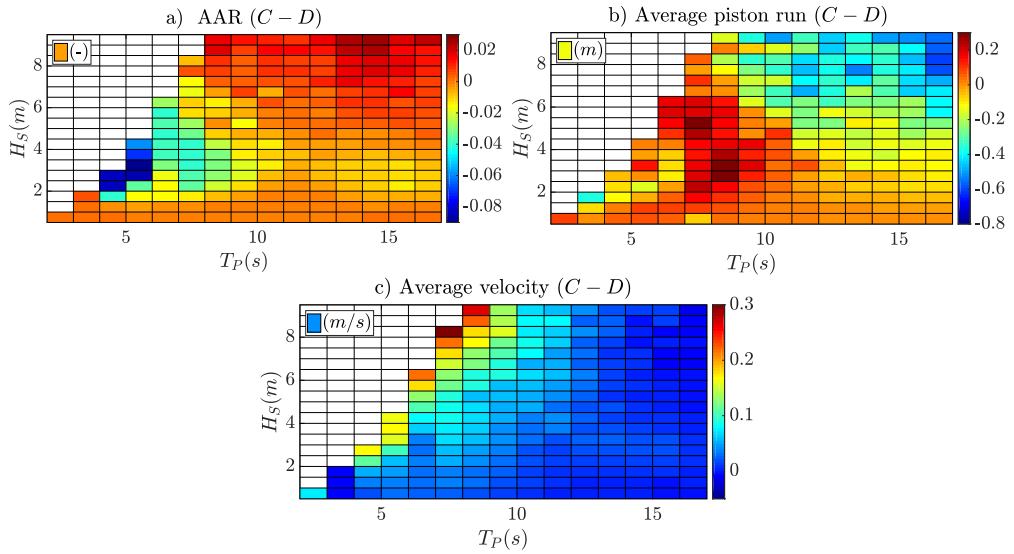

Figure 6.6: *Three-body device difference matrices between heave-only mode and heave & surge mode. a) Active Area Ratio, b) Average amplitude of the piston's motion, c) Average piston's velocity*

For the three-body device instead, a clear pattern can be distinguished for steep waves. The AAR difference is negative, which implies that the piston oscillates more effectively when the surge mode is taken into account. Nevertheless, the average piston's run and velocity differences are positive and so it means that it also oscillates less and more slowly. Leaving no doubt to the negative influence of the surge at that region of the matrix, as already confirmed by figures 6.3.b) and 6.4. This phenomenon can be explained through the system's inertia increase due to the sphere. Steeper waves mean higher wave excitation forces, in the surge direction too, but also faster sign fluctuations since these are relatively short waves. A fast sign-changing force is less successful when it comes to excite a heavier object since the momentum that needs to overcome is higher. Furthermore, this momentum transfer is passed from the buoy to the sphere through steel wires (note that the sphere is deeply submerged), bringing up the probability of undesired effects such as, wire-slamming and out-of-phase oscillations.

6.1.2 Site-Specific

The AEP of the simulated devices has been computed for the two selected sites, Alghero and Mazara del Vallo. The results are shown in figure 6.7.

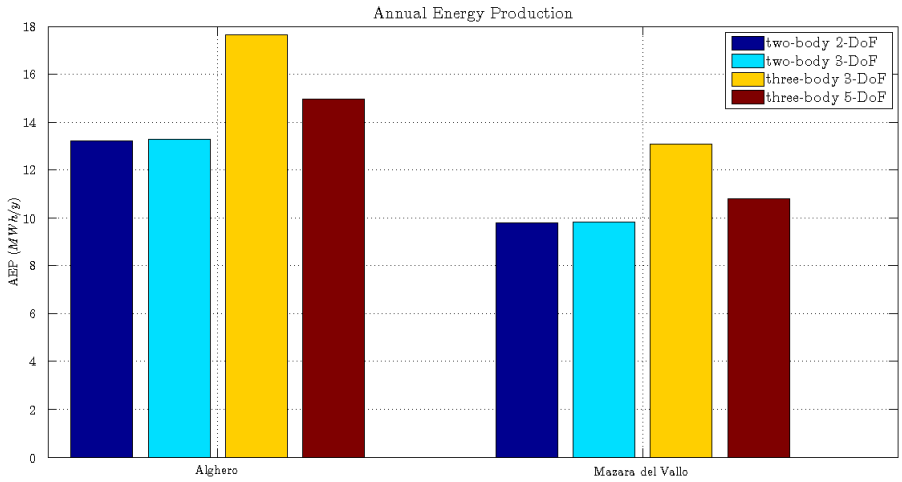

Figure 6.7: *AEP for each device in both sites.*

The three-body device has a higher electricity production, the increase is about $[10 - 25]\%$ at both locations, Alghero and Mazara del Vallo. On the one hand, the surge has no influence on the long-term electricity production for the two-body device, results are almost identical either for Alghero or Mazara del Vallo. On the other hand, for the three-body device instead the production plummets about 15% for Alghero and 17% for Mazara del Vallo, confirming what stated at the previous subsection, i.e: the inertia introduced by the submerged sphere has a large positive contribution for the heave mode but a negative one for the surge mode. However, the three-body device is still more productive than the two-body device.

6.2 MoonWEC

6.2.1 Parametric Instability

A peculiar behaviour of the MoonWEC device in heave and surge modes was identified in section 5.2. The pitch mode appears to have a larger response than expected for waves with a period larger than 5 s, yet being smaller than its natural period. Two phenomena could explain such behaviour. On the one hand, it could be an effect introduced by the mooring system, in which the dynamics of the pitch mode are influenced by the motion in surge due to the moments introduced by the mooring lines and vice-versa. On the other hand, a phenomenon sharing the same principle as the parametric resonance could

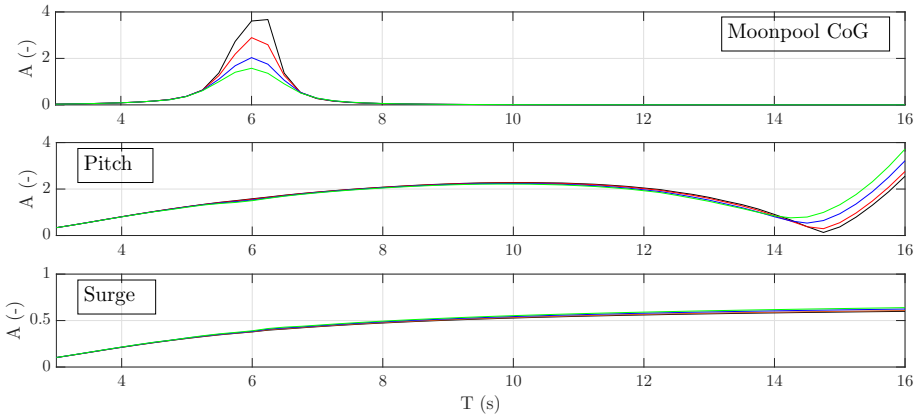

Figure 6.8: *Amplification factor for the meta-centric oscillations, pitch mode and surge for different input waves*

be responsible. The relative motion between the floating structure and the moonpool can give place to boosted motion due the syncing of loads if specific conditions are given. Such effect, known as parametric roll or pitch for ships, is triggered due to the non-linear hydrostatics reflecting the hull's geometry. This is not the case in study as the hydrostatic effect has been considered linear, see section 4.1.3.1. However, the same effect could occur as the location of the meta-centre of the device changes in time due to the relative motion between the moonpool and the structure. As stated by (62), parametric resonances are given for excitation frequencies at around twice the natural frequency of the mode in subject. Furthermore, as shown in (93), its intensity is really sensitive on the damping forces and amplitude of the excitation wave.

In order to determine the nature of the amplification in pitch, the device response for waves in the range of $H = [0.25 - 1.5]\ m$ and $T = [3 - 16]\ s$ has been studied. Besides the surge and pitch mode, the oscillations of the meta-centre have been analysed too. Results are shown in figure 6.8. The responses have been non-dimmensionalised according to the wave steepness, the horizontal component of the water particle orbits and the wave amplitude for the pitch, surge and meta-centric oscillation, respectively.

As expected, a clear resonant behaviour for the meta-centre of the structure is identified for $T = 6\ s$. The surge mode, remains in the sub-resonant region for all cases confirming what previously stated by the stability analysis, see section 5.2.2. The pitch mode has an amplification factor $A > 1$ in the range of periods $T = (4.25 - 14)$; after which continues to decrease until $T = 14.75\ s$, from where on, a rapid growth is observed. This point coincides with half of the natural period in pitch, which is

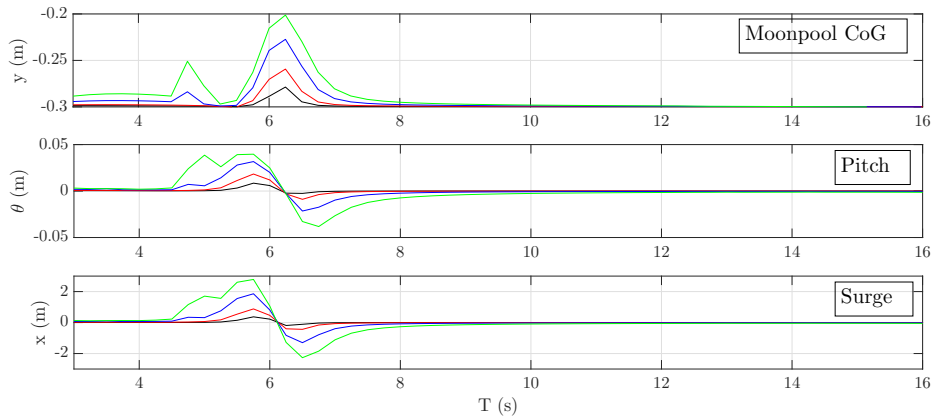

Figure 6.9: *Mean oscillatory position of the meta-centre,the pitch and surge mode for several input waves*

$T_N^p = 28.75\ s$. Therefore, despite being discreet, a parametric resonance is identified. Nevertheless, the cause of the increase in the pitch response in the range $T = [4.25 - 14]$ seems to be the correlation with the surge mode induced by the mooring system as both curves share a common pattern. Furthermore, within this range, a linear response on the wave height is observed since the normalized values match. A tiny perturbation in the pitch mode can be observed for $T = 6\ s$, it is caused by the oscillations of the metacentre. However, the shift in the mean oscillatory position for the surge and pitch modes observed in section 5.2 cannot be explained with the previous figure. The mean oscillatory positions, retrieved from the continuous component of the Fourier analysis, are plotted in figure 6.9 .

Figure 6.9 shows a clear relation between the three DoFs. When the moonpool is resonating, its oscillations switch upwards due to the deformable volume condition, causing a displacement of the application point of the moment creating an imbalance that is compensated with the shift in the mean angle position, which in turn shifts the mean surge position by action of the mooring system. It is also observed, that previous to the resonant period, the shifts in pitch and surge are positive and right after the resonance period become negative while passing through zero at the exact period of resonance. Such effect, clearly non-linear, derives from the phases between the structure and the moonpool, the transition from the out-of-phase, given previous to the resonance, to the in-phase situation found after resonance produces a switch of sign in the moment balance equation.

6.2.2 Net Power

The ability of the device to absorb the wave energy in the energy chain prior to the PTO is assessed by the net power computation. That is, the power entrained in the moonpool by its relative motion with respect to the floating structure. The net power is calculated with the classic relation

$$P(t) = F(t)\dot{\xi}(t) \tag{6.1}$$

where $\dot{\xi}(t)$ is the relative velocity and $F(t)$ is its equivalent force, obtained from the 2^{nd} Newton's law:

$$F(t) = m(t)\ddot{\xi}(t) \tag{6.2}$$

where $\ddot{\xi}(t)$ is the relative acceleration and $m(t)$ is the moonpool mass, which is time varying due to the deformable volume condition and computed as:

$$m(t) = S_{mp}(BG + \xi(t)) \tag{6.3}$$

where, S_{mp} is the cross-section area of the moonpool, BG is the distance from the base of the moonpool to the CoG of the structure and $\xi(t)$ is the moonpol relative position. In order to obtain the global performance, 131 different sea states have been simulated according to the deployment sites characteristics. The duration of the simulations has been set to 500 waves, which is the minimum value to capture both, sea state energy stabilization and extreme events occurrence. Finally, the instantaneous power has been computed following the above described procedure and the average value has been placed in the net power matrix, a bi-variate matrix with respect to the significant wave height and the peak period. Results are shown in figure 6.10. The resonant region is clearly observed around $T_P = 6\ s$, the design resonant period, confirming what the previous analysis stated, in which power absorption by the moonpool is maximised.

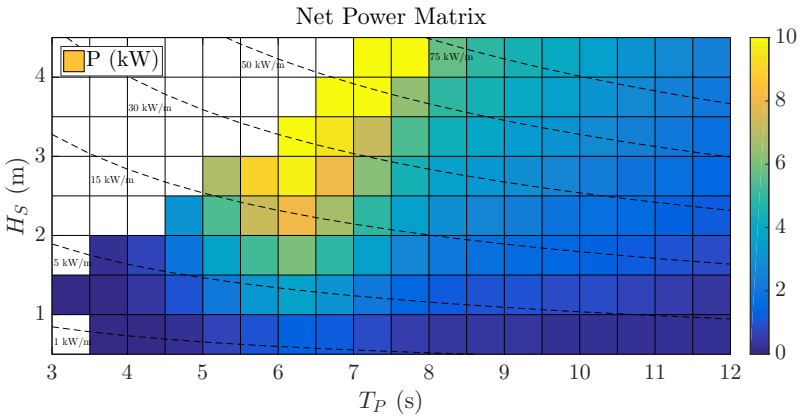

Figure 6.10: *Net Power Matrix for the MoonWEC device*

6.2.3 Wells Turbine Working Conditions

The Wells turbine working conditions assessment is carried out through confrontation between the stationary regime and the actual performance under the presence of waves. Waves' oscillatory motion introduce an acceleration to the moonpool motion which is not taken into account in the stationary simulations. Therefore, it is expected the Wells turbine not to reach optimal conditions. Figure 6.11 shows the comparison between the angular velocity of the several turbines for a monochromatic wave of $H = 0.5\ m$ and $T = 6\ s$ and its equivalent stationary situation, where the instantaneous velocity of the moonpool has been used as the stationary flow velocity, as in figure 5.66.

Figure 6.11 shows that the inertia of the turbine plays a key role in stabilizing the rotation. The energy stored during the moonpool velocity peaks is then used to keep the turbine rotating somewhat evenly when the moonpool relative velocity decreases approaching the stall area. Furthermore, it is observed that the angular velocity decreases with the number of installed blades. It can seem nonsense, as when the number of blades increases so does the turbine tangential force. Nevertheless, the axial force increases too causing a greater damping in the moonpool which in turn causes a decline in the oscillations. Figure 6.12 shows the sensitivity of the tested turbines over the wave height in regular waves.

A separated working area is observed at each turbine for each different wave height. However, the increment in the angular velocity is not proportional to the wave height. Also, no relevant differences on the time the each turbine reaches the stationary state are observed, regardless the wave height input. As expected, the higher the number of blades the sooner the stationary state is reached, not because its angular velocity is

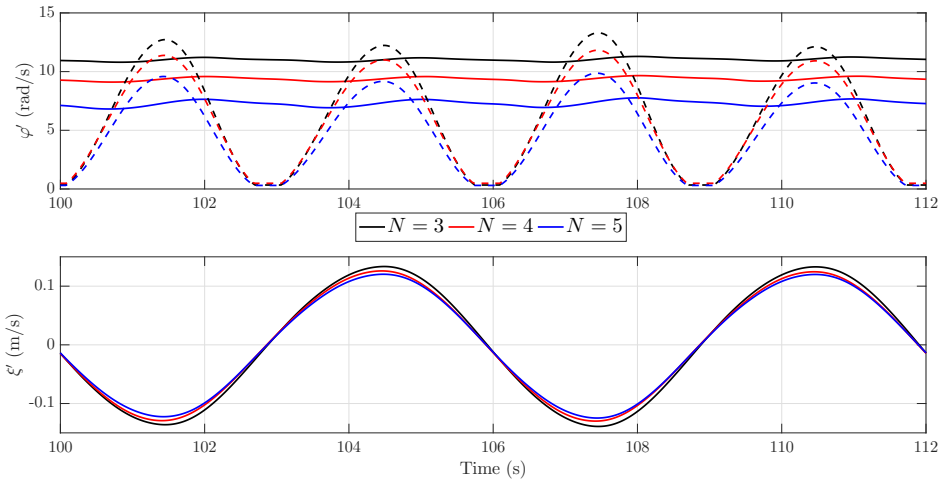

Figure 6.11: *a) Angular Velocity of the different turbines for an input wave of* $H = 0.5$ *m and* $T = 6$ *s. Dashed line show the stationary behaviour. b) Moonpool velocity for the different turbines*

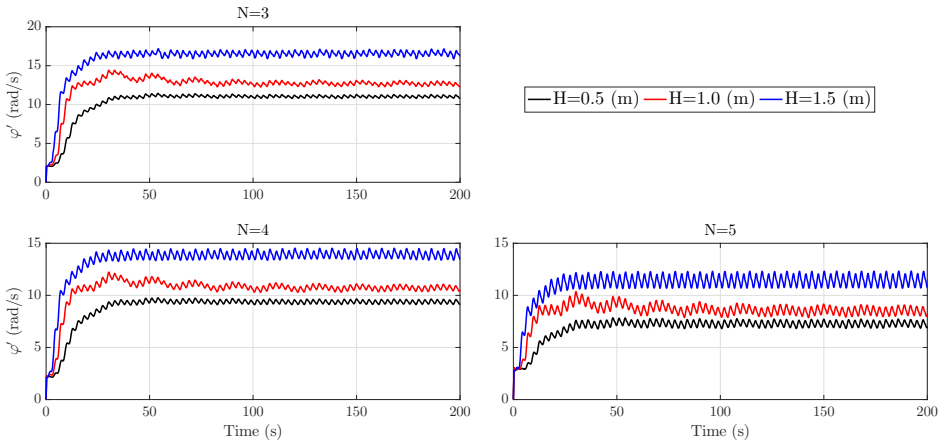

Figure 6.12: *Angular Velocity of the different turbines for different input waves of heights* $H = 0.5$ *m,* $H = 1$ *m,* $H = 1.5$ *m and period* $T = 6$ *s*

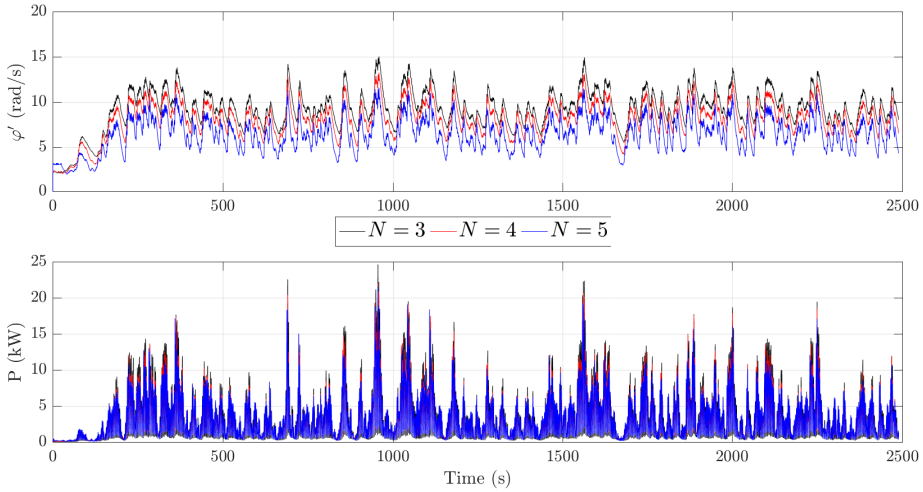

Figure 6.13: *a) Angular Velocity of the different turbines. b) Instantaneous produced power. For an input sea state of $H_S = 1.5$ and $T_P = 6$ s and 500 waves duration*

lower but because the tangential force is larger and hence, so is its acceleration. Finally, the turbines' performances have been tested in irregular waves. Figure 6.13 shows the angular velocity and the instantaneous electric power for the studied turbines under a sea state of $H_S = 1.5$ m and $T_P = 6$ s and a 500 waves duration.

Figure 6.13 shows a common pattern with figures 6.11 and 6.12. The angular velocity is inversely proportional to the number of blades of the turbine. The major effects introduced by irregular waves are identified. Firstly, the variation range of the angular velocity increases substantially, owing to the higher variability of the free surface of irregular waves and secondly, the average angular velocity decreases. As already seen in chapter 5.2.1.2, the energy spreads over several frequencies for irregular waves. Therefore, the resonant effect in the moonpool is weakened and the turbine rotates slower. Instantaneous power, shown in figure 6.13.b), displays a very peaked power output. This pattern, typical from WECs, is due to the variability of the free surface and poses a series of challenges to the WEC's power electronics unit. Peaks are typically an order of magnitude higher than the average production and create large instabilities in the grid, that is why substations on land account with large capacitors in order to rapidly store this peaks of energy and release them to the grid gradually afterwards. The fewer the number of blades in the turbine, the higher the power peaks and, on the contrary; the higher the number of blades the higher the troughs in the instantaneous power series. The average power production for each turbine is shown in table 6.1:

# of blades	$\bar{P}$ kW
3	3.49
4	3.27
5	3.51

Table 6.1: *AEP for a sea state of $H_S = 1.5$ m and $T_P = 6$ s and several W-T.*

No relevant difference is obtained in power production. However, the more stable pattern found in the turbine with 5 blades could be a decisive factor in order to make a choice.

6.2.4 General Performance

In order to assess the performance of the device globally, the power matrix is used. As introduced in section 6.2.2, the power matrix is a bivariate matrix that presents the average power output of a WEC at a given sea state. For this study 120 different sea states, corresponding to the wave climate at the deployment sites, have been simulated for a duration of the single sea state of 500 waves. Afterwards, the instantaneous power production has been averaged over time and placed at the corresponding sea state, defined by the coordinates H_S and T_P. The procedure has been followed by the three simulated variants of the Wells turbine. The power matrices presented in figures 6.14-6.16.

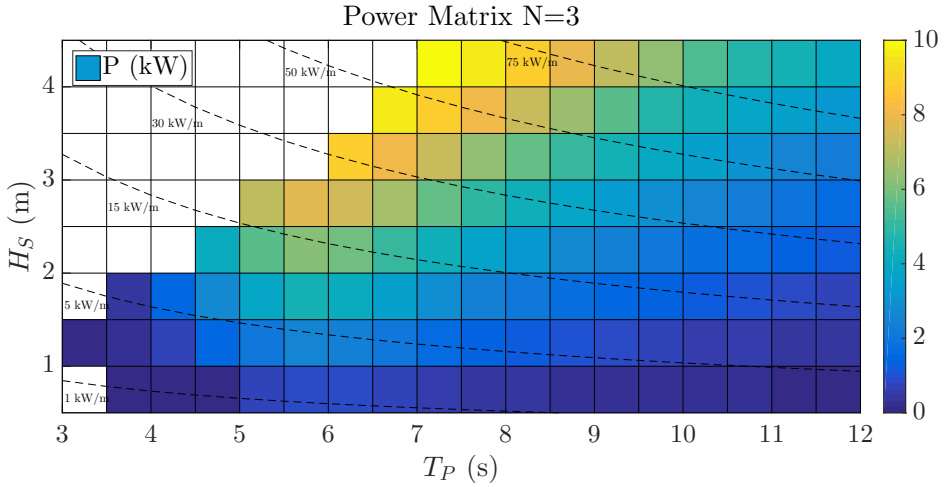

Figure 6.14: *MoonWEC with 3-blade W-T power output relative to the simulated sea states.*

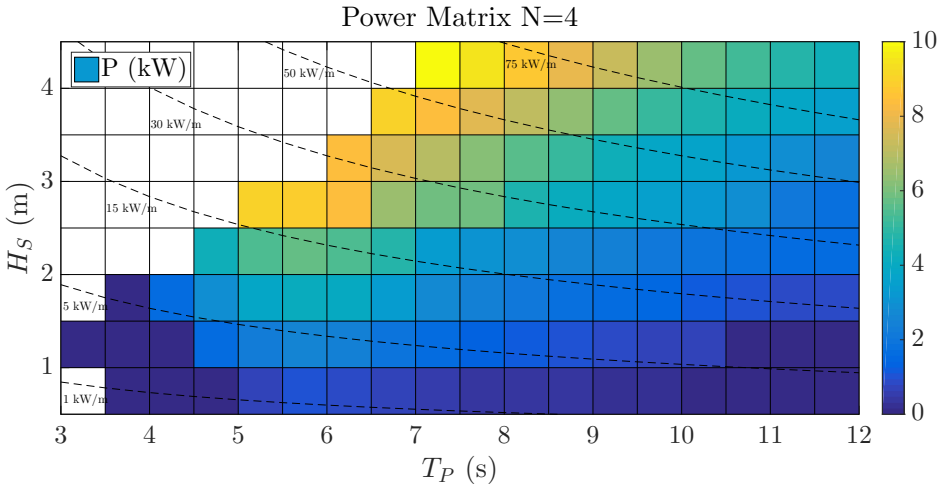

Figure 6.15: *MoonWEC with 4-blade W-T power output relative to the simulated sea states.*

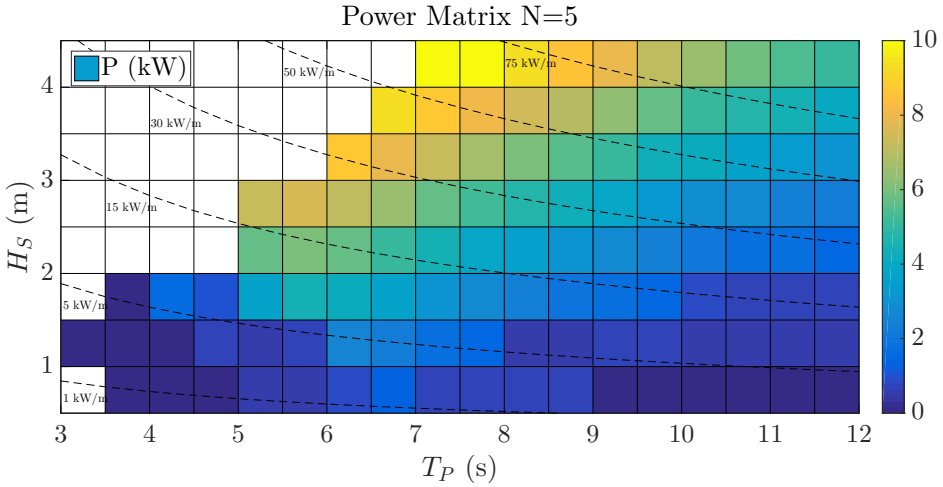

Figure 6.16: *MoonWEC with 5-blade W-T power output relative to the simulated sea states.*

The resonant region is still identified in figures 6.14-6.16, yet with less purity than in figure 6.10. The damping introduced by the turbines is causing a strong attenuation of the moonpool oscillations. This; in turn, is causing a decrease in the relative velocity between the blades and the moonpol, which further reduces the tangential force that generates the turbine's driving torque. Although the performance between the different turbines does not vary significantly. The 5-blade Wells turbine performs slightly better for high waves, the 3-blade turbine achieves higher production rates for small waves and finally, the 4-blade turbine gives better output rates for steep waves.

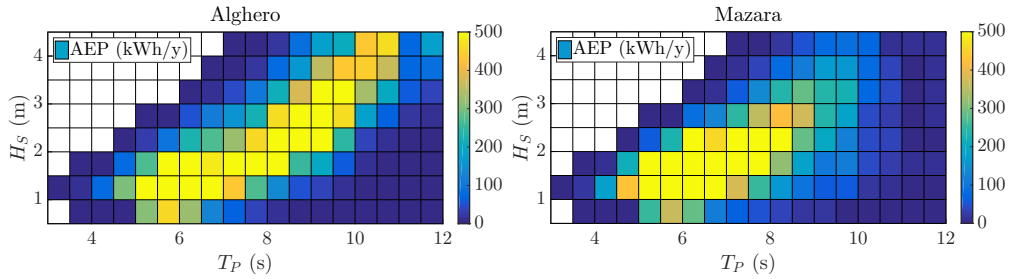

Figure 6.17: *AEP matrices for the 3-blade turbine device at Alghero and Mazara del Vallo*

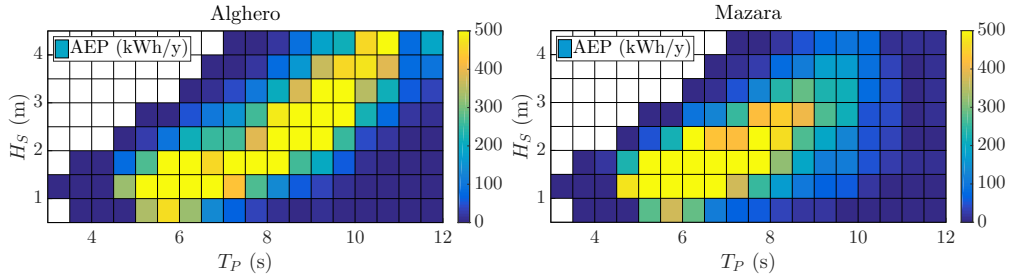

Figure 6.18: *AEP matrices for the 4-blade turbine device at Alghero and Mazara del Vallo*

6.2.5 Site Specific

A device's performance will vary depending on the deployment site since it depends on the wave resource characteristic climate. Therefore, in order to carry out a complete assessment, site-specific indicators must be generated. An efficient way to do so, is to cross the power matrix with the wave climate matrix of the installation site. Afterwards, by scaling it to the yearly hours, the AEP for each sea state is yielded. Hence, combining the matrices represented in figures 3.4 and 3.5 with the power matrices 6.14-6.16 the performance of each variant at both studied locations is obtained. Results for the device with the 3,4 and 5-blade turbine are shown in figures 6.17-6.19, respectively.

Wave climate at the study sites show a clear influence on the device performance. Furthermore, the patterns observed in figures 6.17-6.19 show good agreement with the climate figures 3.4 and 3.5, confirming the tuning of the devices has been done properly, widening the high efficiency range of the device. Also, the traits stated in the previous paragraph related to the power matrices can be identified, i.e. the 5-blade turbine is more suited for high waves and the 3-blade turbine for mild climates. Production rates are not excessively high, fact that would suggest and over-sizing of the Wells turbines.

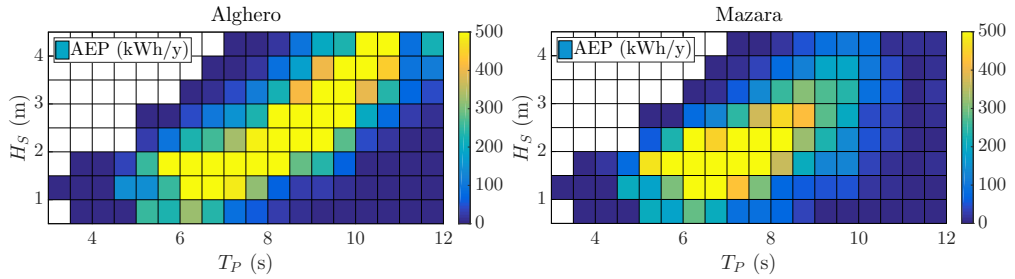

Figure 6.19: *AEP matrices for the 5-blade turbine device at Alghero and Mazara del Vallo*

# of blades	Alghero	Mazara del Vallo	Units
3	24.58	21.48	MWh/y
4	24.47	20.94	MWh/y
5	25.10	20.33	MWh/y

Table 6.2: *AEP at the study sites.*

Smaller turbines would damp less the moonpool oscillations and hence, gain in rotation; either in big waves, where performance is quite decent, and in small waves, where there is a large margin for improvement. Aggregating all the values of the matrices into a number yields the global performance of the device at the site. The general AEPs are shown in table 6.2.

As expected very little variation is found. However, it is confirmed that the 5-blade turbine is more suitable for high wave climates as it achieves the highest production at Alghero, which accounts for the most powerful climate between the study sites. On the other hand, the 3-blade turbine it is found to be more efficient for the milder climate of Mazara del Vallo.

6.3 CFD Reflection Analysis

6.3.1 Empty Numerical Wave Tank

A standard procedure to perform the reflection analysis is by first using an empty wave tank. That way, if the absorption methods were to be perfect, no reflection would be detected as no interfering objects are present. Furthermore, since the generated waves are unidirectional, a 2D numerical wave tank can be used, reducing the numerical domain considerably.

The numerical wave tank dimensions have been fixed for all the simulations, having a length of 25 m, a height of 1 m, a width of 0.025 m and a cell size of $dx = dy = dz = 0.025$ m, which makes a total of 40000 cells. The still water level is set at 0.5 m from the base. Simulated wave conditions are reported in table 6.3. In order to analyse the absorption performance a set of four wave gauges have been set in the domain. Their exact location varies according the wave characteristics, as stipulated by (101).

Case	$H(m)$	$L(m)$	Stokes order
a	0.01	2	1^{st}
b	0.01	4	1^{st}
c	0.04	2	2^{nd}
d	0.04	4	2^{nd}
e	0.1	2	5^{th}
f	0.1	4	2^{nd}

Table 6.3: *Tested wave conditions.*

Each case has been run for 90 s, at this point stability has been observed for all the simulations. Simulations applying the different generation-absorption methods (RM1, RM2, AWA and all the possible combinations between them) have been run for all the conditions in table 6.3, making the total number of run cases amount to 54. Figures 6.20-6.22 show the normalized reflection analysis time series for all wave conditions shown in table 6.3 and the following generation-absorption methods: AWA-AWA, RM1-RM1 and RM2-RM2.

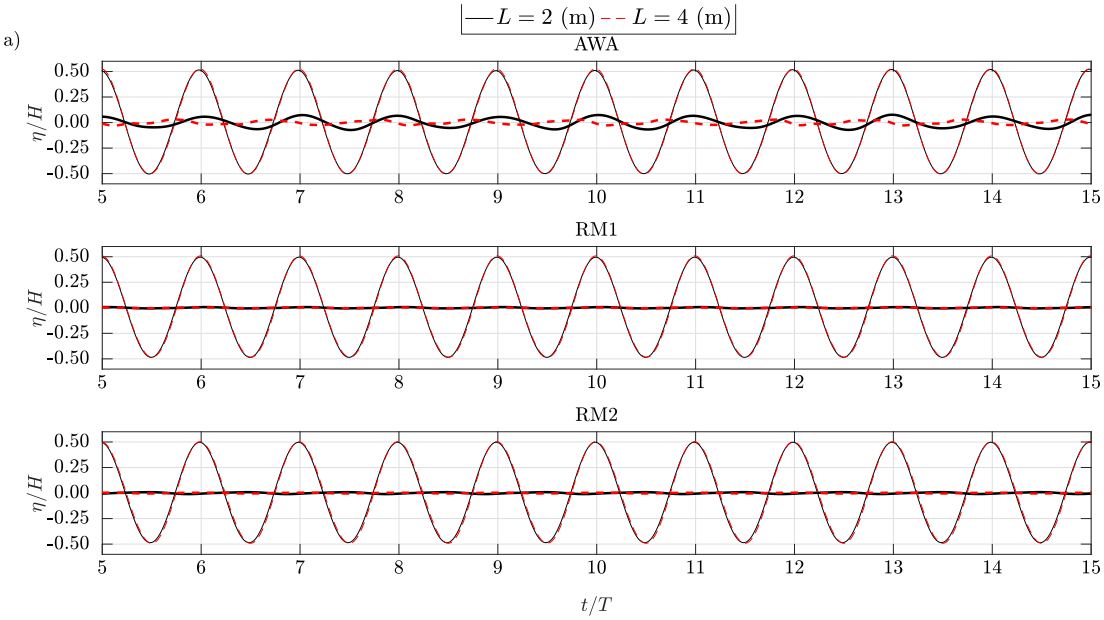

Figure 6.20: *Normalized incident (regular line) and reflected (bold line) components for the three methods. The solid line represents the waves with $L = 2$ m and the dashed line is for the waves with $L = 4$ m. Cases a and b from table 6.3 ($H = 0.01$ m)*

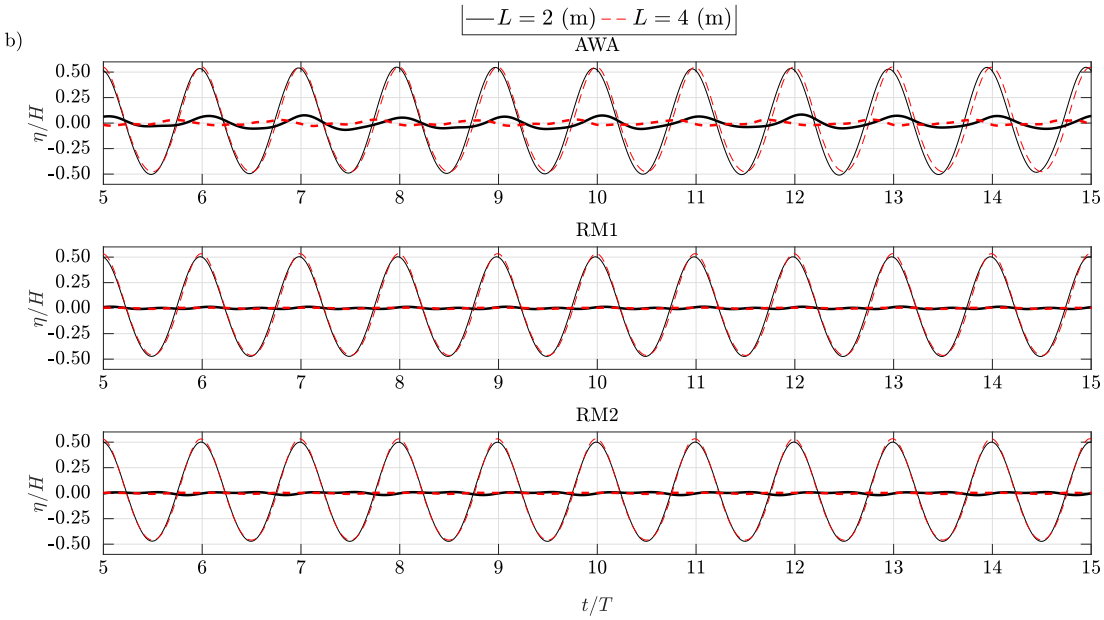

Figure 6.21: *Normalized incident (regular line) and reflected (bold line) components for the three methods. The solid line represents the waves with $L = 2$ m and the dashed line is for the waves with $L = 4$ m. Cases c and d from table 6.3 ($H = 0.04$ m)*

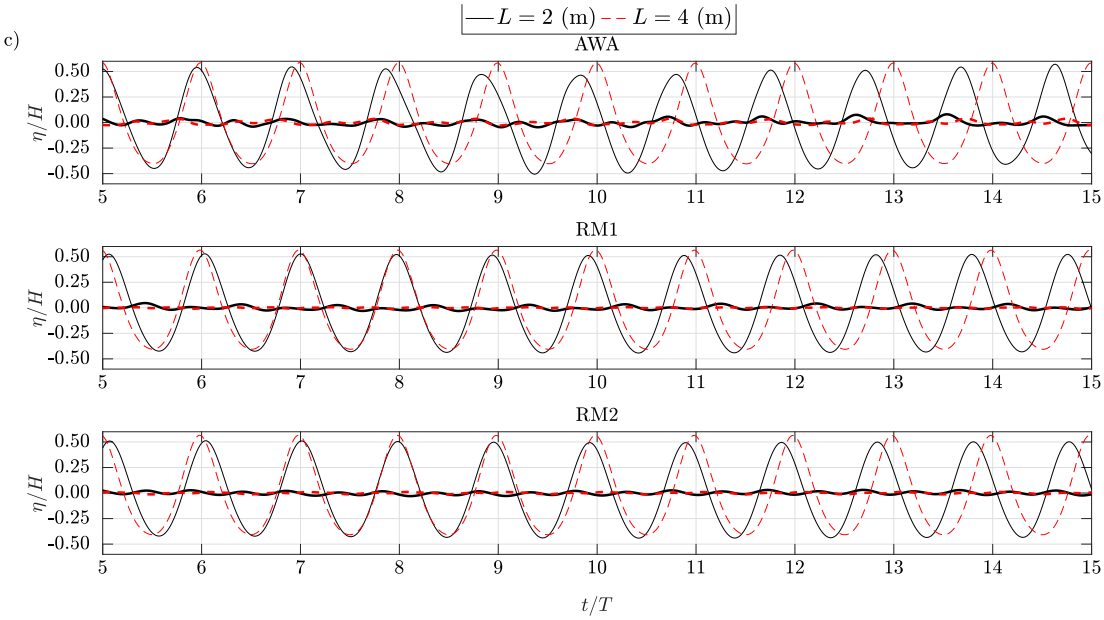

Figure 6.22: *Normalized incident (regular line) and reflected (bold line) components for the three methods. The solid line represents the waves with $L = 2$ m and the dashed line is for the waves with $L = 4$ m. Cases e and f from table 6.3 ($H = 0.1$ m)*

Figures 6.20- 6.22 evidence a general trend; independently from the simulated wave, RMs show better absorption than the AWA. For the latter, the Dirichlet BC is imposed at the generating and absorbing boundaries, see section 4.2.2. As a result, optimal absorption is only achieved under shallow water conditions, since a constant velocity over the vertical is needed in order to have a perfect match between the particle and the boundary velocities.

On the contrary, no relevant difference is found when comparing the RMs. RM1 uses an extra relaxation zone in the generation area (see figure 4.10) and hence, is less computationally efficient confirming that RM2 is globally a better choice.

When analysing figures 6.20-6.22 by wave conditions, it can be noted that figure 6.20 shows the best performance, followed by figure 6.21 and then by figure 6.22. This, denotes a clear absorption sensitivity related to wave steepness, revealing poorer absorption for steeper waves. However, for the case f (table 6.3), the cause for the higher amount of reflection may rely in the analysis method, rather than in the effective absorption itself. Zelt & Skjelbreia's method (101) is meant to be used for linear waves. However, it has shown to provide fairly good results for 2^{nd} order waves if the second harmonic is included in the analysis. In this case, the simulated wave characteristics

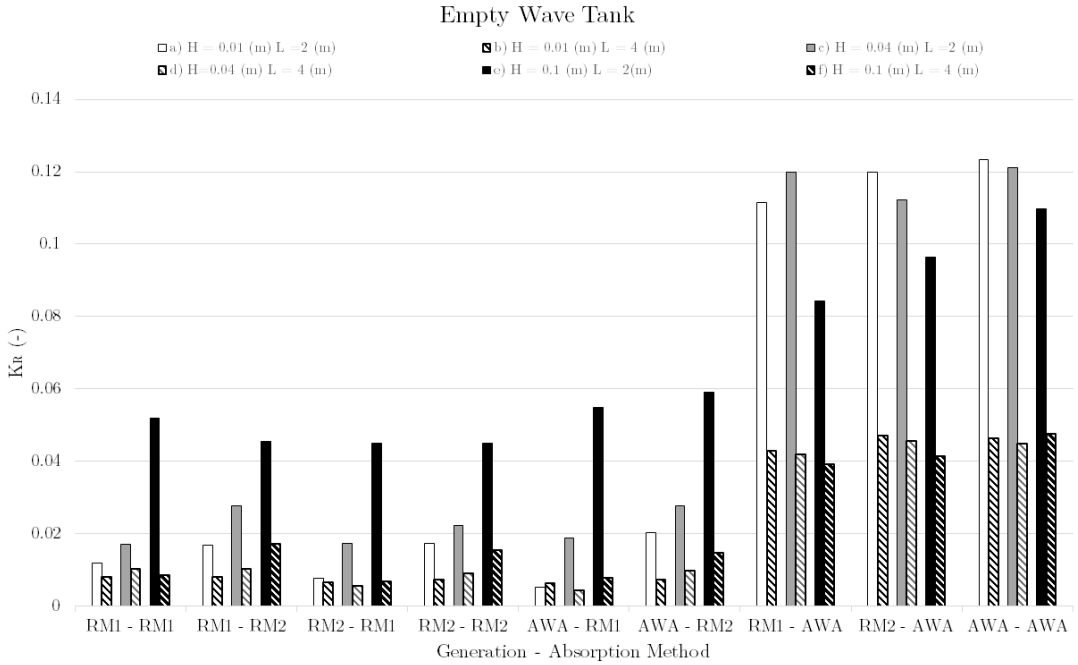

Figure 6.23: *Reflection coefficients for all the different method combinations*

comply the use of the 5^{th} order Stokes theory in generation and therefore, the use of Zelt & Skjelbreia's method (101) may lead to somewhat inaccurate results. In addition, when looking at the shape of the waves in figure 6.22, it can be stated that specifically for steep waves the RMs delivers a higher quality absorption than the AWA method. Figure 6.23 synthesizes the global generation-absorption performance of REEF3D for all the possible method combinations.

Several different trends are detected from figure 6.23. Firstly, the RMs achieve a higher absorption quota, as already detected in figures 6.20-6.22. Secondly, the long waves ($L = 4$ m) are much better absorbed than the short one ($L = 2\ m$) in all cases. Thirdly, reflection coefficients rocket for high order waves (case f in table 6.3) when using RMs, whereas the AWA method appears to be less sensitive to steep waves. Finally, the best contribution of figure 6.23 is that shows that through a convenient combination of different methods, high absorption rates can be obtained without sacrificing computational efficiency. For instance, applying wave generation with the AWA and setting a numerical beach (RM) at the back of the flume allows to gain in both, quality of absorption and simulation-running time.

To conclude the analysis in the empty numerical wave tank, two different irregular

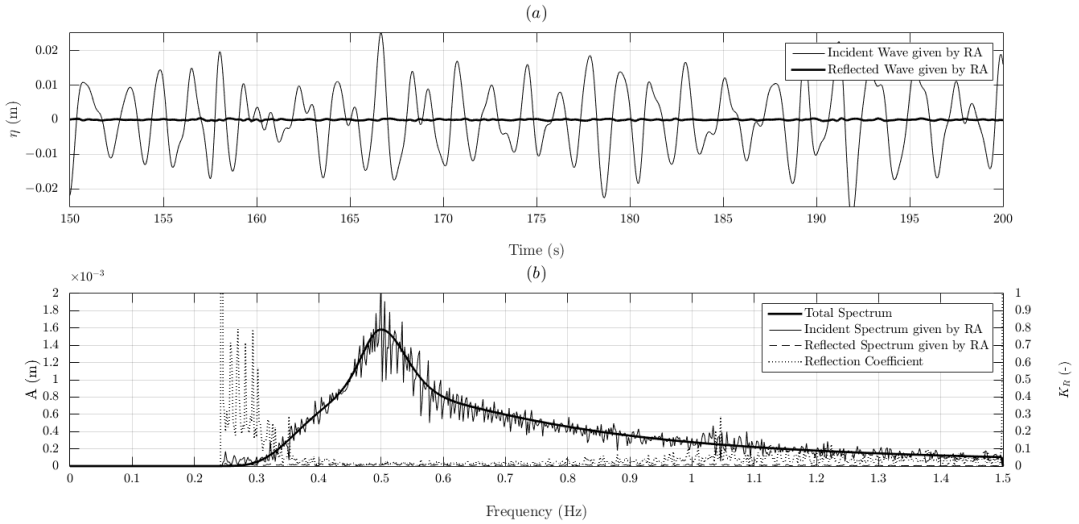

Figure 6.24: *Surface elevation generated according to JONSWAP $H_S = 0.04$ m and $T_P = 2.0$ s with the RM1. (a) Time series of incident (regular line) and reflected (**bold** line) irregular wave. (b) Wave amplitude components, total in **bold**, incident in regular, reflected in dashed and the reflection coefficient in dotted line.*

wave sea states have been generated according to the JONSWAP spectrum. Both spectra are defined by a common peak enhancement parameter of $\gamma = 3.3$ and $H_S = 0.04$ m, and two different peak periods of $T_P = 1.2$ s and $T_P = 2.0$ s. For irregular waves, simulations have been run for 500 s. The duration of simulation was determined after an spectral analysis which concluded that for 500 s, 90% of the theoretical spectrum components were generated. Figures 6.24 and 6.25 show the results of the reflection analysis, for the spectra described above. In sections (a) a 50 s fragment of the incident and reflected component is displayed, whereas in sections (b) the spectral compositions of wave amplitudes are presented. The results shown in the next two figure have been obtained by applying with the RM2.

A common pattern between regular and irregular waves is recognized from the time series. Figure 6.24.(a) shows a lower reflected component than figure 6.25.(a). The former corresponds to the $T_P = 2$ s spectrum, denoting longer waves within the spectral range; whereas the latter is obtained from the $T_P = 1.2$ s spectrum, which defines a shorter waves sea state. Thus, it can be concluded that also for irregular waves, longer waves are more efficiently absorbed than shorter waves.

However, different trends are observed in figures 6.24.(b) and 6.25.(b), their reflected spectra have different shapes. The reflected spectrum of figure (6.24.b) has the typical

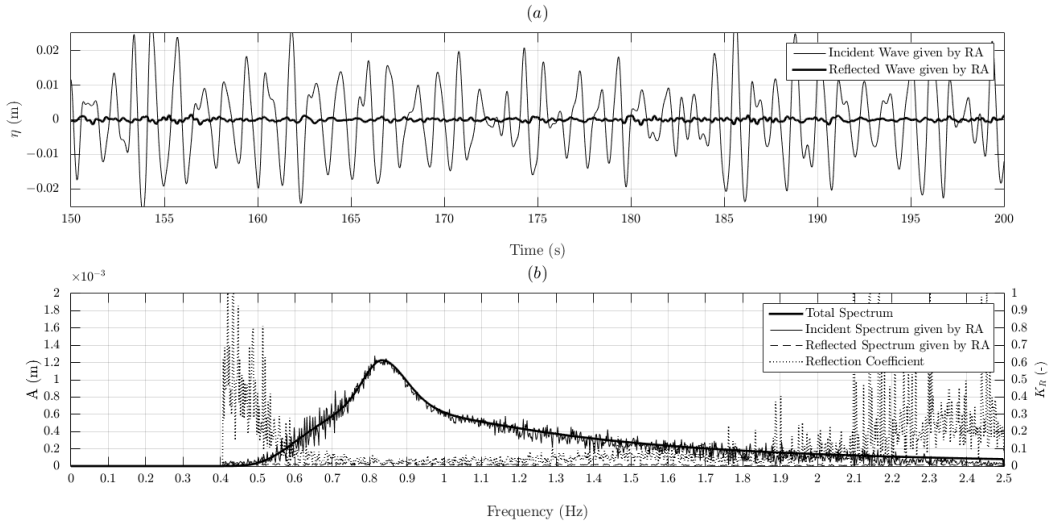

Figure 6.25: *Surface elevation generated according to JONSWAP $H_S = 0.04$ m and $T_P = 1.2$ s with the AWA method. (a) Time series of incident (regular line) and reflected (**bold** line) irregular wave. (b) Wave amplitude components, total in **bold**, incident in regular, reflected in dashed and the reflection coefficient in dotted line.*

JONSWAP shape, yet the one from figure (6.25.b) adopts a flat shape and seems to have a minimum below which no values are present. Since the order of magnitude of such values is 10^{-6} m, the numerical minimum might have been reached, as it is strictly related to the element size. Furthermore, two high reflection areas are identified towards the edges of the spectra. At low frequency edge, this merely given by the reduction of the incident wave spectrum. On the contrary, at the high frequency edge, increase of K_R and numerical stability is detected only from $2.1Hz$ (figure 6.25.b). This manifests the absorption limit for this particular numerical wave tank configuration.

Like in the case of regular waves, a complete analysis of the generation-absorption methods has been carried out for the two spectra shown in the figures above. Results are presented in figure 6.26.

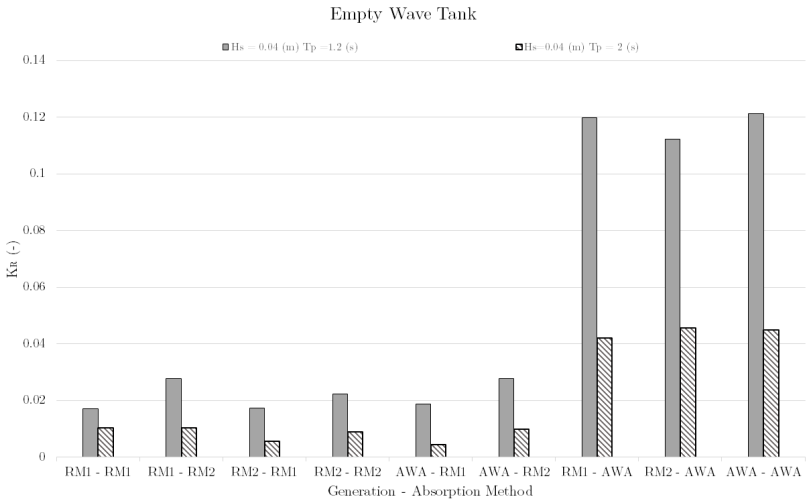

Figure 6.26: *Reflection coefficients for all the different method combinations for irregular waves.*

Results for irregular waves, show a high degree of consistency with the ones obtained for regular waves; in other words, same trends are identified for both cases, regular and irregular waves. Such as higher absorption rates for the RMs, higher reflection for shorter and steeper waves and the possibility to obtain an optimal solution by combining different methods. This solution would apply if using RMs for the primary absorption and AWA at the generation area only, indeed AWA-RM1 gives the best performance for $T_P = 2s$ and the third for $T_P = 1.2s$. This last idea is crucial when simulating irregular waves, because the required simulation timespan needs to be large if a realistic sea state is to be simulated. Consequently, any decrease of computation times gains in relevance, particularly if the simulation time-pans are very large and hence, costly from the computational point of view.

6.3.2 Cylinder Tests

A three-dimensional tank has been set to realize a series of tests including a fixed vertical cylinder placed at its centre. Dimensions of the numerical wave tank are variable. The only fixed dimensions are the tank width, which is $5m$, the cylinder diameter $\varnothing = 0.25m$, the depth $0.5m$ and the cell size $dx = dy = dz = 0.025m$. The length of the tank is been left variable according to the simulated wavelength and the generation-absorption method used. Figure 6.27 displays a section view of the described numerical wave tank.

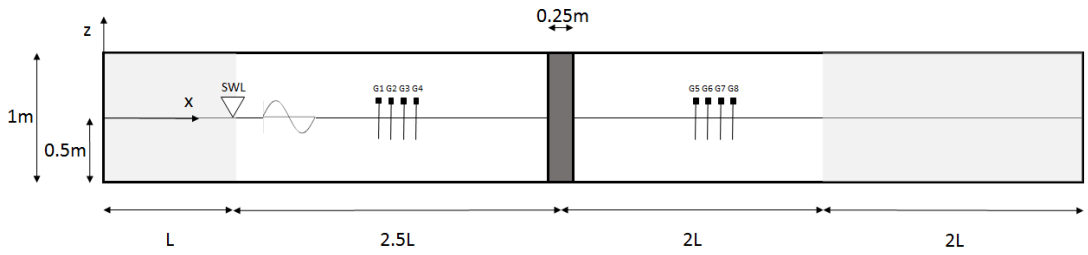

Figure 6.27: *NWT used for simulations.*

The cases described in table 6.3 have been selected to run the simulations. The reflection analysis procedure is, again, the (101) with four wave gauges. The variable length of the tank and its proportions have been chosen in order to obtain the smallest tank possible but leaving space enough to perform a high-quality reflection analysis. By using this system the number of elements of the mesh varies within a range of $[3-6]M$ and therefore, the computational gain is substantial, specially if the large number of elements is taken into account.

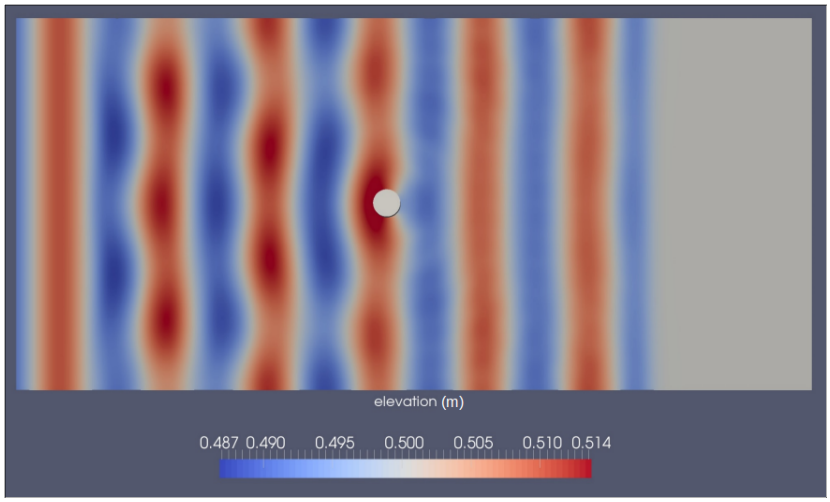

Figure 6.28: *Free surface elevation in NWT.*

Figure 6.28 shows the free surface (η) at time $t = 38.3$ s for the case a in table 6.3, using the RM2 either for wave generation and absorption with the numerical beach at the back of the tank. The relaxation areas can be clearly identified from the figure at both edges of the basin; the generation area where the wave is neat and clear and the numerical beach where no waves are present. Reflection originated at the cylinder can be well appreciated in a qualitative way; nonetheless, a quantitative analysis is

presented in hereinafter.

For this particular analysis, not only the water free surface has been studied but also the force exerted by the waves onto the cylinder. Furthermore, this force has been compared to the classical theory developed by McCamy&Fuchs in (68). Moreover, a relationship between the reflection from the cylinder and the wave forces has been sought. The results from this analysis are presented in figure 6.29.

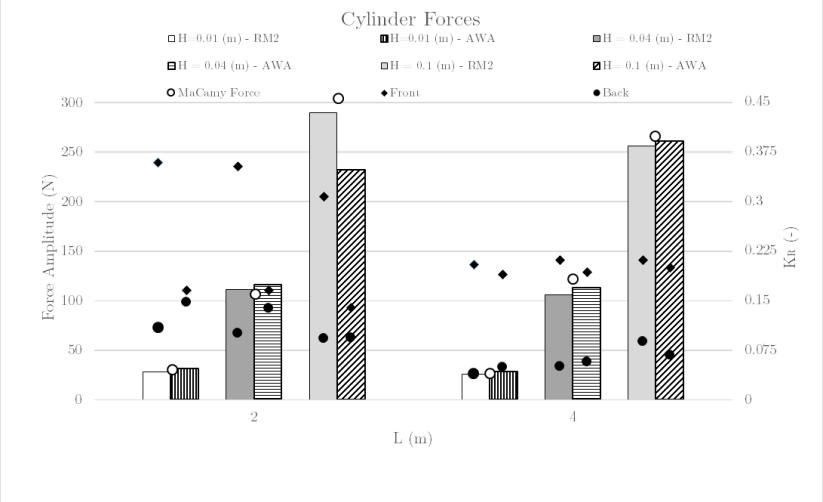

Figure 6.29: *Amplitude Forces and reflection coefficients at the front and at the back of the cylinder.*

The forces computed around the cylinder match fairly well with the theoretical approach in every case. Furthermore, no major discrepancy is found between RM2 and AWA, but in case f of table 6.3.

Reflection has been computed at the front and at the back of the cylinder, see wave gauge sets in figure 6.27. The reason why it has been decided to control reflection at the rear part of the cylinder, where reflection is of no relevance for this analysis' purposes, is to operate as a double-check that simulation is going as planned. On the one hand, reflection at the back of the cylinder is stable for each case, although cross-modes and oblique reflections make reflection slightly higher than what obtained for the empty numerical wave tank. On the other hand, reflection at the front of the cylinder varies depending on the generation method for the short waves $L = 2m$ (cases a,c,e in table 6.3). A short length from the relaxation area could explain poor absorbing behaviour when the reflected wave is beyond a certain size, i.e: reflected wave from a structure. If this is the case, re-reflection should occur. Re-reflection is no other than a reflected

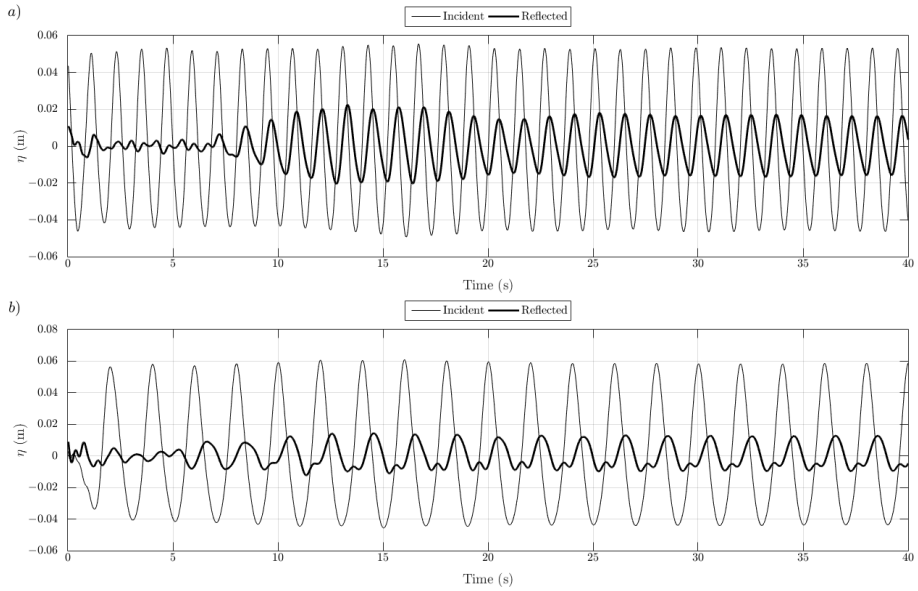

Figure 6.30: *Time-series of incident and reflected waves in front of the cylinder. (a) and (b), cases e and f in 6.3, respectively*

wave which is reflected again with the same direction as the incident wave. In order to check that effect, time-series of case e and f are displayed in figure 6.30.

Whereas no re-reflection is identified in figure 6.30.a), a clear trend is observed within the time span $[10 - 20]s$, in figure 6.30.b). Since the water level is the composition of incident and reflected waves, the re-reflection phenomenon should also be appreciated when observing the time series of the force on the cylinder. Figure 6.31 shows the force for the two cases described above.

The re-reflection pattern can be identified also from figure 6.31.a), although is very subtle. The phenomenon can be explained in the following way: the peak of the force corresponds to the first fully developed wave, then due to the reflection force tends to decrease and finally, when re-reflection reaches the cylinder the force begins to increase as re-reflections travels in the same direction of the incident wave. On the contrary, no effect can be detected from figure 6.31.b) as the force amplitude remains constant after the initial transient period.

In conclusion, the RM may have some difficulties in absorbing high reflected waves with the actual configuration (relaxation length=L). Although longer relaxation areas for wave generation could be defined, it is recommended to switch to the AWA. The domain is smaller and therefore the simulations shorter and the re-reflection issue is

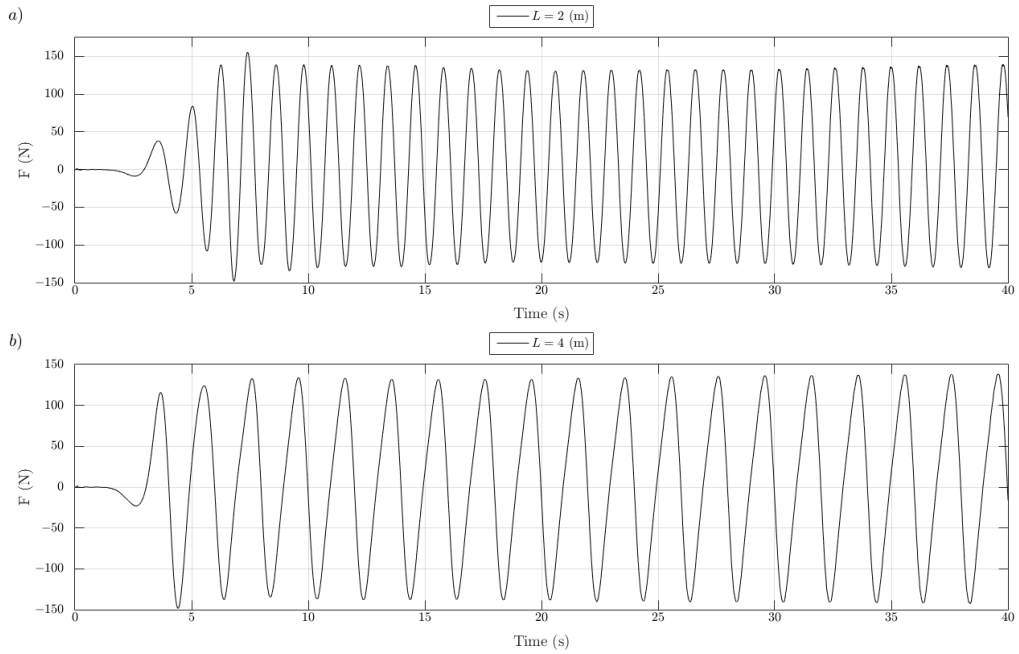

Figure 6.31: *Force measurements at the cylinder. (a) and (b), cases e and f in 6.3, respectively*

avoided.

6.3.3 Slope Tests

The combined effect of wave breaking and bottom slope is of interest to the authors and reflection could be a suitable indicator to describe such influence. For this series of test a two-dimensional numerical wave tank has been set. As for the cylinder case, the length of the tank is not fixed and depends on the generated wave length and the bottom slope, see figure 6.32. Since the element size is extremely reduced $dx = dy = dz = 0.005m$ in order to capture the breaking phenomenon properly, a variable size domain allows to maximise the computational efficiency for each particular simulation.

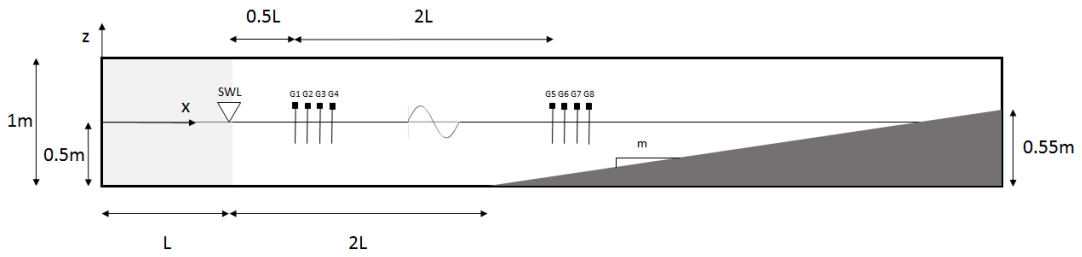

Figure 6.32: *NWT used for simulations.*

Simulations have been based on three parameters, wave height H, wave length L and bottom slope m. Out of these three parameters, the well known surf similarity parameter is obtained ($\zeta = \frac{m}{\sqrt{(\frac{H_0}{L_0})}}$), giving good insight of the type of wave breaking as defined by (20). Table 6.4 defines all the simulated cases. Actually, each case has been run twice, first using the RM2 and then using the AWA in order to generate waves. No numerical beach is used at this section since the slope is totally impermeable.

Case	$H_0(m)$	$L_0(m)$	m	ζ	Breaking
a	0.01	2	1/35	0.40	Spilling
b	0.01	4	1/35	0.57	Transition
c	0.01	2	1/25	0.57	Transition
d	0.01	4	1/25	0.80	Plunging
e	0.01	2	1/15	0.94	Plunging
f	0.01	4	1/15	1.33	Plunging

Table 6.4: *Tested wave conditions.*

(20) also defined, from empirical experience the following relation: $K_R = 0.1\zeta$, which links the reflection and the surf similarity parameter. In figure 6.33 it has been represented as Battjes Reflection.

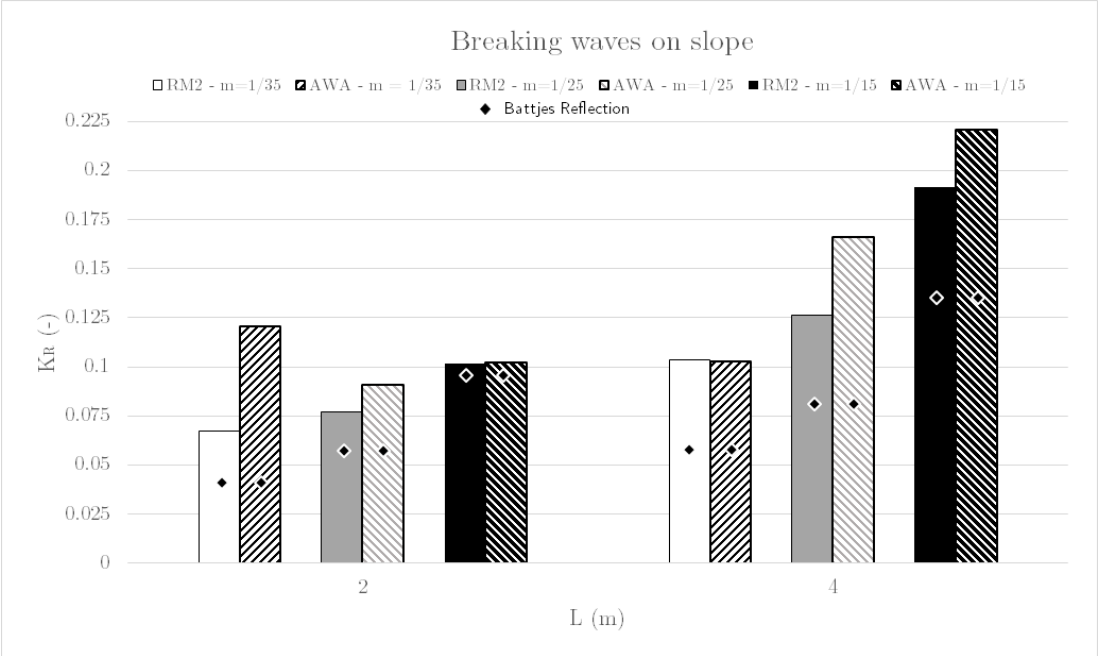

Figure 6.33: *Reflection coefficients for different methods, waves and slopes*

For both waves, as expected reflection increases as the slope of the bottom does. In general, the RM2 achieve higher absorption rates compared to AWA. However, reflection is always higher than the Battjes assumption. This could be due to the fact that wave breaking is a very complex process. In CFD, it is usually assumed to be a turbulent phenomenon in which energy is dissipated. A lack of accuracy in describing the turbulent processes would decrease the energy dissipation and therefore, this energy would be compelled to travel back and thus, increasing reflection in the tank as observed in figure 6.33.

6.3.4 OpenFOAM Comparison

Since (55) gave a very detailed overview of different showcases, on the performance of their AWA algorithm for a numerical wave tank using OpenFOAM. A comparison has been set up in order to compare both open source codes. In (55), the numerical set-up was the following: a 2D wave flume 20.62 m long, 0.58 m wide and 0.70 m high with a cell size of 0.02 m on the horizontal plane and 0.01 m in the vertical. REEF3D works on a cartesian grid that compels DiveMESH (REEF3D's meshing tool) to generate cubic elements, the chosen element size for the mesh is $dx = dy = dz = 0.02$ m which makes a total of 36085 elements. The still water level is set at 0.40 m from the base.

Under this set-up 8 different wave conditions have been tested: Two Solitary waves with Heights of .05 m and 0.15 m respectively. And then six regular waves, with periods 2,3 and 4 s, combining the previous wave heights. Using the linear wave theory for $H = 0.05$ m and $T = 2.0$ s, the Stokes 2^{nd} order for $H = 0.05$ m and $T = 3.0$ s and Cnoidal theory for the rest of the cases. For regular waves, the simulation time is set to 120 s and for the solitary waves is set to 60 s instead. To measure reflection in the solitary waves a surface elevation gauge has been set at 7.5 m from the inlet. To analyse reflection for the regular waves the Mansard and Funke method has been used (70) with the gauges' spacing specified in (55). The exact same set up and method have been used in this work in order to obtain the reflection coefficients. Furthermore, results obtained from simulations accounting with the RM 2 have also been included. When using the RM for the solitary wave cases ($L = \infty$) the length of the corresponding relaxation zones was set to 8 m. Results are shown in table (6.5):

$T(s)$	$H(m)$					
	0.05			0.15		
	REEF3D		Higuera	REEF3D		Higuera
	RM	AWA		RM	AWA	
Solitary	5.50%	1.45%	1.51%	1.16%	1.07%	2.63%
2	1.2%	4.4%	4.6%	2.8%	2.4%	11.2%
3	0.3%	1.5%	3.8%	2.1%	2.8%	7.3%
4	0.8%	0.4%	2.3%	5.9%	2.0%	6.7%

Table 6.5: *Reflection Coefficients.*

The AWA module in REEF3D obtains lower reflection coefficients for all cases. The differences are generally low for the small waves ($H = 0.05$ m), especially for $T = 2$ s. As for the high waves ($H = 0.15$ m), they become quite substantial, moving in the range of $[2 - 3]$% for REEF3D and $[6 - 12]$% for OpenFOAM. Generally, reflections decrease with wave steepness, showing good agreement with what stated in the first part of this section. No clear trend is observed when comparing the method performance for these cases. For some cases, RM obtains slightly lower reflection coefficients than the AWA, such as for $H = 0.05$ m and $T = 3$ s, but for some others the AWA performs marginally better, like for $H = 0.05$ m and $T = 3$ s. However, the differences are so small on average that can be considered as irrelevant driving the focus of the choice to the computational costs. For the solitary waves AWA presents lower reflection coefficients, a reason for this is that the relaxation areas are too short to deliver an acceptable wave absorption,

and increasing their size would ultimately rise the computational costs.

In order to obtain comparable results among the simulations computational costs, the following index has been developed:

$$C_E = \frac{t_{sim} * N_{Pr}}{D} = \left(\frac{h}{s}\right) \tag{6.4}$$

where the t_{sim} is the computational time of the simulation, N_{Pr} is the number of processors used and D is the duration of the simulation. Unlike in fig. (6.23) the size of the numerical domain has been modified according the requirements of the simulation. In other words, for all the simulations run with the RM mode the numerical domain changes due to the relaxation zone length, which is proportional to the wavelength (71). On the other hand, the size of the domain remains untouched when the AWA is active, giving the perfect conditions to compare the relevance of the method choice.

$T(s)$	$H(m)$			
	0.05		0.15	
	AWA	RM	AWA	RM
2	0.735	1.14	1.21	1.88
3	0.679	1.28	1.32	3.05
4	0.735	1.36	1.26	3.56

Table 6.6: *Computational Effort* $\left(\frac{h}{s}\right)$.

Table 6.6 shows quite clearly the relevance of the method choice. A constant increase of the computational effort is observed for the RM as the period increases perfectly matching the theory, which states that longer waves mean longer numerical domains due to the relaxation zones. The AWA does not show any signs of correlation with wavelengths revealing its convenience for certain conditions, such as long waves. For the worst case ($H = 0.15\ m$ and $T = 4\ s$), the computational effort is tripled, whereas for the best case ($H = 0.15\ m$ and $T = 4\ s$) it stands slightly above than the 55% increase.

7

Conclusions

In this thesis, wave energy conversion in the Mediterranean Sea is explored via the numerical modelling of two different WEC devices. A numerical model based on the potential flow theory has been set. The code written with the commercial software Matlab ®, allows parallel computing and implements several tools to improve its computational efficiency; such as the Prony's method to compute the hydrodynamic forces in the time domain and optimized Newton-Raphson algorithm to handle iterative processes. Besides, the performance of the CFD open-source code REEF3D (23) is investigated through wave reflection analysis.

A wave energy resource characterisation of the Italian coasts has been carried out in order to determine the most promising locations for wave energy conversion. Up to 25 years of wave data from the National Italian Wave Measurement Network (RON) (2) have been thoroughly analysed. From the eight different locations involved in the analysis, the two most energetic sites have been identified and selected as possible future wave energy exploitation spots. Both areas are located in islands; the most energetic is Alghero, in Sardinia and the second most energetic is Mazara del Vallo, in the south-western corner of Sicily. Dimensioning and optimization of both WEC has been carried out according to the wave climate given at the chosen locations.

Both WEC numerical models are based on the potential flow theory and simulate the device behaviour upon several DoFs in irregular waves. The first modelled device, named HPA-LG, is a point absorber composed by a heaving buoy and a permanent magnet linear generator. The second studied WEC is a new technology developed in this thesis. It merges several current working principles willing to aggregate the assets of each type. It is a floating OWC but with the particularity that the reduced size of

the floating structure makes it a point absorber as well with the characteristics of an oscillating body. Energy conversion is achieved by a Wells turbine placed directly in the water column.

Several tests have been conducted for REEF3D performance assessment. Different wave types have been simulated in several environments, such as an empty wave tank, a mono-pile and a slope. Furthermore, several wave generation and absorption methods have been tested and compared.

7.1 HPA-LG

With the aim to estimate the feasibility of wave energy conversion in the Mediterranean Sea, this thesis thoroughly analyses the body dynamics of the HPA-LG device, with particular focus on the surge effect and in the energy production. Four variants of the WEC, whose characteristics are reported in table 5.2, have been modelled. The model runs in the time domain, uses irregular waves, is able to handle multi-body systems with various degrees of freedom and delivers the instantaneous electric power, which is later used to obtain both, generic and site-specific performance indicators. In order to increase its computational efficiency, the code has been parallelized and the prony's method has been adopted, reducing the total simulation-time by an order of magnitude.

A sensitivity analysis on the dimension of the submerged body has been performed by running several free oscillation tests. These, have confirmed that the optimal submerged sphere diameter is $\varnothing = 1.50m$. Figures 5.1 and 6.2 show that the resonant frequency of the system is shifted towards the most persistent sea state period range. On the one hand, the presence of the submerged body increases the electric production by approximately 25% when considering only heave and by 10% when tanking into account both, heave and surge. On the other hand, it could lead to undesired effects from the technical/operational point of view, such as the increase of the working time of the end-stop survival mechanism or the appearance of slamming effects occurring in the interconnecting lines due to its large inertia. For all the stated above, it is reasonable to worry about the technical/economical feasibility of a point absorber with a submerged body disposed in such configuration, particularly when considering the increase of the electricity production when accounting for the surge.

Another remarkable conclusion that can be drawn from the previous section is that the surge can either, have no relevant contribution (two-body device) or even cause a slight decrease on the production (three-body device) as presented in figure 6.7. De-

pending on the wave characteristics, as identified in figures 6.3 and 6.4, the device tends to reduce its production rate as the wave steepness grows when including the surge mode. On the contrary, when the wave steepness is relatively low the electric production is increased, yet in smaller proportion since the available wave energy flux is lower for flatter waves. However, these variations do not represent substantial alterations in the device productivity. From this, it can be assumed that the surge mode may be neglected when modelling a two-body point absorber WEC for energy production assessment only.

The shift of the piston not only affects the electric production directly, but more importantly, the dynamic behaviour of the device. Since the piston offset makes it easier to reach the survival position of the device, for the same wave conditions, when considering the surge, the end-stop mechanism is activated sooner and the more the end-stop mechanism is working, the higher the probability of breakdowns, which may be induced by slamming effects and high tensions in wires and springs. Consequently, the surge mode should be always considered when assessing the mechanical performance of the device and the survivability conditions.

The average annual production, is rather low for the single device. Therefore, the exploitation concept for this kind of the devices lies in the wave energy farm. Deploying a substantially elevated number of devices in arrays. Some studies (18, 27, 28) conclude that, if well spatially distributed, a wave energy farm can produce at a higher rate than the single device. Since the available wave power resource in the Mediterranean Sea is much lower than in other seas, nowadays the only way to make wave energy exploitation feasible with point absorbers is by means of multiple-device plants.

7.2 MoonWEC

The first step in the MoonWEC's development process consist in the determination of the general dimensions of the device through the frequency domain tests. The optimal draft, for which the moonpool resonates at the established period of $T = 6\ s$ is $d = 9\ m$. The draft of the moonpool is equivalent to the draft of the structure. Furthermore, frequency domain tests also show that the external diameter of the structure must be $\varnothing = 5\ m$ in order to achieve resonance for that period.

Time domain tests, aimed to define more precisely the dimensional parameters of the device, reveal good agreement with the results obtained in the frequency domain tests, defining the natural periods of the device in heave and pitch, $T_0^h = 6\ s$ and

$T_0^p = 31.5\ s$, respectively. Whereas resonance in heave is the main dimensioning target, resonance in pitch is a rather undesired effect. That is why such natural period in pitch is a satisfactory result since it lies at the limit of the linear wave theory making the resonance event highly improbable. Extra elements, such a disc at the bottom and a cone at the top, have been added to the structure in order to create a phase lag between the structure and the moonpool. By increasing the phase between the two parts of the device, their relative motion is amplified, thus maximising the power absorption. Figure 7.1 shows a technical drawing with the dimensions of the optimized device.

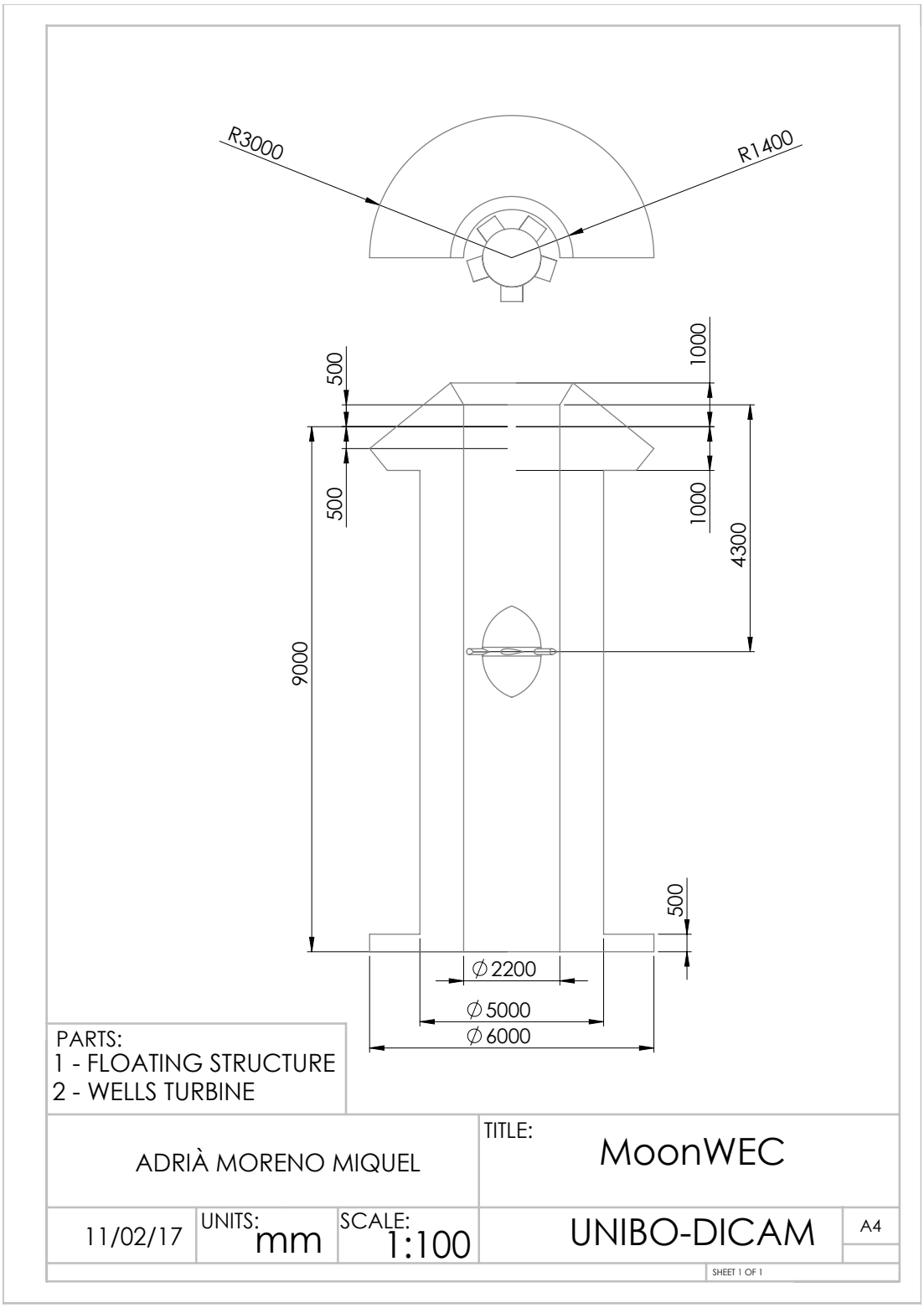

Figure 7.1: *Technical sheet of the MoonWEC device*

Afterwards, the mooring system of the device has been designed. The CALM is the mooring type that best fulfils the dynamic requirements, as exerts very little influence on the heave mode while preventing the device from drifting away. Six different configurations have been tested. A description of the different variants is provided in table 5.4 and figure 5.26. Results show that all variants have very little influence on the heave mode. Also, it is found that the most pre-tensioned schemes reduce considerably the natural period in pitch, taking it to a dangerous region where it may likely be excited during stormy events. Regarding the connection point to the structure, the best performance is achieved when the mooring is attached at the level of the structure's CoG, having very little influence in the pitch mode as well. Also, very stable results have been obtained for the double-line mooring system, where one line is attached at the base of the structure while binding the other is bound at the top. However, this configuration has been disregarded due to the extra cost that an extra line represents for very little gain in performance. The natural period of the system in surge has been found to be $T_0^s > 100\ s$ assuring the stability of the system for that mode. Finally, the mooring system has been tested under the 25-year return period stormy conditions at Alghero. Results show a good performance, either geometrically and dynamically never reaching the limit position and minimum breaking load of the wire. However, further investigation should be done in the future at that step, since until now free surface elevation has been modelled according to the linear wave theory. Loads may increase drastically due to non-linearity of waves and stormy free surfaces have a non-linear behaviour as non-linearity increases with steepness.

A low parametric instability has been found due to the interaction between the moonpool and the structure. Owing to the relative moonpool oscillation the device metacentre is not static. When the device is resonating, the metacentric oscillations are maximised and that causes a shift in the average position of the oscillations in pitch and surge. The short distance between the moonpool and the structure CoG makes this effect bounded and allows the mooring system to absorb it posing no threat to the device general stability.

In figure 6.10, the net power is shown. That is, the wave energy absorbed by the moonpool, which shows higher rates around the natural period in heave $T_0^h = 6\ s$ backing the design procedure followed until now. Furthermore, these levels of power absorption suggest electricity production is feasible, since in the energy chain, they represent the available power for the PTO.

The PTO system is composed by two elements, a Wells turbine and a PM generator.

Three different models of W-T have been tested, accounting with 3, 4 and 5 blades. W-T have truly narrow working conditions; therefore, its efficiency is extremely variable, being quite elevated for very precise conditions and really low for the rest. In order to maximise the power production a joint control law has been designed in which, the PM generator exerts the sufficient resistance to ensure the W-T is always working in the optimal range regardless external conditions. A closed feedback loop has been implemented in which, the active control system, based on the moonpool velocity, applies the right rotation resistance. In such way, it is ensured that the energy extracted from the moonpool is maximal.

In stationary conditions, the angular velocity is proportional to the number of blades. However, this is not the case in the presence of waves; in fact, the opposite occurs and as the number of blades increases, the angular velocity decreases. This is due to the increasing drag component of the turbines that smooths the moonpool oscillations. This is an important factor in the design process of the turbine as there is the risk of over-damping the moonpool and dissipate the energy from the waves. Furthermore, it is seen that variability in the instantaneous power signal decreases as the number of blades grows. This is an important remark, as one of the major inconveniences in wave energy conversion is smoothing the highly peaked power signal generated by the converters. Hence, if the work is partially done in the turbine the power electronics system may work more efficiently.

Power outputs ranging from $(1 - 15)\ kW$ have been obtained for the three tested turbines. Also, an increase of power is identified around the design natural period for the moonpool and the floating structure confirming its proper tuning. The sensitivity analysis on the number of blades of the turbine shows very similar results among turbines; as for example in the annual energy production rates, where at Alghero and Mazara are around $25MWh/y$ and $20MWh/y$, respectively. A slight higher production is found for the 5-blade turbine for high waves, performing better at Alghero, and for the 3-blade turbine for mild waves, achieving higher production rates at Mazara del Vallo. However, the results indicate the turbine is over dimensioned.

Several modifications in the design of the device will be introduced in the future. A sensitivity analysis will be conducted on the diameters of the turbine and the moonpool. By increasing the moonpool diameter its mass is augmented while its natural period is being kept as it only depends on the draft. That increase in inertia will make the moonpool less sensitive to the drag introduced by the turbine. Thus, having the moonpool higher oscillations will allow the turbine to increase its driving torque. Also, a shift of

the natural periods of the moonpool and the floating structure in opposite directions may be tested. Having the moonpool and structure resonating at different frequencies will no longer concentrate the energy at a single frequency but spread it into a wider range instead, increasing the energy capture for disseminated wave climates such as the one given at Alghero.

The work done in this thesis is purely numerical, validation through experimental tests needs to be done. Especially for the MoonWEC model, being a novel device, to complete the proof of concept phase and proceed to further development stages, is of outmost importance to be certain that the model predicts accurately the device behaviour.

Comparison with the HPA-LG The HPA-LG power matrices show a higher rated power of the WEC and a broader production regime. Meaning that for high and long waves performance of the HPA-LG is more efficient. On the contrary, the MoonWEC has a narrower action range. The MoonWEC takes advantage of the relative motion between the structure and the moonpool and this is practically null in the over-resonant region, as both moonpool and structure, account with a static response for these conditions. However, performance of the MoonWEC is superior for mild waves, having substantial higher rates, especially for the resonant frequency range. When comparing both annual energy productions it can be seen that the MoonWEC practically doubles the production of the 2-body HPA-LG, whereas with respect to the 3-body HPA-LG, the produced energy is increased by a 50 %. Furthermore, the undesired effects of wire slamming and end-stop mechanism activation are not given in the MoonWEC. There are no end-stop in the MoonWEC as the PTO system is completely different and does not require a maximum safety position. Also, extreme wave climates test has shown that the mooring system wires are far from reaching the limit condition for a 25-year return storm. For all the stated above, the MoonWEC seems a more reasonable choice for Mediterranean wave climates.

7.3 Reflection Analysis

This section of the thesis explores the performance of the CFD open-source software REEF3D in wave generation and wave absorption in a numerical wave tank. REEF3D has two different wave absorption and generation modules; the RM and the AWA, performance between them has also been analysed.

Several tests have been conducted. First, an empty numerical tank has been tested, in regular and irregular waves. Afterwards, a 3D tank with a fixed vertical cylinder has been simulated for several regular waves. Subsequently, a 2D tank with a steep bed has been set and different several slope values and waves have been analysed. Finally, the tests carried in (55) have been replicated with REEF3D and the results compared to the original ones published in (55).

Six different regular waves, going from linear up to 5^{th} order Stokes waves, and 2 irregular sea states based on the JONSWAP spectrum have been used in the empty tank. It has been common for all tests that the numerical beach implemented with the RM has higher absorption rates than the AWA. Another common result is that short and steep waves are more easily reflected than long and flat waves regardless the implemented absorption method. Reflection rates for irregular sea states are slightly higher than for regular waves, since high and low frequency components of the spectrum are not well absorbed.

It must be stressed that the biggest advantage though, lies in the combination of different modules in the same simulation; i.e. to generate waves the AWA module is selected and to absorb them a numerical beach is set through the RM2. This particular configuration delivers the best overall performance, obtaining elevated absorption rates and reduced computation times, since no extra space for relaxation zones is needed in the wave generation boundary of the numerical domain.

The same regular wave characteristics have been used for the cylinder tests. However, the wave generation-absorption modules have been restricted only to RM2 and AWA since are the most promising ones. The AWA module has proved to be more resilient to highly reflected waves, such as the ones generated by the structure. Re-reflection phenomena were observed when using the RM2 for wave generation. A wavelength for the relaxation zone is not enough to absorb such waves and therefore the size of the area should be increased, causing a substantial loss of computational efficiency.

Forces computed around the cylinder are in good agreement with the theoretical values given by (68). Re-reflection phenomena can also be observed in the time-series of the force, although is not as evident as in the reflection analysis.

Three different slopes and two different regular waves have been simulated in the last tests. Wave breaking influence on reflection was intended to be shown. The AWA tends to deliver higher reflection than the RM2, specially for long waves. Furthermore, reflection coefficients tend to be higher than the empirical values, this could be due to non ideal capture of the turbulent wave breaking.

Regarding the comparison with OpenFOAM, REEF3D has proved to have reached the same level for this matter. It is better performant for regular waves when using RM module, whereas for the AWA performance is similar. The computational cost of the simulations is presented proving the high efficiency of the AWA module.

Bibliography

[1] The naca airfoil series. Technical report, National Advisory Committee Aerodynamics.

[2] URL http://www.telemisura.net.

[3] *AQWA User Manual*. http://www.ansys.com/Products/Structures/ANSYS-Aqwa,.

[4] NOTUR. The Norwegian Metacenter for Computational Science. http://www.notur.no/hardware/vilje. Accessed: 2016-02-16.

[5] URL http://plotdigitizer.sourceforge.net/.

[6] Wamit user manual. http://www.wamit.com/manual.htm.

[7] *Analytic Geometry*. Encyclopaedia Britannica, 2008.

[8] *Anchor Manual 2010, The guide to Anchoring*, 2010.

[9] A. B. Aalbers. The water motions in a moonpool. *Ocean Engineering*, 11:557–559, 1984.

[10] International Energy Agency. Key world energy statistics 2010, 2010.

[11] George B. Airy. On tides and waves. *Encyclopaedia Metropolitania*, 5(192):241–396, 1845.

[12] Mayilvahanan Alagan Chella, Hans Bihs, Dag Myrhaug, and Michael Muskulus. Breaking characteristics and geometric properties of spilling breakers over slopes. *Coastal Engineering*, 95:4–19, 2015.

[13] Alessandro Antonini, Adrià Moreno Miquel, Renata Archetti, Silvia Bozzi, and Giuseppe Passoni. Preliminary design of a point absorber with linear generator designed for energy production off the Italian coasts. In *Tenth European Wave and Tidal Energy Connference (EWTEC)*, 2013.

[14] Alessandro Antonini, Alberto Lamberti, Renata Archetti, and Adrià Moreno Miquel. Dynamic overset rans simulation for a wave-driven device for the oxygenation of deep layers. *Ocean Engineering*, 127: 335–348, 2016.

[15] Alessandro Antonini, Alberto Lamberti, Renata Archetti, and Adrià Moreno Miquel. Cfd investigations of oxyflux device, an innovative wave pump technology for artificial downwelling of surface water. *Applied Ocean Research*, pages 16–31, 2016.

[16] R. Archetti, S. Bozzi, and G. Passoni. Feasibility study of a wave energy farm in the western mediterranean sea: Comparison among different technologies. In *Proceedings of the International Conference on Offshore Mechanics and Arctic Engineering - OMAE*, volume 5, pages 447–452, 2011.

[17] A. Babarit and G. Delhommeau. Theoretical and numerical aspects of the open source bem solver nemoh. In *Proc. of the 11th European Wave and Tidal Energy Conference (EWTEC2015), Nantes, France*, 2015.

[18] A. Babaritl. On the park effect in arrays of oscillating wave energy converters. *Renewable Energy*, 58:68 – 78, 2013.

[19] R. Barreia, S. H. Sphaier, and I. Q. Masetti. Behavior of a mono-column structure (monobr) in waves. In *Proc., 24th International Conference on Offshore Mechanics and Arctic Engineering, Halkidiki, Greece*, 2005.

[20] J. A. Battjes. Surf similarity. In *Proc., 14th International Conference on Coastal Engineering, Copenhagen, Denmark*, pages 466–480, 1974.

[21] Alvin Bayliss and Eli Turkel. Radiation Boundary Conditions for Wave-Like Equations. *Communications on Pure and Applied Mathematics*, 33(ii):707–725, 1980.

[22] Jean-Pierre Berenger. A perfectly matched layer for the absorption of electromagnetic waves. *Journal of Computational Physics*, 114(2):185–200, 1994.

[23] H. Bihs. REEF3D : Open source CFD. *www.reef3d.com*, 2013.

[24] G.W. Boehlert, G. R. McMurray, and C. E. Tortorici. Ecological effects of wave energy development in the pacific northwest. Technical report, 2007.

[25] Ion Boldea and S.A. Nasar. *Electric Drives*. 2016.

[26] Silvia Bozzi, Adrià Moreno Miquel, Alessandro Antonini, Giuseppe Passoni, and Renata Archetti. Modeling of a point absorber for energy conversion in Italian seas. *Energies*, 6(6):3033–3051, 2013.

[27] Silvia Bozzi, Mariana Giassi, Adriá Moreno Miquel, Alessandro Antonini, Federica Bizzozero, Giambattista Gruosso, Renata Archetti, and Giuseppe Passoni. Wave energy farm design in real wave climates: the Italian offshore. *Energy*, 2017.

[28] B. F. M. Child and V. Venugopal. Optimal configurations of wave energy device arrays. *Ocean Engineering*, 37(16):1402 – 1417, 2010.

[29] A. Chorin. Numerical solution of the Navier-Stokes equations. *Mathematics of Computation*, 22:745–762, 1968.

[30] Core Writing Team, R. K. Pachauri, and Meyer L. A. (Eds.). Ipcc, 2014: Climate change 2014: Synthesis report. contribution of working groups I, II and III to the fifth assessment report of the intergovernmental panel on climate change, 2014.

BIBLIOGRAPHY

[31] S. Corsini, L. Franco, Inghilesi R., and Piscopia R. *Italian Wave Atlas*. APAT- UNIVERSITA' ROMA TRE.

[32] J. Cruz. *Ocean Wave Energy*. Springer, 2008.

[33] G. Delhommeau. *Les problemèmes de diffraction-radiation et de résistance de vagues: étude théeorique et résolution numérique par le method des singularités*. PhD thesis, E.N.S.M. Nantes, 1987.

[34] O. Edenhofer, R. Pichs-Madruga, Y. Sokona, K. Seyboth, P. Matschoss, S. Kadner, T. Zwickel, P. Eickemeier, G. Hansen, S. Schlö mer, and C. von Stechow. Ipcc, 2011: Summary for policymakers, 2011.

[35] A.V. Efimov, Y. G. Zolotarev, and V.M. Terpigoreva. Mir Publishers, Moscow, 1985.

[36] Bjorn Engquist and Andrew Majda. Numerical radiation boundary conditions for unsteady transonic flow. *Journal of Computational Physics*, 40(1): 91–103, 1981.

[37] A. P. Engsig-Karup. *Unstructured nodal DG-FEM solution of high-order boussinesq-type equations*. PhD thesis, Technical University of Denmark, Lyngby, Denmark, 2006.

[38] E. Esmailzhade and A. Goodarzi. Stability analysis of a calm floating offshore structure. *International Journal of Non-linear Mechanics*, 36:917–926, 2001.

[39] A. F. de O. Falcão and L. M. C. Gato. *Air turbines*. Elselvier, Oxford, 2012.

[40] António F De O Falcão. Wave energy utilization: A review of the technologies. *Renewable and Sustainable Energy Reviews*, 14(3):899–918, 2010.

[41] J. Falnes and K. Budal. Wave-power conversion by power absorbers. *Norwegian Maritime Research*, 6: 6–11, 1978.

[42] Peter Frigaard and Michael Brorsen. A time-domain method for separating incident and reflected irregular waves. *Coastal Engineering*, 24(3–4):205 – 215, 1995.

[43] Duclos G., A. Clément, and G. Chatry. Absorption of outgoing waves in a numerical wave tank using a self-adaptative boundary condition. *International Journal of Offshore and Polar Engineering*, 3(11): 168–175, 2001.

[44] L.M. Gato and A.F. de O. Falão. Aerodynamics of the wells turbine. *International Journal of Mechanic Sciences*, 30:383–395, 1988.

[45] Dan Givoli. High-order local non-reflecting boundary conditions: A review. *Wave Motion*, 39(4):319–326, 2004.

[46] Y. Goda. Random seas and design of maritime structures. 2000.

[47] Yoshimi Goda. On the methodology of selecting design wave height. volume 1, pages 899–913, 1988.

[48] Yoshimi Goda and Yasumasa Suzuki. Estimation of Incident and Reflected Waves in Random Wave Experiments. volume 1, pages 828–845, 1976.

[49] W. P. Graebel. *Engineering fluid mechanics*. Taylor % Francis, 2001.

[50] John Gronbech, Thomas Jensen, and Henning Andersen. Reflection analysis with separation of cross modes. volume 1, pages 968 – 980, Orlando, FL, USA, 1997.

[51] H. Gupta, R. Belvins, and R. Banon. Effect of moonpool hydrodynamics on spar heave. In *Proc. of 27^{th} International Conference on Offshore Mechanics and Arctic Engineering, Estoril, Portugal*, 2007.

[52] G. Hagerman and T. Heller. Wave energy: a survey of twelve near-term technologies. In *Proceedings of the international Renewable Energy Conference, Honolulu, HAWAII*, 1988.

[53] Hansen, A. G. *Fluid Mechanics*. John Wiley and Sons, New York, NY, 1967.

[54] P. K. Hasselmann, T. P. Barnett, E. Bouws, H. Carlson, D. E. Cartwright, K. Enke, J. A. Ewing, H. Gienapp, D. E. Hasselmann, P. Kruseman, A. Meerburg, P. Miler, D. J. Olbers, K. Richter, W. Sell, and Walden H. Measurements of wind-wave growth and swell decay during the joint north sea wave project (jonswap). *Ergnzungsheft zur Deutschen Hydrographischen Zeitschrift Reihe*, 12:95, 1973.

[55] P. Higuera, L. J. Lara, and I. J. Losada. Realistic wave generation and active wave absorption for Navier-Stokes models application to OpenFOAM. *Coastal Engineering*, 71:102–118, 2013.

[56] P. Higuera, L. J. Lara, and I. J. Losada. Simulating coastal engineering processes with OpenFOAM. *Coastal Engineering*, 71:119–134, 2013.

[57] N. G. Jacobsen, D. R. Fuhrman, and J. Fredsøe. A wave generation toolbox for the open-source CFD library: OpenFOAM. *International Journal for Numerical Methods in Fluids*, 70(9):1073–1088, 2012.

[58] Niels G. Jacobsen, Marcel R. A. van Gent, and Guido Wolters. Numerical analysis of the interaction of irregular waves with two dimensional permeable coastal structures. *Coastal Engineering*, (102):13–29, 2015.

[59] G. S. Jiang and C. W. Shu. Efficient implementation of weighted ENO schemes. *Journal of Computational Physics*, 126:202–228, 1996.

[60] A. Kamath, M. Alagan Chella, H. Bihs, and Ø. A. Arntsen. Cfd simulations of wave propagation and shoaling over a submerged bar. *Aquatic Procedia*, 4: 308–316, 2015.

[61] Joseph B. Keller and Dan Givoli. Exact non-reflecting boundary conditions. *Journal of Computational Physics*, 82(1):172–192, 1989.

[62] B. J. Koo, M. H. Kim, and Randall R. E. Mathieu instability of a spar platform with mooring and risers. *Ocean Engineering*, 31:2175–2208, 2004.

[63] Petri Lampola. *Directly Driven, Low-Speed Permanent-Magnet Generators for Wind Applications*. PhD thesis, Helsinki University of Technology, Finland, 2000.

[64] J. L. Lara, M. Del Jesus, and I. J. Losada. Three-dimensional interaction of waves and porous coastal structures using OpenFOAM®. Part II: Experimental validation. *Coastal Engineering*, 83: 259–270, 2012.

[65] Luca Liberti, Adriana Carillo, and Gianmaria Sannino. Wave energy resource assessment in the Mediterranean, the Italian perspective. *Renewable Energy*, 50: 938–949, 2013.

[66] L. Q. Liu, B. Zhou, and Y. G. Tang. Study on the nonlinear dynamic behavior of deep sea spar platform by numerical simulation and model experiment. *J. Vib. Control*, 10:1528–1537, 2014.

[67] M. S. Longuet-Higgins. On the statistical distribution of the heights of sea waves. *Journal of Marine Research*, 1952.

[68] R.C. MacCamy and R.A. Fuchs. *Wave forces on piles: A diffraction theory*. University of California, Dept. of Engineering, 1954.

[69] F. Magnusen. *On design and analysis of synchronous permanent magnet machines for field weakening operation in hybrid electric vehicles*. PhD thesis, Royal Institute of Technology, Sweden, 2004.

[70] E P D Mansard and E R Funke. The Measurement of Incident and Reflected Spectra Using a Least Squares Method. pages 154–172, 1980.

[71] S. Mayer, A. Garapon, and L. S. Sørensen. A fractional step method for unsteady free surface flow with applications to non-linear wave dynamics. *International Journal for Numerical Methods in Fluids*, 28:293–315, 1998.

[72] M. E. McCormick. Analysis of a wave-energy conversion buoy. *AIAA Journal of Hydrodynautics*, 8: 77–82, 1974.

[73] Michael E. McCormick. *Ocean Engineering Mechanics*. Cambridge University Press, 2010.

[74] G. Møork, A. Kabuth, and M. Pontes. Assessing the global wave energy potential. In *Proc., 29th International Conference on Offshore Mechanics and Arctic Engineering*, pages 447–454, 2010.

[75] J.N. Newman. The evaluation of free surface green functions. In *Proc., 4th Inernational Conference on Ship Hydrodynamics, Washington*, 1985.

[76] I. Orlanski. A simple boundary condition for unbounded hyperbolic flows. *Journal of Computational Physics*, 21(3):251–269, 1976.

[77] S. Osher and J. A. Sethian. Fronts propagating with curvature- dependent speed: algorithms based on Hamilton-Jacobi formulations. *Journal of Computational Physics*, 79:12–49, 1988.

[78] W. J. Pierson and L. A. Moskowitz. Proposed spectral form for fully developed wind seas based on the similarity theory of s. a. kitaigorodskii. *Journal of Geophyisical Research*, 69:5181–5190, 1964.

[79] S. Raghunathan. Aerodynamic forces on aerofoils at high angles of attack. In *AIAA National Fluid Dynamics Congress, Cincinnati, USA*, 1988.

[80] S. Raghunathan. The wells air turbine for wave energy conversion. *Prog. Aerospace Sci.*, 31:335–386, 1995.

[81] S. Raghunathan, C. P. Tan, and O. O. Ombaka. The performance of wells self rectifying air turbine. *Aeronautics Journal RAeS*, 89:369–379, 1986.

[82] Shin Hyung Rhee and Fred Stern. RANS Model for Spilling Breaking Waves. *Journal of Fluids Engineering*, 124(2):424, 2002.

[83] P. Ricci, J. Saulnier, A.F. ao, and T. Pontes. Time-domain models and wave energy converters performance assessment. In *Proc., 27th International Conference on Offshore, Mechanics and Arctic Engineering, Portugal*, 2008.

[84] M. Sadraey. *Aircraft Performance*. VDM Verlag, 2011.

[85] S. Salter. Wave power. *Nature*, 249:720–724, 1974.

[86] N. Scholtz and A. and Klein. *Aerodynamics of Cascades*. Neuilly sur Seine, France, Advisory Group for Aerospace Research and Development, North Atlantic Treaty Organization, 1977.

[87] C. W. Shu and S. Osher. Efficient implementation of essentially non-oscillatory shock capturing schemes. *Journal of Computational Physics*, 77:439–471, 1988.

[88] A. Sommerfeld. Lectures on theoretical physics. In *Academic Press. New York*, 1956.

[89] P.D. Spanos, Vincenzo R. Nava, and F. Arena. Coupled surge-heave-pitch dynamic modelling of spar-moonpool-riser interaction. *Journal Offshore Mechanic Arctic Engineering*, 2011.

[90] S. H. Sphaier, F. G. S. Torres, I. Q. Masetti, A. P. Costa, and C. Levi. Monocolumn behavior in waves: experimental analysis. *Ocean Engineering*, pages 1724–1733, 2007.

[91] D. P. Struge. Prediction of performance of wells wave power turbine. In *I.E.E. Conference*, 1981.

[92] R. Tagori, C. Arakawa, and M. Suzuki. Estimation of prototype performance and optimum design of wells turbine. *Research in Natural Energy*, 20:127–132, 1987.

[93] K. Tarrant and C. Meskell. Investigation on parametrically excited motions of point absorbers in regular waves. *Ocean Engineering*, 111(1):67–81, 2015.

BIBLIOGRAPHY

[94] E. Turkel and a. Yefet. Absorbing PML boundary layers for wave-like equations. *Applied Numerical Mathematics*, 27(4):533–557, 1998.

[95] J. Twidell and Weir T. *Renewable Energy Resources*. Routledge, 2015.

[96] H. van der Vorst. BiCGStab: A fast and smoothly converging variant of Bi-CG for the solution of nonsymmetric linear systems. *SIAM Journal on Scientific and Statistical Computing*, 13:631–644, 1992.

[97] D. Vicinanza, L. Capietti, V. Ferrante, and P. Contestabile. Estimation of the wave energy in the italian offshore. *Journal of Coastal Research*, 64: 613–617, 2011.

[98] Z. Wang, J. Yang, and F. Stern. An improved particle correction procedure for the particle level set method. *Journal of Computational Physics*, 228:5819–5837, 2009.

[99] B. Whittaker, W. Beattie, M. Folley, C. Boake, A. Whright, and M. Osterried. The limpet wave power project - the first years of operation. URL http://web.sbe.hw.ac.uk/staffprofiles/bdgsa/shsg/Documents/2004sem/limpet 2006. Renewable Energy.

[100] D. C. Wilcox. *Turbulence modeling for CFD*. DCW Industries Inc., La Canada, California., 1994.

[101] J.A. Zelt and James E. Skjelbreia. Estimating incident and reflected wave fields using an arbitrary number of wave gaugesl. In *Proc., International Conference on Coastal Engineering*, 1992.

[102] D. Zwillinger. *CRC Standard Mathematical Tables and Formulae*. 2011.